NOVEL GROUND STATES AND EXCITATIONS IN CLARINGBULLITE AND AVERIEIVITE QUANTUM MAGNETS: ROUTES TO KAGOME SPIN LIQUIDS

Madeleine Georgopoulou

A dissertation submitted in partial fulfillment
of the requirements for the degree of
Doctor of Philosophy
of
University College London.

Department of Chemistry
University College London

May 26, 2023

I, Madeleine Georgopoulou, confirm that the work presented in this thesis is my own. Where information has been derived from other sources, I confirm that this has been indicated in the work.

Τα πάντα ρει, μηδέποτε κατά τ'αυτό μένειν.

–Ηράκλειτος

Everything flows, nothing stays the same.

–Heraclitus

Abstract

Quantum spin liquids (QSLs) are novel states of matter that exhibit exotic electronic ground states and fractionalized excitations as a consequence of many-body entanglement. They do not break symmetry or any Landau-type order parameters and are instead better characterised by their projective symmetry groups. An ideal candidate is the two-dimensional $S = 1/2$ kagome Heisenberg antiferromagnet (KHAFM), where quantum spins form a geometrically frustrated lattice of corner-sharing triangles. Research into experimental realisations of QSLs was fuelled in 1973 when Phillip W. Anderson proposed that these states could underpin the transition to high-T_C superconductivity.

The syntheses, crystal and magnetic structures, bulk magnetometry and inelastic neutron scattering (INS) studies of two series of frustrated $S = 1/2$ magnets are presented. The claringbullite series, $Zn_xCu_{4-x}(OD)_6FCl$, includes the $x = 0$ sample that is orthorhombically distorted and the $x = 1$ material that represents the 'ideal' KHAFM. Seven exchange interactions, including Dzyaloshinskii-Moryia, were used to model the gapped spin wave excitations of the $x = 0$ sample, using semi-classical linear spin wave theory (LSWT). The $x = 1$ sample has gapless ($E \geq 0.27$ meV) diffuse magnetic scattering and is found to be a good quantum spin liquid candidate, where the strongest correlations are between the kagome layers.

The averievite series, $Zn_xCu_{5-x}(VO_4)_2O_2CsCl$, includes the $x = 0$ sample that has a monoclinic distortion, and the $x = 1$ and $x = 2$ materials (the latter is the KHAFM) where the kagome lattices are found to be distorted by an in-plane rotation of equilateral triangles. Preliminary LSWT calculations based on two Heisenberg exchanges and a collinear magnetic structure, capture the main features of the aver-

ievite spin waves. Despite a transition in the magnetic susceptibility of $x = 1$ averievite and the spin wave-like excitations, no magnetic Bragg peaks are observed, suggesting a glassy ground state. For $x = 2$ averievite, the gapless ($E \geq 0.3$ meV) diffuse scattering evidences a QSL and obeys a scaling behaviour, indicating proximity to a quantum critical point.

Impact Statement

Quantum spin liquids (QSLs) are novel states of highly entangled matter, found in *crystalline solids*, where atomic magnetic moments do not freeze their directions even at $T = 0$ K. Instead, due to quantum mechanical effects, they continue to fluctuate and point along many directions simultaneously. Research into their experimental realisation was fuelled when Phillip W. Anderson suggested in 1973 that they could be manipulated to form high-temperature superconductors. Superconductivity arises when an electric current flows with zero resistance, producing no thermal energy. Superconductors are already being used in nuclear magnetic resonance (NMR) equipment and magnetic resonance imaging (MRI) in the medical field, but are only effective at low temperatures of the order of 10 Kelvin. By better understanding exotic quantum states such as superconductivity it is hoped that the states could become available at higher temperatures, where expensive cryogenic equipment would not be required to apply these technologies. This is particularly interesting for the use of superconductors and quantum computers.

Classical computers store information in bits with values of "0" or "1", whereas in quantum computers information is stored in quantum bits (qubits) in a superposition state of "0" and "1" simultaneously. The other crucial aspect of quantum computing is entanglement – in a pair of entangled qubits, changing the state of one qubit instantaneously changes that of the other, speeding up computer processing times by several orders of magnitude. This can hugely impact areas where progress is hindered by processing times, such as in the fields of artificial intelligence, drug design and cryptography.

Highly entangled QSL states could therefore provide the grounds for robust

quantum computation. However, quantum entanglement and how to manipulate it is still not well understood necessitating further study of QSL states. The most promising materials to realise QSLs are the kagome magnets, where the magnetic moments form a lattice of corner-sharing triangles. QSL states arise from the geometry of the kagome lattice *frustrating* conventional magnetic order, combined with strong quantum fluctuations of small atomic magnetic moments.

Few good experimental examples of the QSL state exist in the literature, so this thesis aims to expand the library of materials. This thesis presents studies of two series of materials, the Zn-doped claringbullite and Zn-doped averievite series, where chemical doping leads to end-members with a kagome lattice. Studies of the magnetic behaviours of the end-members Zn-claringbullite, $ZnCu_3(OD)_6FCl$, and Zn_2-averievite, $Zn_2Cu_3(VO_4)_2O_2CsCl$, show them to be good QSL candidates.

This thesis also furthers the academic study of frustrated magnets. Semi-classical linear spin wave theory (LSWT) was used to model the spin waves observed in powder inelastic neutron scattering data of claringbullite using different exchange energies. A sizeable model of seven exchange parameters (including Dzyaloshinskii-Moriya) is proposed. The phase space of possible exchange models, which also stabilise the experimentally determined magnetic structure, was probed using a new protocol developed for the analysis of claringbullite. Using it in conjunction with LSWT has pushed the bounds of inelastic powder data analysis and shown the possibilities to study complicated spin wave spectra of other complex magnets.

Acknowledgements

Behind every thesis author there is always a group of individuals who have contributed in their progress. First and foremost I would like to thank my supervisors Dr. Björn Fåk and Prof. Andrew Wills for their patience, criticisms and encouragement – without these I would not be the scientist, and more importantly, the person I am today.

Andrew always inspired me to push the limits of what can be done, never letting me shy away from a challenge. Attempting to present a reasonable model of the claringbullite spin waves would not have been possible without the Serendipity program he authored, so I am grateful to Andrew for taking the time to write and develop it, as well as spending many hours running SpinW calculations together.

Björn was a great supervisor and mentor: his door was always open for scientific discussions, explanations and inspiration. Björn introduced me to the world of inelastic neutron scattering and taught me a lot about the physics outlook in frustrated magnetism, without which it would have been much harder to pull together the multiple facets of this thesis.

I am sincerely grateful to Dr. David Boldrin, as a colleague and as a friend, for his tireless help particularly during the first Covid lockdown, and for reading many of my thesis chapters!

A big thanks must go to a previous member of the Wills group, Dr. Eamonn Connolly, for teaching me about Rietveld refinements during my Masters and with whom I now have the good fortune of collaborating.

I spent a lot of time doing neutron scattering experiments at both the ILL and the ISIS Neutron and Muon Source with many instrument scientists who helped

me along the way. I would like to thank: Dr. Emmanuelle Suard, Dr. Jacques Ollivier, Dr. Clemens Ritter, Dr. Helen Walker, Dr. Ross Stewart, Dr. Alexandra Gibbs and Dr. Pascal Manuel. For the use of the SEM-EDX instrument at ESRF I thank Dr. Irina Snigireva. At UCL I would like to thank Martin Vickers for use of the laboratory powder x-ray diffractometer during my first year. I would also like to acknowledge the provision of a studentship from the UCL Department of Chemistry and the ILL.

Doing a PhD at both UCL and the ILL was a unique experience with amazing student communities. For always believing in me, a special thanks to: Shelby, Daniela, Mohamed, Irina, Arianna, Carmen, Edmond, Miloš, Bettina, Malavika and Neal.

To my mother, my father, Natalie and Josie – your achievements have been my inspiration, thank you for always standing by me. Last but not least, Shaddy – thank you for your unwavering care, love and support during this challenging journey.

Contents

μμ

List of acronyms

µSR Muon spin relaxation.

DFT Density functional theory.

DHO Damped harmonic oscillator.

DMI Dzyaloshinskii-Moriya interaction.

FWHM Full-width half-maximum.

INS Inelastic neutron scattering.

KAFM Kagome antiferromagnet.

LSWT Linear spin wave theory.

n.n. Nearest-neighbour.

PSD Position-sensitive detector.

PXRD Powder x-ray diffraction.

QCP Quantum critical point.

QEL Quasi-elastic Lorentzian.

QSL Quantum spin liquid.

RMC Reverse Monte Carlo.

RVB Resonating valence bond.

SOC Spin-orbit coupling.

SQUID Superconducting quantum interference device.

VB Valence bond.

VBC Valence bond crystal.

VSM Vibrating sample magnetometry.

Chapter 1

Introduction

The earliest records we have of magnetism date back to the Ancient Greeks in 600 B.C.E., when Thales of Miletus noted that lodestone, a form of the mineral magnetite Fe_3O_4, attracts iron [1]. Its first practical use is attributed to the Chinese with the invention of the compass, which by the 12^{th} century had also been introduced in Europe [2]. However, magnetism was not systematically studied as a physical phenomenon until the work of W. Gilbert in the 16^{th} century [3]. At a time when it was still believed that lodestone had healing powers and could be demagnetised with garlic, Gilbert's experiments were a crucial step forward in understanding, for example, how iron could be magnetised and even identified that the Earth itself behaves like a magnet [4]. One of the most significant advancements in the study of magnetism was its unification in classical physics with electricity in electromagnetic theory through the works of Faraday, Ampere, Ørsted [4] and most notably Maxwell [5] during the 19^{th} century. Another turning point came in the early 20^{th} century with the developments of quantum mechanics, and relativity, by Einstein, Schrödinger, Dirac, Heisenberg, Bohr and many others, which provided insight into the microscopic properties of magnetism [4]. Later in the 20^{th} century, in addition to academic progress, advancements in magnetism were also crucial in technological developments of consumer electronics, including magnetic resonance imaging (MRI) in radiology [6], memory storage [7] and cooling devices [8].

The magnetism we are concerned with in this thesis is *frustrated* magnetism. Frustration is a term introduced in the field of magnetism in 1977 by G. Toulouse

and describes the inability of a system to satisfy all pairwise interactions simultaneously due to local constraints [9]. Experimental and theoretical research on frustrated magnets was fuelled in the late 20$^{\text{th}}$ century, when P. W. Anderson proposed the resonating valence bond (RVB) model as a new type of electronic state that underpins the transition to high-T_C superconductivity [10, 11]. Valence bonds (VBs) are nonmagnetic singlets formed from quantum entangled spin pairs. Within this model, different spin pairings on a lattice can give rise to an extensive manifold of degenerate VB configurations and in the presence of strong quantum fluctuations, a resonance between them occurs that results in a superposition state. The RVB state arises when VBs are exclusively formed from nearest-neighbour (n.n.) spin interactions, but VBs can also form from long-ranged entangled spins producing a family of states known as *quantum spin liquids* (QSLs). Unlike conventional magnets that are characterised by a phase transition to long-range order, QSLs do not break symmetry in the conventional way and are instead characterised by their macroscopic degeneracies, entanglement and exotic phenomena, such as fractional excitations [12]. QSLs represent a class of topological materials and attempts to classify them are based on their properties at zero temperature using their 'quantum order' [13].

In 2-dimensions, the most promising model for realising a QSL ground state is the kagome lattice of vertex-sharing triangles made of $S = 1/2$ Heisenberg spins [14]. However, its experimental realisation has proven to be challenging and remains at the forefront of experimental condensed matter physics. The best material realisations include: herbertsmithite, γ−$ZnCu_3(OH)_6Cl_2$, which is perhaps the only known experimental example of the $S = 1/2$ RVB state [15]; kapellasite, α−$ZnCu_3(OH)_6Cl_2$, a chiral QSL [16]; and the more recent Zn-barlowite, $ZnCu_3(OH)_6FCl$, reported to be a Z_2 QSL [17] – the simplest type of spin liquid in 2-dimensions with short-range correlations and gapped excitations [14]. Elucidating the intrinsic kagome physics in these materials has been complicated by material imperfections, such as site defects or possible lattice distortions and other energy scales such as antisymmetric exchange. Further understanding of QSL ground

states that occur in experimental systems demands the expansion of the library of experimental materials.

In this thesis two series of $S = 1/2$ kagome magnets are synthesised and studied: the deuterated claringbullite series, $Zn_xCu_{4-x}(OD)_6FCl$ for $x = 0$ and 1 and the averievite series, $Zn_xCu_{5-x}(VO_4)_2O_2CsCl$ for $x = 0$, 1 and 2.

Claringbullite and its $x = 1$ Zn-doped variant, 'Zn-claringbullite', are hydroxide materials previously synthesised and characterised structurally and using bulk magnetometry [18]. Chapter 5 presents the syntheses of claringbullite and Zn-claringbullite and diffraction studies that show the crystal structures to be in agreement with previous reports. The magnetic structure of the parent material is found to be similar to that of its polymorph barlowite [19] and to the recently reported claringbullite magnetic structure [20]. Chapter 6 details inelastic neutron scattering measurements on both claringbullite and Zn-claringbullite. The analyses of the spin-pair correlations of both materials, strongly suggest that the correlations between kagome layers are critical in understanding their magnetic behaviours. Therefore, a key aspect in understanding Zn-claringbullite as a candidate quantum spin liquid is in the limit of observed dynamic interlayer correlations being stronger than intra-kagome ones.

Undoped averievite is formed of Cu^{2+} pyrochlore slabs and has been previously synthesised and doped to the $x = 1$ level [21], whilst the $x = 2$ material, to the best of our knowledge, is synthesised and studied here for the first time. Chapter 7 details structural, bulk magnetometry and imaging studies and Chapter 8 presents inelastic neutron scattering measurements. The $x = 0$ undoped material has a magnetic phase transition below $T_N = 22$ K, in agreement with the literature [21]. For the $x = 1$ material, magnetic susceptibility evidences a transition at $T = 3.5$ K, but no magnetic Bragg peaks are observed using neutron scattering. It is possible that the ordered moments are too small to be differentiated from the background of the data, however the phase transition and absence of magnetic Bragg peaks could indicate a spin glass-like system. For the previously unreported $x = 2$ material, we suggest that the kagome lattice is formed of equilateral triangles rotated in the plane, thereby

distorting the hexagons. No magnetic phase transition is observed in its magnetic susceptibility down to $T = 2$ K and a continuum of excitations is observed using inelastic neutron scattering at $T = 1.5$ K. The energy dependence of its magnetic scattering follows a scaling behaviour that indicates proximity to a quantum critical point and evidences that $x = 2$ averievite is a good candidate quantum spin liquid. The study of three members of the averievite series indicates at least three different types of ground states in this set of materials, providing an ideal playground for tuning magnetic order.

Bibliography

[1] Aristotle, *Peri Psihis (On the Soul) I.2*, edited by I. S. Christodoulou, 6th ed. (Zitros, Thessaloniki, 2003), 405a19.

[2] D. C. Mattis, *History of Magnetism* (Springer, Berlin, Heidelberg, 1981), pp. 1–38.

[3] W. Gilbert, *De Magnete*, edited by P. F. Mottelay (Dover Publications Inc., New York, 1893).

[4] S. J. Blundell, *Magnetism: A Very Short Introduction* (Oxford University Press, Oxford, 2012).

[5] J. C. Maxwell, Philos. Trans. R. Soc. **155**, 459 (1865).

[6] R. R. Edelman, Radiology **273**, S181 (2014).

[7] R. P. Cowburn, Philos. Trans. Royal Soc. A **358**, edited by J. M. T. Thompson, 281 (2000).

[8] B. Wolf, Y. Tsui, D. Jaiswal-Nagar, U. Tutsch, A. Honecker, K. Remović-Langer, G. Hofmann, A. Prokofiev, W. Assmus, G. Donath, and M. Lang, Proc. Natl. Acad. Sci. U.S.A. **108**, 6862 (2011).

[9] G. Toulouse, Commun. Phys. **2**, 115 (1977).

[10] P. W. Anderson, G. Baskaran, Z. Zou, and T. Hsu, Phys. Rev. Lett. **58**, 2790 (1987).

[11] P. W. Anderson, Mat. Res. Bull. **8**, 153 (1973).

[12] L. Balents, Nature **464**, 199 (2010).

[13] X. G. Wen, Phys. Rev. B **65**, 165113 (2002).

[14] C. Lacroix, P. Mendels, and F. Mila, *Introduction to Frustrated Magnetism : Materials, Experiments, Theory* (Springer-Verlag Berlin and Heidelberg, 2011).

[15] T.-H. Han, J. S. Helton, S. Chu, D. G. Nocera, J. A. Rodriguez-Rivera, C. Broholm, and Y. S. Lee, Nature **492**, 406 (2012).

[16] B. Fåk, E. Kermarrec, L. Messio, B. Bernu, C. Lhuillier, F. Bert, P. Mendels, B. Koteswararao, F. Bouquet, J. Ollivier, A. D. Hillier, A. Amato, R. H. Colman, and A. S. Wills, Phys. Rev. Lett. **109**, 037208 (2012).

[17] Y. Wei, Z. Feng, W. Lohstroh, D. H. Yu, D. Le, C. d. Cruz, W. Yi, Z. F. Ding, J. Zhang, C. Tan, L. Shu, Y.-C. Wang, H.-Q. Wu, J. Luo, J.-W. Mei, F. Yang, X.-L. Sheng, W. Li, Y. Qi, Z. Y. Meng, Y. Shi, and S. Li, arXiv:1710.02991v3 (2020).

[18] Z. Feng, W. Yi, K. Zhu, Y. Wei, S. Miao, J. Ma, J. Luo, S. Li, Z. Y. Meng, and Y. Shi, Chin. Phys. Lett. **36**, 017502 (2018).

[19] K. Tustain, G. J. Nilsen, C. Ritter, I. Da Silva, and L. Clark, Phys. Rev. Mater. **2**, 111405 (2018).

[20] K. Tustain, E. E. McCabe, A. M. Arevalo-Lopez, A. S. Gibbs, S. P. Thompson, C. A. Murray, C. Ritter, and L. Clark, Chem. Mater. **33**, 9638 (2021).

[21] A. S. Botana, H. Zheng, S. H. Lapidus, J. F. Mitchell, and M. R. Norman, Phys. Rev. B **98**, 054421 (2018).

Chapter 2

Brief introduction to magnetism

This chapter introduces some fundamental concepts of magnetism, which are required to understand the magnetic properties of the claringbullite and averievite series presented in this thesis. Both series of materials are insulators and to understand their magnetic behaviours, we need to understand spin and orbital angular momentum in a free ion, the effect of a crystal field and exchange interactions. Much of this chapter is based on *Blundell* [1] and *Khomskii* [2], and these should be referred to for more details. For an understanding of critical phenomena *Collins* [3] was referred to and for the theory of scattering *Squires* [4] and the less mathematical *Boothroyd* [5] texts were used.

2.1 The atomic magnetic moment

The basic component in the field of magnetism is the magnetic moment. Classically, it is most easily understood as an orbiting electric charge equatable to a current loop. The magnetic moment, $d\mu$, lies perpendicular to the plane of the loop of current, I, that has area, $|\mathrm{d}\mathbf{S}|$. For a finite sized current loop, many equal infinitesimal current loops with an associated magnetic moment, $\mathrm{d}\mu$, are summed over to give the total μ:

$$\mu = \int \mathrm{d}\mu = I \int \mathrm{d}\mathbf{S}, \tag{2.1}$$

where μ is in units of A m^2. The magnetic moment is a magnetic dipole, analogous to an electric dipole, with two monopoles separated by a distance parallel to the

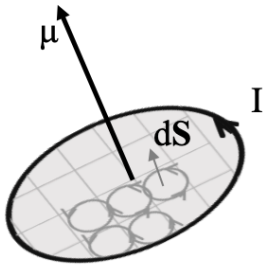

Figure 2.1: Schematic of a magnetic moment μ lying perpendicular to a loop of current I with a total area equal to the sum of all the infinitesimal equal current loops that have area $|\mathrm{d}\mathbf{S}|$.

vector d**S** (see Figure 2.1).

In this classical picture, at the atomic level, the electrons are massive particles with orbital motion. Therefore both their electric charge and orbital angular momentum contribute to the resulting magnetic moment. This moment lies in the same direction to its angular momentum, **L**, and they are related by

$$\mu = \gamma \mathbf{L}, \tag{2.2}$$

where γ (in SI units of C kg^{-1}) is the gyromagnetic ratio.

The magnitude of a magnetic moment is usually expressed in Bohr magnetons, μ_{B}, which is approximately equal to the magnetic moment of an electron spin. The Bohr magneton is derived by considering a hydrogen atom where an electron with charge $-e$ and mass m_e orbits a proton. For a circular orbit with radius r, velocity v and an orbital period τ, the angular momentum in the ground state is given as $m_e v r = \hbar$ and the current produced by the electron is $I = -e/\tau$. Therefore its magnetic moment is given as

$$\mu = \pi r^2 I = -\frac{e\hbar}{2m_e} \equiv -\mu_{\mathrm{B}} = -9.274x10^{-24} \text{ A m}^2. \tag{2.3}$$

2.2 Isolated magnetic moments

In a free ion the magnetic properties are determined by unpaired electrons in partially filled shells, which result in non-zero spin and orbital angular momenta. These

are both quantum mechanical properties where the latter was introduced in Section 2.1. The electron spin is the intrinsic angular momentum of the electron and results from its internal structure.

2.2.1 Orbital and spin angular momenta

The Pauli exclusion principle states that no two fermions can occupy the same quantum states, and for an electron in an atom these are commonly defined by four quantum numbers [6]. These are the principle quantum number n corresponding to the electron's energy level, the orbital quantum number l, the orbital magnetic quantum number m_l and the spin quantum number m_s.

The orbital angular momentum has a magnitude $\sqrt{l(l+1)}\hbar$, where l takes values from 0 to $n-1$. The component of the orbital angular momentum along a particular direction is $m_l\hbar$, where m_l takes values from $-l$ to l and distinguishes between the orbitals in a subshell.

Along a particular direction an electronic spin with quantum number s has a magnitude $m_s\hbar$, where m_s can have $2s+1$ possible values ranging from $-s$ to s in integer steps. For an electron the spin angular momentum is $s=\frac{1}{2}$, so $m_s=\pm\frac{1}{2}$ and the spin angular momentum has a component of $\pm\frac{\hbar}{2}$ along a particular axis, also referred to as spin "up" or "down". Similarly to the orbital angular momentum, the spin angular momentum has a magnitude of $\sqrt{s(s+1)}\hbar$.

The total spin and orbital angular momenta of an ion are given as $\mathbf{S}=\sum_i \mathbf{s}_i$ and $\mathbf{L}=\sum_i \mathbf{l}_i$, respectively. According to these summations, only unpaired electrons contribute to the magnetic moment and electrons in closed shells cancel to give net zero spin and orbital momenta. So far we have considered the consequence of electrons moving around a nucleus. In a real atom, the nucleus is not stationary, which affects the energy levels of the electrons. This is a relativistic effect that results in a coupling between the spin and orbital angular momenta and is termed spin-orbit coupling (SOC). For weak SOC, the total angular momentum is then given as

$$\mathbf{J}=\mathbf{L}+\mathbf{S}, \tag{2.4}$$

which is known as Russel-Saunders or L-S coupling. The strength of SOC increases following a Z^4 dependence and for heavier atoms the individual spin and orbital angular momenta of an electron couple to give a new quantum number j. This results in the total angular momentum better described as $\mathbf{J} = \sum_i j_i$.

Each electronic energy state with L and S has a total angular momentum quantum number J that can take values from $|L-S|$ to $L+S$. In the absence of SOC or an external magnetic field all J levels are degenerate. The SOC then acts as a perturbation that removes the degeneracy, resulting in what is knows as the fine structure. Each J level has a multiplicity of $2J+1$, with the different levels m_J taking values from $-J$ to J in integer intervals. The degenerate m_J levels can be split by applying a magnetic field, which is known as Zeeman splitting [7].

2.2.2 Hund's rules

The most energetically favourable combinations of L and S in the electronic ground state of an ion, are determined by Hund's rules [8]. These are given below in order of decreasing importance, such that the first has to be satisfied before the subsequent ones are considered.

1. The electronic wave function is arranged such that S is maximised. In this case, the Coulomb energy is minimised as a result of the Pauli exclusion principle, which does not allow electrons with the same spin to be in the same place.

2. Electrons must be placed in orbitals such that L is maximised. Clasically, this can be pictured as electrons orbiting in the same direction, therefore minimizing the Coulomb repulsion.

3. Spin-orbit energy must be minimized: if a shell is less than half full then $J = |L-S|$ and if it is more than half full $J = |L+S|$.

Based on Hund's rules, the effective magnetic moment of the ground state is given by

$$\mu_{\text{eff}} = g_J[J(J+1)]^{1/2}\mu_{\text{B}}, \tag{2.5}$$

where g_J is the Landé g-factor given by

$$g_J = \frac{3}{2} + \frac{S(S+1) - L(L+1)}{2J(J+1)}. \tag{2.6}$$

For $4f$ atoms, the experimental effective magnetic moments from bulk magnetometry measurements are usually in agreement with equation 2.5. In the case of the $3d$ transition metals the agreement is often poorer following the common assumption that the orbital momentum in $3d$ ions is quenched as the crystal field is assumed to be larger than the SOC, giving $L = 0$ and $J = S$. However, the SOC does often have to be considered as a small perturbation that leads to a non-zero L. In this thesis, the only magnetic ion considered is Cu^{2+} that has an outer shell electron configuration $3d^9$ with one unpaired electron or hole. Following Hund's rules, there are 5 spin up and 4 spin down electrons resulting in $S = 1/2$ and if the orbital momentum ($L = 2$) is assumed to be quenched, the effective total angular momentum $J = S = 1/2$. This is an approximation and it will be seen that for both claringbullite and averievite (in Chapters 6 and 8, respectively), SOC is present and its effects lead to anisotropic magnetic interactions, which will be explained in Section 2.4.2.

2.2.3 Crystal field effects

The behaviour of magnetic ions depends on both their own electronic states, as well as the electric field arising from their coordination environment. In d ions the degeneracy of the energy levels is lifted due to the orbital overlap with neighbouring atoms. However, in $4f$ ions this effect is less prevalent as there is poor orbital overlap between the ligands and the shielded f orbitals. As this thesis only deals with the Cu^{2+} magnetic ion, this section will focus on the $3d$ orbitals.

In a spherical environment the $3d$ orbitals are degenerate, but in a crystal lattice the orbital degeneracy is lifted. Often they split into two groups: the t_{2g} orbitals which point between the x, y and z axes and are triply degenerate (d_{xy}, d_{xz} and d_{yz}); and the e_g orbitals which point along these axes and are doubly degenerate (d_{z^2} or $d_{3z^2-r^2}$ and $d_{x^2-y^2}$). In an octahedral environment, the e_g orbitals directly overlap with the ligand orbitals and the strong Coulombic repulsion leads to an increase in

the energy of their occupying electrons. On the other hand, the t_{2g} orbitals have less overlap and their electrons do not experience a strong Coulombic repulsion and their energy is lowered. The energy difference between electrons in the two sets of orbitals is known as the crystal field energy. Importantly, there are other coordination environments, such as the tetrahedral one where the e_g levels have a lower energy than the t_{2g} ones.

In partially filled 3*d* orbitals, the electrons occupy the lowest energy ones first. However, the precise order of orbital occupation is determined by the relative magnitudes of the crystal field energy and the Coulomb energy cost of placing two electrons in the same orbital. When the crystal field energy is smaller than the Coulomb energy the electrons singly occupy the orbitals, whereas for the opposite case the electrons pair up in the lowest energy orbitals first.

In certain cases, there is an energy gain in further lifting the degeneracy of the

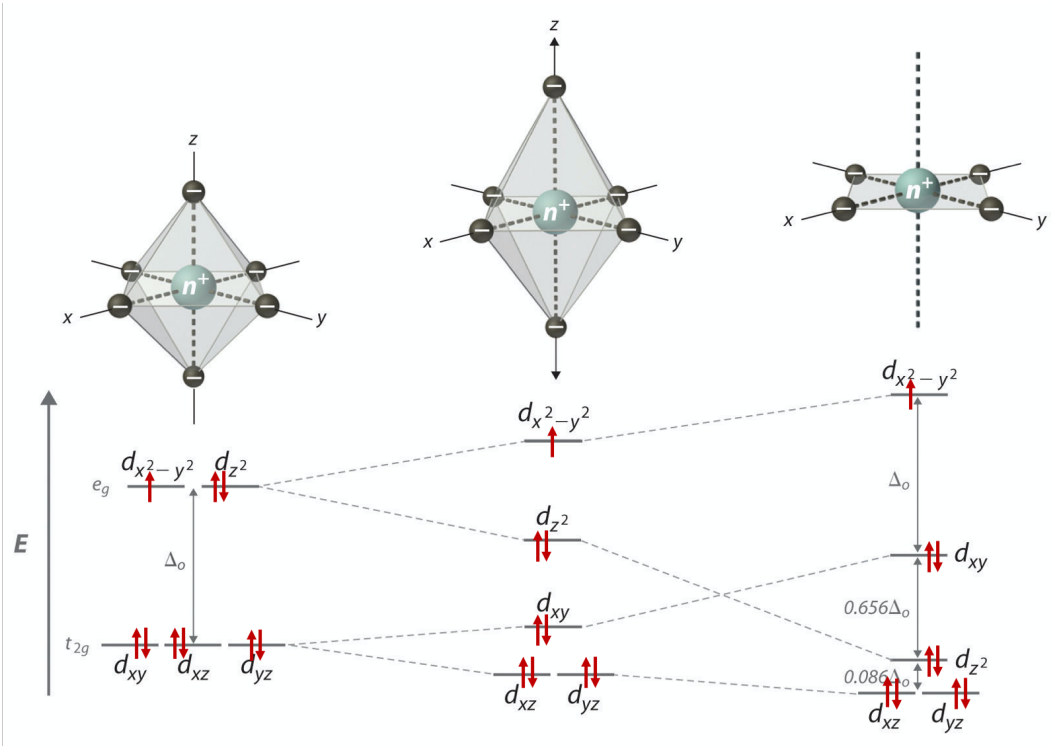

Figure 2.2: Orbital splitting for a Cu^{2+} $3d^9$ ion in an octahedral environment. To remove the degeneracy of the e_g orbitals, a distortion occurs and the axial ligands moved away from the metal ion along the z axis. Eventually a square planar coordination environment is realised. The corresponding orbital energy levels are shown. Adapted from [9].

$3d$ orbitals by a spontaneous geometric distortion. This is named the Jahn-Teller effect [10]. Taking the example of a Cu^{2+} $3d^9$ ion in an octahedral coordination environment, where the e_g orbitals directly overlap with the ligand ones, there is a significant gain in energy through a distortion. In both the averievite and claringbullite series, the octahedral coordination environments are distorted around the Jahn Teller active Cu^{2+} ion. A schematic of this is shown in Figure 2.2. On the other hand, in the Zn-doped compounds the coordination environment around the non-Jahn Teller active Zn^{2+} ion (which has a full outer shell) is more spherical. The differences in the coordination environment symmetries can be seen in crystal structure refinements by looking at the bond lengths between Cu^{2+}/Zn^{2+} ions and the surrounding ligands. Equal equatorial and axial bond lengths can indicate the site has a more spherical environment and therefore is preferentially occupied by the Zn^{2+} ion.

For a Jahn-Teller active ion at high temperature, the thermal fluctuations will cause degenerate configurations of the highest energy orbital to be occupied interchangeably and this is known as the *dynamic* Jahn-Teller effect (see Figure 2.3) [12]. As temperature decreases and thermal fluctuations become weaker, the Jahn-Teller effect can lead to a static distortion accompanied by a crystallographic symmetry lowering as the energy barrier between degenerate states cannot be overcome. In systems where there is a high concentration of Jahn-Teller ions, a cooperative dis-

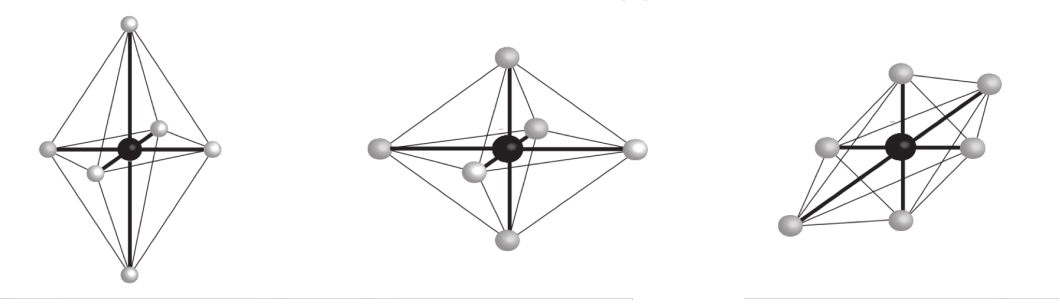

Figure 2.3: The Jahn-Teller distortion of a $3d^9$ ion in an octahedral environment is often an axial elongation of the metal-ligand bonds as shown in Figure 2.2. Three states are usually possible where the axial elongation occurs along one of the three axes. When the thermal energy is larger than the energetic barrier between the three states, the system will fluctuate between them. This is known as the *dynamic* Jahn-Teller effect. Taken from [11].

tortion may occur as the local distortion around one ion requires a distortion in the environments of all other ions [13].

These effects indicate that the the local coordination environment of a magnetic ion, which affects the relative orbital energies, therefore also has important consequences in the electronic orbital occupancy. This in turn affects the spin interactions in a magnet, which will be expanded on in Section 2.4.

2.3 Magnetisation and magnetic susceptibility

A material's bulk magnetic properties are a consequence of the magnetic field generated on an atomic scale. Magnetic solids have a large number of magnetic moments which, per unit volume, are defined as the magnetisation, **M**, of a material. When these materials are subject to an external magnetic field, **H**, a magnetic flux, **B**, is induced such that

$$\mathbf{B} = \mu_0(\mathbf{H} + \mathbf{M}), \tag{2.7}$$

where μ_0 is the permeability of free space. The degree of magnetisation in response to an applied magnetic field is given by the magnetic susceptibility, χ:

$$\mathbf{M} = \chi\mathbf{H}. \tag{2.8}$$

The units of χ in SI units are dimensionless, but these are not conventionally used. Instead, χ is expressed in electromagnetic units (emu), which come from the centimetre-gram-second (cgs) system. In this thesis, the magnetic susceptibility is typically quoted as the molar susceptibility per magnetic ion, with units "emu mol^{-1} Cu^{-1}", given by

$$\chi_m = \frac{\chi M_r}{mn}, \tag{2.9}$$

where M_r is the relative molecular mass of the material, m is the sample mass and n is the number of magnetic atoms per formula unit. When $\chi > 0$, the material is gov-

erned by an attractive force to the applied magnetic field known as paramagnetism, whereas when $\chi < 0$ the material is repelled and this is termed diamagnetism. The origins of paramagnetism and diamagnetism will be detailed in the following sections.

2.3.1 Diamagnetism

In a classical picture of Langevin, diamagnetism arises from an applied magnetic field inducing an opposing magnetic field in the orbiting electrons. Therefore, all materials experience a degree of diamagnetism that can be approximated to be proportional to the number of electrons in a system [1, 14] The contribution of diamagnetism to the magnetic susceptibility is often an order of magnitude weaker than paramagnetism. In this thesis, a diamagnetic correction has been made in all magnetometry studies and will be detailed in the relevant sections.

2.3.2 Paramagnetism

Paramagnetism arises from unpaired electrons. In the absence of an external magnetic field and assuming weak interactions between the electrons, the magnetic moments point in random directions. When an external magnetic field is applied, the magnetic moments align parallel to it.

In a classical description of paramagnetism the quantization of magnetic moments is ignored and effectively this equates to $J = \infty$, though an accurate dependency of χ with temperature is still obtained [1]. When a magnetic field **B** is applied in the z direction, the average moment that aligns along it, μ_z, is given by the Langevin function, $L(y)$:

$$L(y) \equiv \coth(y) - \frac{1}{y} = \frac{\mu_z}{\mu}, \tag{2.10}$$

where $y = \mu B/k_{\mathrm{B}}T$, T is the temperature and μ is the total magnetic moment. In a weak magnetic field, y is small and equation 2.10 becomes

$$L(y) = \frac{\mu_z}{\mu} \approx \frac{y}{3} = \frac{\mu B}{3k_{\mathrm{B}}T}. \tag{2.11}$$

When all moments are aligned along the field, the saturation magnetisation is reached $M_{\text{sat}} = n\mu$, where n is the number of magnetic moments per unit volume. The measured magnetisation is given as $M = n\mu_z = n\mu L(y)$. In small fields, χ from equation 2.8 can also be approximated as $\chi = \mu_0 M/B$. Combining this with equation 2.11 gives the temperature dependence of the magnetic susceptibility:

$$\chi = \frac{n\mu_0\mu^2}{3k_{\text{B}}T} = \frac{C}{T}, \tag{2.12}$$

where C is the Curie constant. The inverse temperature dependence of magnetic susceptibility was first described by Pierre Curie and is known as the Curie law.

Within quantum mechanics, these classical moments are treated as quantum spins with $J = 1/2$, so $m_J = \pm 1/2$. The spins are quantised along the z direction and the resulting magnetisation can take two values $\pm n g_J \mu_{\text{B}} m_J$, where g_J is the Landé g-factor that is the electronic gyromagnetic ratio. The response of a paramagnet to an applied magnetic field is then described by the Brillouin function, $B_J(y)$, for any half-integer value of J:

$$B_J(y) = \frac{2J+1}{2J}\coth\left(\frac{2J+1}{2J}y\right) - \frac{1}{2J}\coth\frac{y}{2J}. \tag{2.13}$$

In the limit of $J = \infty$, $B_J(y)$ can be reduced to the Langevin function $L(y)$ (equation 2.10) and in the limit of $J = 1/2$ it becomes $\tanh(y)$. In a weak field y becomes small and equation 2.13 can be written as

$$B_J(y) = \frac{(J+1)y}{3J}. \tag{2.14}$$

The magnetisation is given as $M = M_{\text{sat}} B_J(y)$, where M_{sat} is the saturation magnetisation, and by substitution in equation 2.14, the magnetic susceptibility can be defined as

$$\chi = \frac{n\mu_0 g_J^2 \mu_{\text{B}}^2 J(J+1)}{3k_{\text{B}}T} = \frac{n\mu_0\mu_{\text{eff}}^2}{3k_{\text{B}}T}. \tag{2.15}$$

Although equation 2.15 is very similar to equation 2.12, this quantum mechanical

approach gives the effective magnetic moment as expressed in equation 2.5, enabling the determination of the Landé g-factor. In real materials, spin correlations often lead to a deviation from an ideal paramagnet and the Brillouin function is no longer a good description of a system's magnetic behaviour. These correlations arise from interactions between the spins that will be detailed in Section 2.4.

2.3.3 The Curie-Weiss law

The Curie law, equation 2.12, is used to describe an ideal paramagnet of non-interacting spins for which the magnetic susceptibility is inversely dependent on temperature. As temperature decreases the strength of magnetic interactions begins to outweigh thermal disorder and correlations build up and strengthen between the magnetic moments. This is seen as an increase in the curvature of the measured magnetic susceptibility away from the linear behaviour of the Curie law.

The magnetisation of a material can be approximated by an internal magnetic field that arises from each magnetic moment experiencing an average magnetic field from all other spins in the system that it interacts with. This internal field is known as the Weiss molecular field, λ, and although not an accurate representation of a real system, it helps to understand the magnetic behaviour of experimental materials. The strength of the Weiss molecular field must be incorporated in the definition of a material's transition temperature. A ferromagnet spontaneously orders below a critical temperature termed the Curie temperature, which is defined as

$$T_{\mathrm{C}} = \frac{g_J \mu_{\mathrm{B}} J(J+1) \lambda M_{\mathrm{sat}}}{3k_{\mathrm{B}}}. \tag{2.16}$$

Similarly, an antiferromagnet orders below the Néel temperature, which is defined as

$$T_{\mathrm{N}} = \frac{g_J \mu_{\mathrm{B}} J(J+1) |\lambda| M_{\mathrm{sat}}}{3k_{\mathrm{B}}}. \tag{2.17}$$

Including λ in the Brillouin function results in

$$B_J(y) = \frac{M}{M_{\text{sat}}} \approx \frac{g_J \mu_B (J+1)}{3k_B} \left(\frac{B + \lambda M}{T} \right). \tag{2.18}$$

For the magnetic susceptibility of a ferromagnet, we can combine equations 2.16 and 2.18 to get

$$\chi \propto \frac{C}{T - T_C}. \tag{2.19}$$

The same can be done for an antiferromagnet by replacing $-T_C$ in equation 2.19 with $+T_N$. A more general equation can be written known as the Curie-Weiss equation, where $-T_C$ and $+T_N$ are replaced by the Weiss temperature, θ_W. $\theta_W > 0$ corresponds to a ferromagnetic mean field and $\theta_W < 0$ indicates an antiferromagnetic mean field [15]. If the spin correlations are zero $\theta_W = 0$. However, the opposite is not always true as $\theta_W = 0$ could arise from competing exchange interactions of opposite signs cancelling each other out to create a net mean field of zero. This is important to consider in frustrated materials as they often have many competing exchange interactions contributing to the mean field.

A plot of the inverse susceptibility as a function of temperature is shown in Fig-

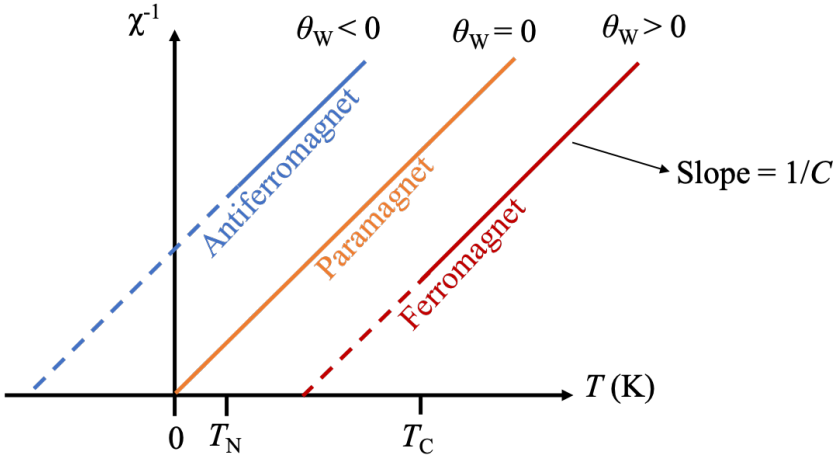

Figure 2.4: Inverse susceptibility as a function of temperature for an ideal paramagnet (orange), an antiferromagnet (blue) that goes through a magnetic phase transition at T_N and a ferromagnet (red) with a Curie temperature T_C. The linear regions can be extrapolated to determine the Weiss temperature θ_W and the Curie constant, C.

ure 2.4 for a paramagnet, an antiferromagnet and a ferromagnet. It can be seen that the linear high-temperature paramagnetic regions, can be extrapolated to $\chi^{-1} = 0$ to determine the Weiss temperature, θ_W, from the x intercept and the Curie constant, C, from the slope. It should be noted that in experimental materials, there is often curvature in the paramagnetic region above the critical temperature due to the build-up of short-range correlations. Therefore, care should be taken experimentally with choosing an appropriate linear region for application of the Curie-Weiss law.

2.4 Magnetic order and excitations

The interactions between magnetic moments can lead to various types of magnetic order, from long-range magnetic order to exotic quantum spin liquid states. There exist different properties that a system must possess to be classified as a quantum spin liquid, such as not breaking Landau type symmetry and experimental signatures of exotic spinon excitations, which can be challenging to determine conclusively [16]. On the other hand, long-range magnetic order can be clearly observed in experiment. In this thesis, phase transitions to magnetic long-range order were observed as a discontinuity in direct current (DC) magnetic susceptibility measurements as a function of temperature. Below the phase transition, the magnetic scattering was measured using neutron diffraction and used to refine a model magnetic structure.

2.4.1 Isotropic magnetic interactions

Magnetic moments interact with each other *via* different interactions. The simplest one is the through space magnetic dipolar interaction, the strength of which depends on the relative orientations of the magnetic moments and the distance between them. This is a weak interaction typically of the order of ~ 1 K that in most studies does not lead to long-range magnetic order, only becoming significant in materials that order at milliKelvin temperatures.

Electrostatic interactions between the unpaired electrons of neighbouring magnetic atoms, can lead to magnetic exchange interactions. These are understood quantum mechanically in terms of Pauli's exclusion principle, which requires the

electronic wavefunction to be antisymmetric for electrons in spatially overlapping orbitals. For a two-spin system, $\mathbf{S}_1$ and $\mathbf{S}_2$, the Hamiltonian is written as

$$\mathscr{H} = E_0 + J\mathbf{S}_1 \cdot \mathbf{S}_2, \tag{2.20}$$

where J is the exchange integral and E_0 is a constant energy term. The sign of J leads to an energy minimisation of the Hamiltonian for a parallel ($J < 0$) or antiparallel ($J > 0$) alignment of spins. For a system with multiple spins, each spin $\mathbf{S}_i$ will have a pairwise interaction with every other spin $\mathbf{S}_j$, according to the mean field arguments introduced earlier. The spin part of the Hamiltonian, termed the Heisenberg Hamiltonian, is given as

$$\mathscr{H} = \sum_{i,j} J_{ij}\, \mathbf{S}_i \cdot \mathbf{S}_j, \tag{2.21}$$

where J_{ij} is the exchange integral for the interaction between sites i and j. Exchange interactions can occur between neighbouring atoms (direct exchange) or *via* one or more intermediate ions, known as superexchange. The strength and sign of superexchange depends on the degree of orbital overlap, which is in turn strongly dependent on the ∠M-O-M angle as shown in Figure 2.5. For a metal ion with a single electron in the $d_{x^2-y^2}$ orbital, an ∠M-O-M angle of 180° kinetically favours antiferromagnetic interactions over ferromagnetic ones, because the anti-parallel spin alignment allows the spins to be delocalized over the magnetic and non-magnetic orbitals. The geometry of the $d_{x^2-y^2}$ orbitals allows for direct overlap with the oxygen p_x orbital that facilitates the superexchange. If the spins were parallel, the Pauli exclusion principle would prevent this delocalization and the interaction would be less energetically favourable. Figure 2.5b shows that for a 90° ∠M-O-M angle a ferromagnetic superexchange would be favoured.

This type of analysis has led to the semi-empirical series of Goodenough-Kanamori rules, which can be used to predict the sign of J based on the ∠M-O-M superexchange angle and orbital occupation [17, 18]. It is however important to

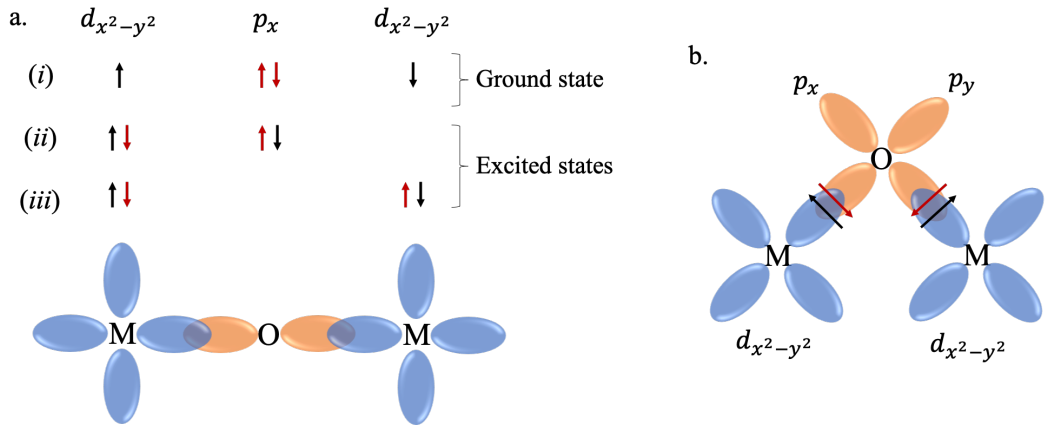

Figure 2.5: a. Antiferromagnetic superexchange in a metal oxide with an 180° orbital overlap between the $d_{x^2-y^2}$ orbitals of the metal ions and the p_x orbital of the oxygen atom. Three possible spin arrangements are shown for an antiferromagnetic interaction. For parallel spins in the two $3d_{x^2-y^2}$ orbitals, only one configuration would be allowed according to Pauli's exclusion principle. An anti-parallel spin alignment is kinetically favoured. **b.** Ferromagnetic superexchange is preferred for a 90° ∠M-O-M angle. Based on a figure in [1].

note that these rules are limited to μ_2-O bridging ligands[1]. When there are more ligands, such as for a μ_3-O bridging group, it is best to compare with other experimental materials and results from electronic structure calculations. In this thesis, averievite has Cu-(μ_2-O)-Cu superexchange pathways whereas claringbullite has Cu-(μ_3-OH)-Cu pathways, so the Goodenough-Kanamori rules are only applicable to the former.

2.4.2 Anisotropic magnetic interactions

In the presence of spin-orbit coupling (SOC), the interaction between the orbitals and the crystal field give a directional dependence to the magnetic moments. This is best known as affecting $4f$ ions, but also affects to a lesser degree the $3d$ transition metals, where SOC is much weaker. One kind of anisotropy that can arise is the anisotropic symmetric exchange interaction, which is bond-dependant and results in J having different strengths in different directions. An example of this is seen in the spin Hamiltonian of the $S = 1/2$ kagome antiferromagnet vesignieite [19], which will be discussed in Section 3.3.4. Another type of anisotropic interaction is

[1]The prefix μ_n denotes a bridging ligand between metal ions, where n is the number of atoms bridged.

antisymmetric exchange also referred to as the Dzyaloshinskii-Moriya interaction (DMI) [20, 21], which occurs between an ion in a spin-orbit excited state and a neighbouring ion in the ground state. It can be expressed by

$$\mathscr{H}_{DM} = \mathbf{D}_{ij} \cdot \mathbf{S}_i \times \mathbf{S}_j, \tag{2.22}$$

where $\mathbf{D}_{ij}$ is the Dzyaloshinskii-Moriya vector. The DMI acts to align $\mathbf{S}_i$ and $\mathbf{S}_j$ to be at right angles to each other in a plane perpendicular to $\mathbf{D}_{ij}$ and is a common cause of spin canting in antiferromagnets, where collinear or coplanar spins are tilted away from their common axis or plane inducing weak ferromagnetism. In the absence of a magnetic structure, from which the degree of spin canting can be determined, key characteristics include an antiferromagnetic Weiss temperature and weak ferromagnetism observed as a hysteresis in magnetic field-dependent magnetisation data. A non-zero DMI only occurs when the midpoint between two magnetic atoms is not a centre of inversion symmetry, unlike anisotropic symmetric exchange which can be non-zero when there is such symmetry [22]. In this thesis the DMI will be considered for both claringbullite and averievite, as it is allowed by symmetry in their low orthorhombic and monoclinic symmetries, respectively.

2.4.3 Long-ranged magnetic structures

A magnetic structure is a long-range ordered arrangement of spins, where the arrangement depends on the type and strength of the various exchange interactions. Some examples of magnetic structures are shown in Figure 2.6. In the high-temperature limit, where thermal fluctuations are much stronger than the exchange interactions, the system acts as a paramagnet with non-interacting or isolated magnetic moments. Below a transition temperature, the magnetic exchange interactions typically result in long-range magnetic order. Such a spin ordering transition depends on the geometry and dimensionality of the crystal lattice, as well as the spin dimensionality arising from *e.g.* single-ion anisotropy effects.

The simplest magnetic structure is a ferromagnetic one in which all spins are parallel, giving a net magnetisation in the direction of the moments. Another com-

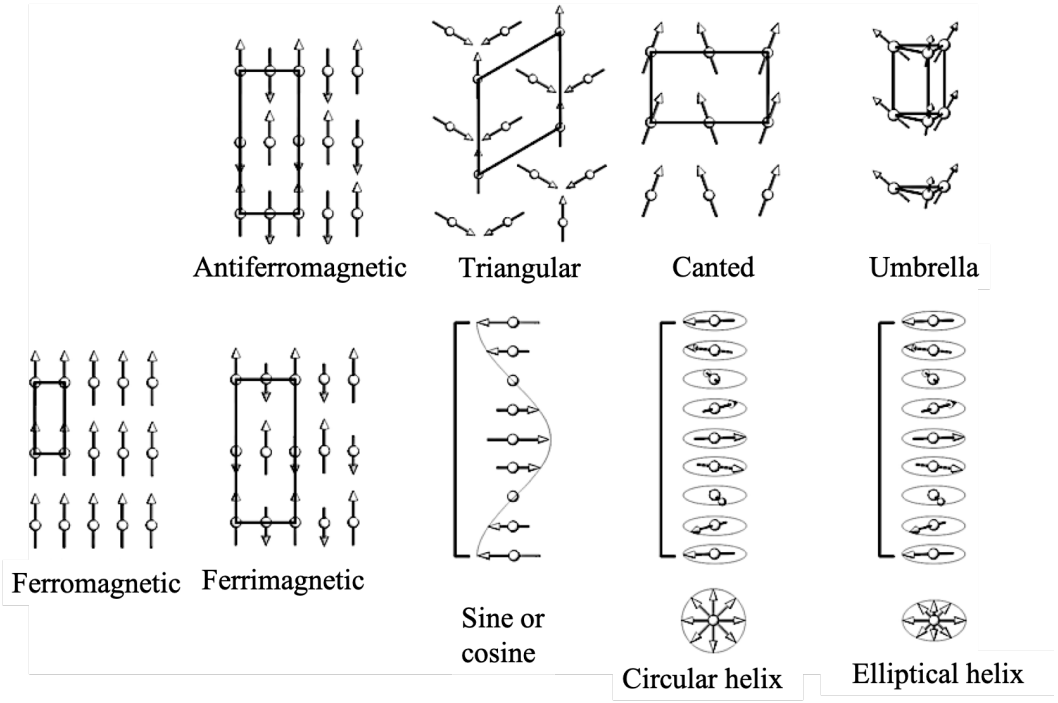

Figure 2.6: Examples of different magnetic structures arising from various exchange interactions. Taken from [23].

mon structure is the collinear antiferromagnet, which can be thought of as two sublattices of parallel spins aligned anti-parallel to each other resulting in a net zero magnetisation. Similar to antiferromagnets are ferrimagnetic structures, where two sublattices point in opposite directions and have different moment sizes, resulting in a non-zero magnetisation. In some other materials competition between further-neighbour exchange interactions can cause helimagnetism, where the spins are rotated about an axis from one layer to the other. In such structures, the magnetic unit cell may not be an integer multiple of the underlying crystallographic unit cell *i.e.* not commensurate with it, and is termed an incommensurate magnetic structure. The types of magnetic structures that can be realised can be expanded by introducing magnetic frustration, which can lead to more complicated non-collinear or non-coplanar magnetic structures.

2.4.4 Phase transitions in magnetic systems

Spontaneous magnetic order appears below a critical temperature, T_C, and gives rise to the magnetic structures as described in the previous section. These phase tran-

sitions involve a symmetry lowering, whereby the removal of symmetry elements results in a defined symmetry-breaking. For example, a ferromagnet in its paramagnetic phase has complete rotational symmetry as the spins can point in any direction. But below T_C, the spins will all point in a unique direction thereby reducing the rotational symmetry, as well as breaking time-reversal symmetry that relates a magnetic moment with its reversed state. Such magnetic phase transitions can be understood in terms of various simple models, with one of the mean-field approaches given by Landau's theory of continuous (second order) phase transitions. In this theory, the magnetic behaviour near T_C is written in terms of a Taylor series expansion of the free energy as a function of an order parameter. The order parameter characterises a symmetry breaking at the phase transition, taking a finite value below T_C and a zero value above it. The order parameter that characterises the transition from para- to ferromagnet is the magnetisation and the free energy $F(M)$ is expanded as

$$F(M) = F_0 + \alpha(T)M^2 + bM^4, \tag{2.23}$$

where F_0 and b are constants, and $\alpha(T)$ is a temperature dependent parameter. The ground state is that which minimises the free energy *i.e.* when $dF(M)/dM = 0$ and $d^2F(M)/dM^2 > 0$. The expressions for these conditions are then

$$2\alpha(T)M + 4bM^3 = 0 \qquad \text{and} \qquad 2\alpha(T) + 12bM^2 > 0. \tag{2.24}$$

Above T_C, in the paramagnetic phase, the magnetisation must be zero, therefore $\alpha(T) > 0$. Below T_C, M must have a finite value leading to

$$\alpha(T) = -2bM^2. \tag{2.25}$$

This then requires a change of sign in $\alpha(T)$ above and below the critical temperature. Therefore $\alpha(T)$ can be replaced by $(T - T_C)\alpha_0$, where α_0 is a positive constant. Substituting this back into equation 2.23 gives the graphical results in Figure

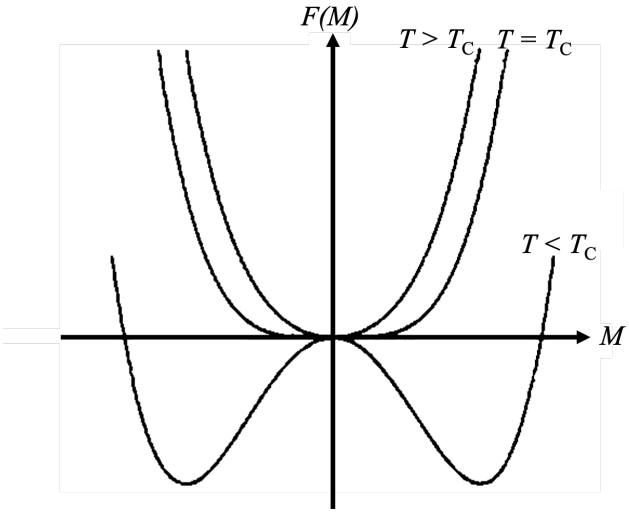

Figure 2.7: Free energy of a ferromagnet, $F(M)$, as a function of the magnetisation order parameter M above, below and at the critical temperature T_C. At and above T_C the magnetisation is zero, below T_C the minima of $F(M)$ are non-zero values of M. Taken from [1].

2.7. The solutions to $dF(M)/dM = 0$ can now be written as

$$M = 0 \qquad \text{and} \qquad M = \pm \left(\frac{(T_C - T)\alpha_0}{2b} \right)^{\beta = \frac{1}{2}}, \tag{2.26}$$

where $\beta = 1/2$ is the critical exponent using this mean-field approach. The second solution is only valid for $T < T_C$. It is important to keep in mind that mean field theories do not account for correlations and fluctuations that become important near T_C, but these fluctuations are reflected in the broad and flat minimum of $F(M)$ at $M = 0$.

Within this macroscopic theory magnetic behaviours can also be understood using microsopic models, such as the nearest-neighbour Heisenberg model (see equation 2.21). In this model, the dimensionality of the lattice and spin is represented in terms of the different interactions between spins.

Critical exponents can be calculated from the various microscopic models using the renormalisation group method, which is a mathematical formulation that can be applied due to the exponents being unrelated to the microscopic interactions in the system. The value of a critical exponent depends on three things: (*i.*) the dimensionality of the system, (*ii.*) the symmetry of the order parameter and (*iii.*)

whether the interactions are short- or long-ranged. Experimental and theoretical studies have found that some systems share the same critical exponents despite differences in their microscopic properties, and so can be grouped into *universality classes*. For example, in experimental materials the magnetisation is indeed found to behave as $(T_C - T)^{\beta}$, but β is not always $1/2$, as results from Landau theory in equation 2.26, and its value depends on the nature of the phase transition [2].

In the Ising model of spins that are constrained to lie along the z-axis, the Heisenberg Hamiltonian becomes

$$\mathscr{H} = \sum_{i,j} J_{ij}\, \mathbf{S}_i^z \cdot \mathbf{S}_j^z. \tag{2.27}$$

On a 1-dimensional lattice a spin chain is formed and no magnetic ordering transition occurs: the energy cost of flipping a spin is always $E = J$ and this becomes negligible compared to the increasing entropy gain as the spin chain becomes larger. Therefore at $T > 0$, spin flipping occurs spontaneously and the critical temperature is zero. In a 2-dimensional lattice, both the entropy gain and the energy cost related to flipping the Ising spins scale with the size of the spin flipped region. This competition results in these systems having a magnetic ordering transition at a non-zero critical temperature.

Materials with weak spin-orbit coupling and quenched orbital moments have isotropic Heisenberg spins and are thought of as 3-dimensional vectors that can point in any direction in real space. However, these microscopic models can be difficult to solve exactly leading to discrepancies between experimental and theoretical values of critical exponents [1].

The discussion so far has focused on phase transitions at finite temperatures, but when T_C is suppressed to $T = 0$ K quantum effects become important [2]. In such a case, the system is disordered even at $T = 0$ as a result of quantum fluctuations and the point at $T = 0$ is named the quantum critical point (QCP). In many cases, the suppression of T_C requires an external perturbation such as pressure or a magnetic field, expressed by the parameter g. Figure 2.8 shows the QCP occurs when g is at the critical strength, g_C. At g_C quantum fluctuations dominate the

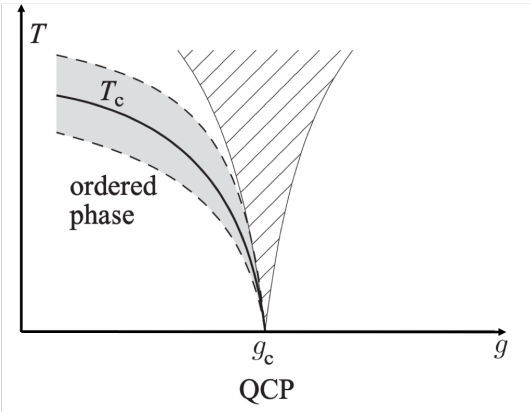

Figure 2.8: Suppression of the critical temperature T_C as a function of a parameter g, such as pressure. At the critical strength g_c, T_C is suppressed to $T = 0$ and is known as the quantum crtical point (QCP). The hatched region indicates the part of the phase diagram where quantum fluctuations dominate and the solid grey region shows where classical fluctuations dominate. The rest of the phase diagram corresponds to the ordered phase. Taken from [2].

system, but become less intense with increasing temperature.

2.4.5 Representational analysis applied to magnetic structures

A magnetic structure comprises of a series of components that are defined with respect to the underlying crystallographic unit cell, using a reciprocal space vector known as the magnetic propagation vector, **k**. The propagation vector can be experimentally determined by the positions of the magnetic Bragg peaks in a diffraction pattern. For a ferromagnet a magnetic unit cell can be defined that is equivalent to the crystallographic one according to $\mathbf{k} = \mathbf{0}$, with the magnetic Bragg peaks occurring at the same positions as the nuclear Bragg peaks. In the case of antiferromagnets, a $\mathbf{k} = \mathbf{0}$ magnetic structure can also arise when there is more than one magnetic atom per unit cell, which is the case for claringbullite as will be detailed in Chapter 5. However, taking the example of averievite (see Chapter 7), a doubling of the crystallographic unit cell in the *a* direction is required to describe the magnetic structure, which corresponds to the propagation vector $\mathbf{k} = (1/2, 0, 0)$.

To fully define a magnetic structure, the relative spin orientations are needed in addition to the propagation vector. One way to obtain these spin orientations is using representational analysis [24, 25], where irreducible representations (irreps) describe the transformations of the magnetic structure under the symmetry opera-

tions of the crystal space group [26]. This provides a number of possible magnetic structures that can be restricted by using Landau's theory of second-order phase transitions, which, within a simple application, says that only one irrep is involved in a second-order phase transition and all others are zero [27, 28]. This is often the case in experimental materials, though more complex structures can arise depending on the details of the terms in the Landau free energy expansion.

Understanding the propagation of a magnetic structure is analogous to describing the propagation of an electronic wavefunction through a periodic potential in a crystalline material [29], for which the eigenfunctions are given by Bloch waves:

$$U_{\mathbf{k}}(\mathbf{r}) = U_{\mathbf{k}}(0)e^{-2\pi i\mathbf{k}\cdot\mathbf{t}}, \tag{2.28}$$

where the wavefunction at a position $\mathbf{r}$ from the origin (0) is given by the translation vector $\mathbf{t}$ and the propagation vector $\mathbf{k}$.

The total magnetisation, Ψ, for the general case of a magnetic structure with multiple propagation vectors, is also given by a summation of Bloch waves:

$$\Psi(\mathbf{r}) = \sum_{\mathbf{k},j} C^j_{\mathbf{k}} \psi^j_{\mathbf{k}}(0)e^{-2\pi i\mathbf{k}\cdot\mathbf{t}}. \tag{2.29}$$

This describes a symmetry adapted linear combination (SALC) of basis vectors $\psi^j_{\mathbf{k}}$ for atom j, where $\psi^j_{\mathbf{k}}$ describes the projection of the magnetic moment along an axis. The contribution of a basis vector to Ψ depends on the mixing coefficient $C^j_{\mathbf{k}}$ and their product determines the magnitude of a magnetic moment.

The group of symmetry elements that leave $\mathbf{k}$ invariant within a reciprocal lattice translation form the little group $G_{\mathbf{k}}$. The irreps of $G_{\mathbf{k}}$ then determine the possible magnetic structures. When the symmetry elements of $G_{\mathbf{k}}$ are applied to the magnetic sites in the crystal structure, the result is represented by the permutation representation, Γ_{perm}. The magnetic moments must be treated separately as axial vectors; if they are thought of as current loops (as described in Section 2.1) then inversion symmetry leaves these currents invariant. Applying the symmetry elements to the magnetic moments, results in the axial representation, Γ_{axial}. The magnetic

representation, Γ_{mag}, is then given by

$$\Gamma_{\text{mag}} = \Gamma_{\text{perm}} \times \Gamma_{\text{axial}}, \tag{2.30}$$

which can be decomposed into the irreducible representations of $G_{\mathbf{k}}$, Γ_{ν}:

$$\Gamma_{\text{mag}} = n\Gamma_{\nu}, \tag{2.31}$$

where n is the number of times that an irrep appears in Γ_{mag}. For a given propagation vector, these irreps are used to project the basis vectors and the mixing coefficients are refined to determine the magnetic structure (see equation 2.29).

2.4.6 Magnetic excitations

At non-zero temperatures the magnetic order in a system is disrupted by thermal fluctuations. In a crystalline solid the thermally excited lattice vibrations are quantised as phonons, whereas for magnetic order the excitations are termed spin waves and are quantised as magnons. Measuring spin waves is important in understanding the ground states of magnets and comparison with predictions from models enables the determination of the exchange parameters.

Spin waves are collective excitations of spin correlations and depend on the exchange interactions between the spins and single ion spin anisotropies. The dispersion of a spin wave can be calculated from the spin Hamiltonian. Such a calculation requires knowledge of the ground state of the magnetic system *i.e.* the low-temperature long-range ordered magnetic structure, and the exchange interactions. A commonly used method to calculate spin wave dispersions is linear spin wave theory (LSWT), which describes small fluctuations around the classical magnetic ground state and so works best at low temperatures and for large spins ($S \geq 3/2$) [30]. LSWT involves: *(i.)* substituting the spin operators with expressions involving the boson creation and annihilation operators; *(ii.)* simplifying the real magnetic Hamiltonian to a quadratic form, which is then diagonalized to obtain the energy eigenvalues that describe the dispersion [5]. As LSWT is a semi-classical method it is used as an approximation for $S = 1/2$ systems and higher order corrections are

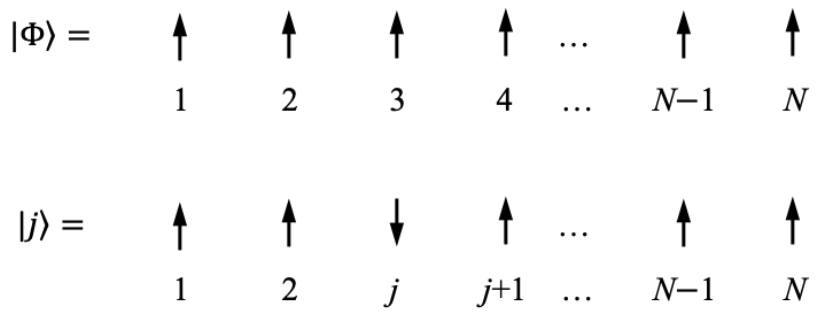

Figure 2.9: (**Top.**) The ground state $|\Phi\rangle$ of a spin-1/2 ferromagnetic spin chain with N spins. (**Bottom.**) An excitation is created by flipping a spin at site j, resulting in the spin state $|j\rangle$. The resulting spin wave has changed the total spin by $\Delta S = 1$. Adapted from [1].

necessary [30].

A simple example to understand LSWT is the $S = 1/2$ ferromagnetic spin chain with one magnetic site per unit cell, which has a ground state $|\Phi\rangle$ where all spins point along the z direction (see Figure 2.9). Assuming only nearest-neighbour isotropic exchange, the Heisenberg Hamiltonian (equation 2.21) becomes

$$\mathscr{H} = J\sum_i \mathbf{S}_i \cdot \mathbf{S}_{i+1}. \tag{2.32}$$

Equation 2.32 can be re-written using spin ladder operators $S^{\pm} = S^x \pm iS^y$, where the raising (lowering) operator S^+ (S^-) will raise (lower) the z component of the spin angular momentum by $\hbar$ [1]. If the spin angular momentum is at its maximum (minimum), the raising (lowering) operator will annihilate the state *i.e.* $S^+|\uparrow_z\rangle = 0$, $S^-|\downarrow_z\rangle = 0$. Using these ladder operators, equation 2.32 becomes:

$$\mathscr{H} = J\sum_i \left[S_i^z S_{i+1}^z + \frac{1}{2}\left(S_i^+ S_{i+1}^- + S_i^- S_{i+1}^+\right)\right]. \tag{2.33}$$

The ground state energy can be calculated by applying the Hamiltonian to the ground state, $|\Phi\rangle$, following the Schrödinger equation $\mathscr{H}|\Phi\rangle = E_\Phi|\Phi\rangle$. The spin ladder operators in equation 2.33 describe the fluctuations of the spins about the z axis and are therefore zero in the ground state. The ground state energy is then

given by the first term in equation 2.33 and $E_\Phi = NJS^2$ where N is the total number of spins and $S = |S_i^z|$ will be used hereafter. To induce an excitation, a single spin is flipped at site j as demonstrated in Figure 2.9 and this changes the total spin of the system by $\Delta S = 1$. The integer spin value of this change defines the excitation as a boson and such quanta can be experimentally created or annihilated with a neutron.

The excited state can be expressed as $|j\rangle = S_j^- |\Phi\rangle$, for which the energy is again found by applying the Hamiltonian of equation 2.33:

$$\mathscr{H}|j\rangle = (-NS^2J + 2SJ)|j\rangle - SJ|j+1\rangle - SJ|j-1\rangle . \tag{2.34}$$

The Hamiltonian is then diagonalized to obtain the spin wave dispersion by searching for plane wave solutions of type

$$|q\rangle = \frac{1}{\sqrt{N}} \sum_j e^{i\mathbf{q}\cdot\mathbf{R}_j} |j\rangle , \tag{2.35}$$

where $\mathbf{q}$ is the wave vector along the spin chain direction, $\mathbf{R}_j$ is the position of the spin j and the state $|q\rangle$ corresponds to a spin flip delocalized over all N sites. The perturbation caused by a single spin flip has a short wavelength and so a large energy cost would be associated with it. If this energy is delocalized over many sites, the perturbation has a long wavelength where the spins deviate a small amount from their equilibrium position; this excitation requires a vanishingly small amount of energy to create. Equation 2.35 essentially defines a spin wave and the spin procession around their z axes is illustrated in Figure 2.10.

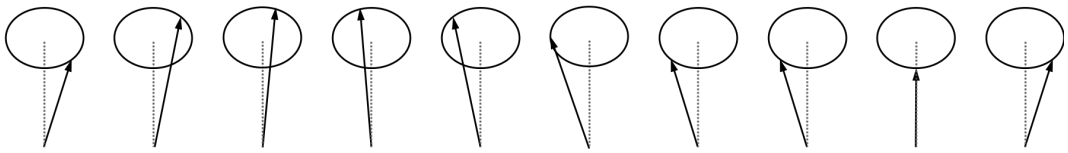

Figure 2.10: The spin precession around the z axis in a ferromagnetic spin chain caused by a spin wave excitation. Based on a figure in [1].

Applying the Hamiltonian to the state $|q\rangle$, $\mathscr{H}|q\rangle = E_q|q\rangle$, yields

$$E_q = NS^2J - 2JS(1-\cos(qa)), \tag{2.36}$$

where a is the lattice parameter of the magnetic unit cell. The first part of equation 2.36 is the ground state energy and the second part gives the spin wave dispersion relation for an isotropic ferromagnetic spin chain:

$$\hbar\omega_{\mathrm{FM}} = 2|J|S(1-\cos(qa)). \tag{2.37}$$

This dispersion is shown in Figure 2.11a and there are two important features to note: (*i.*) the amplitude is given by $\hbar\omega = 4|J|S$, thus enabling the largest J to be estimated, and (*ii.*) the low q region can be approximated as a quadratic dispersion where $\hbar\omega \approx |J|Sq^2a^2$.

A similar calculation can be done to find the dispersion relation for a $S = 1/2$ antiferromagnetic spin chain, which is given by

$$\hbar\omega_{\mathrm{AFM}} = 2|JS\sin(qa)|. \tag{2.38}$$

This dispersion is shown in Figure 2.11b and for small values of q is approximately linear with the relationship $\hbar\omega \approx 2|J|Sqa$, which is useful to experimentally differ-

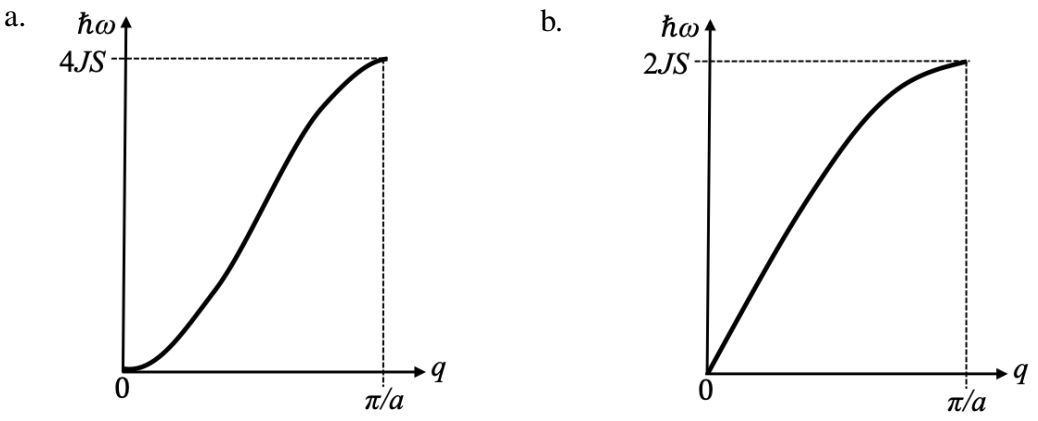

Figure 2.11: Spin wave dispersions for **a.** a ferromagnetic spin chain and **b.** an antiferromagnetic spin chain.

entiate between ferro- and antiferromagnets.

Usually, spin waves are experimentally measured using inelastic neutron scattering (INS). INS allows the measurement of the dynamical structure factor, which is the Fourier transform of the spin-spin correlation function as will be further detailed in Chapter 4. In the case of strongly correlated systems with only short-range order, the magnetic excitations are not spin waves and diffuse scattering is observed instead. Extracting the spin-spin correlation function of such systems, can give valuable information about the relative spin orientations. INS has been extensively used to measure excitations of strongly correlated and highly frustrated magnets where exotic states with well-defined correlations may arise, such as quantum spin liquids (QSLs). The most celebrated excitations in antiferromagnetic QSLs are exotic $S = 1/2$ quasiparticles that are termed spinons and the experimental signatures of spinons will be further discussed in relation to real materials in Chapter 3.

In complex magnetic systems there can be many competing exchange interactions that contribute to the Hamiltonian. Experimentally, the challenge is then to determine these by calculating the spin wave spectra from correspondingly complicated exchange models and compare them against inelastic neutron scattering data. This task is made challenging both by the size of the possible phase space of required parameters, as well as the requirement that the trial values lead to a Hamiltonian that is diagonalizable. In this thesis, linear spin wave theory was used for both averievite and claringbullite to determine the defining exchange interactions of their magnetic systems. For claringbullite in particular, a complex exchange model with seven parameters was needed to capture the main features of the complex spin wave spectra (Chapter 6).

Bibliography

[1] S. Blundell, *Magnetism in Condensed Matter* (Oxford University Press, New York, U.S.A., 2001).

[2] D. I. Khomskii, *Basic Aspects of The Quantum Theory of Solids* (Cambridge University Press, Cambridge, 2010).

[3] M. F. Collins, *Magnetic Critical Scattering* (Oxford University Press, 1989).

[4] G. L. Squires, *Introduction to the Theory of Thermal Neutron Scattering*, 3rd ed. (Cambridge University Press, Cambridge, 2012).

[5] A. T. Boothroyd, *Principles of Neutron Scattering from Condensed Matter* (Oxford University Press, July 2020).

[6] W. Pauli, Z. Physik **31**, 765 (1925).

[7] P. Zeeman, Nature **55**, 347 (1897).

[8] F. Hund, Z. Physik **33**, 345 (1925).

[9] B. Averill and P. Eldredge, *General Chemistry: Principles, Patterns, and Applications.* (Saylor Foundation, 2011).

[10] H. A. Jahn and E. Teller, Proc. R. Soc. Lond. A **161**, 220 (1937).

[11] E. Connolly, "Structure and magnetic properties of model S = 1/2 and S = 1 kagome magnets", Ph.D. thesis (University College London, 2019), pp. 175–178.

[12] C. A. Kilner, E. J. L. McInnes, M. A. Leech, G. S. Beddard, J. A. K. Howard, F. E. Mabbs, D. Collison, A. J. Bridgeman, and M. A. Halcrow, Dalton Trans. **4**, 236 (2004).

[13] G. A. Gehring and K. A. Gehring, Rep. Prog. Phys. **38**, 1 (1975).

[14] J. Crangle, *Solid State Magnetism* (Springer, New York, 1991).

[15] M. P. Marder, *Condensed Matter Physics* (John Wiley & Sons, New Jersey, 2010), p. 732.

[16] C. Lacroix, P. Mendels, and F. Mila, *Introduction to Frustrated Magnetism : Materials, Experiments, Theory* (Springer-Verlag Berlin and Heidelberg, 2011).

[17] J. B. Goodenough, Phys. Rev. **100**, 564 (1955).

[18] J. Kanamori, J. Phys. Chem. Solids **10**, 87 (1959).

[19] D. Boldrin, B. Fåk, E. Canévet, J. Ollivier, H. C. Walker, P. Manuel, D. D. Khalyavin, and A. S. Wills, Phys. Rev. Lett. **121**, 107203 (2018).

[20] I. Dzyaloshinsky, J. Phys. Chem. Solids **4**, 241 (1958).

[21] T. Moriya, Phys. Rev. **120**, 91 (1960).

[22] T. Matsumoto and S. Hayami, Phys. Rev. B **101**, 224419 (2020).

[23] A. S. Wills, S. Raymond, and J.-Y. Henry, J. Magn. Magn. Mater., 850 (2004).

[24] E. F. Bertaut, J. Magn. Magn. **24**, 267 (1981).

[25] A. S. Wills, Phys. Rev. B **63**, 064430 (2001).

[26] O. V. Kovalev, *Representations of the Crystallographic Space Groups: Irreducible Representations, Induced Representations and Corepresentations*, edited by H. T. Stokes and D. M. Hatch, 2nd ed. (Gordon and Breach, London, 1993).

[27] A. S. Wills, J. Mater. Chem. **15**, 245 (2005).

[28] A. Wills, J. Phys.IV France **11**, 133 (2001).

[29] E. F. Bertaut, J. Phys. Colloq. **32**, 462 (1971).

[30] S. Toth and B. Lake, J. Phys. Condens. Matter **27**, 166002 (2015).

Chapter 3

Frustrated magnetism

Many magnetic materials go through a phase transition at a temperature equal to the Weiss temperature, which constitutes a symmetry breaking from the para- to the ferro- or antiferromagnetic phase. However, such magnetic order can be 'frustrated' in magnetic systems where the pairwise interactions compete so that they cannot all be satisfied simultaneously. In magnetism, frustration leads to a degeneracy of the spin ground state that can be destroyed by thermal or quantum fluctuations, but can persist to $T = 0$ in particular systems, giving rise to exotic ground states. This chapter will discuss geometric frustration with reference to 2-dimensional and 3-dimensional lattices and give a brief overview of some significant experimental materials. As this thesis is focused on insulators, where the electrons are well localised, most of the materials discussed in this chapter are insulating magnets.

3.1 Geometric frustration in antiferromagnets

Frustration in magnetic systems can destabilise the Néel ground state, so that magnetic order occurs at a suppressed temperature or not at all. Finding experimental materials where the competing exchanges are simple enough to understand but large enough to reveal exotic physics be an arduous task. Much effort is focused on systems where the geometry of the magnetic lattice simply causes frustration, even when only nearest-neighbour exchanges are considered. The degree of frustration

is often experimentally determined by the frustration index, f, given by

$$f = \frac{|\theta_W|}{T_N}, \tag{3.1}$$

which characterises the suppression of the observed magnetic ordering temperature T_N with respect to the Weiss temperature θ_W. Care must be taken to differentiate between the effects of geometric frustration and low dimensionality of the lattice [1]. For example, a 1-dimensional system inherently prevents long-range magnetic order, irrespective of spin dimensionality, and so the suppression of T_N with respect to θ_W is not related to geometric frustration but to the dimensionality of the lattice. Similarly, in 2-dimensional lattices, such as the kagome lattice of corner-sharing triangles, long-range magnetic order is suppressed for a spin dimensionality larger than one. At low temperatures, exotic physics is only expected to arise for geometrically frustrated systems rather than purely low dimensional ones [1].

3.1.1 Triangular motif lattices

The simplest 2-D lattice to host geometrical frustration is the triangular lattice, where the triangles can either be edge-sharing or corner-sharing. To visualise geometric frustration, we look at a single triangle with Ising spins that can only point along a single axis and have nearest-neighbour antiferromagnetic interactions, as shown in Figure 3.1a [2]. The lattice geometry only allows two out of three antiferromagnetic interactions to be satisfied and by consecutive spin flips a total of six degenerate configurations can be formed, with each being a classical Néel state.

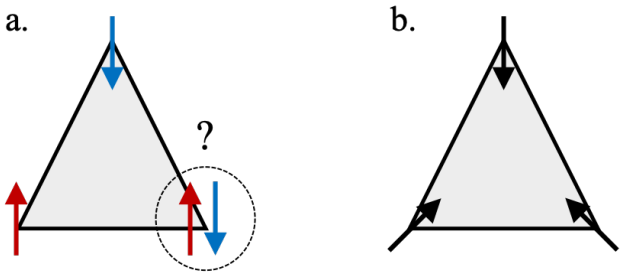

Figure 3.1: a. Ising spins on a triangle with nearest-neighbour antiferromagnetic interactions showing that not all interactions can be satisfied simultaneously. **b.** An example of a coplanar 120° compromise structure formed for XY or Heisenberg spins.

Away from the Ising limit where spins can only point along one axis, for classical XY or Heisenberg spins a compromise 120° structure is formed as shown in Figure 3.1b.

The most common extended triangular lattice is the edge-sharing one shown in Figure 3.2a. This lattice was used to introduce the resonating valence bond (RVB) model for quantum spins in Anderson's seminal paper [3]. Although it was later found that the ground state of this model is an 120° long-range ordered one, computational studies found quantum spin liquid phases when next neighbour interactions are present [4]. Much research has recently focused on rare-earth triangular magnets, where the spin anisotropy reduces the spin dimensionality and works with the inherent frustration of the lattice to suppress magnetic order [5].

An example of such rare-earth antiferromagnets is $YbMgGaO_4$, formed of an undistorted Yb^{3+} triangular lattice with an effective spin-$1/2$ ($J_{\text{eff}} = 1/2$). Inelastic neutron scattering measurements showed a continuum of excitations down to $T = 60$ mK, an experimental signature of the quantum spin liquid ground state [6]. It was found that its disordered ground state is a result of competing nearest- and further-neighbour exchange interactions [6] and anisotropic spins due to strong spin-orbit coupling [7], whilst the role of the Mg/Ga site disorder remains a topic of debate [8]. Much attention has also been given to the rare-earth delafossites, such as $NaYbS_2$ that has been proposed to be an experimental realisation of the $S = 1/2$ triangular lattice quantum spin liquid [9]. A variety of magnetic behaviours have actually been observed in triangular magnets, another example being magnetic vor-

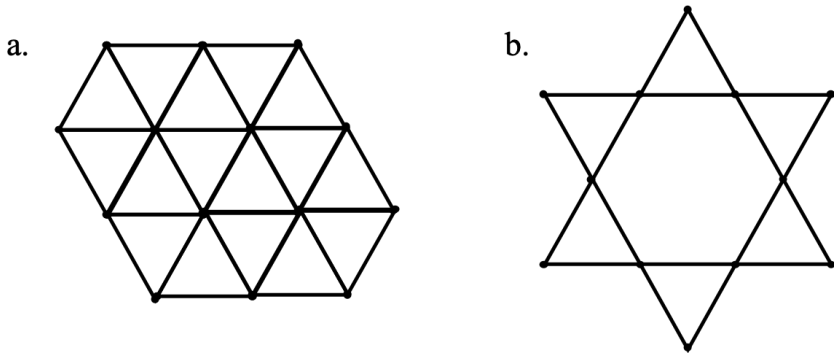

Figure 3.2: a. A triangular lattice of edge-sharing triangles. **b.** A kagome hexagon of vertex-sharing triangles.

tices in $NaCrO_2$ that may have applications in the field of spintronics [10, 11]. These examples showcase the exotic physics that can be realised in materials with magnetic triangular lattices.

Expanding the triangular lattice to 3-dimensions yields the pyrochlore lattice formed of corner-sharing tetrahedra (see Figure 3.3a). The rare-earth titanates are the most widely studied pyrochlores with the general formula $R_2T_2O_7$, where two sublattices of tetrahedra are formed by the magnetic rare-earth cation R and the diamagnetic transition metal T. Single-ion effects lead to the magnetic moments behaving as Ising spins, pointing towards the centre of each tetrahedron with n.n. ferromagnetic interactions [13]. The ground state depends on the relative energy scales of the dipolar and exchange interactions. Dominant dipolar interactions lead to long-range magnetic order, whereas dominant exchange interactions form exotic magnetic states due to the inherent frustration of the magnetic lattice. When the two interactions are of similar energy scales, short-range order prevails and the spins obey a local constraint – the 2-in-2-out 'ice rule' (Figure 3.3b). These systems are termed 'spin ices' because the arrangement of spins is analogous to the proton positions in ice, H_2O, where two are located closer and two further away from a central oxygen atom. Perhaps the most intriguing realisation in spin ices is the magnetic monopole. Treating each spin as having a positive and a negative charge

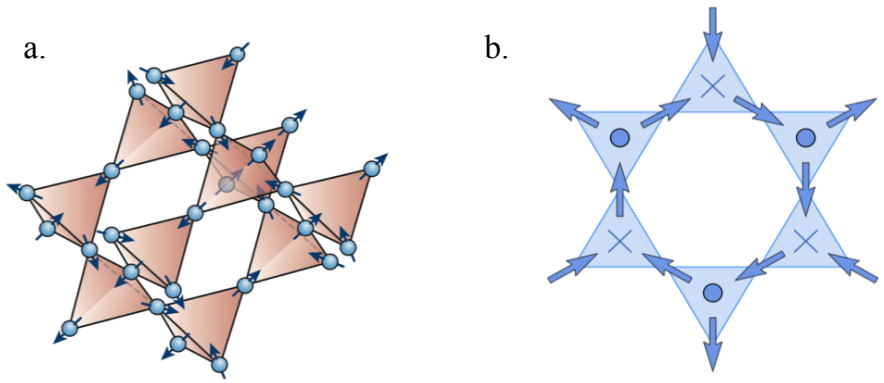

Figure 3.3: a. A pyrochlore lattice of corner-shared tetrahedra. Taken from [2]. **b.** A 2-D representation of the spin configuration of a pyrochlore lattice on a kagome plane. Shown at the centre of each triangle are the out-of-plane spins: dots (crosses) refer to spins pointing inwards (outwards) of each tetrahedron. Taken from [12].

yields charge-neutral tetrahedra. However, an excitation caused by a single spin flip results in two neighbouring tetrahedra having net opposite charges, which can be spatially separated into two magnetic monopoles by consecutive spin flips [14–16].

Apart from spin ices, a 3-dimensional quantum spin liquid may also be realised on the pyrochlore lattice as shown by exact diagonalization studies based on the $S = 1/2$ Heisenberg Hamiltonian [17]. An experimental realisation of this is Sc-doped YMn_2, which is an itinerant magnet *i.e.* the unpaired electrons are in the conduction band. In this material, the Mn ions form the pyrochlore lattice and Y (or Sc) occupy the cavities. The undoped material undergoes a magnetic phase transition at $T \approx 100$ K [18] and by doping Sc onto the Y sites, chemical pressure is created that suppresses the long-range magnetic order [19]. The magnetic structure factor of $Y_{0.97}Sc_{0.03}Mn_2$, probed using single crystal inelastic neutron scattering [19], was found to be similar to that of the $S = 1/2$ Heisenberg model [17], demonstrating that the magnetic behaviour of $Y(Sc)Mn_2$ is mainly due to quantum fluctuations.

3.1.2 The kagome lattice

The vertex-sharing connectivity of the kagome lattice (Figure 3.2b) is insufficient to allow a unique ground state to propagate leading to a macroscopic degeneracy that scales with lattice size. It is the 2-D lattice with the largest macroscopic ground state degeneracy and supports zero energy excitations, predicted to suppress magnetic order even at $T = 0$ [20, 21]. For $S = 1/2$ systems, quantum fluctuations become important yielding a quantum spin liquid ground state, whilst for larger spins other states such as spin glasses are realised.

Historically, the most widely studied kagome magnets belong to the jarosite family. These have the general formula $AB_3(SO_4)_2(OH)_6$ where $A = Na^+$, K^+, Rb^+, NH_4^+, Ag^+ and H_3O^+, and $B = Fe^{3+}$, Cr^{3+} and V^{3+} [21]. Depending on the magnetic ion, various spin states are realised from quantum to more classical ones including $S = 1,\ 3/2$ and $5/2$ [22]. They crystallise in the $R\bar{3}m$ space group and the transition metals sit in distorted octahedral environments, coordinated by four equatorial hydroxide groups and two axial oxygens belonging to the $(SO_4)_2$ groups. Therefore, the superexchange interactions are mediated by μ_3-O groups.

Despite the macroscopic degeneracy of the kagome lattice, long-range order is seen as a result of coupling between kagome planes, spin-orbit coupling effects or site disorder [23]. In earlier works, long-range order was thought to be primarily caused by the site disorder, but studies on single crystals of stoichiometrically pure jarosites ($A = Na^+$, K^+, Rb^+ and $B = Fe^{3+}$) indicated it to be an intrinsic effect [24]. In the original jarosite ($A = K^+$ and $B = Fe^{3+}$), the complex magnetic order results from strong nearest-neighbour antiferromagnetic interactions ($|\theta_W| > 600$ K) with a significant Dzyaloshinskii-Moriya component [25], as well as interplanar coupling ($\mathbf{k} = (0,\ 0,\ 3/2)$ with respect to the hexagonal setting of the rhombohedral cell) [21]. The Cr analogue ($A = K^+$ and $B = Cr^{3+}$) exhibits simultaneous static and dynamic fluctuations with a partial antiferromagnetic ordering at $T_N \approx 2$ K and the residual spins form a gapless spin liquid [26]. In fact, replacing the Fe^{3+} B-site cation with Cr^{3+}, leads to magnetic order with a $\mathbf{k} = \mathbf{0}$ propagation vector, indicating a significant change in the interplanar coupling [21]. A different behaviour is observed when substituting vanadium on the B-site, as it relieves the frustration and long-range ordered collinear antiferromagnetic states were observed [27].

Deuteronium iron jarosite ($A = H_3O^+$ and $B = Fe^{3+}$) attracted a lot of attention due to its spin glass ground state, which is unlike all the other ground states observed in this family of materials [22]. This glassy state is unconventional, in that it does not arise from random disorder, but from a spin anisotropy resulting from the distorted octahedral environment around Fe^{3+} [28].

The wide variety of materials that belong to the jarosite family have furthered the understanding of unconventional magnetic behaviours in frustrated systems with different spin values and highlighted the importance of DMIs and interplanar correlations. The latter is an essential characteristic that will be brought up again in the context of the claringbullite series in Chapters 5 and 6.

3.1.3 The pyrochlore slab lattice

The pyrochlore slab lattice is formed of distinct tetrahedra bilayers. This structure is present in the widely studied Cr based $S = 3/2$ materials $SrCr_{9p}Ga_{12-9p}O_{19}$ (SCGO) and $Ba_2Sn_2ZnCr_{7p}Ga_{10-7p}O_{22}$ (BSZCGO). In BSZCGO the pyrochlore

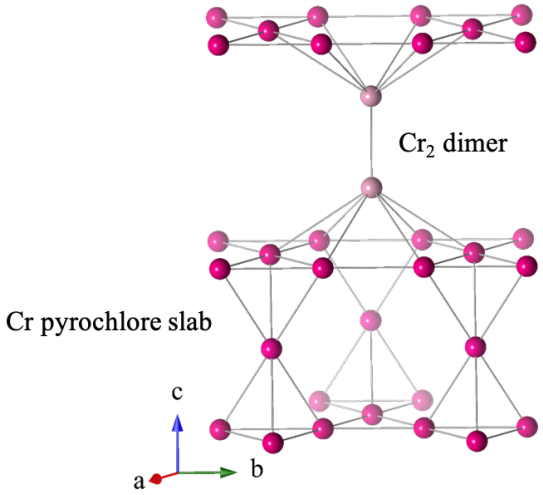

Figure 3.4: $SrCr_{9p}Ga_{12-9p}O_{19}$ (SCGO) pyrochlore slab structure formed of Cr ions separated by Cr dimers.

slabs are well-separated, whereas in SCGO there are Cr-Cr dimers between the layers (see Figure 3.4) that form singlets and do not affect its low-temperature magnetic behaviour [29]. Both materials suffer from Ga/Cr site disorder that depletes the magnetic lattice by 3-4% [21], but the robustness of the ground state is demonstrated by the dynamic spin fluctuations persisting to $T \sim 100$ mK, well below the glass-like transition at $T_g \sim 2-5$ K [30].

A type of pyrochlore slab lattice also appears in the averievite series studied in Chapters 7 and 8, but is formed of $S = 1/2$ Cu^{2+} ions. In SCGO the pyrochlore slabs are made of kagome-triangular-kagome layers with a slab separation of $\sim$ 11 Å, whereas in averievite the formation is triangular-kagome-triangular with a $\sim$ 5 Å separation. Unlike SCGO, the spin correlations in averievite are 3-dimensional and it has a magnetic phase transition at $T_N = 23$ K.

The materials discussed so far focus on $S > 1/2$, but the role of quantum fluctuations is best assessed when $S = 1/2$ and this will be discussed in the next section.

3.2 Quantum frustration

In low-dimensional quantum systems long-range magnetic order is not expected to prevail, instead strong quantum fluctuations can lead to exotic states that do not break symmetry as conventional magnets do [21]. Entanglement of nearest-

neighbour unpaired spins ($S = 1/2$) form non-magnetic singlets ($S = 0$), called valence bonds, and can be treated as "quantum paramagnets". Valence bonds can either form a long-range ordered structure known as a valence bond crystal or remain dynamic with no long-range order. The latter model is the resonating valence bond (RVB) model, the simplest type of quantum spin liquid (QSL).

3.2.1 Valence bond crystals

In many Heisenberg models, the valence bond (VB) configuration is favoured and these systems do not develop Néel order down to $T = 0$ [21]. The ground state of the valence bond crystal (VBC) is a single VB configuration (Figure 3.5a), however this VB configuration is not usually an eigenstate of the Hamiltonian and the ground state is stabilised by local quantum fluctuations in a mechanism known as "order by disorder" [21]. The quantum fluctuations create states similar to the "parent" VB configuration, which are less energetically favourable (*e.g.* Figure 3.5b).

The excitations of a VBC entail $\Delta S = 1$ transitions, which are gapped and can be observed as sharp modes in inelastic neutron scattering experiments. Unlike quantum spin liquids, VBCs do not support fractionalised $S = 1/2$ (spinon) excitations. Spinon excitations would require a singlet to break, as shown in Figure 3.5c, resulting in misaligned dimers between the two $S = 1/2$ entities that would lead to a state higher in energy than the parent VB configuration. The energetic cost of creating two spinons is roughly proportionate to the distance between them, preventing their infinite separation. At a certain distance it becomes energetically favourable to break another singlet and confine the spinons to their point of creation, returning the state to the VBC pattern (see Figure 3.5d).

3.2.2 Resonating valence bond liquids and spin liquids

In the case of a VBC, a single VB configuration is chosen as the ground state, which breaks translational symmetry and leads to a long-ranged dimer order. Monte-Carlo studies on the $S = 1/2$ kagome Heisenberg antiferromagnet, have shown that such order may occur in the presence of a small next nearest-neighbour exchange in addition to a nearest-neighbour exchange interaction [31]. When there is no en-

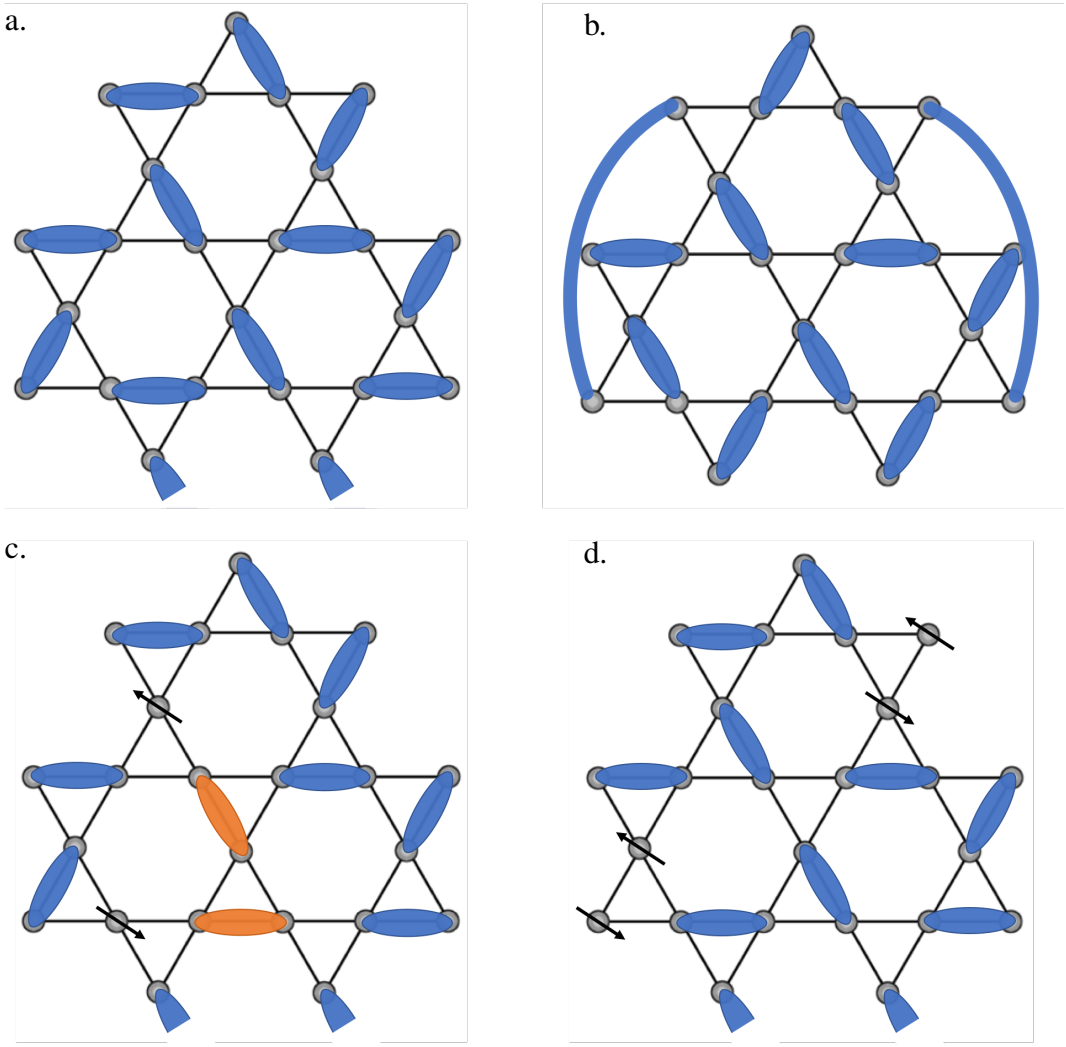

Figure 3.5: a. A single valence bond configuration formed of nearest-neighbour singlets. **b.** Long-range entanglement can lead to different valence bond configurations with further neighbour singlets. **c.** Breaking a valence bond (or singlet) results in two spinons ($S = 1/2$), which propagate through the lattice causing a rearrangement of valence bonds that has an energy cost which scales with the distance between the two spinons. **d.** At a large distance it becomes energetically favourable to break another singlet. The spinons are confined and cannot freely propagate, so valence bond crystals do not support spinon excitations.

ergetic preference for a particular VB configuration, the ground state arises from a superposition of an extensive manifold of equally weighted VB configurations (see Figure 3.6). This ground state is known as a resonating valence bond liquid and has no long-range order (of the spins or dimers). Importantly, the absence of a favoured VB configuration, as in VBCs, implies that spinons cannot be confined and therefore freely propagate in the lattice. In fact, spinon excitations are one of

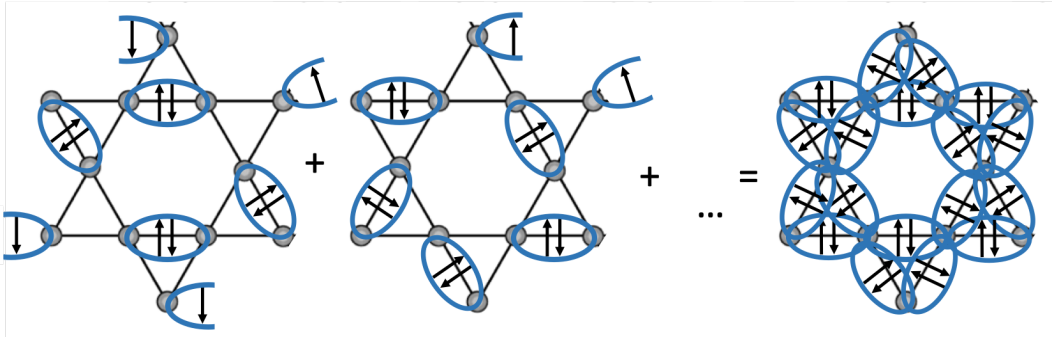

Figure 3.6: A resonating valence bond liquid ground state, arising from the superposition of equally weighted valence bond configurations with strong quantum fluctuations.

the signatures of a quantum spin liquid state and are observed in inelastic neutron scattering experiments as a continuum of excitations in energy and momentum.

As QSLs do not break symmetry in the classical sense, they cannot be characterised by Landau's theory for second order transitions. Instead, they are characterised by a "quantum order" and are classified according to their topology [32]. In fact, there are different QSLs within the RVB model and beyond this model there exist many other QSL "flavours". Classifying QSLs relies on both experimental and theoretical work. For example, on the experimental side, inelastic neutron scattering or NMR measurements can be used to determine whether the excitations are gapped or gapless. As will be seen for the experimental materials presented in Section 3.3, as well as Chapters 6 and 8, finding experimental signatures of these states is not straightforward.

3.3 Experimental $S = 1/2$ kagome magnets

Few experimental $S = 1/2$ kagome antiferromagnets (KAFMs) have been shown to host a quantum spin liquid ground state. Most of the synthetic materials studied stem from naturally occurring minerals such as the paratacamite family, $(Zn,Mg)_xCu_{4-x}(OH)_6Cl_2$ (see Figure 3.7). The most well-studied of these are the Zn-paratacamites, which include the best known $S = 1/2$ kagome antiferromagnet (KAFM), herbertsmithite, γ-$ZnCu_3(OH)_6Cl_2$, reported to host a $S = 1/2$ resonating valence bond (RVB) spin liquid [33–35]. Other notable materials in this series include kapellasite, α-$ZnCu_3(OH)_6Cl_2$ [36], haydeeite, α-$MgCu_3(OH)_6Cl_2$ [37] and

'Mg-herbertsmithite', γ-$MgCu_3(OH)_6Cl_2$ [38]. Instead of Zn or Mg, variants with Cd [39], Ca [40] or even trivalent ions such as Y^{3+} [41] have been synthesised. The search for experimental realisations of QSLs beyond the nearest-neighbour RVB model has driven a lot of research into other $S = 1/2$ KAFMs, some of which will be discussed below.

3.3.1 Clinoatacamite and Herbertsmithite, γ-$Zn_xCu_{4-x}(OH)_6Cl_2$

The thermodynamically stable form of copper hydroxychloride, $Cu(OH)_3Cl$, is the $\gamma-$polymorph clinoatacamite, the parent material of herbertsmithite [42, 43]. Clinoatacamite crystallises in the monoclinic $P12_1/n1$ space group and has a distorted Cu^{2+} pyrochlore lattice [44, 45]. This is formed of three Cu sites: two that are coordinated by $Cu(OH)_4Cl_2$ and form distorted kagome layers, and the interlayer site that has a $Cu(OH)_6$ coordination [43]. Clinoatacamite is strongly frustrated with a suppressed magnetic transition at $T_N \approx 6$ K despite the strong antiferromagnetic interactions ($\theta_W \approx 180$ K) [46]. Its magnetic structure was found to be almost collinear in the kagome planes with the interlayer site having significant out-of-

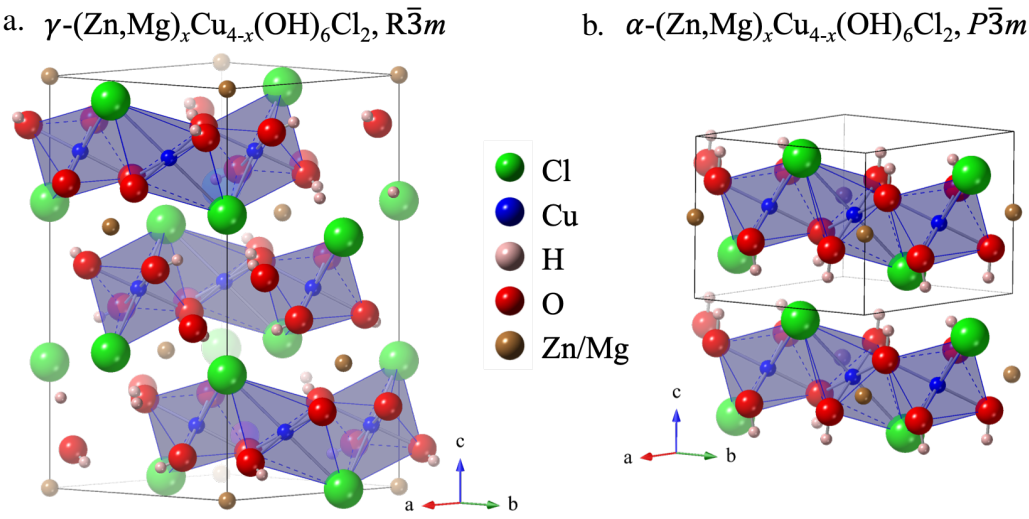

Figure 3.7: Crystal structures of the **a.** γ-phase and **b.** the α-phase of the paratacamite family, $(Zn,Mg)_xCu_{4-x}(OH)_6Cl_2$. The diamagnetic ions lie between the kagome layers in the γ-phase possibly providing superexchange pathways between the kagome layers if there is subsitution by the magnetic ion, Cu^{2+}. In the α-phase the diamagnetic ions occupy the centre of the kagome hexagons, in the same plane as the Cu^{2+} ions, affording a highly 2-dimensional system.

plane canting [46]. Interestingly the magnetic excitations observed using inelastic neutron scattering, do not represent typical spin waves expected from a long-range ordered magnet. Instead, two responses are seen at ~ 7 meV and ~ 1.3 meV, where the higher energy scattering corresponds to short-range correlations and at low-energy there is a band of magnetic scattering with a weak dispersion and a zero-energy gap [45]. The low-energy band could not be well described by spin wave theory and it was proposed that large anisotropic effects must be taken into account [45]. The remarkable aspect of these excitations is that the signatures of short-range correlations and long-ranged order, indicate the coexistence of ordered and disordered spins in the system as a result of the frustration [45].

Diamagnetic doping of clinoatacamite at the $\geq 1/3$ level of the interlayer Cu^{2+} sites, suppresses the monoclinic distortion and the low-temperature crystal structure remains in the rhombohedral space group $R\bar{3}m$ [47]. Replacing all interlayer Cu sites with Zn yields another mineral herbertsmithite, $\gamma-ZnCu_3(OH)_6Cl_2$. When doping clinoatacamite with Zn^{2+}, the diamagnetic ions can either occupy the more spherically symmetrical interlayer site or the kagome site that has an axially elongated octahedral environment. As Zn^{2+} is not a Jahn-Teller active ion, it was expected that it would preferentially dope onto the interlayer site. However, neutron diffraction, ^{17}O-NMR and magnetic susceptibility measurements indicated 6-10% Zn/Cu antisite disorder, due to the similar ionic radii of Zn^{2+} and Cu^{2+} and their similar coordination environments [48–50]. The presence of interlayer Cu ions and a non-magnetic dilution of the kagome layers, has led to a dispute in the literature about whether the magnetic excitations are gapped and therefore the type of quantum spin liquid that it hosts [51, 52].

Herbertsmithite was shown to be a highly frustrated magnet from magnetic susceptibility and muon spin relaxation (μSR) measurements, as no magnetic phase transition was observed down to $T = 50$ mK despite the large Curie-Weiss temperature of about -300 K [35, 53, 54]. The nearest-neighbour exchange interaction was calculated to be $J \simeq 17$ meV , demonstrating strong antiferromagnetic Cu-Cu interactions [35]. The suppression of a magnetic phase transition was evidence of

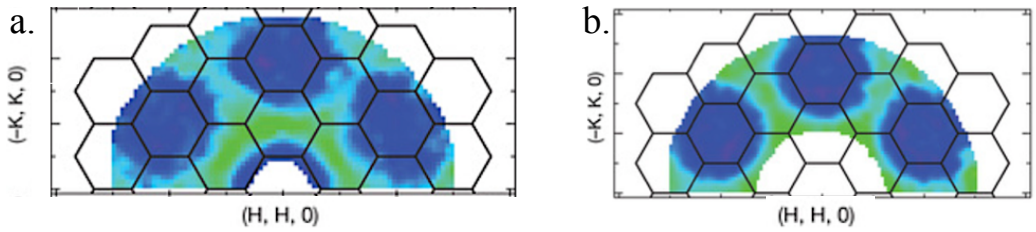

Figure 3.8: a. Inelastic neutron scattering data collected on single crystals of herbertsmithite at $T = 1.6$ K. The diffuse continuum of excitations evidence fractionalised excitations, which are characteristic of quantum spin liquids. **b**. Calculated spectra of the dynamical structure factor using the nearest-neighbour resonating valence bond model. Taken from [33].

a dynamic ground state and diffuse magnetic excitations were observed in single crystal inelastic neutron scattering measurements indicating short-range spin correlations (see Figure 3.8a) [33]. The excitation continuum suggested fractionalized excitations, a signature of quantum spin liquids, and the magnetic scattering was well-described by the nearest-neighbour Heisenberg antiferromagnet model on a kagome lattice (the RVB model) as shown in Figure 3.8b [33]. To date, this is the best experimental realisation of the RVB state.

3.3.2 Kapellasite, α-$ZnCu_3(OH)_6Cl_2$

A common polymorph of herbertsmisthite is the mineral kapellasite, α-$ZnCu_3(OH)_6Cl_2$, which has been shown to be a quantum spin liquid with nearest-neighbour (J_1) ferromagnetic and "across hexagon" (J_d) antiferromagnetic interactions (see Figure 3.9a). It crystallises in the $P\bar{3}m1$ space group, retaining the three-fold symmetry of the kagome triangles and the Zn^{2+} lies in the centre of the kagome hexagons, rather than between the kagome layers as in herbertsmithite [55]. This affords a more two dimensional structure than herbertsmithite, as any Cu/Zn antisite disorder would not encourage coupling between kagome layers, but it could affect the superexchange pathways going through the kagome hexagons. μSR measurements showed no long-range order down to $T = 20$ mK and powder inelastic neutron scattering measurements evidenced gapless diffuse excitations arising from short-range correlations of the non-coplanar cuboc2 type (see Figure 3.9b) [36]. High temperature series fits to the magnetic susceptibility gave a $J_1 - J_d$

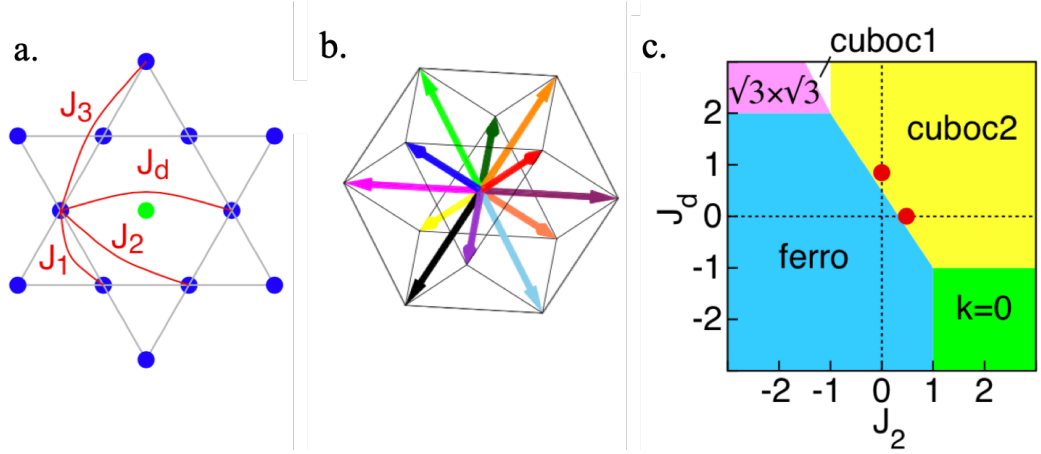

Figure 3.9: a. Kagome lattice of kapellasite formed of Cu^{2+} (blue) with diamagnetic Zn^{2+} (green) in the hexagon centre. The exchange interactions up to the third n.n. are shown by the red lines. **b.** Cuboc2 structure showing the spin directions as pointing to the vertices of a cuboctahedron. **c.** Phase diagram of J_2-J_d exchange interactions for a ground state with ferromagnetic J_1, as in kapellasite. All taken from [36].

solution shown on the classical $J_2 - J_d$ phase diagram of the nearest-neighbour ferromagnetic kagome lattice ($J_1 = -1$ and $J_3 = 0$) in Figure 3.9c [36]. Moreover, the quantum phase diagram for J_1, $J_2 \leq 0$ and $J_d \geq 0$ showed that for these exchange interactions, kapellasite has a chiral quantum spin liquid ground state [56]. The results on kapellasite emphasise the exotic spin liquid physics that is possible beyond the nearest-neighbour antiferromagnet, calling for the characterisation of other $S = 1/2$ kagome magnets that may host different quantum spin liquid types.

3.3.3 Barlowite and its Zn-doped variants, $Zn_xCu_{4-x}(OH)_6FBr$

Beyond the nearest-neighbour $S = 1/2$ kagome antiferromagnet, long-range entanglement in highly correlated systems can lead to other types of QSLs. Recently much attention in the literature has been given to the mineral barlowite, $Cu_4(OH)_6FBr$, which crystallises in the hexagonal $P6_3/mmc$ space group at room-temperature, for both natural and synthetic crystals [57–59]. Similarly to clinoatacamite, it has a Cu^{2+} pyrochlore lattice but with an *AA* stacking of kagome layers instead of *ABC*. This results from the substitution of half the Cl^- ions in herbertsmithite with F^- ones, resulting in stronger H-bonding with the hydroxide groups that drives a change in the kagome layering (see Figure 3.10) [60]. At high temperature, the interlayer Cu is disordered over three sites and on cooling it orders

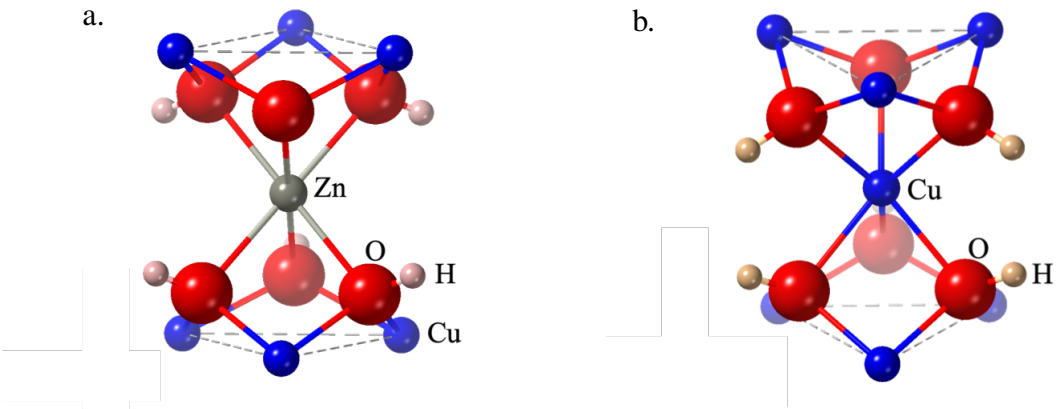

Figure 3.10: a. Stacking of kagome lattice in herbertsmithite showing the triangles are rotated by 60° from one layer to the next. **b.** In barlowite the kagome layers have *AA* stacking and the interlayer Cu here is shown on the average site. The dashed lines show the Cu kagome triangles.

onto one of them, driving a hexagonal-orthorhombic distortion between $T = 220$ and 276 K [60–62]. Single crystal neutron and x-ray studies down to $T = 15$ K showed that although there is a preference for the Cu to order onto one of the three sites, $\sim 16\%$ of them order onto the other two sites [63]. This could locally affect the superexchange pathways and local magnetic behaviour, but will not necessarily affect the bulk magnetic properties and collective excitations.

A discrepancy between the low-temperature crystal structures is seen due to the different hydrothermal syntheses used in the literature. Specifically, electron diffraction on one set of single crystals indicated a *Cmcm* low-symmetry phase [64], whilst other powder and single crystal samples, synthesised using similar reagents, showed a *Pnma* phase from synchrotron x-ray and neutron diffraction studies [60, 62, 65]. Another synthetic route was developed to produce single crystals that retained a hexagonal symmetry ($P6_3/m$) down to $T = 15$ K, due to the interlayer Cu ordering with a more even distribution onto the three possible sites [63]. These structural differences affect the magnetic behaviour and two magnetic phase transitions were observed in the magnetic susceptibility instead of one [63]. Additionally, a slightly different magnetic structure was found for this sample than for barlowite crystallising in the *Pnma* space group [63, 65].

A more detailed study on powder samples of barlowite using combined neutron

and synchrotron diffraction, indicated that for $1.5 \leq T \leq 90$ K the sample comprised of both a $P6_3/mmc$ and a *Pnma* phase ($\sim 65\%$ weight percentage) [61, 65]. This introduces a further complexity in these materials as the exchange interactions can be significantly different around the distorted interlayer Cu and the "disordered" Cu in $P6_3/mmc$, making it harder to elucidate its magnetic ground state. These studies highlight a sample dependency in barlowite that in turn underlines the importance of crystallographic characterisation for each synthetic sample.

Magnetometry and heat capacity measurements showed that barlowite is highly frustrated with a suppressed ordering temperature of $T = 15$ K, despite the strong antiferromagnetic interactions ($\theta_W = -136$ K) [58, 62]. In an attempt to suppress the magnetic phase transition, barlowite was chemically doped with diamagnetic Zn^{2+} [62, 64, 66–68]. Powder x-ray synchrotron and neutron diffraction studies indicated that for doping levels above $\sim 66\%$ of the interlayer sites, the hexagonal $P6_3/mmc$ symmetry is retained down to $T = 1.5$ K [68, 69]. The *AA* kagome stacking in barlowite had been predicted to decrease the antisite disorder observed in herbertsmithite, as the interlayer site is trigonal prismatic (instead of octahedral in herbertsmithite) and the closed-shell Zn^{2+} ion prefers it to the more distorted square planar kagome site [66]. Indeed, μSR measurements suggested that the kagome dilution by Zn^{2+} is lower than in herbertsmithite [68], whilst x-ray anomalous diffraction combined with single crystal x-ray diffraction on a different sample showed only 5% Cu occupancy of the interlayer sites [69, 70].

Zn-barlowite, $Zn_xCu_{4-x}(OH)_6FBr$, has been synthesised with several substitution levels, the highest ones being $x = 0.95$ [69] and $x = 0.99$ [68]. These samples have a high degree of frustration, showing no magnetic phase transition in magnetic susceptibility and heat capacity measurements down to $T = 50$ mK, despite having a stronger antiferromagnetic mean field ($\theta_W \approx -200$ K) than the parent compound barlowite [62–64]. Furthermore, local probe μSR measurements showed that the spins continue to fluctuate down to $T = 50$ mK and a phase diagram of its ground state showed a robust QSL ground state that prevails down to a substitution level of $x = 0.66$ [68, 71]. ^{19}F NMR, INS and μSR measurements down to $T \approx 1.5$ K have

demonstrated gapped magnetic excitations in Zn-barlowite and its ground state has been proposed to be a topological Z_2 spin liquid – the simplest type of gapped spin liquid, which is essentially an RVB state with short-range correlations [71–73]. If this is in fact the topological symmetry of Zn-barlowite, it indicates a different quantum spin liquid flavour to *e.g.* the chiral spin liquid in kapellasite (which has gapless excitations) [56].

Closely related to the Zn-barlowite series is the isostructural Zn-claringbullite series, $Zn_xCu_{4-x}(OH)_6FCl$ [74]. Its structure has been previously characterised at room temperature, and magnetic susceptibility and heat capacity measurements showed no magnetic phase transition down to $T = 0.8\,\mathrm{K}$. Chapters 5 and 6 will present the synthesis and structural characterisation of the protonated and deuterated claringbullite, $Cu_4(OD)_6FCl$, and Zn-claringbullite, $ZnCu_3(OD)_6FCl$, as well as inelastic neutron scattering measurements showing $ZnCu_3(OD)_6FCl$ to have a quantum spin liquid ground state with gapless magnetic excitations.

3.3.4 Vesignieite, $BaCu_3V_2O_8(OH)_2$

Another hydroxide material, unrelated to the paratacamite family, is vesignieite, $BaCu_3V_2O_8(OH)_2$. In this material, CuO_6 octahedra form kagome layers separated by large VO_4 tetrahedra and Ba^{2+} ions (Figure 3.11a), which suppress interlayer coupling. In addition, the difference in the charges of Cu^{2+} and V^{5+} prevents antisite disorder that could affect the superexchange pathways between the kagome layers. In fact, vesignieite is one of the most 'ideal' realisations of a $S = 1/2$ kagome antiferromagnet with almost perfect kagome layers and offered strong grounds for realising a quantum spin liquid.

Polycrystalline samples have been reported to crystallise in the $C12/m1$ monoclinic space group with a small ($< 1\%$) distortion in the kagome triangles [38, 77], whereas one set of single crystals was found to crystallise in the high-symmetry $R\bar{3}m$ space group at room temperature [78]. Powder samples produced using a different synthetic route, developed for the related Sr-vesignieite ($SrCu_3V_2O_8(OH)_2$) [79], were shown to crystallise in the $P3_121$ space group using synchrotron x-ray and neutron diffraction [75]. In the $P3_121$ model, the unpaired electron occupies

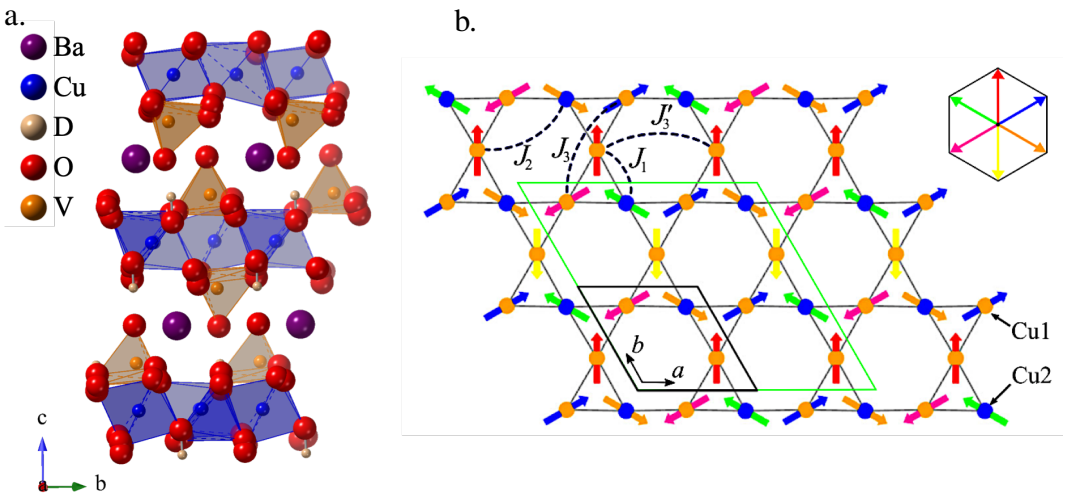

Figure 3.11: a. Vesignieite $P3_121$ crystal structure [75]. The Cu atoms (blue) form kagome layers which are separated by VO_4 groups (orange polyhedra) and Ba^{2+} ions (purple). **b.** The hexagonal coplanar multi-**k** magnetic structure of vesignieite. The dominant exchange interaction is the antiferromagnetic third nearest-neighbour one, J_3. Taken from [76].

the $d_{x^2-y^2}$ orbital [75] rather than the d_{z^2} one as in the $C12/m1$ structure [77]. In addition, one of the two Cu sites making up the kagome layers sits in an axially compressed octahedral environment suggesting a dynamic Jahn-Teller effect, whereby the $d_{x^2-y^2}$ orbital fluctuates between two configurations [75].

Despite the distortion in the kagome layers being small and a moderate degree of frustration ($\theta_W \approx -75$ K), magnetic susceptibility measurements showed a phase transition at $T \approx 9$ K (irrespective of the high-temperature crystal symmetry) [76, 78, 80]. Below the magnetic phase transition temperature, neutron scattering measurements on deuterated samples indicated a hexagonal coplanar multi-**k** magnetic structure shown in Figure 3.11b [76]. Powder inelastic neutron scattering measurements were used to measure the magnetic excitations and linear spin wave theory was used to model them. It was found that the dominant exchange interaction is the antiferromagnetic third-neighbour one and has a value of $J_3 = 2$ meV with a weak symmetric exchange anisotropy ($\sim 0.006 J_3$) [76].

3.4 Experimental *S*=1 and *S*=3/2 semi-classical magnets

The magnitude of the spin affects the strength and nature of quantum fluctuations, potentially changing the ground state of a frustrated magnet. In a system with $S = 1$ or $S = 3/2$ we enter a semi-classical regime. Theoretical studies for integer spins on a kagome lattice, suggest that they behave differently to half-integer spin systems [81] and can lead to exotic phases such as spin nematics [82]. However, few experimental examples of $S = 1$ kagome materials are known [83]. For example, the aforementioned jarosites include the series of $S = 1$ vanadium jarosites, $AV_3(OH)_6(SO_4)_2$ where A = H_3O^+, Na^+, K^+, Rb^+, NH^+, Tl^+ [84–87]. However, the strong V^{3+}-V^{3+} intra-planar ferromagnetic interactions and lack of magnetic frustration, with long-range order setting in below $T = 50\,\mathrm{K}$, makes them less studied in the frustrated magnetism community.

Another example of a V-based kagome magnet is NaV_6O_{11}, which has three vanadium sites: the V(1) site that is a $S = 1$ V^{3+} ion and forms the kagome lattice; and two crystallographically different $S = 1/2$ V^{4+} ions (V(2) and V(3)) that occupy interplanar sites [88]. Initially it was expected that the $S = 1/2$ ions would provide superexchange pathways between the kagome layers, leading to long-range magnetic order. However, magnetometry and ^{23}Na-NMR studies found that this material orders into a spin-singlet ground state below $T_t = 245\,\mathrm{K}$ with V(1) forming trimers in the kagome layers [88, 89]. Laboratory powder XRD measurements evidenced a distortion in the kagome layers below T_t and it was suggested that orbital ordering was the driving factor in the formation of the nonmagnetic ground state [89]. This material highlights the importance of considering the effects of orbital interactions, in addition to spin-spin interactions, on magnetic behaviours.

Away from vanadium based magnets, interesting cases of Ni-based magnets have been studied in the context of $S = 1$ systems, such as $Ni_3V_2O_8$ where it has been shown that the magnetic order generates ferroelectricity [90]. Another recently studied Ni magnet is $NH_4Ni_{2.5}V_2O_7(OH)_2 \cdot H_2O$, which crystallises in the hexagonal $P6_3/mmc$ space group and the Ni^{2+} ions form depleted kagome layers

(∼77% site occupancy) separated by bivanadate units [83]. Despite dominant antiferromagnetic interactions ($\theta_W = -42$ K), there is a ferromagnetic-like ordering that is suppressed to $T = 17$ K indicating magnetic frustration and competing ferro- and antiferromagnetic interactions [83]. For a more in-depth understanding of the ground state and the Hamiltonian that describes it, inelastic neutron scattering measurements are required. These studies will also be interesting in the context of understanding the differences between integer and half-integer spins on the kagome lattice.

Experimentally it has been shown that increasing the spin to $S = 3/2$ still allows for quantum fluctuations to prevail as $T \to 0$ K. The most well-known example is SCGO, discussed earlier in the context of pyrcochlore slab lattices [91, 92]. The Cr^{3+} ions form pyrochlore slabs (bilayers of tetrahedra), separated by non-magnetic Cr dimers, with Ga atoms partially substituting the kagome layers [21, 93]. It has strong antiferromagnetic exchange interactions, ($\theta_W = -492$ K) and the nearest-neighbour exchange interactions between Cr ions is mediated through direct overlap of their orbitals, known as direct exchange, so the Hamiltonian used to describe this system only involves nearest-neighbour Heisenberg exchange [21, 94]. Magnetic susceptibility measurements evidence a transition to a spin glass state at $T_g \sim 2-5$ K, but μSR measurements showed that despite the magnetic sublattice dilution the spins remain dynamic down to $T = 100$ mK (with a noticeable slowing down around T_g) [94]. Although the paramagnetic defects occupying part of the magnetic sublattice freeze at T_g, Ga-NMR showed them not to be the driving force of the freezing [95]. This implies an unconventional glassy behaviour not directly related to the concentration of defect spins. Neutron scattering measurements have shown that an intrinsic spin-glass state arises from quantum fluctuations, possibly providing evidence for a class of topological glassy states [96].

Although it is evident that exotic ground states can be realised in larger spin systems such as $S = 3/2$, the quantum fluctuations will be reduced relative to $S = 1/2$ materials and so the search for QSLs retains its focus on $S = 1/2$ kagome magnets. This thesis will discuss two series of materials, the claringbullite and aver-

ievite series, which have end-members that are $S = 1/2$ kagome Heisenberg antiferromagnets and are proposed to host a quantum spin liquid ground state. Chapter 5 will present the structural characterisation of the claringbullite series, followed by inelastic neutron scattering measurements in Chapter 6 to investigate the magnetic excitations. Similarly, Chapters 7 and 8 will detail the structural and magnetic characterisations of the averievite series.

Bibliography

[1] A. P. Ramirez, Annu. Rev. Mater. Sci. **24**, 453 (1994).

[2] L. Balents, Nature **464**, 199 (2010).

[3] P. W. Anderson, Mat. Res. Bull. **8**, 153 (1973).

[4] Z. Zhu and S. R. White, Phys. Rev. B **92**, 041105 (2015).

[5] M. Zhang, C. Wang, S. Dong, H. Zhang, Y. Han, and L. He, Phys. Rev. B **105**, 024411 (2022).

[6] J. A. Paddison, M. Daum, Z. Dun, G. Ehlers, Y. Liu, M. B. Stone, H. Zhou, and M. Mourigal, Nat. Phys. **13**, 117 (2016).

[7] Y. Li, G. Chen, W. Tong, L. Pi, J. Liu, Z. Yang, X. Wang, and Q. Zhang, Phys. Rev. Lett. **115**, 167203 (2015).

[8] R. Sarkar, P. Schlender, V. Grinenko, E. Haeussler, P. J. Baker, T. Doert, and H.-H. Klauss, Phys. Rev. B **100**, 241116 (2019).

[9] M. Baenitz, P. Schlender, J. Sichelschmidt, Y. A. Onykiienko, Z. Zangeneh, K. M. Ranjith, R. Sarkar, L. Hozoi, H. C. Walker, J.-C. Orain, H. Yasuoka, J. van den Brink, H. H. Klauss, D. S. Inosov, and T. Doert, Phys. Rev. B **98**, 220409 (2018).

[10] A. Olariu, P. Mendels, F. Bert, B. G. Ueland, P. Schiffer, R. F. Berger, and R. J. Cava, Phys. Rev. Lett. **97**, 167203 (2006).

[11] K. Tomiyasu, Y. P. Mizuta, M. Matsuura, K. Aoyama, and H. Kawamura, Phys. Rev. B **106**, 54407 (2022).

[12] J. Carrasquilla, Z. Hao, and R. G. Melko, Nat. Commun. **6**, 7421 (2015).

[13] B. C. den Hertog and M. J. P. Gingras, Phys. Rev. Lett. **84**, 3430 (2000).

[14] C. Castelnovo, R. Moessner, and S. L. Sondhi, Nature **451**, 42 (2008).

[15] T. Fennell, P. P. Deen, A. R. Wildes, K. Schmalzl, D. Prabhakaran, A. T. Boothroyd, R. J. Aldus, D. F. McMorrow, and S. T. Bramwell, Science **326**, 415 (2009).

[16] H. Kadowaki, N. Doi, Y. Aoki, Y. Tabata, T. J. Sato, J. W. Lynn, K. Matsuhira, and Z. Hiroi, J. Phys. Soc. Jpn. **78**, 103706 (2009).

[17] B. Canals and C. Lacroix, Phys. Rev. Lett. **80**, 2933 (1998).

[18] I. Y. Gaidukova, V. V. Kelarev, A. S. Markosyan, A. Z. Menshikov, and A. N. Pirogov, J. Magn. Magn. Mater. **72**, 357 (1988).

[19] R. Ballou, E. Lelièvre-Berna, and B. Fåk, Phys. Rev. Lett. **76**, 2125 (1996).

[20] P. Lecheminant, B. Bernu, C. Lhuillier, L. Pierre, and P. Sindzingre, Phys. Rev. B **56**, 2521 (1997).

[21] C. Lacroix, P. Mendels, and F. Mila, *Introduction to Frustrated Magnetism : Materials, Experiments, Theory* (Springer-Verlag Berlin and Heidelberg, 2011).

[22] A. S. Wills, V. Dupuis, E. Vincent, J. Hammann, and R. Calemczuk, Phys. Rev. B **62**, R9264 (2000).

[23] B. M. Bartlett, "Synthesis, structure, and magnetic properties of extended 2-D triangular lattices", Ph.D. thesis (2005).

[24] D. Grohol, D. G. Nocera, and D. Papoutsakis, Phys. Rev. B **67**, 064401 (2003).

[25] T. Yildirim and A. B. Harris, Phys. Rev. B **73**, 214446 (2006).

[26] S.-H. Lee, C. Broholm, M. F. Collins, L. Heller, A. P. Ramirez, C. Kloc, E. Bucher, R. W. Erwin, and N. Lacevic, Phys. Rev. B **56**, 8091 (1997).

[27] D. Grohol, Q. Huang, B. H. Toby, J. W. Lynn, Y. S. Lee, and D. G. Nocera, Phys. Rev. B **68**, 094404 (2003).

[28] W. G. Bisson and A. S. Wills, J. Phys. Condens. Matter **20**, 452204 (2008).

[29] S.-H. Lee, C. Broholm, G. Aeppli, T. G. Perring, B. Hessen, and A. Taylor, Phys. Rev. Lett. **76**, 4424 (1996).

[30] Y. J. Uemura, A. Keren, K. Kojima, L. P. Le, G. M. Luke, W. D. Wu, Y. Ajiro, T. Asano, Y. Kuriyama, M. Mekata, H. Kikuchi, and K. Kakurai, Phys. Rev. Lett. **73**, 3306 (1994).

[31] Y. Iqbal, F. Becca, and D. Poilblanc, New J. Phys. **14**, 115031 (2012).

[32] X. G. Wen, Phys. Rev. B **65**, 165113 (2002).

[33] T.-H. Han, J. S. Helton, S. Chu, D. G. Nocera, J. A. Rodriguez-Rivera, C. Broholm, and Y. S. Lee, Nature **492**, 406 (2012).

[34] M. P. Shores, E. A. Nytko, B. M. Bartlett, and D. G. Nocera, J. Am. Chem. Soc. **127**, 13462 (2005).

[35] J. S. Helton, K. Matan, M. P. Shores, E. A. Nytko, B. M. Bartlett, Y. Yoshida, Y. Takano, A. Suslov, Y. Qiu, J.-H. Chung, D. G. Nocera, and Y. S. Lee, Phys. Rev. Lett. **98**, 107204 (2007).

[36] B. Fåk, E. Kermarrec, L. Messio, B. Bernu, C. Lhuillier, F. Bert, P. Mendels, B. Koteswararao, F. Bouquet, J. Ollivier, A. D. Hillier, A. Amato, R. H. Colman, and A. S. Wills, Phys. Rev. Lett. **109**, 037208 (2012).

[37] D. Boldrin, B. Fåk, M. Enderle, S. Bieri, J. Ollivier, S. Rols, P. Manuel, and A. S. Wills, Phys. Rev. B **91**, 220408 (2015).

[38] R. H. Colman, F. Bert, D. Boldrin, A. D. Hillier, P. Manuel, P. Mendels, and A. S. Wills, Phys. Rev. B **83**, 180416 (2011).

[39] R. Okuma, T. Yajima, D. Nishio-Hamane, T. Okubo, and Z. Hiroi, Phys. Rev. B **95**, 094427 (2017).

[40] H. Yoshida, N. Noguchi, Y. Matsushita, Y. Ishii, Y. Ihara, M. Oda, H. Okabe, S. Yamashita, Y. Nakazawa, A. Takata, T. Kida, Y. Narumi, and M. Hagiwara, J. Phys. Soc. Jpn. **86**, 033704 (2017).

[41] W. Sun, Y. X. Huang, S. Nokhrin, Y. Pan, and J. X. Mi, J. Mater. Chem. C **4**, 8772 (2016).

[42] D. S. Inosov, Adv. Phys. **67**, 149 (2018).

[43] M. R. Norman, Rev. Mod. Phys. **88**, 41002 (2016).

[44] X. G. Zheng, T. Kawae, Y. Kashitani, C. S. Li, N. Tateiwa, K. Takeda, H. Yamada, C. N. Xu, and Y. Ren, Phys. Rev. B. **71**, 052409 (2005).

[45] A. S. Wills, T. G. Perring, S. Raymond, B. Fåk, J.-Y. Henry, and M. Telling, J. Phys. Conf. Ser. **145**, 012056 (2009).

[46] A. S. Wills and J.-Y. Henry, J. Phys. Condens. Matter **20**, 472206 (2008).

[47] R. S. W. Braithwaite, K. Mereiter, W. H. Paar, and A. M. Clark, Mineral. Mag. **68**, 527 (2004).

[48] F. Bert, S. Nakamae, F. Ladieu, D. L'Hôte, P. Bonville, F. Duc, J. C. Trombe, and P. Mendels, Phys. Rev. B **76**, 132411 (2007).

[49] M. A. de Vries, J. R. Stewart, P. P. Deen, J. O. Piatek, G. J. Nilsen, H. M. Rønnow, and A. Harrison, Phys. Rev. Lett. **103**, 237201 (2009).

[50] A. Olariu, P. Mendels, F. Bert, F. Duc, J. C. Trombe, M. A. De Vries, and A. Harrison, Phys. Rev. Lett. **100**, 087202 (2008).

[51] P. Khuntia, M. Velazquez, Q. Barthélemy, F. Bert, E. Kermarrec, A. Legros, B. Bernu, L. Messio, A. Zorko, and P. Mendels, Nat. Phys. **16**, 469 (2020).

[52] M. Fu, T. Imai, T.-H. Han, and Y. S. Lee, Science **350**, 655 (2015).

[53] P. Mendels, F. Bert, M. A. de Vries, A. Olariu, A. Harrison, F. Duc, J. C. Trombe, J. S. Lord, A. Amato, and C. Baines, Phys. Rev. Lett. **98**, 077204 (2007).

[54] S. Blundell, *Magnetism in Condensed Matter* (Oxford University Press, New York, U.S.A., 2001).

[55] R. H. Colman, C. Ritter, and A. S. Wills, Chem. Mater. **20**, 6897 (2008).

[56] S. Bieri, L. Messio, B. Bernu, and C. Lhuillier, Phys. Rev. B **92**, 060407 (2015).

[57] P. Elliott, M. A. Cooper, and A. Pring, Mineral. Mag. **78**, 1755 (2014).

[58] T.-H. Han, J. Singleton, and J. A. Schlueter, Phys. Rev. Lett. **113**, 227203 (2014).

[59] H. O. Jeschke, F. Salvat-Pujol, E. Gati, N. H. Hoang, B. Wolf, M. Lang, J. A. Schlueter, and R. Valentí, Phys. Rev. B **92**, 094417 (2015).

[60] A. Henderson, L. Dong, S. Biswas, H. I. Revell, Y. Xin, R. Valenti, J. A. Schlueter, and T. Siegrist, Chem. Commun. **55**, 11587 (2019).

[61] K. Tustain, E. E. McCabe, A. M. Arevalo-Lopez, A. S. Gibbs, S. P. Thompson, C. A. Murray, C. Ritter, and L. Clark, Chem. Mater. **33**, 9638 (2021).

[62] Z. Feng, Y. Wei, R. Liu, D. Yan, Y.-C. Wang, J. Luo, A. Senyshyn, C. d. Cruz, W. Yi, J.-W. Mei, Z. Y. Meng, Y. Shi, and S. Li, Phys. Rev. B **98**, 155127 (2018).

[63] R. W. Smaha, W. He, J. M. Jiang, J. Wen, Y.-F. Jiang, J. P. Sheckelton, C. J. Titus, S. G. Wang, Y.-S. Chen, S. J. Teat, A. A. Aczel, Y. Zhao, G. Xu, J. W. Lynn, H.-C. Jiang, and Y. S. Lee, npj Quantum Mater. **5**, 23 (2020).

[64] C. M. Pasco, B. A. Trump, T. T. Tran, Z. A. Kelly, C. Hoffmann, I. Heinmaa, R. Stern, and T. M. McQueen, Phys. Rev. Mater. **2**, 44406 (2018).

[65] K. Tustain, G. J. Nilsen, C. Ritter, I. Da Silva, and L. Clark, Phys. Rev. Mater. **2**, 111405 (2018).

[66] Z. Liu, X. Zou, J. W. Mei, and F. Liu, Phys. Rev. B **92**, 220102 (2015).

[67] R. W. Smaha, W. He, J. P. Sheckelton, J. Wen, and Y. S. Lee, J. Solid State Chem. **268**, 123 (2018).

[68] K. Tustain, B. Ward-O'Brien, F. Bert, T.-H. Han, H. Luetkens, T. Lancaster, B. M. Huddart, P. J. Baker, and L. Clark, npj Quantum Mater. **5**, 74 (2020).

[69] R. W. Smaha, I. Boukahil, C. J. Titus, J. M. Jiang, J. P. Sheckelton, W. He, J. Wen, J. Vinson, S. G. Wang, Y. S. Chen, S. J. Teat, T. P. Devereaux, C. Das Pemmaraju, and Y. S. Lee, Phys. Rev. Mater. **4**, 124406 (2020).

[70] D. E. Freedman, T. H. Han, A. Prodi, P. Müller, Q.-Z. Huang, Y.-S. Chen, S. M. Webb, Y. S. Lee, T. M. McQueen, and D. G. Nocera, J. Am. Chem. Soc. **132**, 16185 (2010).

[71] Y. Wei, X. Ma, Z. Feng, D. Adroja, A. Hillier, P. Biswas, A. Senyshyn, A. Hoser, J.-W. Mei, Z. Y. Meng, H. Luo, Y. Shi, and S. Li, Chin. Phys. Lett. **37**, 107503 (2020).

[72] Y. Wei, Z. Feng, W. Lohstroh, D. H. Yu, D. Le, C. d. Cruz, W. Yi, Z. F. Ding, J. Zhang, C. Tan, L. Shu, Y.-C. Wang, H.-Q. Wu, J. Luo, J.-W. Mei, F. Yang, X.-L. Sheng, W. Li, Y. Qi, Z. Y. Meng, Y. Shi, and S. Li, arXiv:1710.02991v3 (2020).

[73] Z. Feng, Z. Li, X. Meng, W. Yi, Y. Wei, J. Zhang, Y.-C. Wang, W. Jiang, Z. Liu, S. Li, F. Liu, J. Luo, S. Li, G.-q. Zheng, Z. Y. Meng, J.-W. Mei, and Y. Shi, Chin. Phys. Lett. **34**, 077502 (2017).

[74] Z. Feng, W. Yi, K. Zhu, Y. Wei, S. Miao, J. Ma, J. Luo, S. Li, Z. Y. Meng, and Y. Shi, Chin. Phys. Lett. **36**, 017502 (2018).

[75] D. Boldrin, K. Knight, and A. S. Wills, J. Mater. Chem. C **4**, 10315 (2016).

[76] D. Boldrin, B. Fåk, E. Canévet, J. Ollivier, H. C. Walker, P. Manuel, D. D. Khalyavin, and A. S. Wills, Phys. Rev. Lett. **121**, 107203 (2018).

[77] Y. Okamoto, H. Yoshida, and Z. Hiroi, J. Phys. Soc. Jpn. **78**, 33701 (2009).

[78] H. Yoshida, Y. Michiue, E. Takayama-Muromachi, and M. Isobe, J. Mater. Chem. **22**, 18793 (2012).

[79] D. Boldrin and A. S. Wills, J. Mater. Chem. C **3**, 4308 (2015).

[80] M. Yoshida, Y. Okamoto, M. Takigawa, and Z. Hiroi, J. Phys. Soc. Jpn. **82**, 013702 (2013).

[81] S. K. Pati and C. N. Rao, J. Chem. Phys. **123**, 234703 (2005).

[82] K. Damle and T. Senthil, Phys. Rev. Lett. **97**, 067202 (2006).

[83] E. T. Connolly, P. Reeves, D. Boldrin, and A. S. Wills, J. Phys. Condens. Matter **30**, 025801 (2018).

[84] A. S. Wills, Phys. Rev. B **63**, 064430 (2001).

[85] D. Grohol, Q. Huang, B. H. Toby, J. W. Lynn, Y. S. Lee, and D. G. Nocera, Phys. Rev. B **68**, 94404 (2003).

[86] J. Dutrizac and T. Chen, Can. Metall. Q. **42**, 187 (2014).

[87] D. Papoutsakis, D. Grohol, and D. G. Nocera, J. Am. Chem. Soc. **124**, 2647 (2002).

[88] Y. Uchida, Y. Kanke, E. Takayama-Muromachi, and K. Kato, J. Phys. Soc. Jpn. **60**, 2530 (1991).

[89] H. Kato, M. Kato, K. Yoshimura, and K. Kosuge, J. Phys. Condens. Matter **13**, 9311 (2001).

[90] G. Lawes, A. B. Harris, T. Kimura, N. Rogado, R. J. Cava, A. Aharony, O. Entin-Wohlman, T. Yildirim, M. Kenzelmann, C. Broholm, and A. P. Ramirez, Phys. Rev. Lett. **95**, 087205 (2005).

[91] X. Obradors, A. Labarta, A. Isalgué, J. Tejada, J. Rodriguez, M. Pernet, A. Isalgue, J. Tejada, J. Rodriguez, and M. Pernet, Solid State Commun. **65**, 189 (1988).

[92] A. P. Ramirez, B. Hessen, and M. Winklemann, Phys. Rev. Lett. **84**, 2957 (2000).

[93] A. Keren, K. Kojima, L. P. Le, G. M. Luke, W. D. Wu, Y. J. Uemura, M. Takano, H. Dabkowska, and M. J. P. Gingras, Phys. Rev. B **53**, 6451 (1996).

[94] Y. J. Uemura, A. Keren, K. Kojima, L. P. Le, G. M. Luke, W. D. Wu, Y. Ajiro, T. Asano, Y. Kuriyama, M. Mekata, H. Kikuchi, and K. Kakurai, Phys. Rev. Lett. **73**, 3306 (1994).

[95] L. Limot, P. Mendels, G. Collin, C. Mondelli, B. Ouladdiaf, H. Mutka, N. Blanchard, and M. Mekata, Phys. Rev. B **65**, 144447 (2002).

[96] J. Yang, A. Samarakoon, S. Dissanayake, H. Ueda, I. Klich, K. Iida, D. Pajerowski, N. P. Butch, Q. Huang, J. R. Copley, and S. H. Lee, Proc. Natl. Acad. Sci. U. S. A. **112**, 11519 (2015).

Chapter 4

Experimental techniques

This chapter outlines the synthetic methods and characterisation techniques used in this thesis. For each characterisation, a brief theoretical background is given followed by an instrument description and an explanation of the data analysis. For the theory of x-ray and neutron scattering, the texts by *Squires* [1] and *Boothroyd* [2] were used.

4.1 Synthetic methods

Material synthesis was done *via* two routes: the hydrothermal method and solid state synthesis. Hydrothermal synthesis was carried out in 'Parr Instruments' stainless steel autoclave bombs containing a 15 mL Teflon-lined acid-digestion vessel. All bombs were equipped with spring-loaded closures to maintain an internal pressure and could be heated up to a maximum of 220 °C, above which the Teflon lining could be impaired. Hydrothermal synthesis was used for the claringbullite series samples and the specific synthetic steps are detailed in Chapter 5.

Solid state synthesis was used for the averievite series samples in Chapter 7. The reagents were either ground manually using a pestle and mortar or pulverised using the Pulverisette 0 (Fritsch) agate ball mill and pressed into pellets. The pellets were heated in alumina crucibles in a Carbolite chamber furnace. Further details on the syntheses are given in Chapter 7.

4.2 Powder diffraction

The materials presented in this work were characterised using powder X-ray diffraction (PXRD) and powder neutron diffraction (PND). Initial characterisation of all samples was done using PXRD on a laboratory diffractometer. For the averievite series, PXRD was also carried out on the beamline 11-BM at the synchrotron Advanced Photon Source (APS), Argonne National Laboratory, USA. Neutron diffraction was carried out for the averievite series on HRPD and WISH at the ISIS Neutron and Muon source, UK (see Chapter 7) and for the claringbullite series on D2B and D20 at the ILL, France (see Chapter 5).

4.2.1 Diffraction theory

The Bragg peaks measured in a scattering experiment arise from the elastic scattering of radiation, usually neutrons, photons or electrons, from a sample. In a diffraction experiment, the total scattering is measured as no differentiation is made between the elastic and inelastic processes. Diffraction is based on crystalline materials acting as diffraction gratings, when the incident radiation has a wavelength similar to the inter-planar separation, d. The diffracted waves can undergo constructive or deconstructive interference, with only the former being observed. For waves to interfere constructively, the well-known Bragg's law must be satisfied:

$$n\lambda = 2d\sin\theta, \tag{4.1}$$

where θ is the angle of incidence and constructive interference occurs for integer values n of the incident wavelength λ (Figure 4.1a). In general, a scattering event can be characterised by the changes in momentum and energy of the impacting particle. The momentum transfer, $\mathbf{Q}$, is given by

$$\mathbf{Q} = \mathbf{k}_i - \mathbf{k}_f, \tag{4.2}$$

where $\mathbf{k}_i$ and $\mathbf{k}_f$ are the initial and final wavevectors, respectively. Diffraction is an elastic scattering process, so the energy transfer, E, is zero and $|\mathbf{k}_i| = |\mathbf{k}_f| = 2\pi/\lambda$.

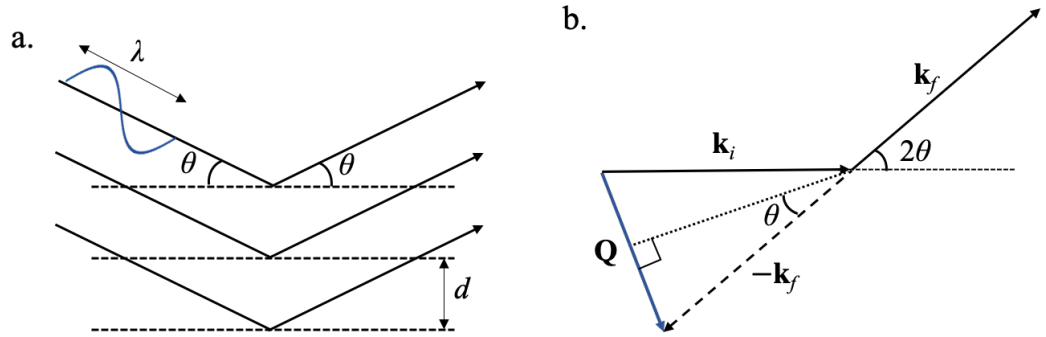

Figure 4.1: a. Illustration of Bragg's law for radiation with wavelength λ and an incident angle θ, scattering from parallel planes of atoms separated by a distance d. **b.** Vector diagram showing the momentum transfer, $\mathbf{Q}$, for elastic scattering with initial and final wavevectors $\mathbf{k}_i$ and $\mathbf{k}_f$. Adapted from [3].

From the vector diagram for elastic scattering depicted in Figure 4.1b it can be shown that

$$Q = |\mathbf{Q}| = \frac{4\pi \sin\theta}{\lambda}. \tag{4.3}$$

Bragg's law indicates that diffraction provides information on the lattice spacings, d. However, information is also gained about the positions and types of atoms in a sample through the measured peak intensities, I, which are related to the structure factor, F_{hkl}, by

$$I \propto F_{hkl}^2. \tag{4.4}$$

F_{hkl} is the sum of scattering amplitudes of all waves from each atom in a unit cell. It is expressed as

$$F_{hkl} = \sum_{j=1}^{N} f_j \exp[-2i\pi(hx+ky+lz)], \tag{4.5}$$

where f_j is the scattering form factor for an atom j, with fractional coordinates x, y and z on a Miller plane defined by the indices h, k, and l, and N is the total number of atoms in a unit cell.

The type of radiation used, determines the details of the scattering and the

type of atomic information Bragg diffraction can give. X-rays interact with the diffuse electron cloud around an atom and so f_j is the Fourier transform of an atom's electron density. The form factor decays with $\sin\theta/\lambda$, therefore diminishing the observed intensities at high scattering angles. As the scattering strength of X-rays depends on the atomic number, it can be difficult to distinguish elements located near each other in the periodic table and light elements with few atoms are often challenging to identify.

When the incident radiation consists of neutrons, two types of scattering occur: nuclear and magnetic scattering. The former arises from an interaction with the atomic nuclei and the form factor is usually denoted as the scattering length, b_j. The scattering length varies drastically across the periodic table and for isotopes of an element, which can allow light elements and ones with a similar atomic number to be differentiated. In addition, the nucleus is several orders of magnitude smaller than the electron cloud, making nuclei point scattering centres and so b_j shows no Q dependence. Magnetic scattering arises from the interaction between the neutron spin and unpaired electrons. Therefore, the form factor is similar to that for X-ray scattering, but decays even faster with Q as the interaction is only with one (or a few) electron(s).

Thus far, the atoms have been assumed to be stationary in the lattice. In reality, thermal and quantum vibrations result in the atoms being temporarily displaced from their equilibrium position. The former is accounted for by the Debye-Waller factor and leads to a modification of equation 4.5 to become

$$F_{hkl} = \sum_{j=1}^{N} f_j \exp[-2i\pi(hx+ky+lz)] \exp\left(\frac{-Q^2\langle u^2\rangle}{2}\right), \tag{4.6}$$

where $\langle u^2\rangle$ is the mean squared displacement of an atom from its equilibrium position. This describes an isotropic displacement and can be expanded to describe anisotropic displacement ellipsoids using six terms: u_{11}, u_{22}, u_{33}, u_{12}, u_{13} and u_{23}.

Another effect in polycrystalline samples that affects the peak intensities resulting from F_{hkl}^2, is preferred orientation of crystallites. Contrary to atomic thermal

vibrations, preferred orientation redistributes peak intensity systematically and is a result of crystallites having two or fewer axes of preferential growth. Therefore, needle-like or sheet-like crystallites are often not packed with a random orientation. To minimise this effect, all samples were ground using a pestle and mortar prior to diffraction measurements.

Neutrons have an advantage over X-rays with regards to the Q dependence of nuclear scattering, however X-rays are more easily accessible as they are available in laboratory diffractometers or even portable devices. In addition, the flux and resolution that can be obtained with synchrotron radiation is a few orders of magnitude higher than with neutrons. An advantage of neutrons is that it enables the measurement of magnetic scattering, though advances have been made in X-ray magnetic scattering in recent years. Due to the magnetic form factor discussed earlier, low Q data is particularly important for the characterisation of magnetic Bragg peaks.

4.2.2 Laboratory powder X-ray diffraction

Laboratory powder X-ray diffraction was used in this thesis to check sample purity after synthesis. In the lab, X-rays are generated by releasing electrons from a heated tungsten filament cathode and accelerating them towards a metal target (anode). When the impacting beam energy is higher than a certain threshold (that depends on the metal target), core electrons are ejected and an electron from a higher atomic shell relaxes into the vacancy by releasing an X-ray photon. This photon has an energy equal to the difference between its initial and final state, and so the wavelengths of the characteristic X-rays depend on the choice of metal target.

In general, diffractometers operate in one of two geometries: Debye-Scherrer (transmission mode) or Bragg-Bretano (reflection mode). In the Debye-Scherrer geometry, a collimator is used on the incident radiation to achieve a parallel beam that illuminates a stationary sample and the detector is rotated. The sample is usually loaded into a capillary to reduce the effects of preferred orientation, but a drawback of transmission geometry is absorption by heavy atoms. Bragg-Bretano geometry has two modes: (*i.*) the sample and detector are rotated or (*ii.*) the source and the detector are rotated about a fixed sample. This geometry is better suited for samples

with heavier atoms that are highly absorbing.

In this thesis, measurements were made on two Stoe Stadi-P diffractometers in Debye-Scherrer geometry: one equipped with a Mo source ($\lambda = 0.7093$ Å) in flat-plate mode and the other with a Cu source ($\lambda = 1.5406$ Å) where the sample was mounted in 0.2 mm capillaries. They have micro strip solid state Dectris Mythen 1K position-sensitive detectors (PSDs) that give high-resolution data due to the low dead time. For the Cu source, a Ge(111) monochromator is employed to remove Kα_2 radiation, only letting through Kα_1 X-rays. The flat-plate mode allowed for use of a larger sample and fast counting times, but is more prone to the effects of preferred orientation than a capillary, and so the measurements were only used to determine lattice parameters.

4.2.3 Synchrotron powder X-ray diffraction

At synchrotron facilities, radiation is produced by accelerating electrons in a circular path to relativistic speeds. Electrons are produced by heating a cathode under vacuum and are accelerated in a linear accelerator (linac) using radio frequency cavities. They enter a booster ring where they are further accelerated to an energy of a few GeV and are injected into the storage ring as electron 'bunches'. In the storage ring, magnets are used to change the path of the electron bunches causing electromagnetic radiation to be emitted in a tangential direction to their path of travel and go down the beamlines to the sample. The magnetic devices in the storage ring, either result in more focused beams with discreet energies or less focused beams with a continuous energy spectrum and their use depends on the type of data required.

In this thesis, the 11-BM beamline at the APS, USA was used for the averievite series (Chapter 7), as high resolution data was required for structural characterisation. A diagram of 11-BM is shown in Figure 4.2. It operates at an energy of $15-30$ keV. The white beam is collimated in the initial hutch by a mirror with Si and Pt stripes, and the desired wavelength is chosen using a Si(111) double-crystal monochromator. The second crystal focusses the beam horizontally and a mirror is used for vertical focusing. This beamline uses 12 independent Si(111) crystal analysers and $LaCl_3$ scintillation detectors for high-resolution data collection in $\sim$1 h

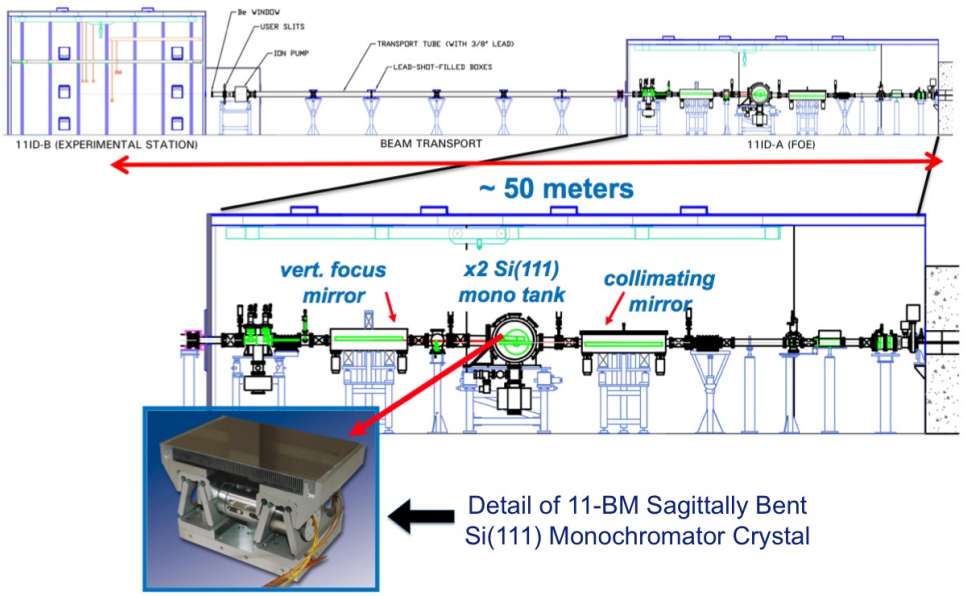

Figure 4.2: Diagram of the high-resolution 11-BM beamline at the Advanced Photon Source (APS), Argonne National Laboratory, USA. Experiments in Chapter 7 were performed with $\lambda \approx 0.46$ Å. Taken from [4].

($\Delta Q/Q \approx 1.4 \cdot 10^{-4}$). For these experiments, samples were put into Kapton tubes with an inner diameter of 0.8 mm.

4.2.4 Neutron powder diffraction

In this thesis, powder neutron diffraction was carried out on the instruments WISH and HRPD at the ISIS Neutron and Muon Source, UK, and on D2B and D20 at the ILL. The neutrons at the two facilities are produced in different ways: ISIS has a spallation source whereas the ILL has a reactor source. Spallation involves bombarding a heavy metal with protons that excite the metal nuclei, causing them to disintegrate and release neutrons. At ISIS, the neutrons are released in short (<1 ms) intense pulses. A reactor source operates on the basis of fission and produces neutrons constantly. The ILL is in fact one of the most intense neutron sources in the world. The neutrons produced at both facilities are thermalised in moderators to change their energy before being delivered to different beamlines. They can be approximately classified as cold neutrons ($\sim$ 20 K, 3 – 20 Å), thermal neutrons ($\sim$ 300 K, 1 – 3 Å) and hot neutrons ($\sim$ 2000 K, 0.3 – 1 Å).

As WISH and HRPD are at a spallation source, the pulsed neutron beam is exploited in the time-of-flight (TOF) technique. The neutron has a de Broglie wavelength

$$\lambda = \frac{ht}{m_n L}, \tag{4.7}$$

where m_n is the mass of the neutron, L is the path length and t is the time-of-flight. Combining this with Bragg's law (equation 4.3) yields

$$t = \frac{4\pi m_n L \sin\theta}{hQ}, \tag{4.8}$$

where $Q = 2\pi/d$. Many detectors arranged in banks are therefore placed at fixed scattering angles around the sample and each detector measures a full diffraction pattern. High Q values are accessed from low-angle banks where the flux is also highest, whereas high-angle banks provide higher resolution data up to lower Q and with lower flux.

TOF diffractometers can be optimised for either higher resolution or higher intensity. The resolution of the diffraction peaks in Q, δQ, depends on the uncertainties in the time-of-flight, δt, the path length, δL, and the scattering angle, $\delta\theta$. These are related by

$$\left(\frac{\delta Q}{Q}\right)^2 = \left(\frac{\delta t}{t}\right)^2 + \left(\frac{\delta L}{L}\right)^2 + (\cot\theta\,\delta\theta)^2. \tag{4.9}$$

Therefore, the resolution in Q can be optimised by using long flight paths, consequently increasing t. Detectors are placed in banks at different scattering angles and the highest resolution data is obtained from the high-angle banks as $\cot\theta$ tends to zero.

HRPD is one of the world's highest resolution neutron powder diffractometers due to the long neutron flight path, ~ 96 m, that ensures an almost Q independent $\delta Q/Q$ in backscattering geometry. This makes it the ideal instrument for studying subtle structural distortions. WISH receives a high flux of cold neutrons from a

solid methane moderator, which combined with the inherent low background of a pulsed neutron source, makes it optimal for measuring magnetic Bragg peaks.

D2B and D20, being found at a reactor source, are constant wavelength diffractomters. Similarly to the lab-based x-ray diffractometers discussed earlier, they are in Debye-Scherrer transmission mode. The resolution function is very similar to that for TOF and is expressed as:

$$\left(\frac{\delta Q}{Q}\right)^2 = \left(\frac{\delta\lambda}{\lambda}\right)^2 + (\cot\theta\delta\theta)^2 . \tag{4.10}$$

For high-resolution, the incident wavelength dispersion $\delta\lambda$ must be minimised, which is achieved by a high monochromator take-off angle. On D2B, this takes a value of 135°, making it a very high-resolution thermal neutron diffractometer. A sum over the 2-D Debye-Scherrer cones is used to obtain 1-D diffraction patterns. The sum either yields high intensity data (full detector height) or higher resolution data (middle third of the detectors). The latter was used for the Rietveld refinements in Chapters 5 and 7. D20 is a high-intensity two-axis diffractometer, used in this work to observe the weak magnetic Bragg peaks of claringbullite in Chapter 5.

4.2.5 Powder diffraction data analysis

Powders are a collection of crystallites, hence the analysis of powder diffraction data involves data averaged over all crystallite orientations so multiple structural solutions may exist for a given data set. Analysis of diffraction data usually begins with a known nuclear structural model, which is then refined using least-squares refinement methods. Care must be taken as multiple local minima can exist in the refinement and in some cases the related structures do not make physical or chemical sense.

The first step in a structural refinement is to assign an *hkl* index to the observed Bragg peaks in order to determine the space group. This can be a challenge for low symmetry systems as many peak positions may contribute to a single reflection. In general, the correct Bravais lattice[2] can be determined, but finding the exact space

[2]A Bravais lattice is an infinite periodic array of discrete lattice points where each point has

group may involve doing a full structural refinement for all possible solutions to determine the one that gives the best fit and makes the most physical and chemical sense. This task can be further complicated by additional impurity peaks. To minimise peak overlap, high-resolution data is preferred, as the instrumental broadening of the peaks is minimised making it easier to index the peaks. Appropriate lattice constants and profile function parameters are found using a whole pattern fitting method, such as the Pawley [5] or Le Bail [6] methods, where intensity is treated as an individual refinement parameter and the unit cell contents are not taken into account.

Once the phase has been verified, a full structural analysis is done to determine the atomic positions. In most cases, the initial atomic positions are based on isostructural materials and Fourier difference maps can be useful to locate unknown atoms based on missing electron density. The structure is then refined using non-linear least-squares minimisation in a method known as Rietveld refinement [7]. In this technique, each data point is treated as an observable y_i and the difference between all calculated y_{ic} and observed values must be minimised. The quantity minimised in a refinement is given by

$$\sum_i w_i (y_i - y_{ic})^2, \tag{4.11}$$

where $w_i = 1/y_i$ is the statistical weighting of y_i. Parameters of each phase that are convoluted into y_i include lattice parameters, unit cell symmetry, atomic coordinates and site occupancies (also affected by thermal factors). Global parameters are also included such as a background function, sample absorption and the instrumental contribution to the peak profile. Several programs exist for structural refinement and in this thesis they were done using the TOPAS 7 software [8] and the FullProf suite [9]. The advantages of TOPAS 7 used in this thesis were the ability to model atypical peak shapes and define new functions. On the other hand, FullProf is particularly useful for magnetic structure refinement. Potential magnetic structures for refinement, were formed using the software SARAh [10] that uses representational

identical surroundings and the translation of a single point defines every other point.

analysis.

4.3 Inelastic neutron scattering

Inelastic neutron scattering (INS) differentiates between elastic processes, that give rise to Bragg peaks, and inelastic processes, where excitations in the system are created or annihilated through energy exchange with the incident neutrons. Excitations in a sample include *e.g.* magnons, collective excitations of spins, phonons, collective vibrations of the crystal lattice, and crystal-field excitations.

In an inelastic scattering event, $|\mathbf{k}_i| \neq |\mathbf{k}_f|$ and $Q = |\mathbf{Q}|$ is related to the scattering angle 2θ through

$$Q^2 = k_i^2 + k_f^2 - 2k_i k_f \cos 2\theta. \tag{4.12}$$

For a neutron with mass m_n, the energy change during the scattering process is given by

$$E = E_i - E_f = \hbar\omega = \frac{h^2}{2m_n}\left(\frac{1}{\lambda_i^2} - \frac{1}{\lambda_f^2}\right) = \frac{\hbar^2}{2m_n}(k_i^2 - k_f^2). \tag{4.13}$$

The aim of a scattering experiment is to measure the energy transfer E and momentum transfer Q. Usually, this is achieved by either keeping k_i or k_f constant and spectrometers usually work in one of these modes, known as direct and indirect geometries, respectively. These two types of instruments result in different trajectories as shown in Figure 4.3. All experiments in this thesis were performed on direct geometry instruments.

Inelastic scattering is a measurement of the partial differential cross-section, which is the number of neutrons scattered by the sample into a solid angle $d\Omega$ with an energy E_f between E' and dE'. This is given by

$$\frac{d^2\sigma}{d\Omega dE'} = N\frac{k_f}{k_i} b^2 S(\mathbf{Q}, \omega), \tag{4.14}$$

where $S(\mathbf{Q}, \omega)$ is the dynamic structure factor and b is the scattering length related

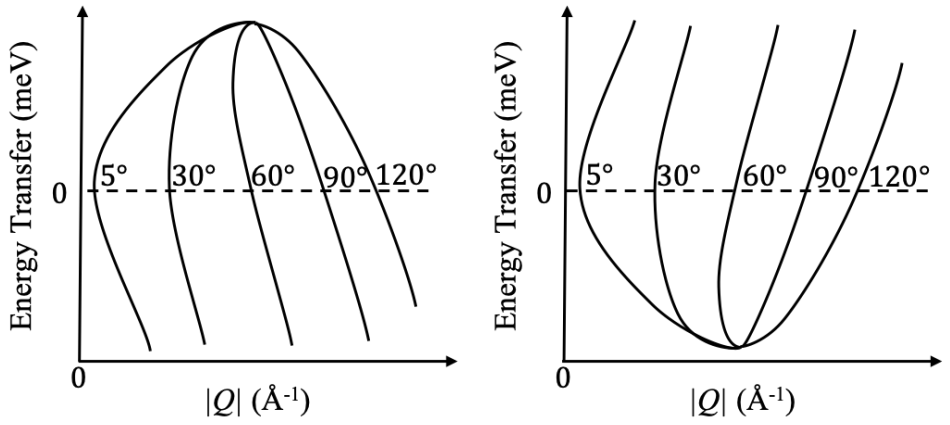

Figure 4.3: Trajectories for time-of-flight spectrometers with detectors at various angles for (**left.**) direct and (**right.**) indirect geometries. Reproduced from [11].

to the scattering cross-section by $b^2 = \sigma/4\pi$. The dynamic structure factor is a double Fourier transform in space and time of the time-dependent pair-correlation function, $G(r,t)$:

$$S(\mathbf{Q},\omega) = \frac{1}{2\pi\hbar}\int G(\mathbf{r},t)e^{i(\mathbf{Q}\cdot r-\omega t)}d\mathbf{r}dt. \tag{4.15}$$

Its Q dependence gives information about the relative positions of the atoms, whereas its E or time dependence gives information about the atom dynamics. Throughout this thesis the convention $S(\mathbf{Q},E=\hbar\omega)$ will be used which has dimension 1/energy.

For nuclear scattering, equation 4.14 has a coherent and an incoherent contribution:

$$\frac{d^2\sigma}{d\Omega dE'} = \left(\frac{d^2\sigma}{d\Omega dE'}\right)_{\text{coh}} + \left(\frac{d^2\sigma}{d\Omega dE'}\right)_{\text{inc}}. \tag{4.16}$$

Essentially these correspond to measuring the correlations between atoms or following the dynamics of a single atom by measuring a self-correlation function. For the two scenarios, b^2 is substituted for b^2_{coh} or b^2_{inc} and $S(\mathbf{Q},\omega)$ for $S_{\text{coh}}(\mathbf{Q},\omega)$ or $S_{\text{inc}}(\mathbf{Q},\omega)$.

Magnetic scattering arises when the neutron interacts with the spin and orbital

momenta of an unpaired electron. The partial differential cross-section is given as:

$$\frac{d^2\sigma}{d\Omega dE'} = N\frac{k_f}{k_i}(\gamma r_0^2)S_{\text{mag}}(\mathbf{Q},\omega), \tag{4.17}$$

where γ is the neutron magnetic moment and r_0 is the classical electron radius. The product $\gamma r_0 = 1.348$ fm is the strength of the dipole interaction between the neutron and the unpaired electron. $S_{\text{mag}}(\mathbf{Q},\omega)$ is the Fourier transform of the spin-spin correlation function and gives information on the positions and dynamics of magnetic moments.

All INS measurements in this thesis were performed on direct geometry time-of-flight (TOF) instruments at the ILL and the ISIS Neutron and Muon Source. The essential components of a TOF instrument will be described here and specific details on the instruments used will be given in Sections 4.3.2 and 4.3.1. At a reactor source, the continuous neutron beam is pulsed using a chopper (the beam at a spallation source is already pulsed) and then monochromated by a second chopper or a crystal monochromator. The monochromated and pulsed beam scatters from the sample into a wide array of position-sensitive detectors, which are used to analyse the final positions and energies of the neutrons by measuring their time of flight. Instruments that deliver cold neutrons were used to probe low-energy excitations, whilst thermal-neutron instruments were used to measure high-energy excitations up to $E \sim 30$ meV. Section 4.3.3 will detail how the raw data was reduced and treated before it was analysed.

4.3.1 Thermal neutrons: PANTHER & MERLIN

The thermal-neutron TOF spectrometers PANTHER at the ILL and MERLIN at the ISIS Neutron and Muon Source, were used to measure high-energy magnetic excitations. PANTHER is a high-flux medium-resolution spectrometer, receiving a constant beam of neutrons from the ILL reactor source and is shown in Figure 4.4. It has an optional sapphire filter and five disk choppers (only two at the time of the experiments in this thesis), which pulse the continuous beam into packets, exclude the neutrons that are too fast/slow from each packet and reduce the background. A

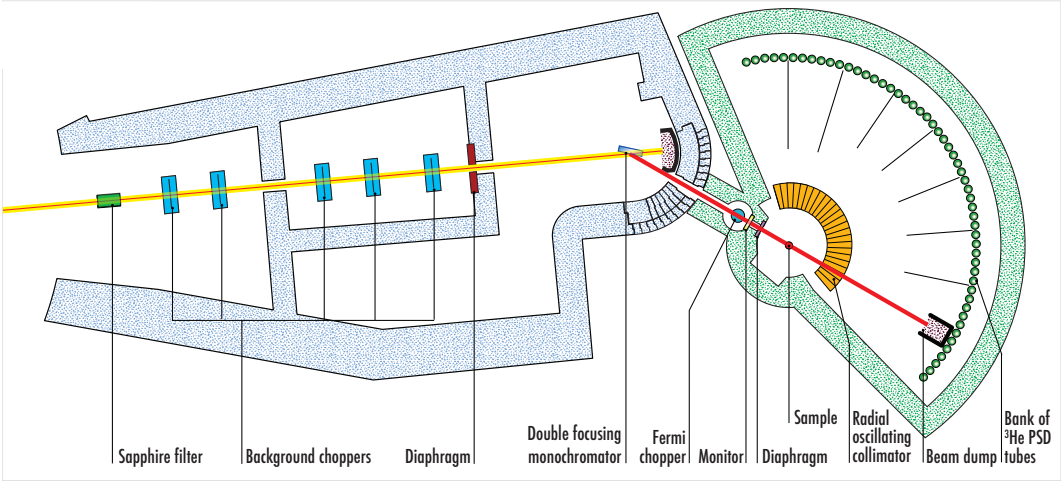

Figure 4.4: Diagram of the thermal-neutron time-of-flight spectrometer PANTHER at the ILL, France. Taken from [12].

double-focusing monochromator is used to select the incident neutron energy and controls the neutron flux by altering the beam divergence. The beam is further pulsed using a Fermi chopper before it is delivered to the sample. The neutrons scatter onto PSDs that are located 2.5 m from the sample inside a vacuum chamber. The array of PSDs consists of 2 m high and 22 mm wide tubes filled with ^{3}He gas, covering an angular range of $-16°$ to $136°$.

MERLIN is a medium intensity medium-resolution spectrometer at the ISIS Neutron and Muon Source. It includes a background chopper and Fermi chopper to monochromate the beam and has an array of PSDs located 2.5 m from the sample that are 3 m high and cover an angular range of $-45°$ to $135°$. The combination of a Gd chopper and a disk chopper allows measurements with several incident energies to be made simultaneously.

4.3.2 Cold neutrons: IN5 & LET

In order to observe low-energy magnetic excitations, INS data were collected on the cold-neutron TOF spectrometers IN5 at the ILL and LET at the ISIS Neutron and Muon Source. IN5 has six choppers to deliver a pulsed monochromatic beam to the sample. The first set of choppers cut the beam into packets, the second set of choppers removes contamination from very slow or very fast neutrons that have made it into these packets and the final set of choppers monochromate the beam by further reducing the allowed wavelengths of the beam packets. The neutrons then scatter off the sample into PSDs which are 4 m high 25.4 mm wide tubes filled with ^{3}He that cover an angular range from $-12°$ to $135°$.

LET receives a pulsed source of neutrons and has five choppers: two which further chop the neutron bunches that arrive from the source, two which exclude the very fast or very slow neutrons that contaminate each packet due to frame overlap and one which reduces the background noise. The PSDs cover an angular range from $-40°$ to $140°$. Similar to MERLIN, measurements using multiple incident energies can be made simultaneously.

4.3.3 Data treatment

All data treatment was done using the Mantid Workbench software [13]. In general, the reduction included the following steps:

1. The raw data counts were normalized to the beam monitor counts to correct for the fluctuating neutron flux from the neutron source;
2. The detector efficiency was corrected for by normalizing to a vanadium run;
3. An absorption correction based on the elemental composition was applied;
4. A flat time-independent background was subtracted;
5. If available an empty can measurement collected with the same incident energy as the sample was subtracted;
6. Defective detectors were masked;

7. Normalization to the number of formula units;

8. The time-of-flight axis was converted to energy transfer, E, and the spectrum numbers were converted to momentum transfer, Q, to give the dynamic structure factor $S(Q,E)$.

During the averievite measurements on IN5 (Chapter 8) there was an issue with the beam monitor and it could not be used for normalization. So instead of dividing by the beam monitor counts, the raw data counts were divided by the time of data collection in seconds.

Empty can measurements were made at the lowest measured temperature of the sample for all incident energies for all the experiments PANTHER and the IN5 averievite experiment. The empty can measurements multiplied by a scale factor were subtracted from the sample data. When no empty can measurement was made, the flat background multiplied by a scale factor was subtracted. These scale factors were determined using detailed balance analysis, described below.

During a scattering process with fixed incident energy, an incident neutron can either create or annihilate an excitation in the scattering system, causing the neutron to either lose ($E > 0$) or gain ($E < 0$) energy. At $T = 0\,\mathrm{K}$, there are no thermal fluctuations in the scattering system so the neutron cannot gain energy resulting in $S(Q,E < 0) = 0$. At finite temperatures the probability of energy gain and loss, $S(Q,E)$ and $S(Q,-E)$, is described by the principle of detailed balance:

$$S(Q,-E) = e^{(-E/k_BT)}S(Q,E), \tag{4.18}$$

where k_B is the Boltzmann constant and T is the temperature of the scattering system [1]. This principle must be obeyed for a system in thermal equilibrium. Data collected at temperatures comparable to the incident neutron energy ($E = k_BT$) was used to ensure that the reduced $S(Q,E)$ is correct. The fulfilment of equation 4.18 was ensured by altering the sample transmission, the scale factor of the empty can subtraction, and the scale factor of the flat background in the data reduction process.

At finite temperatures, thermal fluctuations lead to the population of excited

magnetic states and phonons of a material. To extract the response function of a system in the absence of thermal fluctuations, $S(Q,E)$ is divided by the Bose population factor resulting in the imaginary part of the dynamic susceptibility, $\chi''(Q,E)$. This is described by the fluctuation dissipation theorem:

$$\chi''(Q,E) = (1 - e^{-E/k_BT})\, S(Q,E), \tag{4.19}$$

where the exponential is the Bose factor, k_B is the Boltzmann constant and T is the temperature.

4.3.4 Normalisation to absolute units

In Chapter 6, the inelastic neutron scattering data of claringbullite and its Zn-doped variant is normalised to the nuclear Bragg peaks, to provide a meaningful comparison between data collected on different instruments. The nuclear Bragg peaks were obtained by integrating over the elastic lines of $S(Q,E)$ (–0.2 $\leq E \leq$ 0.2 meV) at $T = 25$ K for claringbullite ($E_i = 19.2$ meV) and $T = 1.7$ K for Zn-claringbullite ($E_i = 20.03$ meV). A Rietveld refinement was done in FullProf and the FullProf scale factor was used to normalise $S(Q,E)$, by dividing it by the scale factor s. This is given by

$$s = \text{FPScale} \times \frac{2\pi^2 NV}{45\lambda^3}, \tag{4.20}$$

where FPScale is the FullProf scale factor for the relevant phase, λ is the wavelength of the incident neutron beam and N is the number of atoms in a unit cell with volume V [14]. The Rietveld refinements for the elastic lines of the two data sets are shown in Appendix A. The crystal structures were fixed to those obtained on D2B at $T = 1.5$ K (refinements shown in Chapter 5), and the isotropic displacement parameters were refined.

4.3.5 Linear spin wave theory

Semi-classical linear spin wave theory (LSWT) is used in Chapters 6 and 8 as realised in the program SpinW [15], to model the spin wave excitations observed

using inelastic neutron scattering data collected below T_N. The key steps of LSWT were outlined in Section 2.4.6. Although LSWT is a powerful tool for calculating spin wave dispersions, there are some drawbacks. As it is a semi-classical method it works best for systems with $S \geq 3/2$, whilst for quantum $S = 1/2$ systems it is an approximation and higher order corrections are necessary [15]. Furthermore, reduced moment sizes in magnetic structures determined by diffraction cannot be taken into account as LSWT considers spin values, rather than moment sizes. This can have consequences on the energies and/or intensities of the spin waves and the implications in relation to claringbullite are detailed in Chapter 6.

The main difficulty we faced when using SpinW for claringbullite, was that the Hamiltonian was not positive definite and diagonalization led to complex solutions rather than positive real values. This occurs when the magnetic structure does not correspond to the classical ground state of the Hamiltonian. Claringbullite was particularly challenging in this regard, because the frustration leads to a canted spin structure that is very sensitive to the different energy terms. Therefore, it was necessary to relax the magnetic structure to the ground state of the energy terms and for this we used the classical optimisation *optmagsteep* provided in SpinW [15]. Treating the spins as vectors, for a fixed propagation vector and magnetic unit cell, it iteratively rotates the spins towards the local magnetic field in order to produce the minimum energy structure. It should be noted that this procedure relates to a local energy minimum and not necessarily the global minimum, which may be problematic in the case of complex and/or frustrated systems. When using this method for claringbullite, we argue that the spin waves of the resultant magnetic structures remain suitable within the limit of the magnetic moments represented as $S = 1/2$ spins. A more detailed discussion is presented in Chapter 6. Furthermore, it is noted that this method of optimisation has previously been used in the study of the frustrated triangular magnet $YbZnGaO_4$ [16].

4.3.6 Reverse Monte Carlo

When a magnetic system only has short-range order, such as in the paramagnetic state, the magnetic excitations are not spatially extended magnons and diffuse mag-

netic scattering is observed. In this case, linear spin wave theory no longer holds. One way to analyse the inelastic diffuse scattering is using the reverse Monte Carlo (RMC) method, which minimises the least-square difference between the calculated and experimental data. The advantage of such an approach is that it provides a model-free analysis as it is not based on a Hamiltonian and therefore yields unbiased solutions. The corresponding disadvantage is that for powder data much spatial information is averaged.

This method was used as implemented in the program SPINVERT [17], which calculates the magnetic scattering cross-section, $S_{\mathrm{mag}}(Q)$, and compares it to the experimental one. Without a spin Hamiltonian the spin-pair correlation function $\langle \mathbf{S}_i \cdot \mathbf{S}_j \rangle$ can be determined, but not the exchange interactions J. Furthermore, since the samples investigated in this thesis are powders, the directional component of the spin correlations is lost as an averaging occurs over all spatial directions.

SPINVERT takes into account the magnetic unit cell and the magnetic atom sites, and generates a supercell (whose size is determined by the user) in which random spins are rotated by a small amount. The cost function that is minimised at each atom site is

$$\chi^2 = W \sum_Q \left[\frac{I_{\mathrm{calc}}(Q) - I_{\mathrm{exp}}(Q)}{\sigma(Q)} \right]^2, \tag{4.21}$$

where $I_{\mathrm{calc}}(Q)$ and $I_{\mathrm{exp}}(Q)$ correspond to the calculated and experimental $S_{\mathrm{mag}}(Q)$, respectively, W is an empirical weighting factor and $\sigma(Q)$ is the experimental uncertainty. The magnitude of the magnetic moments are included in an overall scale factor s that is also refined. For data placed on an absolute scale, s can be used to determine the refined effective magnetic moment μ through the relation

$$s = \mu^2 = g^2 S(S+1), \tag{4.22}$$

where g is the Landé g-factor.

The RMC method as realised in SPINVERT is based on the following assumptions: *(i.)* the input data is solely of magnetic origin; *(ii.)* all atoms are assumed

to have the same magnetic properties; *(iii.)* all atoms and their corresponding spins must be fixed to a specific site, so displacive disorder (such as that found for the $x = 2$ Zn-doped averievite sample in Chapter 7) cannot be taken into account; *(iv.)* there is no magnetoelastic coupling.

The Fourier transform of $S_{\mathrm{mag}}(Q)$ is the spin-pair correlation function in real space. For the best $S_{\mathrm{mag}}(Q)$ calculated by SPINVERT, the spin-pair correlation function can be plotted using the program SPINCORREL [17].

4.4 Magnetometry

Bulk magnetometry measurements were made on all samples to measure the magnetic susceptibility as a function of temperature and the sample magnetisation as a function of field. These data were useful to extract mean-field information about the paramagnetic states of the samples and their ordering temperatures. Data were collected using vibrating sample magnetometry (VSM) and a superconducting quantum interference device (SQUID).

A SQUID is an ideal device to measure bulk magnetometry as its resolution can reach 10^{-17} T [18], which is important for frustrated systems with small moments. Data were collected on a Magnetic Property Measurement System (MPMS-XL) using the DC-SQUID. The sample was placed in a plastic capsule with cotton to keep it in place and the capsule was inserted into a plastic straw with two additional straws on either side to keep it in place. This was then attached to a non-magnetic rod, placed inside a cryostat and liquid helium was used to reach a temperature of $T = 2$ K. A SQUID operates using the DC Josephson effect, where quantum tunnelling enables current to flow indefinitely between two superconducting wires connected by two insulating links. The DC-SQUID includes two Josephson junctions as shown in Figure 4.5a, which each allow the flow of a maximum amount of current, I_C. In the absence of a magnetic field, a current I_C applied to the superconducting loop will split into two equal currents, $I_C/2$. When the sample is oscillated through the coil it produces a magnetic flux that induces a current in the superconducting loop in one direction. This decreases the current at one junction and increases it at

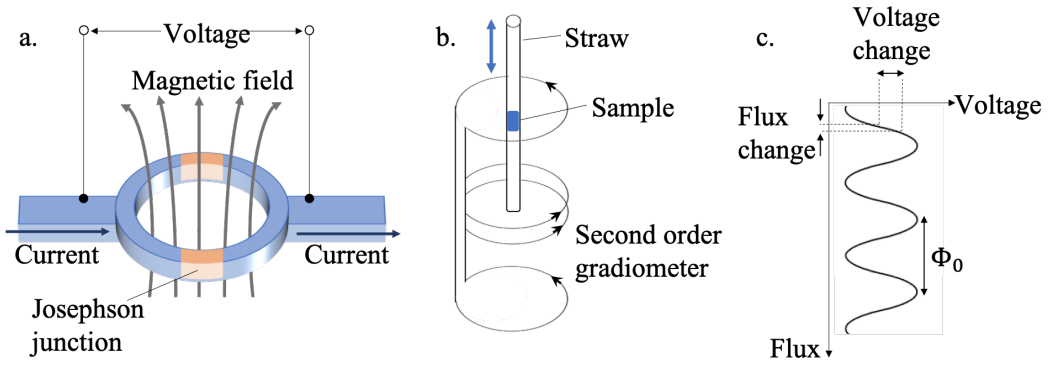

Figure 4.5: a. Schematic of superconducting loop in a DC-SQUID with two Josephson junctions. **b.** A schematic of the second order gradiometer setup of a SQUID with two coils in the middle wound one way and two parallel coils on either side wound the other. The sample is moved perpendicular to the coils creating a changing magnetic flux which is quantised as described in the text. **c.** The periodic change of flux in one coil related to the output voltage. The periodicity is equal to one quantum flux, Φ_0. Based on figures from [19] and [20].

the other one up to a maximum value of I_C, after which it is energetically favourable for the current to change direction. The induced current increases proportionally to the magnetic flux, which is quantised in units of $\Phi_0 = 2\pi\hbar/2e \approx 2.07 \cdot 10^{-15}$ T m^2, so the current changes periodically with the flux quanta. The flux quanta are directly related to the change in voltage across the superconducting loop, which is measured using an amplifier. In order to minimise effects from magnetic fields unrelated to the experiment, a SQUID is normally set up as a second order gradiometer whereby two coils are placed on either side of a parallel double coil wound in the opposite direction (see Figure 4.5b).

Vibrating sample magnetometry (VSM) data were collected on a Quantum Design Physical Property Measurement System (PPMS-9T), where the sample is oscillated at a particular frequency (40 Hz) and amplitude (1-3 mm) through fixed pickup coils. The sample causes an alternating magnetic flux that induces a voltage in the pickup coil, which is then converted to the magnetisation. This method offers rapid data collection times but the sensitivity is about three times lower than for a SQUID [18].

4.5 Scanning electron microscopy

Scanning electron microscopy (SEM) is a technique used to image solid samples at the nano- or micro-metre scale. It uses a focused beam of high-energy electrons with a resolution of ~ 1 nm. The beam is scanned across the surface of the sample, ionizing the atoms and the emission of secondary electrons produces high-resolution images. Insulating samples must be coated with a conducting layer of sputtered carbon or gold, which also prevents the build-up of charge. The narrow electron beam results in a large depth of field that produces images with a characteristic 3-dimensional appearance to them. This is useful for characterising the surface structure of a sample.

As well as being used for imaging, SEMs can also be fitted with energy dispersive X-ray (EDX) detectors for compositional analysis. As each element has a different characteristic emission wavelength, analysis of the emitted X-ray energies provides qualitative information about the existent elements. To determine the concentration percentages of the elements present, a quantitative analysis is done on the peaks in the spectra using automated software. For accurate results the instrument must be calibrated against a standard and the spectrum is best collected from a flat, polished sample surface. This method is less sensitive for lighter elements and when elements have a similar electron count, Z, emission-line overlap can complicate analysis.

The Zn-doped averievite samples that were measured by SEM-EDX (Chapter 7) are insulators and were placed on conductive carbon tape instead of being sputtered with a conductive layer. Measurements were made on a LEO 1530 microscope fitted with an EDX detector at room temperature.

Bibliography

[1] G. L. Squires, *Introduction to the Theory of Thermal Neutron Scattering*, 3rd ed. (Cambridge University Press, Cambridge, 2012).

[2] A. T. Boothroyd, *Principles of Neutron Scattering from Condensed Matter* (Oxford University Press, July 2020).

[3] D. S. Sivia, *Elementary Scattering Theory: For X-ray and Neutron Users* (Oxford University Press, Oxford, 2011).

[4] M. Suchomel, B. Toby, R. Von Dreele, M. Ramanathan, Y. Amer, D. Shu, J. Wang, P. Lee, S. Antao, J. Doebbler, C. Kurtz, M. Engbretson, C. Preissner, R. Ranay, X. Jiao, D. Cline, T. Mooney, Y. Huang, Sheehan Bill, D. Cyl, M. Beno, G. Long, and G. Srajer, *Technical Description*, https://11bm.xray.aps.anl.gov/description.html.

[5] G. S. Pawley, J. Appl. Crystallogr. **14**, 357 (1981).

[6] A. Le Bail, Powder Diffr. **20**, 316 (2005).

[7] R. A. Young, ed., *The Rietveld Method*, 5th edn. (Oxford University Press, Oxford, 2002), pp. 254–257.

[8] A. Coelho, *Topas Academic Version 4.1.* 2007.

[9] J. Rodríguez-Carvajal, Physica B. Condens. Matter **192**, 55 (1993).

[10] A. S. Wills, Phys. B **278**, 680 (2000).

[11] F. Hippert, E. Geissler, J. E. Hodeau, E. Lelièvre-Berna, and J. R. Regnard, *Neutron and X-ray Spectroscopy* (Springer, Dordrecht, 2006).

[12] B. Fåk and M. M. Koza, *PANTHER - Thermal Neutron Time-of-Flight Spectrometer*, https://www.ill.eu/users/instruments/instruments-list/panther/description/instrument-layout.

[13] O. Arnold, J. Bilheux, J. Borreguero, A. Buts, S. Campbell, L. Chapon, M. Doucet, N. Draper, R. Ferraz Leal, M. Gigg, V. Lynch, A. Markvardsen, D. Mikkelson, R. Mikkelson, R. Miller, K. Palmen, P. Parker, G. Passos, T. Perring, P. Peterson, S. Ren, M. Reuter, A. Savici, J. Taylor, R. Taylor, R. Tolchenov, W. Zhou, and J. Zikovsky, Nuclear Instruments and Methods in Physics Research Section A: Accelerators, Spectrometers, Detectors and Associated Equipment **764**, 156 (2014).

[14] *Software – Joe Paddison*, https://joepaddison.com/software/.

[15] S. Toth and B. Lake, J. Phys. Condens. Matter **27**, 166002 (2015).

[16] W. Steinhardt, P. A. Maksimov, S. Dissanayake, Z. Shi, N. P. Butch, D. Graf, A. Podlesnyak, Y. Liu, Y. Zhao, G. Xu, J. W. Lynn, C. Marjerrison, A. L. Chernyshev, and S. Haravifard, npj Quantum Mater. **6**, 78 (2021).

[17] J. A. M. Paddison, J. Ross Stewart, and A. L. Goodwin, J. Phys. Condens. Matter **25**, 454220 (2013).

[18] R. L. Fagaly, Rev. Sci. Instrum. **77**, 101101 (2006).

[19] D. Boldrin, "Synthesis and Study of Quantum Kagome Magnets", Ph.D. thesis (University College of London, 2015).

[20] M. Buchner, K. Höfler, B. Henne, V. Ney, and A. Ney, J. Appl. Phys. **124**, 161101 (2018).

Chapter 5

Crystallographic and bulk magnetisation studies of the claringbullite series: $Zn_xCu_{4-x}(OD)_6FCl$ for $x = 0$ and 1

5.1 Introduction

The most widely studied material in the context of the $S = 1/2$ KAFM is herbertsmithite, but beyond the n.n. dimer QSL there exist other flavours of QSLs. In the search for new candidate QSL materials, one that has recently gained attention is barlowite and its Zn-doped variants, for which an overview of the current findings were given in Chapter 1. Inelastic neutron scattering and μSR measurements on Zn-doped barlowite samples have evidenced a quantum spin liquid ground state [1, 2] and these findings have sparked interest in the isostructural claringbullite and its Zn-doped variant, $Zn_xCu_{4-x}(OH)_6FCl$ for $x = 0$ and 1 [3].

Single crystal diffraction measurements on barlowite have shown a hexagonal-orthorhombic phase transition at $T = 276$ K [4]. A similar phase transition has also been observed using single crystals of undoped claringbullite, with some crystals undergoing a crystallographic phase transition to *Pnma* below $T = 100$ K and another below $T = 10$ K [4]. This difference could change the magnetic phase tran-

sition temperature, which for a different single crystal has been reported to be at $T_1 = 15$ K [5], and could imply different exchange couplings. The difference in the ordering temperatures between claringbullite and barlowite has been studied using static density functional theory and was attributed to the competing interactions at the interlayer site between those from the kagome layers and the ordering of the interstitial Br^- *vs.* Cl^- ions [4].

A different synthesis has been developed to grow barlowite single crystals that crystallise in the hexagonal space group $P6_3/m$ at $T = 2$ K [6]. This indicates that different synthetic methods can alter the low-temperature crystal structures of these materials, thereby altering their magnetic properties.

Yue *et. al.* reported claringbullite to have strong net antiferromagnetic exchange ($\theta_W = -135$ K) and a suppressed magnetic phase transition at $T = 15$ K evidencing magnetic frustration, as well as a weak ferromagnetic component [5]. Similar to barlowite and many other antiferromagnets, claringbullite has been chemially doped with diamagnetic Zn^{2+} *i.e.* $ZnCu_3(OH)_6FCl$, in an effort to suppress the magnetic order. Room temperature laboratory XRD measurements showed it to also crystallise in the $P6_3/mmc$ space group [7]. However, to the best of our knowledge, temperature studies to explore the possibility of a transition to lower crystal symmetry at low temperature, have not yet been done. Magnetometry and heat capacity studies on $ZnCu_3(OH)_6FCl$ showed suppression of long-range magnetic order down to at least $T = 0.8$ K and evidenced a similar entropic behaviour to herbertsmithite and the new QSL candidate Zn-barlowite, $ZnCu_3(OH)_6FBr$, suggesting it is also a QSL candidate [2, 3, 7, 8].

The synthesis of $ZnCu_3(OH)_6FCl$, from now on referred to as Zn-claringbullite, was previously achieved with only a Zn to Cu ratio of 0.7:3 instead of the stoichiometric one, indicating the presence of Cu^{2+} 'impurities' on the kagome lattice [7]. Although magnetic order was found to be suppressed at this level of diamagnetic doping, the sample still suffered from similar site disorder to herbertsmithite. To further investigate its ground state magnetic behaviour, we synthesised undoped claringbullite and Zn-claringbullite to provide a fuller comparison with

the magnetically ordered state.

5.2 Synthesis

In the literature, single crystals and polycrystalline samples of claringbullite and Zn-claringbullite were synthesised using hydrothermal methods [4, 5, 7] and a solution method [4]. This section details the synthetic methods attempted to produce claringbullite and Zn/Mg-doped claringbullite samples, and the final syntheses used to produce the claringbullite and Zn-claringbullite samples for diffraction, bulk magnetometry and inelastic neutron scattering measurements.

5.2.1 Preliminary work

A previous study on claringbullite used powder samples prepared using a solution method [4]. We attempted this method using half the reagent amounts previously reported, as fluorides destroy glass and the solutions had to be prepared in 15 mL Teflon containers that must be less than 2/3 full. For this synthesis, NH_4F (Alfa Aesar, 0.067 g, 1.81 mmol) and NaOH (Sigma, 0.054 g, 1.34 mmol) were dissolved in H_2O (distilled, 10 mL) at room temperature in a 15 mL Teflon container. In another 15 mL Teflon container, $CuCl_2 \cdot 2H_2O$ (Sigma, 0.155 g, 0.91 mmol) was dissolved in H_2O (distilled, 5 mL) at room temperature. The two solutions were combined into one 15 mL Teflon container, but no powder formed as previously reported [4]. In an attempt to overcome the activation energy of the reaction, the Teflon container was placed into a water bath and the solution was monitored with a temperature probe. The solution was heated to 25, 30 and 35 °C with 15 min of magnetic stirring after each temperature increase and no change was observed. The solution was heated to 50 °C and stirred for 1.5 h. No powder was observed and the solution was removed from the water bath, allowed to cool to room temperature and filtered to produce a powder that was washed *via* centrifugation (4000 rpm, 4 min) with distilled water (3 x 20 mL). Laboratory powder x-ray diffraction (PXRD) was used to determine that the product was not claringbullite.

Since the solution method was unsuccessful, the synthesis adopted for both samples was the previously reported hydrothermal synthesis of Zn-doped claring-

bullite [7]. This method led to unidentifiable impurities in the Zn-claringbullite samples and attempts to synthesise pure samples included increasing the heating time from 24 h to 72 h and raising the synthesis temperature from 200 °C to 220 °C (the maximum temperature that the Teflon containers could be heated to), but these were unsuccessful. It was found that successful Zn-doping at the $x = 1$ level of $Zn_xCu_{4-x}(OH)_6FCl$, required an acidic reagent environment with pH values ~ 3 (instead of ~ 5). This was also previously found in the unpublished version 1 of Ref. [7] ([9]). Hydrothermal syntheses yielding $Zn_xCu_{4-x}(OH)_6FCl$ for $0 < x \leq 1.6$ were attempted in both pH ~ 3 and ~ 5, and it was concluded that the lower pH values are only required to produce pure samples for $x \geq 1$.

Previous density functional theory (DFT) studies predicted that Mg^{2+} is also a good candidate for diamagnetic doping of barlowite [10] and given the structural similarities between barlowite and claringbullite we attempted Mg-doping for $0.1 < x < 1$. This was done using the hydrothermal method outlined in Section 5.2.2 for $ZnCu_3(OH)_6FCl$ by replacing $ZnCl_2 \cdot xH_2O$ with $MgCl_2$ (Alfa Aesar, anhydrous 99%). Laboratory PXRD showed that no level of doping was successful, as the diffraction patterns of the products could not be described in the claringbullite high-temperature $P6_3/mmc$ space group.

5.2.2 Protonated samples

The final syntheses of protonated claringbullite and Zn-claringbullite are as follows. To synthesise $Cu_4(OH)_6FCl$, $Cu_2(OH)_2CO_3$ (Sigma, 0.275 g, 1.25 mmol), $CuCl_2 \cdot 2H_2O$ (Sigma, 0.215 g, 1.26 mmol), NH_4F (Alfa Aesar, 0.093 g, 2.50 mmol), HCl (Sigma, 0.05 g, 37 % w.t. solution) and H_2O (distilled, 10 mL) were placed in a 15 mL Teflon-lined steel autoclave.

For $ZnCu_3(OH)_6FCl$, $Cu_2(OH)_2CO_3$ (Aldrich, 0.250 g, 1.13 mmol), $ZnCl_2 \cdot xH_2O$ (Alfa, 0.190 g, 0.910 mmol), NH_4F (Alfa Aesar, 0.048 g, 1.29 mmol), HCl (Sigma, 0.1 g, 37 % w.t. solution) and H_2O (distilled, 10 mL) were placed in a 15 mL Teflon-lined steel autoclave.

For both materials the autoclaves were held at 200 °C for 24 h and naturally cooled in the oven to room temperature over 1 h to produce a green powder for

$Cu_4(OH)_6FCl$ and a blue powder for $ZnCu_3(OH)_6FCl$. The products were washed *via* centrifugation (5000 rpm, 5 min) with distilled water (3 x 20 mL) and dried in an oven at 50 °C for 5 h. Each synthesis produced approximately 0.2 g of material.

In general, for $Zn_xCu_{4-x}(OH)_6FCl$ for $0 < x \leq 1.6$, the same method was followed and the amount of HCl used was 0.05 g for $x < 1$ and 0.1 g for $x \geq 1$ (to achieve a pH of ~ 5 and ~ 3, respectively). For $x \leq 1$, the amounts of $ZnCl_2 \cdot xH_2O$ and $CuCl_2 \cdot 2H_2O$ were altered such that they stoichiometrically added up to $x = 1$. For $x > 1$, the amount of $ZnCl_2 \cdot xH_2O$ was increased stoichiometrically as the amount of $Cu_2(OH)_2CO_3$ was reduced accordingly.

5.2.3 Deuterated samples

Neutron scattering experiments require deuterated samples as H has a large incoherent scattering length (25.274 fm), which causes large background scattering in the data [11]. They also require a much larger sample than magnetometry or x-ray diffraction, so each synthesis was repeated multiple times and the products combined. For claringbullite ~ 5 g were prepared and ~ 7 g were synthesised for Zn-claringbullite (nominal $x = 1$ sample). The synthetic method was the same as for the protonated materials, but H_2O was replaced with D_2O. The products were washed *via* centrifugation (5000 rpm, 5 min) with D_2O (3 x 10 mL) and dried in an oven at 60 °C for 4 h.

5.3 Crystallographic studies

Synthetic products were initially characterised using room temperature laboratory powder x-ray diffraction (PXRD). To characterise crystal phase transitions in the $x = 0$ and 1 samples, and determine the atomic positions of the light atoms (D, O and Cl), neutron diffraction data were collected on D2B at the ILL down to $T = 1.5$ K. Characterising the low-temperature structure is also crucial for understanding the results of the inelastic neutron scattering studies, which will be discussed in Chapter 6. Before discussing the results of the diffraction measurements, the literature crystal structure will be presented.

5.3.1 Literature crystal structure

In the literature, studies of natural single crystals had concluded that the chemical formula of claringbullite was $Cu_4Cl(OH)_7{\cdot}nH_2O$ [12, 13]. This formula was revised for synthetic claringbullite and determined to be $Cu_4(OH)_6FCl$ [14]. Laboratory and synchrotron single crystal XRD, powder XRD and neutron powder diffraction have shown that at room temperature claringbullite orders in the $P6_3/mmc$ space group and one set of lattice parameters and atomic positions are included in Table 5.1 [4, 5, 14, 15]. Henderson *et al.* carried out temperature-dependent studies of single crystals using a synchrotron beamline and found that two of three samples showed superstructure reflections at $T = 100\,\mathrm{K}$, best described in the *Pnma* space group, whilst the other sample remained $P6_3/mmc$ down to $T = 10\,\mathrm{K}$ [4]. For completion the lattice parameters and atomic positions at $T = 100\,\mathrm{K}$ are included in Table 5.2. A recent study on powder samples using neutron and synchrotron x-ray diffraction down to $T = 1.5\,\mathrm{K}$, concluded that at low temperature the *Pnma* and $P6_3/mmc$ phases co-exist [15]. This sample dependence at low temperature, reminiscent of barlowite, requires a detailed characterisation of all synthetic samples as these structural differences can affect the exchange interactions.

At room temperature claringbullite is described in the $P6_3/mmc$ space group in which it has two Cu sites: Cu1 forms the kagome lattice that is stacked in an *AA*

Lattice parameters						
a (Å)		b (Å)	c (Å)	α (°)	β (°)	γ (°)
6.67257		6.67257	9.18014	90	90	120
Atomic parameters						
Atom	Wyckoff site	x	y	z	Occupation	U_{iso} (Å^2)
Cu1	6*g*	1/2	0	0	1	0.0125
Cu2	6*h*	0.37086	0.74172	3/4	1/3	0.0095
Cl	2*c*	1/3	2/3	1/4	1	0.0231
F	2*b*	0	0	1/4	1	0.0186
O	12*k*	0.20183	0.79817	0.90838	1	0.0076
H	12*k*	0.1407	0.8593	0.8601	1	0.0500

Table 5.1: Claringbullite. Literature lattice parameters and atomic positions from synchrotron powder XRD data collected at the APS 11-BM beamline at $T = 295\,\mathrm{K}$ in the $P6_3/mmc$ space group [4].

Lattice parameters					
a (Å)	b (Å)	c (Å)	α (°)	β (°)	γ (°)
11.5133	9.1527	6.6726	90	90	90
Atomic parameters					
Atom	Wyckoff site	x	y	z	U_{iso} (Å^2)
Cl	4*c*	0.67227	3/4	0.00919	0.0095
Cu1	4*a*	1/2	1/2	0	0.0050
Cu2	8*d*	0.75074	0.51320	0.24494	0.0047
Cu3	4*c*	0.31467	3/4	–0.05897	0.0070
F	4*c*	0.50230	3/4	–0.49380	0.0082
O1	8*d*	0.60259	0.40922	0.19960	0.0042
O2	8*d*	0.40195	0.58806	0.19810	0.0044
O3	8*d*	0.69984	0.59573	0.50210	0.0069

Table 5.2: Claringbullite. Literature lattice parameters and atomic positions from synchrotron single crystal XRD collected at the APS 15-BM beamline ($\lambda = 0.41328$ Å) at $T = 100$ K in the *Pnma* space group [4]. All sites are fully occupied.

formation along the *c*-axis; Cu2 sits between the kagome layers and is disordered over 3 equivalent positions (each of which is $1/3$ occupied) as shown in Figure 5.1. It has been suggested that the driving factor in the change of layering from *ABA* in herbertsmithite to *AA* in claringbullite (and barlowite), is the strong hydrogen bonding between H^+ and F^- [4].

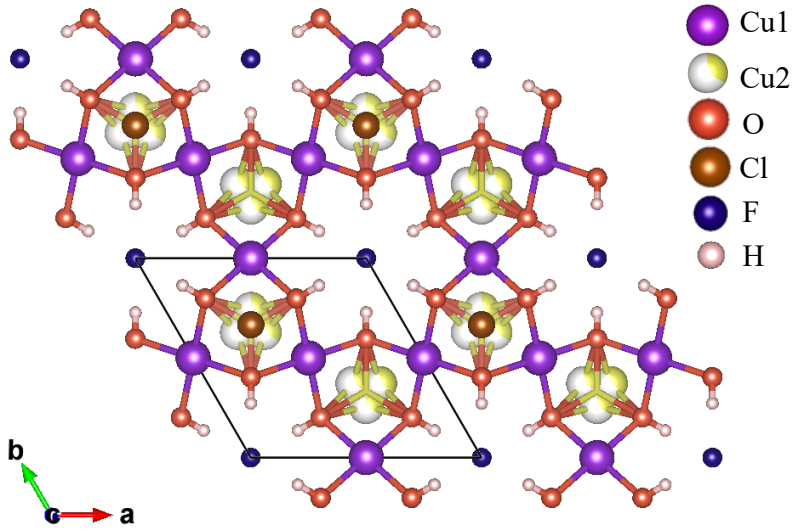

Figure 5.1: The room temperature crystal structure of claringbullite crystallising in the $P6_3/mmc$ group. Note the Cu2 is disordered over 3 equivalent positions, each of which is $1/3$ occupied.

The crystallographic phase transition to *Pnma* at low temperature is attributed to the reduction in symmetry caused by the preferential ordering of the Cu2 at one of the 3 equivalent positions [4]. This is understood in terms of a dynamic−static Jahn-Teller transition. At high temperature, the Cu2 sits on the 6*h* Wyckoff site with $(OH)_6$ coordination giving it a trigonal prismatic environment (point group D_{3h}) where the highest energy orbitals, d_{xz} and d_{yz}, are degenerate and unevenly occupied and a dynamic effect occurs where the two sets of orbitals are occupied interchangeably. However, as the temperature is lowered, a Jahn-Teller distortion occurs to remove the degeneracy by lowering the energy of the d_{yz} orbital causing the unpaired spin to occupy the d_{xz} orbital. This has previously been described as a 'cis' distortion and results in 2 elongated and 4 shortened bonds or vice versa [16]. In claringbullite this results in the interlayer Cu ordering onto one of the 3 sites (with the C_{2v} point group), lowering the crystal symmetry from $P6_3/mmc$ to *Pnma*.

5.3.2 Laboratory powder x-ray diffraction

Protonated samples synthesised according to Section 5.2.2 for $0 \leq x \leq 1.6$ were initially characterised at room temperature using laboratory PXRD. The samples were placed in a rotating borosilicate glass capillary ($d = 0.3$ mm) and measured on a Stoe Stadi-P diffractometer with a Cu-Kα_1 source ($\lambda = 1.5406$ Å). All observed peaks could be indexed with the $P6_3/mmc$ space group and an example of a Rietveld refinement is shown for undoped deuterated claringbullite in Figure 5.2. An absorption correction was applied assuming a packing density of 0.5, giving $\mu R = 1.3$. As $\mu R > 1$, absorption effects are not minimal with this wavelength and could affect the refined displacement parameters. Synchrotron x-ray diffraction or neutron diffraction studies such as those detailed in Section 5.3.3 will give more accurate displacement parameters at room temperature. The background of the laboratory PXRD pattern was modelled using a Chebyshev polynomial and a pseudo-Voigt function to describe the broad peak centred at $Q \approx 1.55$ Å^{-1} resulting from amorphous scattering by the capillary. The profile was described using a pseudo-Voigt function with eight spherical harmonics to account for preferred orientation. The lattice parameters, site positions and isotropic displacement parameters are given in

Table 5.3.

For $x \leq 1.6$ in $Zn_xCu_{4-x}(OH)_6FCl$, all samples were found to be single phase, but attempts to increase the doping percentage further led to the formation of a new phase. It is likely that the non Jahn-Teller active Zn^{2+} ion cannot occupy a high percentage of the kagome sites as its isotropic nature reduces the extent of the Jahn-

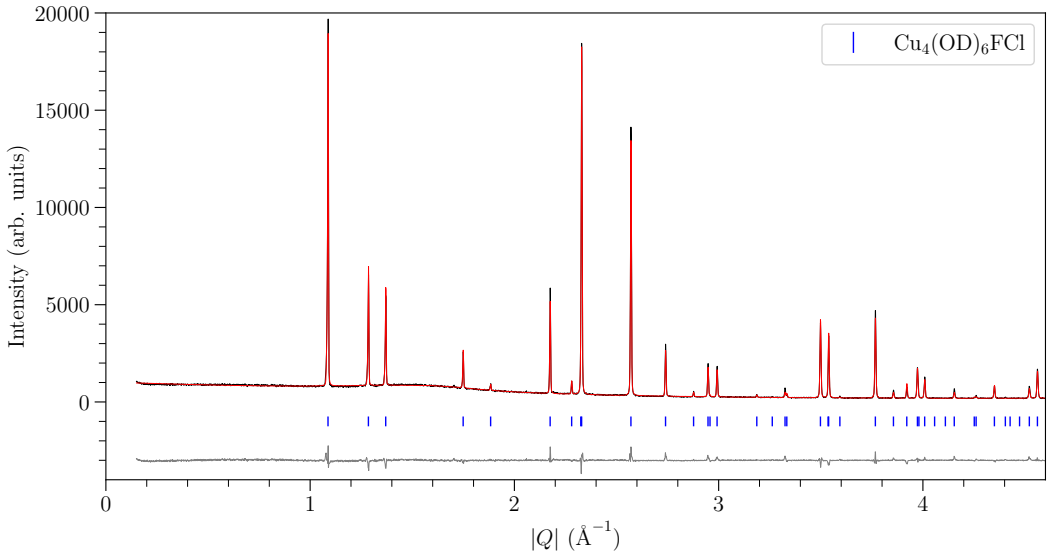

Figure 5.2: Claringbullite laboratory PXRD data collected on a Stoe Stadi-P with a Cu $K\alpha_1$ source ($\lambda = 1.5406$ Å) at room temperature (black). Rietveld refinement (red) in the $P6_3/mmc$ space group with 34 variables and goodness-of-fit parameters $\chi^2 = 1.18$, $R_{wp} = 4.76$. The peak positions are shown in blue and the difference plot in grey.

Lattice parameters						
a (Å)		b (Å)	c (Å)	α (°)	β (°)	γ (°)
6.67289(4)		6.67289(4)	9.17477(6)	90	90	120
Atomic parameters						
Atom	Wyckoff site	x	y	z	Occupation	U_{iso} (Å^2)
Cu1	6g	1/2	0	0	1	0.0239(5)
Cu2	6h	0.3728(4)	0.7456(8)	3/4	1/3	0.0188(2)
Cl	2c	1/3	2/3	1/4	1	0.0282(17)
F	2b	0	0	1/4	1	0.0217(18)
O	12k	0.1991(3)	0.8009(12)	0.9085(4)	1	0.0150(12)

Table 5.3: Claringbullite. Lattice parameters, atomic positions and displacement parameters from Rietveld refinement in the $P6_3/mmc$ space group using laboratory PXRD data ($\lambda = 1.5406$ Å) collected at room temperature. The deuterium site was not included in the refinement.

Teller distortion and leads to the structure breaking down. Successful doping was monitored by looking at the change of lattice parameters with increased Zn content. A full structural characterisation including the determination of the atomic positions of the light atoms required higher flux and better resolution than available with our laboratory equipment.

5.3.3 Neutron powder diffraction on claringbullite - D2B

Neutron diffraction was chosen over synchrotron XRD due to its the ability to better locate the light O, Cl, F and D atoms. Neutron diffraction measurements of deuterated claringbullite were carried out on the high-resolution instrument D2B at the ILL with neutrons of wavelength $\lambda = 1.595226$ Å. Data were collected over 4 h using a ~ 5 g sample at $T = 1.5$ and 295 K. The temperatures were chosen for a comparison against the previously reported crystal structures [4, 5] and to maximise the advantage of neutrons to more accurately locate the H/D atoms. Rietveld refinement analysis was performed using the program TOPAS 7 [17].

At room temperature claringbullite was found to crystallise in the hexagonal $P6_3/mmc$ space group, in agreement with the literature [4, 5], and the sample was found to be single phase. Initial lattice parameters and atomic positions for the room temperature refinement were taken from the powder synchrotron data refinement in [4] at 295 K. The neutron absorption cross-section was calculated using the linear attenuation coefficient, μ, which is the sum of the coherent, absorption and incoherent scattering cross sections for the sample with $\lambda = 1.595226$ Å, and the radius of the sample holder (8.5 mm) giving $\mu R = 0.40$. The profile was adequately modelled using the "simple axial model" provided in TOPAS to describe axial divergence of the beam, with 8 spherical harmonics for the wider peaks at high-Q (due to peak overlap) and a pseudo-Voigt function.

All atomic positions were freely refined within the constraints of the space group symmetry and the hydroxide O-D(H) bond distance refined to 0.9797(11) Å, similar to the previously determined O-D distances of 0.9987 Å and 0.9838 Å in kapellasite and haydeeite [18], respectively, but longer than the O-H bond (0.834 Å) found from previous XRD measurements on claringbullite single crystals [4].

Isotropic displacement parameters for all atoms were stably refined, but the high-Q refinement was improved by using anisotropic displacement parameters. These were stably refined for all sites. The occupation of the D site refined to 96% occupancy, indicating a high level of deuteration in the sample, but was fixed to unity for the final refinement. The final Rietveld refinement gave a good fit to the D2B data with goodness-of-fit parameters $\chi^2 = 2.28$ and $R_{\text{wp}} = 3.32$. It is shown in Figure 5.3 with lattice parameters and atomic positions listed in Table 5.4.

At $T = 1.5$ K the diffraction pattern has additional reflections indicating a crystallographic phase transition occurred on cooling. A Pawley refinement showed that the low-temperature peaks could be successfully indexed in the orthorhombic space group *Pnma* and the Rietveld refinement is included in Figure 5.4. *Pnma* is not a maximal subgroup of $P6_3/mmc$, with the intermediate space group being *Cmcm*, but that space group could not index all observed peaks. The *Cmcm* phase has notably not been observed in other claringbullite temperature studies [4, 15]. Attempts to index our data with other maximal subgroups of $P6_3/mmc$, which are also hexagonal, were unsuccessful. In our refinements, the lattice parameters and atomic positions in *Pnma* were initialised with previously reported values from synchrotron single

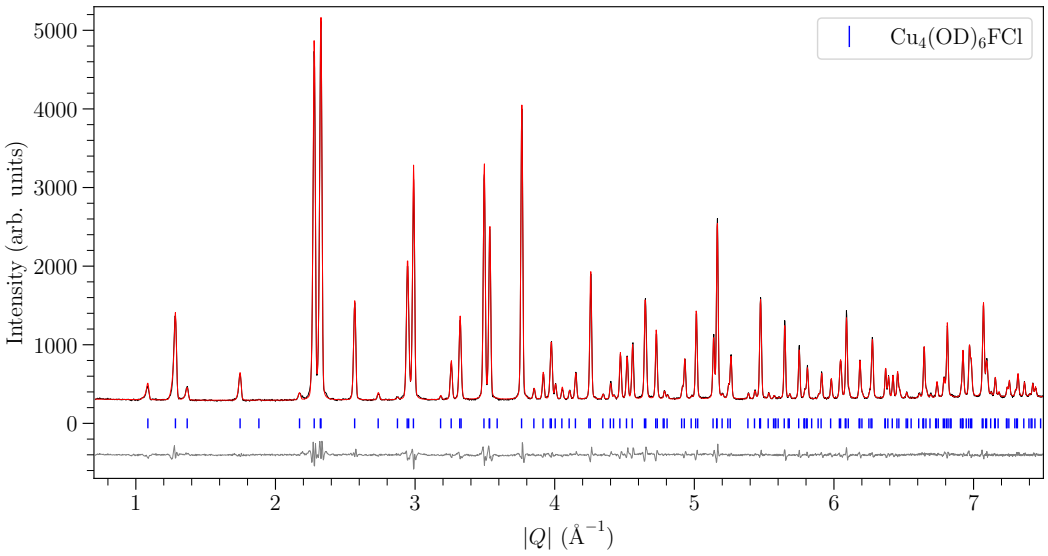

Figure 5.3: Claringbullite, D2B data collected at $T = 295$ K (black) with $\lambda = 1.595226$ Å. Rietveld refinement (red) in the $P6_3/mmc$ space group with 50 variables and goodness-of-fit parameters $\chi^2 = 2.28$, $R_{\text{wp}} = 3.32$. The difference between the experimental data and the fit is shown in grey and the peak positions are in blue.

Lattice parameters						
a (Å)	b (Å)		c (Å)	α (°)	β (°)	γ (°)
6.6791(4)	6.6791(4)		9.1875(6)	90	90	120
Atomic parameters						
Atom	Wyckoff site	x	y	z	Occupation	U_{iso} (Å^2)
Cu1	6g	1/2	0	0	1	0.0124
Cu2	6h	0.3708(2)	0.7415(4)	3/4	1/3	0.0071
Cl	2c	1/3	2/3	1/4	1	0.0210
F	2b	0	0	1/4	1	0.0199
O	12k	0.2020(1)	0.7980(1)	0.9090(1)	1	0.0094
D	12k	0.1246(1)	0.8754(1)	0.8664(1)	1	0.0256
Anisotropic displacement parameters (Å^2)						
Atom	U_{11}	U_{22}	U_{33}	U_{12}	U_{13}	U_{23}
Cu1	0.00753(31)	0.00714(46)	0.0225(5)	0.00357(23)	–0.00251(20)	–0.00502(40)
Cu2	0.0057(11)	0.00698(19)	0.0086(14)	0.00349(95)	0	0
Cl	0.0232(5)	0.0232(5)	0.0166(9)	0.0116(3)	0	0
F	0.0150(7)	0.0150(7)	0.0297(14)	0.00750(37)	0	0
O	0.00748(34)	0.00748(34)	0.0132(5)	0.00407(43)	–0.00138(20)	0.00138(20)
D	0.0229(5)	0.0229(5)	0.0309(6)	0.0140(5)	–0.00116(24)	0.00116(24)

Table 5.4: Claringbullite. Lattice parameters, atomic positions and displacement parameters from Rietveld refinement in the $P6_3/mmc$ space group using data collected on D2B ($\lambda = 1.595226$ Å) at $T = 295$ K. The D site refined to 0.96 showing good deuteration of the sample, and was set to unity for the final refinement. The anisotropic displacement parameters were stably refined for all atoms.

crystal data at $T = 100$ K [4].

The profile was described in the same manner as for the $T = 295$ K refinement. All atomic positions were freely refined, giving an O-D bond distance of 0.978(7) Å. Isotropic atomic displacement parameters were stably refined and the refinement is shown in Figure 5.4 ($\chi^2 = 2.69$ and $R_{wp} = 4.17$). We also consider the recent report of multi-phase samples at low-temperature from synchrotron XRD and NPD experiments, which highlights the $hk4n$ peaks, in particular the (004) and (104) peaks, to be poorly fitted with a single *Pnma* phase [15]. In our D2B neutron diffraction data, the (004) peak is too low in intensity to be assessed and the (104) peak is well-fitted with a single *Pnma* phase. Inspection of all peaks shows no evidence that a second phase is required to model our data. The final atomic positions and isotropic atomic displacement parameters are listed in Table 5.5 and the structure is shown in Figure 5.5. The Cu-Cu distances and ∠Cu-(μ_3-OD)-Cu bond

angles, which are expected to be the relevant superexchange pathways, are listed in Table 5.6. The ∠Cu-(μ_3-OD)-Cu bond angles can be divided into two categories: (*i.*) the kagome triangle ones which range between 114.8° and 120.9°, and (*ii.*) the ones between the kagome Cu1 and Cu2 atoms, and the interlayer Cu3 that range between 90.6° and 98.7°. The Goodenough-Kanamori rules can only be used to a first approximation as they only consider μ_2-O pathways, so comparison with other systems is more appropriate. In herbertsmithite the ∠Cu-(μ_3-OH)-Cu angle of 119° corresponds to an antiferromagnetic exchange [19], and in several cubanes with a [Cu_4(μ_3-$OH)_4$] core the change from ferro- to antiferromagnetic exchange occurs at angles of about $101 - 105°$ [20, 21]. Therefore, the kagome triangles in claringbullite likely have antiferromagnetic exchanges, whereas the exchange interactions between the kagome and interlayer Cu atoms are expected to be ferromagnetic.

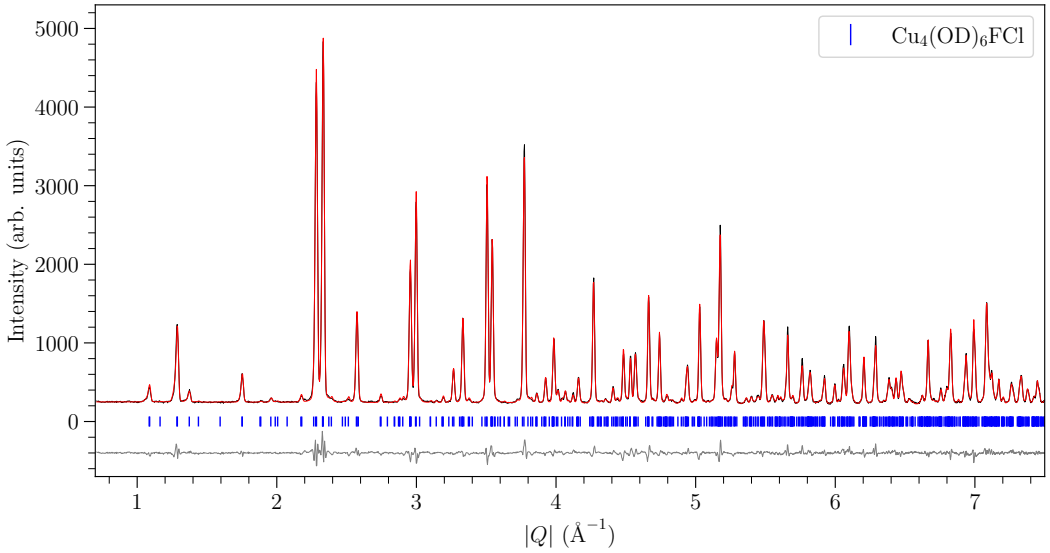

Figure 5.4: Claringbullite, D2B data collected at $T = 1.5$ K (black) with $\lambda = 1.595226$ Å. Rietveld refinement (red) in the *Pnma* space group with 72 variables and goodness-of-fit parameters $\chi^2 = 2.69$ and $R_{wp} = 4.17$. The difference between the experimental data and the fit is shown in grey and the peak positions are in blue.

Lattice parameters					
a (Å)	b (Å)	c (Å)	α (°)	β (°)	γ (°)
11.5359(9)	9.1510(7)	6.6848(5)	90	90	90
Atomic parameters					
Atom	Wyckoff site	x	y	z	B_{iso} (Å^2)
Cl	4c	0.3304(5)	1/4	0.5049(6)	0.00616(37)
Cu1	4a	0	0	0	0.00341(11)
Cu2	8d	0.2492(4)	0.5121(3)	0.2470(5)	0.00238(57)
Cu3	4c	0.1870(6)	1/4	0.0592(6)	0.00381(65)
F	4c	0.5007(11)	1/4	0.0041(13)	0.00876(57)
O1	8d	0.2961(5)	0.0921(6)	0.00062(67)	0.0054(12)
O2	8d	0.1022(5)	0.0919(5)	0.1989(7)	0.00118(90)
O3	8d	0.4003(5)	0.5889(5)	0.3000(7)	0.00062(87)
D1	8d	0.3765(7)	0.1342(7)	1.0030(8)	0.0150(11)
D2	8d	0.0611(5)	0.1294(5)	0.3161(7)	0.0139(11)
D3	8d	0.4401(5)	0.6381(6)	0.1912(7)	0.0173(11)

Table 5.5: Claringbullite. Lattice parameters, atomic positions and isotropic thermal parameters from the Rietveld refinement in the *Pnma* space group using data collected on D2B ($\lambda = 1.595226$ Å) at $T = 1.5$ K. All sites are fully occupied.

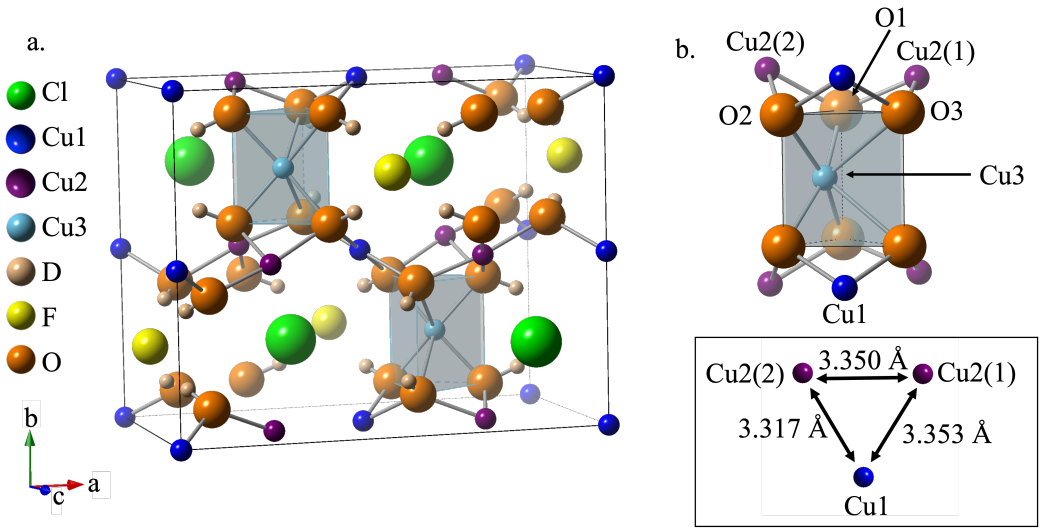

Figure 5.5: Claringbullite. **a.** *Pnma* crystal structure from refinement using D2B data ($\lambda = 1.595226$ Å) at $T = 1.5$ K with lattice parameters $a = 11.5359(9)$ Å, $b = 9.1510(7)$ Å, $c = 6.6848(5)$ Å, $\alpha = \beta = \gamma = 90°$. **b.** The Cu3 interlayer site has undergone a dynamic-static Jahn-Teller distortion resulting in a distorted tetrahedron. The kagome triangles are scalene with a 1.07% distortion.

Cu - Cu	Distance (Å)
Cu1 - Cu2(1)	3.353(5)
Cu1 - Cu2(2)	3.317(5)
Cu2(1) - Cu2(2)	3.3498(5)
Cu1 - Cu3	3.169(5)
Cu2(1) - Cu3	3.104(5)
Cu2(2) - Cu3	2.801(4)

Cu1 - Cu2 Cu2 - Cu2	Angle	Cu1 - Cu3 Cu2 - Cu3	Angle	Average
∠Cu1 - O3(D) - Cu2(1)	120.9°	∠Cu1 - O3(D) - Cu3	90.487°	98.7°
∠Cu1 - O2(D) - Cu2(2)	114.8°	∠Cu1 - O2(D) - Cu3	106.9°	
∠Cu2(1) - O1(D) - Cu2(2)	118.5°	∠Cu2(1) - O1(D) - Cu3	106.5°	97.6°
		∠Cu2(1) - O3(D) - Cu3	88.7°	
		∠Cu2(2) - O1(D) - Cu3	90.8°	90.6°
		∠Cu2(2) - O2(D) - Cu3	90.3°	

Table 5.6: Claringbullite, *Pnma*. Cu-Cu distances in the tetrahedra and Cu-O(D)-Cu superexchange angles. From each Cu1 and Cu2 there are two possible superexchange pathways to Cu3, so the average angle was calculated. The pathways within the kagome triangles are likely to favour more antiferromagnetic exchange and those to the interlayer Cu3 more ferromagnetic exchange interactions [20].

5.3.4 Neutron powder diffraction on Zn-claringbullite - D2B

Similar to claringbullite, a temperature study was done on the crystal structure of Zn-claringbullite on D2B using a ~ 7 g deuterated sample. Data were collected at $T = 1.5$ K, 50 K and 295 K to verify the previously reported room temperature crystal structure [7] and investigate any structural distortions with temperature. All data collected down to $T = 1.5$ K can be indexed in the $P6_3/mmc$ space group indicating no crystallographic phase transitions and a high-symmetry kagome lattice down to the lowest measured temperature. The hexagonal symmetry suggests that the Zn^{2+} ions are mainly located on the interlayer sites, as Zn^{2+} is not a Jahn-Teller active ion so its local symmetry is expected to be higher than that of Cu^{2+}. The kagome site has a square planar environment, so it is expected that Cu^{2+}, which prefers a lower symmetry environment, will favour this site.

Rietveld refinements at $T = 295$ K were initialised using the literature lattice parameters, atomic positions and isotropic thermal parameters [7], and the refined values were used as starting points for the lower temperature refinements. The peak profile was described as for claringbullite and the neutron absorption factor was calculated to be $\mu R = 0.39$. The atomic positions were stably refined and the D site occupancy refined to 96% evidencing the synthetic method for deuterated samples was consistently successful up to the Zn-doping level of $x = 1$. The lattice parameters at all temperatures are in Table 5.7, showing a contraction in all directions as temperature decreases, and the Rietveld refinement at $T = 1.5$ K is shown in Figure 5.6 with the crystal structure in Figure 5.7 and atomic positions in Table 5.8.

Temperature (K)	a (Å)	b (Å)	c (Å)
1.5	6.65918(6)	6.65918(6)	9.17288(9)
50	6.66006(3)	6.66006(3)	9.17626(3)
295	6.6712(1)	6.6712(1)	9.2044(2)

Table 5.7: Lattice parameters of Zn-claringbullite from Rietveld refinements in the $P6_3/mmc$ space group (no. 194) using D2B data ($\lambda = 1.595226$ Å) collected at $T = 1.5,\ 50$ and 295 K.

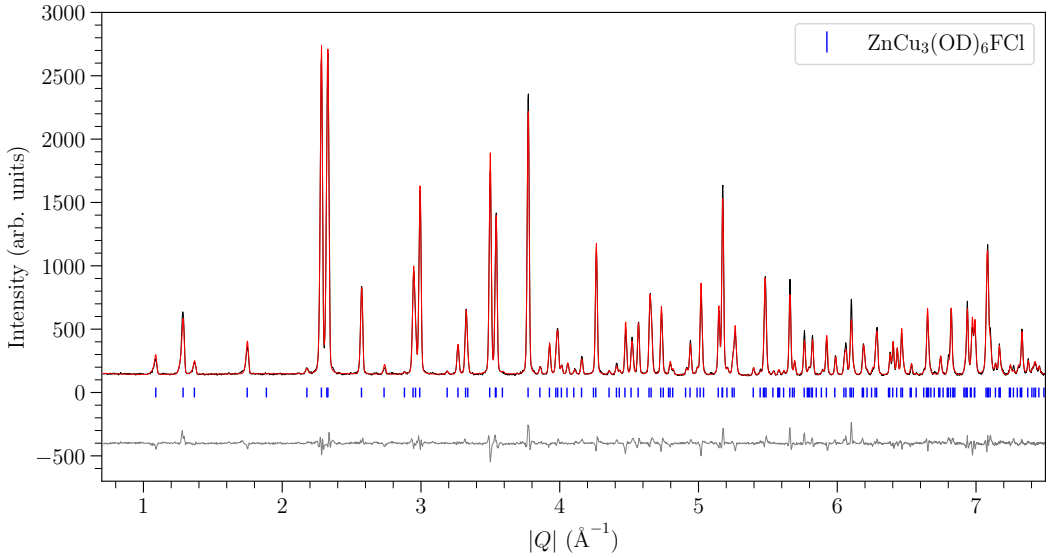

Figure 5.6: Zn-claringbullite, D2B data collected at $T = 1.5$ K with $\lambda = 1.595226$ Å. Neutron diffraction data (black) with a Rietveld refinement (red) in the $P6_3/mmc$ space group with 45 variables and goodness-of-fit parameters $\chi^2 = 2.70$ and $R_{wp} = 5.47$. The difference between the experimental data and the fit is shown in grey and the peak positions are in blue.

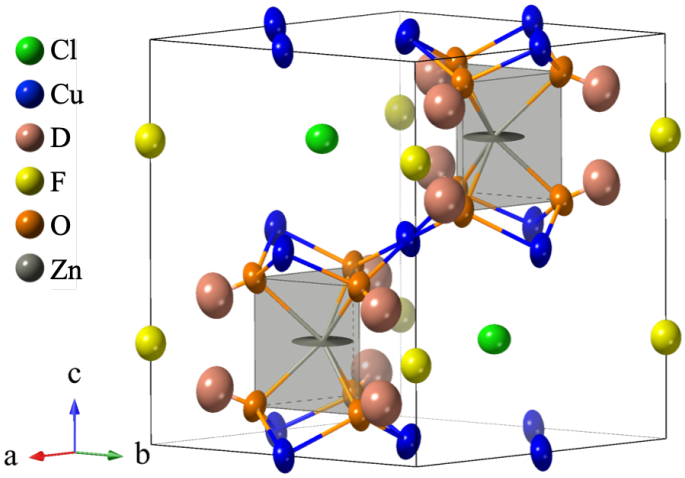

Figure 5.7: Zn-claringbullite crystal structure with anisotropic displacement parameters refined from D2B data at $T = 1.5$ K. These are given with the atomic positions in Table 5.8 and the refinement is shown in Figure 5.6.

Atomic parameters						
Atom	Wyckoff site	x	y	z	Occupation	U_{iso} (Å^2)
Cu	6*g*	0.5	0	0	1	0.0090
Zn	2*d*	1/3	2/3	3/4	1	0.0286
F	2*b*	0	0	3/4	1	0.0116
Cl	2*c*	2/3	1/3	3/4	1	0.0115
O	12*k*	0.20207(10)	0.79793(10)	0.90785(12)	1	0.0075
D	12*k*	0.12383(11)	0.87617(11)	0.86569(13)	1	0.0207
Anisotropic displacement parameters (Å^2)						
Atom	U_{11}	U_{22}	U_{33}	U_{12}	U_{13}	U_{23}
Cu	0.00530	0.00670	0.01500	0.00330	–0.00130	–0.00250
Zn	0.04280	0.04280	0.00010	0.0214	0	0
Cl	0.01220	0.01220	0.01000	0.00610	0	0
F	0.01040	0.01040	0.01400	0.00520	0	0
O	0.00550	0.00550	0.01160	0.00240	–0.00100	0.00100
D	0.01900	0.01900	0.02410	0.01130	–0.00100	0.00100

Table 5.8: Zn-claringbullite. Atomic positions and displacement parameters from Rietveld refinement in the $P6_3/mmc$ space group using D2B data ($\lambda = 1.595226$ Å) collected at $T = 1.5$ K. The D site refined to 0.96 showing good deuteration of the sample and was set to unity for the final refinement. The anisotropic displacements were refined for all atoms.

For the Zn-claringbullite structure, the Zn^{2+} ions sit on top of each kagome triangle on a 3-fold site (6*g* Wyckoff position) with equal bond lengths to all 3 kagome Cu sites. At $T = 1.5$ K, the kagome Cu site has an $(OH)_4Cl_2$ coordination where the Cu-O bond lengths (1.94 Å) are shorter than the Cu-Cl ones (2.99 Å), indicating a Jahn-Teller distortion to a square planar environment where the spin is carried in the $d_{x^2-y^2}$ orbital, as in herbertsmithite [22].

At all temperatures refinement of the anisotropic displacement parameters (ADPs) was stable for all sites and at $T = 1.5$ K they are given in Table 5.8. However, it is noted that the Zn ADP resembles a flat disk in the $a-b$ plane (see Figure 5.7), parallel to the kagome plane, which may be due to the bonding constraints in its trigonal prismatic coordination or due to site disorder. At $T = 1.5$ K, the difference Fourier map showed no indication of missing intensity around this site, but it is possible that some interlayer sites are occupied by Cu. Zn and Cu have slightly different nuclear coherent scattering lengths ($b_{coh,Zn} = 5.680$ fm and $b_{coh,Cu} = 7.485$ fm [11]), but it was not possible to stably refine site occupancies on the interlayer or kagome sites without allowing for unphysical ADPs. The interlayer Zn and Cu occupy different Wyckoff positions (2*d* and 6*h*), but the high correlation with the

ADPs made it difficult to reliably refine them. Elemental composition measurements, using anomalous x-ray diffraction for example, will be important to serve as a more reliable starting point for the site occupancies in these refinements.

5.4 SQUID magnetometry

The DC susceptibility of both the undoped and Zn-doped ($x = 1$) claringbullite samples have previously been measured [5, 7, 15]. In claringbullite, two magnetic transitions have been reported at $T = 15$ and ~ 5 K, more clearly seen in specific heat capacity measurements [5, 15]. In this work, DC susceptibility measurements were carried out on the deuterated samples synthesised for neutron scattering experiments. Data were collected on a SQUID MPMS XL Quantum Design (Institut Néel, Grenoble) and a SQUID Quantum Design MPMS3 (University of Glasgow, UK). The diamagnetic contribution in each sample was subtracted using Pascal's constants for the nominal structural formulas [23]. The results are detailed in sections 5.4.1 and 5.4.2 for claringbullite and Zn-claringbullite, respectively. Field-cooled (FC) measurements were made by cooling the sample to base temperature in a magnetic field and collecting data on heating in the same field.

5.4.1 DC susceptibility of claringbullite

For claringbullite, zero-field cooled (ZFC) and field-cooled (FC) data were collected on a 0.1919 g sample in a field of 1000 G between $T = 2$ and 320 K. The molar magnetic susceptibility is plotted as a function of temperature in Figure 5.8a and shows a transition with a ferromagnetic component at $T_N = 17$ K, with bifurcation between the FC and ZFC data, in agreement with the previously reported $T_1 = 15$ K [5]. Below $T = 9$ K the antiferromagnetic component dominates the susceptibility. Looking at the first derivative of the susceptibility, $d\chi/dT$, it is evident that at $T = 17$ K there is a transition, but at lower temperatures there is no clear magnetic transition (Figure 5.4.1b). The effective magnetic moment, μ_{eff}, as a function of temperature more clearly shows an antiferromagnetic contribution growing rapidly below $T = 9$ K, as μ_{eff} decreases (Figure 5.4.1d). A linear extrapolation of χ^{-1} data between $T = 150$ and 320 K to $\chi^{-1} = 0$ (Figure 5.4.1c) gives a Weiss temperature

$\theta_W = -136(3)$ K, indicating an antiferromagnetic mean-field in agreement with [5]. From θ_W a Curie constant of 0.604(4) emu K mol^{-1} Cu^{-1} is calculated, giving μ_{eff}= 2.20 μ_B Cu^{-1}, which indicates that the sample has the expected 4 mol Cu^{2+} per mole of sample. Calculating μ_{eff} using $\sqrt{8\chi T}$ yields 1.84 μ_B Cu^{-1} at room temperature. As seen in other frustrated Cu magnets, these values are slightly higher than the spin-only theoretical value of 1.73 μ_B per Cu^{2+} ion, suggesting an orbital contribution to the Landé g factor [22, 24, 25].

Magnetisation data, M, as a function of field, H, were measured for temperatures between $T = 2$ and 50 K (Figure 5.9a). Below $T_N = 17\,K$, for $T \leq 15$ K, a

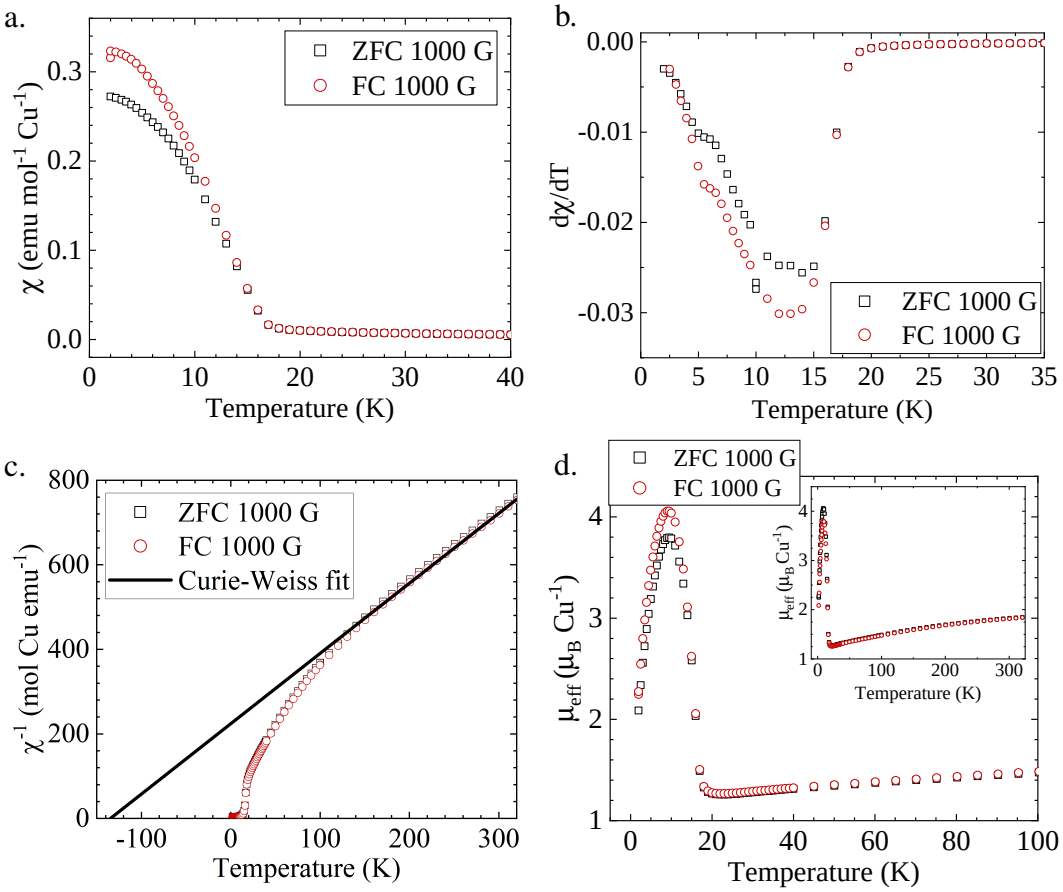

Figure 5.8: Claringbullite. **a.** Field-cooled (red) and zero-field-cooled (black) magnetic susceptibility data collected in a field of 1000 G. There is a transition at $T_N = 17$ K. **b.** First derivative of susceptibility to more clearly show the transition at 17 K. **c.** Inverse susceptibility, χ^{-1}, as a function of temperature, T, of field-cooled and zero-field-cooled data collected in 1000 G with a linear Curie-Weiss fit (black) between 150 K and 320 K which gives $\theta_W = -136(3)$ K. **d.** Effective magnetic moment, μ_{eff}, as a function of temperature, T, calculated using $\mu_{\text{eff}} = \sqrt{8\chi T}$.

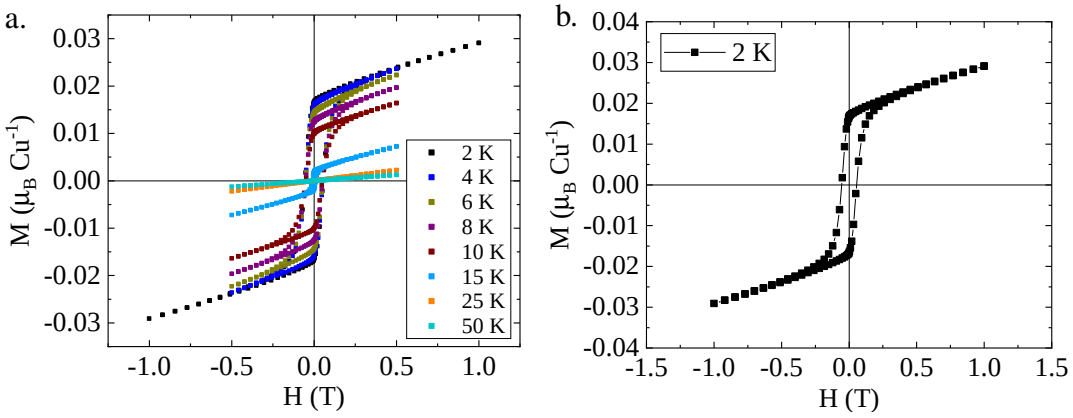

Figure 5.9: Claringbullite. Magnetisation, M, as a function of field, H. **a.** Plots between $T = 2$ K and 50 K show a hysteresis loop opening at $T \leq 15$ K. **b.** At $T = 2$ K the spontaneous moment is 0.017 μ_B Cu^{-1} with a coercivity of 0.05 T.

hysteresis loop opens up indicating the ferromagnetic transition. At $T = 2$ K the magnetisation has a spontaneous moment of $\sim 0.017\,\mu_B$ Cu^{-1}, which is 0.9% of the full ordered moment, and a coercivity of ~ 0.05 T.

5.4.2 DC susceptibility of Zn-claringbullite

For Zn-claringbullite, ZFC and FC measurements were carried out in the same manner as for the undoped claringbullite sample. A plot of the molar magnetic susceptibility as a function of temperature (Figure 5.10a) shows no transition to long-range order down to $T = 2$ K. A linear fit of χ^{-1} data between 150 K $< T <$ 320 K gives $\theta_W = -206(1)$ K (Figure 5.10b), in good agreement with the previously reported $\theta_W = -223$ K measured in a field of 1 T [7]. Below $T = 150$ K, the curvature in χ^{-1} *vs.* T increases, indicating the build-up of short-range correlations. The fit to the Curie-Weiss law gives a Curie constant of 0.538(1) emu K mol^{-1} Cu^{-1}, so $\mu_{\text{eff}} = 2.07\,\mu_B$ Cu^{-1}. This is higher than the spin-only theoretical value as for claringbullite in Section 5.4.1, again indicates there is an orbital contribution to the Landé g-factor. θ_W is more negative than for claringbullite, evidencing that Zn-claringbullite has a stronger antiferromagnetic mean-field perhaps due to the Zn-substitution weakening ferromagnetic exchange pathways. Figure 5.10c shows μ_{eff} falls as temperature decreases as antiferromagnetic correlations are getting stronger, but there is a plateau between $T = 3$ and 5 K that may evidence a competing increase in ferromagnetic spin-spin correlations.

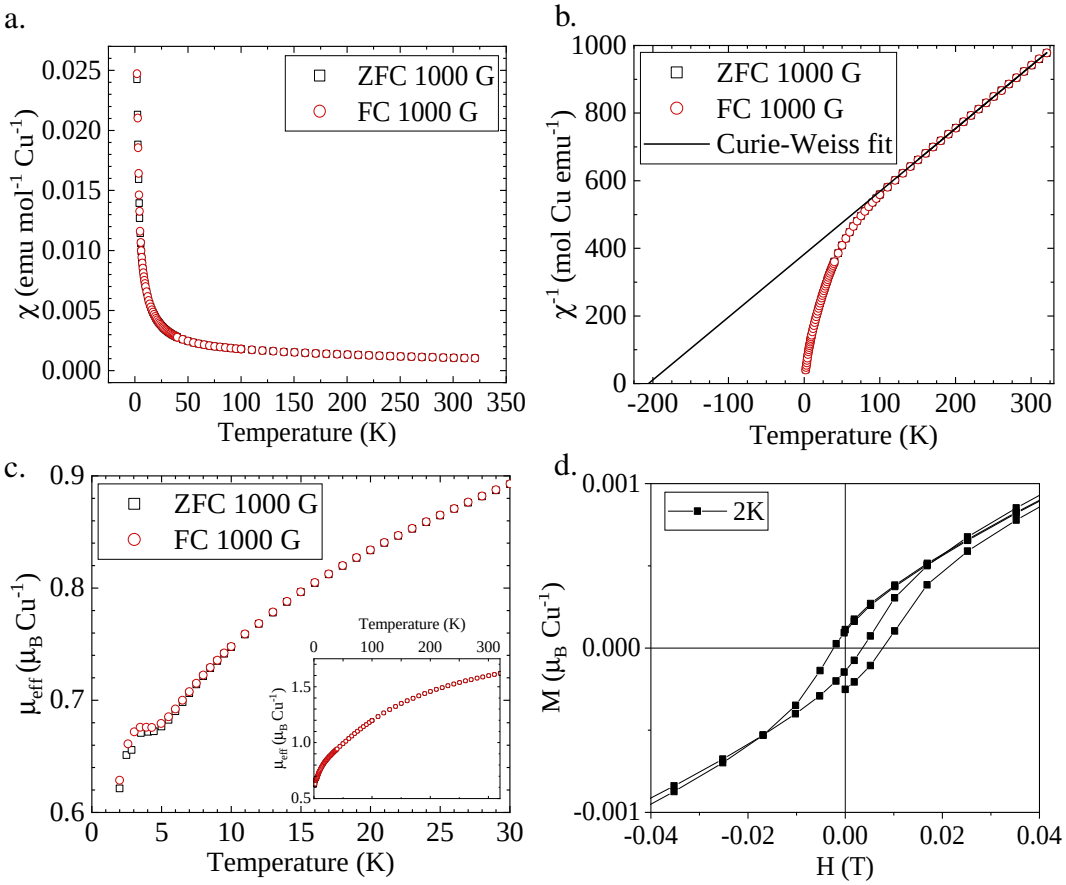

Figure 5.10: Zn-claringbullite. **a.** Field-cooled (red) and zero-field-cooled (black) magnetic susceptibility data collected in a field of 1000 G. There is no transition down to 2 K. **b.** Inverse susceptibility, χ^{-1}, of field-cooled and zero-field-cooled data collected in 1000 G with a linear Curie-Weiss fit (black) between 150 K and 320 K which gives $\theta_W = -206(1)$ K. **c.** Effective magnetic moment, μ_{eff}, as a function of temperature, T, calculated using $\mu_{\text{eff}} = \sqrt{8\chi T}$. **d.** Magnetisation, M, as a function of field, H, at $T = 2$ K showing a hysteresis loop with a spontaneous moment of $\sim 2 \times 10^{-4}\,\mu_{\text{B}}$ Cu^{-1} and a coercivity of $\sim 3 \times 10^{-3}$ T.

Magnetisation, M, was measured as a function of applied field, H, at several temperatures between $T = 2$ and 50 K (Figure 5.11a). At $T = 2$ K there is a small hysteresis (see Figure 5.10d) with a spontaneous moment $\mu_{\text{FM}} \approx 2 \times 10^{-4}\,\mu_{\text{B}}$ mol^{-1} Cu^{-1}, corresponding to 0.01% of the full ordered moment and indicating a very weak ferromagnetic moment in the sample. The possibility that this contribution is from a ferromagnetic impurity interaction can be explored using a phenomenological function to fit the magnetisation for $2 \leq T\,(\text{K}) \leq 50$ given by

$$M(H)/M_{\text{sat}} = (1-f)B_J(H) + f, \tag{5.1}$$

where f accounts for a saturated ferromagnetic component in the sample. $B_J(H)$ is the Brillouin function given by

$$B_{\mathrm{J}}(H) = \tanh(g\mu_{\mathrm{B}}JH/k_{\mathrm{B}}T_{\mathrm{eff}}), \tag{5.2}$$

where $T_{\mathrm{eff}} = T + T_0$ and T_0 is an effective temperature accounting for spin-spin interactions (> 0 for antiferromagnetic and < 0 for ferromagnetic ones) [25, 26]. In this case, g was taken as the value 1.84 derived from the high temperature effective moment $\mu_{\mathrm{eff}} = 1.59\,\mu_{\mathrm{B}}\,\mathrm{Cu}^{-1}$. The variables f, T_0 and M_{sat} were allowed to freely refine and the fits are shown in Figure 5.11 together with the fitted parameters at each temperature. The saturated ferromagnetic component, f, refines to values close to zero for $T \geq 8\,\mathrm{K}$ and a value of 0.0659 at $T = 2\,\mathrm{K}$, indicating that the ferromagnetic signal arises from a small part of the sample. The refined T_0 values show a complicated behaviour of both ferro- and antiferromagnetic interactions in the sample, which may be expected from contrast between the large negative Weiss temperature indicative of a strong antiferromagnetic mean field and the small hysteresis at $T = 2\,\mathrm{K}$ signifying a ferromagnetic component. The magnitude of T_0 is of the order of a few Kelvin, comparable to the defect spin interactions of ~ 1 K in herbertsmithite, which were also determined using M *vs*. H measurements [27, 28]. At $T = 2\,\mathrm{K}$, M_{sat} refines to $0.0631\,\mu_{\mathrm{B}}\,\mathrm{Cu}^{-1}$ that is 3.6% of the theoretical spin-only Cu^{2+} moment ($1.73\,\mu_{\mathrm{B}}\,\mathrm{Cu}^{-1}$) and evidences a slow saturation with increasing field as spin interactions become stronger in a highly frustrated system. For herbertsmithite M_{sat} at $T = 1.7$ K was reported to have a value of $\sim 8\%$, which was attributed to the saturation of defect spin interactions [27, 28].

There is also a possibility that the ferromagnetic signal is not intrinsic to Zn-claringbullite, but instead arises from an impurity phase. Although an impurity phase was not observed in the D2B diffraction data, previous syntheses of claringbullite and Zn-claringbullite have reported that possible impurities include polymorphs of clinoatacamite [15] or herbertsmithite [9]. Clinoatacamite is well-known to order at $T \approx 6$ K [29] and Figure 5.11b shows that for $T \leq 6$ K the saturated ferromagnetic component f has an increasing value. The percentage of a clinoata-

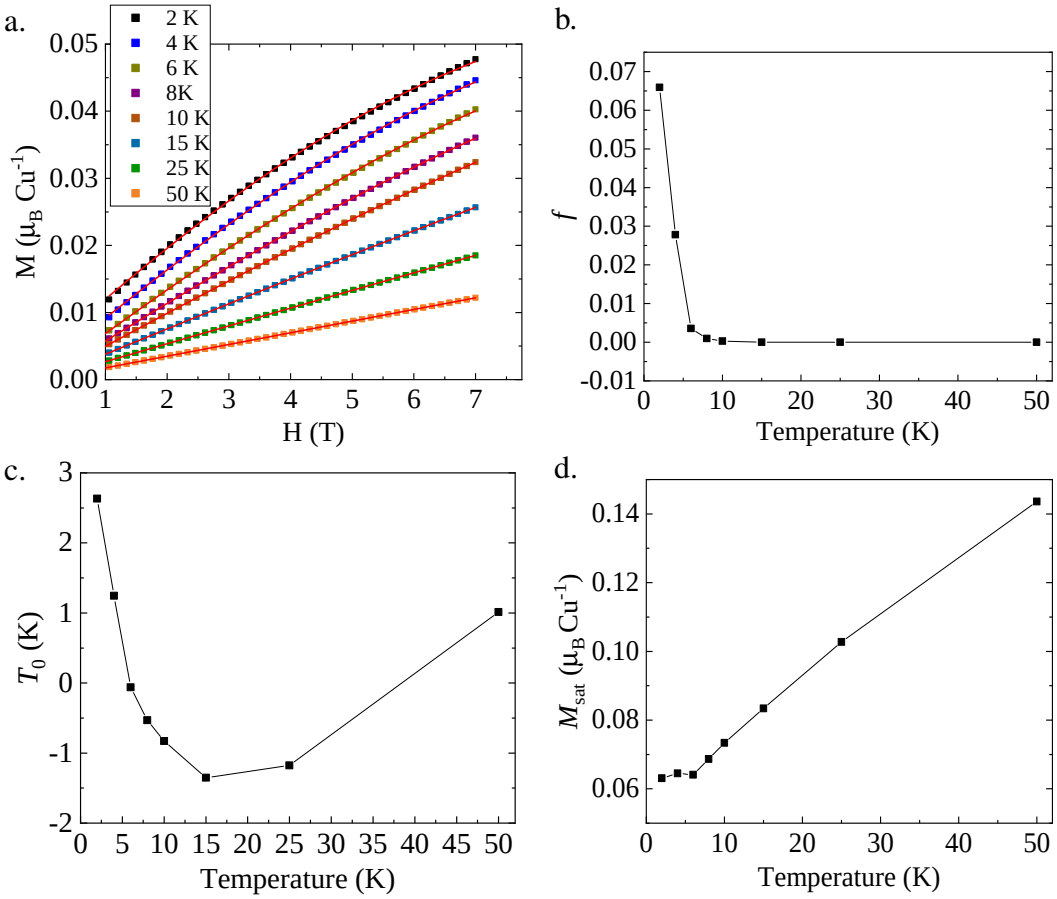

Figure 5.11: Zn-claringbullite. **a.** The red lines are fits to magnetisation, M, as a function of field, H, using the modified Brillouin function given by equation 5.1. **b.** Variation of f with temperature. **c.** Variation of T_0 with temperature. **d.** Variation of M_{sat} with temperature.

Temperature (K)	f	T_0 (K)	M_{sat} (μ_B Cu^{-1})
2	0.0659	2.632	0.0631
4	0.02781	1.24667	0.06449
6	0.00355	−0.06047	0.0641
8	$9.83\cdot10^{-4}$	−0.53055	0.06867
10	$3.03\cdot10^{-4}$	−0.82799	0.07339
15	$1.76\cdot10^{-5}$	−1.35156	0.08338
25	$2.39\cdot10^{-5}$	−1.17662	0.10274
50	$2.81\cdot10^{-5}$	1.0134	0.14359

Table 5.9: Zn-claringbullite. Refined parameters corresponding to equation 5.1 and plotted in Figure 5.11.

camite impurity can be estimated using the known value of its spontaneous moment at $T = 2$ K (0.05 μ_B Cu^{-1} [30]) in comparison to the one observed in Figure 5.10d. For a spontaneous moment of 2×10^{-4} μ_B Cu^{-1}, 0.4% of the sample would have

to be clinoatacamite. Such a small impurity will not affect the magnetic excitations measured using inelastic neutron scattering in Chapter 6 or the determination of exchange interactions.

5.5 Magnetic structure refinement of claringbullite - D20

To determine the magnetic structure of undoped claringbullite below the magnetic phase transition at $T_N = 17$ K observed in the magnetic susceptibility data (Section 5.4.1), neutron diffraction data were collected on the high-flux instrument D20 ($\lambda =$ 2.41 Å). This instrument was chosen as the magnetic moment is small and the flux of D2B is not high enough to observe its magnetic Bragg peaks. Measurements were made above the transition temperature at $T = 25$ K, just below T_N at $T = 15$ K and at $T = 1.7$ K. The diffraction patterns at all temperatures (Figure 5.12) have very similar intensities, making it difficult to extract the magnetic Bragg peaks without a temperature subtraction. At $T = 15$ K magnetic Bragg peaks appear that become more intense at $T = 1.7$ K, but no additional peaks are observed at base temperature (Appendix B). The magnetic peaks are clear in the temperature subtraction of the $T = 1.7$ and 25 K data (see Figure 5.14).

In the subtracted data there are 14 magnetic Bragg peaks which can be indexed with the $\mathbf{k} = (0,0,0)$ propagation vector. Representation analysis using the program SARAh, enabled the symmetry allowed irreducible representations (irreps) for the *Pnma* crystal structure to be determined [31]. There are 3 Cu sites in the unit cell: Cu1 and Cu2 make up the kagome plane at $(0,\ 0,\ 0)$ and $(0.24665,\ 0.49629,\ 0.24920)$, respectively, and Cu3 occupies the interlayer site at $(0.19083,\ 1/4,\ 0.05052)$. The decomposition of the magnetic representation over irreps of $G_{\mathbf{k}}$ is given in Kovalev's notation [32] for these sites as:

$$\text{Cu1} : \Gamma_{Mag} = 3\Gamma_1^1 \oplus 0\Gamma_2^1 \oplus 3\Gamma_3^1 \oplus 0\Gamma_4^1 \oplus 3\Gamma_5^1 \oplus 0\Gamma_6^1 \oplus 3\Gamma_7^1 \oplus 0\Gamma_8^1, \quad (5.3)$$

$$\text{Cu2} : \Gamma_{Mag} = 3\Gamma_1^1 \oplus 3\Gamma_2^1 \oplus 3\Gamma_3^1 \oplus 3\Gamma_4^1 \oplus 3\Gamma_5^1 \oplus 3\Gamma_6^1 \oplus 3\Gamma_7^1 \oplus 3\Gamma_8^1, \quad (5.4)$$

$$\text{Cu3} : \Gamma_{Mag} = 1\Gamma_1^1 \oplus 2\Gamma_2^1 \oplus 2\Gamma_3^1 \oplus 1\Gamma_4^1 \oplus 1\Gamma_5^1 \oplus 2\Gamma_6^1 \oplus 2\Gamma_7^1 \oplus 1\Gamma_8^1. \quad (5.5)$$

The simplest scenario was initially considered, where the second-order magnetic transition involves only one irrep and so the irreps that are common to all 3 Cu sites are Γ_1, Γ_3, Γ_5 and Γ_7. Refinements in each of these irreps showed only Γ_7 (magnetic space group $Pn'm'a$) to give a good fit to the data. The basis vectors in Γ_7 for each Cu site are given in Appendix B. In Γ_7, Cu1 and Cu2 each have 3 basis vectors, ψ_i for $i = 1,2,3$, where ψ_1 and ψ_2 result in a collinear antiferromagnetic structure along the a and b crystallographic directions and ψ_3 is a ferromagnetic component along the c direction. Cu3 has 2 basis vectors in Γ_7, corresponding to an antiferromagnetic alignment of spins along the a direction and a ferromagnetic component in the c direction. Allowing all mixing coefficients, C_i, for the basis vectors in Γ_7 to refine, results in the fit shown in Figure 5.14a (χ^2 =5.15). The magnetic structure is almost collinear in the a direction with a small canting in both the b and c directions.

Since the structure was close to collinear, a refinement with a collinear structure along a was attempted to suppress the presence of canting and the refinement is shown in Figure 5.14b. This structure does not predict the correct peak intensity at ~ 1.3 Å^{-1}, so the out-of-plane rotation of the Cu2 spins and/or the ferromagnetic canting of the Cu3 spins are important in describing the magnetic structure.

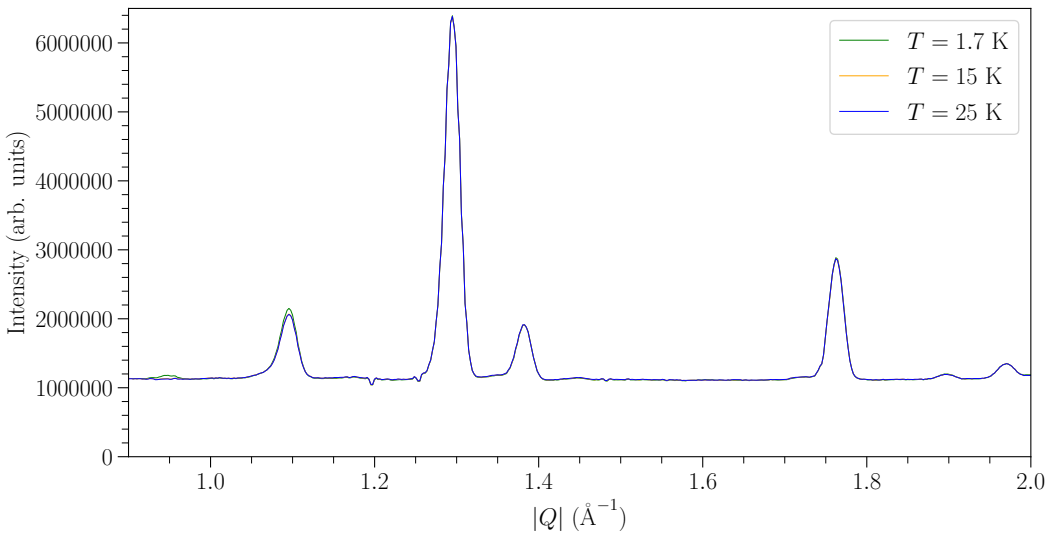

Figure 5.12: Claringbullite D20 diffraction patterns ($\lambda = 2.41$ Å) collected at $T = 1.7$, 15 and 25 K. Their intensities are very similar making it difficult to observe the magnetic Bragg peaks without a temperature subtraction.

Several trials were made to minimise the number of basis vectors required to describe the diffraction data and it was found that a similar result to Figure 5.14a can be achieved with an almost collinear structure along the *a* direction, allowing for antiferromagnetic canting of Cu2 along the *b* direction and ferromagnetic canting of Cu3 along the *c* direction. This refinement is shown in Figure 5.14c with $\chi^2 = 5.21$, which is similar to allowing all basis vectors in Γ_7 to freely refine. The resulting magnetic structure is shown in Figure 5.13 with the magnetic moments of Cu1, Cu2 and Cu3 equal to 0.266, 0.373 and 0.514 μ_B, respectively. The refined mixing coefficients, C_i, for each scenario (all freely refined, collinear structure and minimum number of required basis vectors) are shown in Table 5.10.

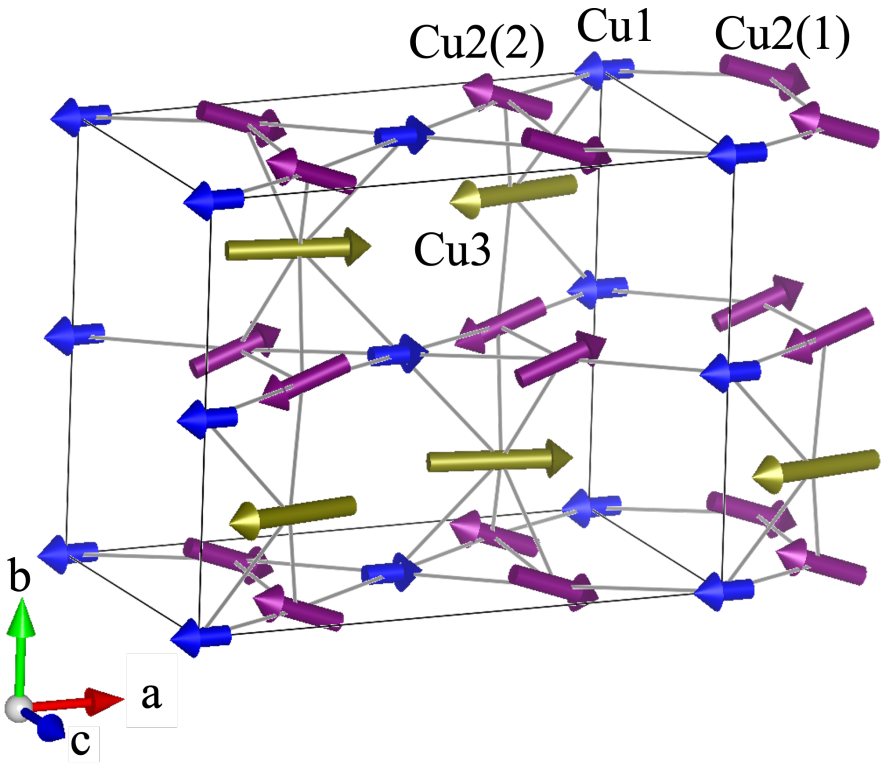

Figure 5.13: Claringbullite magnetic structure refined using temperature subtracted data ($T = 1.7 - 25$ K) collected on the D20 diffractometer ($\lambda = 2.41$ Å). In Γ_7 there are 3 Cu sites: Cu1 (blue); Cu2 (purple), distinguished between Cu2(1) and Cu2(2) due to their different superexchange paths; and Cu3 (yellow). Cu1, Cu2 and Cu3 have ordered magnetic moments of 0.266(8), 0.373(34) and 0.514(91) μ_B, respectively.

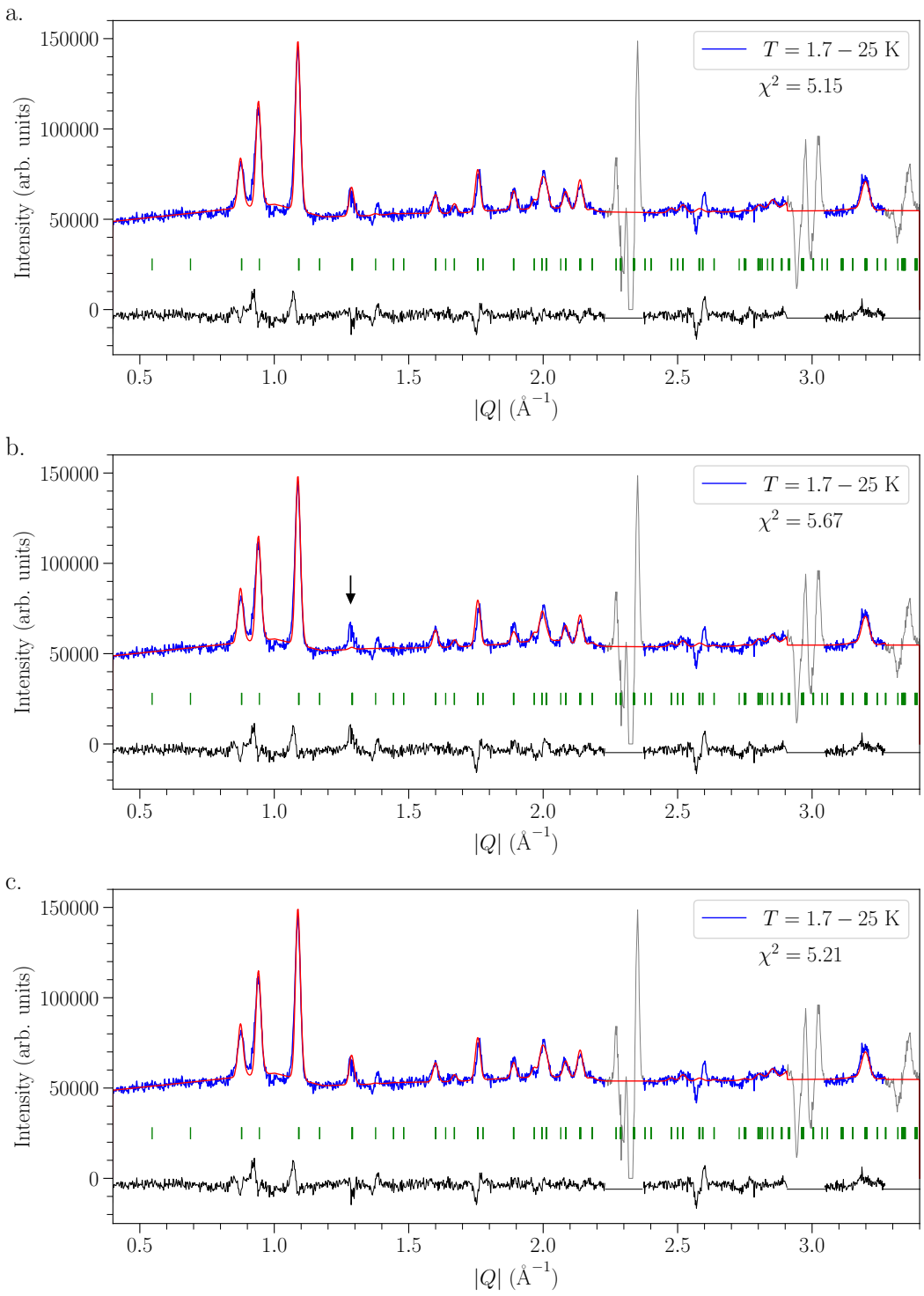

Figure 5.14: Claringbullite, D20 data (blue). Magnetic structure refinements (red) with peak positions shown in green and the difference plot in grey. **a.** All mixing coefficients, C_i, allowed to freely refine. **b.** Collinear structure along the a direction. The arrow shows where model peak intensity is lost. **c.** Refinement with the minimum number of C_i required, as described in the text.

Atom	b-v	C_i		
		All C_i refined	Collinear structure along a	Minimum number of C_i required
Cu1	ψ_1	0.211(10)	0.264(9)	0.266(8)
	ψ_2	–0.0489(1)	0	0
	ψ_3	–0.051(23)	0	0
Cu2	ψ_1	0.360(6)	0.367(3)	0.353(4)
	ψ_2	0.123(9)	0	0.120(11)
	ψ_3	0.003(39)	0	0
Cu3	ψ_1	0.571(10)	0.495(7)	0.491(7)
	ψ_2	0.095(25)	0	0.153(27)

Table 5.10: The refined mixing coefficients, C_i, for each basis vector in Γ_7 of the three Cu sites (Cu1, Cu2 and Cu3) corresponding to the refinements shown in Figure 5.14. These coefficients are for the basis vectors in Appendix B, Tables B.1-B.3.

5.6 Discussion

The crystallographic investigation of both $x = 0$ and 1 claringbullite samples indicated that doping with Zn suppresses the crystallographic phase transition from hexagonal to orthorhombic symmetry, and the high-symmetry kagome lattice is retained down to $T = 1.5\,\mathrm{K}$. Importantly, the bulk magnetometry measurements in this work are in agreement with the literature [7], showing claringbullite to have long-range magnetic order below $T_\mathrm{N} = 17\,\mathrm{K}$ and Zn-claringbullite to have no magnetic transition down to $T = 2\,\mathrm{K}$. Therefore, the Zn-claringbullite sample was a suitable candidate to study exotic QSL physics using inelastic neutron scattering measurements which will be described in Chapter 6.

The claringbullite magnetic structure refined in this thesis is similar to that of the previously reported barlowite and crucially it is similar to the recently published

Cu site	Moment size (μ_B)	
	This work	[15]
Cu1	0.266(8)	0.33
Cu2	0.373(34)	0.44
Cu3	0.514(91)	0.73

Table 5.11: Claringbullite moment sizes resulting from the magnetic structure refinements in this work, compared to the literature reported values [15].

magnetic structure of claringbullite based on a different powder sample, as well as the iodide analogue [1, 15]. For the previously reported claringbullite sample, it was found that at $T = 1.5$ K there is a mixture of a *Pnma* phase ($\sim 70\%$) and a $P6_3/mmc$ phase ($\sim 30\%$) [15], for which we don't find evidence in our samples. Nevertheless, comparing the two *Pnma* phases shows similar crystal structures with a primitive unit cell volume of ~ 704 Å^3 reported in the literature [15], close to the value of ~ 706 Å^3 for our sample. Despite the structural similarities, the magnetic structure refined in the literature [15] has slightly larger magnetic moments than our claringbullite sample and a comparison is shown in Table 5.11. Importantly, there is agreement in the relative moment sizes being Cu1<Cu2<Cu3. As barlowite and claringbullite are hydroxide materials that are structurally similar to clinoatacamite, with the main difference being the stacking of the kagome layers, it is interesting to note the similarities in their magnetic structures: clinoatacamite also has 3 distinct Cu sites and a collinear structure [29].

5.7 Future work

As detailed in Chapter 3, the Cu/Zn antisite disorder in herbertsmithite has led to an ongoing debate about whether its excitations are gapped and therefore the nature of its quantum spin liquid ground state [33]. For this reason it is important to quantify the extent of Cu/Zn antisite disorder in the quantum spin liquid candidate Zn-claringbullite, as it could affect the interpretation of its magnetic excitations. The powder neutron diffraction data presented in this chapter did not suggest the presence of Cu/Zn site disorder, though it is challenging to refine accurate values for the site substitution with powder neutron data. A more powerful method for determining chemical disorder is anomalous x-ray diffraction, which uses element-specific absorption edges to tune the x-ray wavelength and the results indicate the site positions and abundances of the elements.

5.8 Conclusions

This chapter presented the syntheses, structural characterisations and bulk magnetometry measurements of claringbullite, $Cu_4(OD)_6FCl$, and Zn-claringbullite,

$ZnCu_3(OD)_6FCl$. The diffraction measurements showed claringbullite to undergo a crystallographic phase transition in agreement with the literature [4]. In contrast, it was found that Zn-claringbullite retains its hexagonal $P6_3/mmc$ symmetry down to $T = 1.5$ K. The bulk magnetometry measurements indicated claringbullite undergoes a magnetic phase transition at $T_N = 17$ K, similar to that reported in [4], with an antiferromagnetic component below $T = 9$ K. On the other hand, Zn-claringbullite shows no transition to long-range magnetic order in agreement with the literature [7], but contrary to the previous report we find very weak ferromagnetism in the sample. This is either intrinsic to our Zn-claringbullite sample or arises from an impurity phase. An analysis of the saturated ferromagnetic component arising from an impurity (orphan spins or phase impurity) showed it to order below $T \approx 6$ K, which may be attributed to a 0.4% clinoatacamite impurity phase in the sample. This is too small to be observed in the D2B diffraction data and will not affect the magnetic excitations presented in the Chapter 6, as the structure factor is linearly dependent on the phase fractions in the sample. Diffraction measurements on claringbullite were also used to determine its magnetic structure, that was found to be remarkably similar to barlowite and its iodide variant, and in good agreement with the recently reported magnetic structure of powder claringbullite samples [15, 34].

Bibliography

[1] K. Tustain, B. Ward-O'Brien, F. Bert, T.-H. Han, H. Luetkens, T. Lancaster, B. M. Huddart, P. J. Baker, and L. Clark, npj Quantum Mater. **5**, 74 (2020).

[2] Y. Wei, Z. Feng, W. Lohstroh, D. H. Yu, D. Le, C. d. Cruz, W. Yi, Z. F. Ding, J. Zhang, C. Tan, L. Shu, Y.-C. Wang, H.-Q. Wu, J. Luo, J.-W. Mei, F. Yang, X.-L. Sheng, W. Li, Y. Qi, Z. Y. Meng, Y. Shi, and S. Li, arXiv:1710.02991v3 (2020).

[3] Z. Feng, Z. Li, X. Meng, W. Yi, Y. Wei, J. Zhang, Y.-C. Wang, W. Jiang, Z. Liu, S. Li, F. Liu, J. Luo, S. Li, G.-q. Zheng, Z. Y. Meng, J.-W. Mei, and Y. Shi, Chin. Phys. Lett. **34**, 077502 (2017).

[4] A. Henderson, L. Dong, S. Biswas, H. I. Revell, Y. Xin, R. Valenti, J. A. Schlueter, and T. Siegrist, Chem. Commun. **55**, 11587 (2019).

[5] X. Y. Yue, Z. W. Ouyang, J. F. Wang, Z. X. Wang, Z. C. Xia, and Z. Z. He, Phys. Rev. B **97**, 054417 (2018).

[6] R. W. Smaha, W. He, J. P. Sheckelton, J. Wen, and Y. S. Lee, J. Solid State Chem. **268**, 123 (2018).

[7] Z. Feng, W. Yi, K. Zhu, Y. Wei, S. Miao, J. Ma, J. Luo, S. Li, Z. Y. Meng, and Y. Shi, Chin. Phys. Lett. **36**, 017502 (2018).

[8] T.-H. Han, J. Singleton, and J. A. Schlueter, Phys. Rev. Lett. **113**, 227203 (2014).

[9] Z. Feng, W. Yi, K. Zhu, J. Ma, J. Luo, S. Li, Z. Y. Meng, and Y. Shi, arXiv:1806.00803v1 (2018).

[10] Z. Liu, X. Zou, J. W. Mei, and F. Liu, Phys. Rev. B **92**, 220102 (2015).

[11] V. F. Sears, Neutron News **3**, 26 (1992).

[12] E. E. Fejer, A. M. Clark, A. G. Couper, and C. J. Elliott, Mineral. Mag. **41**, 433 (1977).

[13] P. C. Burns, M. A. Cooper, and Hawthorne F. C., Canad. Mineral. **33**, 633 (1995).

[14] E. A. Nytko, "Synthesis, structure, and magnetic properties of spin-1/2 kagomé antiferromagnets", Ph.D. thesis (Massachusetts Institute of Technology, 2008).

[15] K. Tustain, E. E. McCabe, A. M. Arevalo-Lopez, A. S. Gibbs, S. P. Thompson, C. A. Murray, C. Ritter, and L. Clark, Chem. Mater. **33**, 9638 (2021).

[16] J. Echeverría, E. Cremades, A. J. Amoroso, and S. Alvarez, Chem. Commun., 4242 (2009).

[17] A. Coelho, *Topas Academic Version 4.1.* 2007.

[18] R. H. Colman, A. Sinclair, and A. S. Wills, Chem. Mater. **22**, 5774 (2010).

[19] P. Mendels and F. Bert, J. Phys. Soc. Jpn. **79**, 011001 (2010).

[20] L. F. Jones, C. A. Kilner, and M. A. Halcrow, Polyhedron **26**, 1977 (2007).

[21] B. Sarkar, M. S. Ray, Y. Z. Li, Y. Song, A. Figuerola, E. Ruiz, J. Cirera, J. Cano, and A. Ghosh, Chem. Eur. J. **13**, 9297 (2007).

[22] Y. Okamoto, H. Yoshida, and Z. Hiroi, J. Phys. Soc. Jpn. **78**, 33701 (2009).

[23] G. A. Bain and J. F. Berry, J. Chem. Educ. **85**, 532 (2008).

[24] R. H. Colman, F. Bert, D. Boldrin, A. D. Hillier, P. Manuel, P. Mendels, and A. S. Wills, Phys. Rev. B **83**, 180416 (2011).

[25] E. Connolly, "Structure and magnetic properties of model S = 1/2 and S = 1 kagome magnets", Ph.D. thesis (University College London, 2019), pp. 175–178.

[26] S. K. Douglas, S. Nakashima, and J. F. Scott, Phys. Rev. B **29**, 5602 (1984).

[27] F. Bert, S. Nakamae, F. Ladieu, D. L'Hôte, P. Bonville, F. Duc, J. C. Trombe, and P. Mendels, Phys. Rev. B **76**, 132411 (2007).

[28] F. Bert, A. Olariu, A. Zorko, P. Mendels, J. C. Trombe, F. Duc, M. A. de Vries, A. Harrison, A. D. Hillier, J. Lord, A. Amato, and C. Baines, J. Phys.: Conf. Ser. **145**, 012004 (2009).

[29] A. S. Wills and J.-Y. Henry, J. Phys. Condens. Matter **20**, 472206 (2008).

[30] X. G. Zheng, T. Kawae, Y. Kashitani, C. S. Li, N. Tateiwa, K. Takeda, H. Yamada, C. N. Xu, and Y. Ren, Phys. Rev. B **71**, 052409 (2005).

[31] A. S. Wills, Phys. B **278**, 680 (2000).

[32] O. V. Kovalev, *Representations of the Crystallographic Space Groups: Irreducible Representations, Induced Representations and Corepresentations*, edited by H. T. Stokes and D. M. Hatch, 2nd ed. (Gordon and Breach, London, 1993).

[33] A. Olariu, P. Mendels, F. Bert, F. Duc, J. C. Trombe, M. A. De Vries, and A. Harrison, Phys. Rev. Lett. **100**, 087202 (2008).

[34] K. Tustain, G. J. Nilsen, C. Ritter, I. Da Silva, and L. Clark, Phys. Rev. Mater. **2**, 111405 (2018).

Chapter 6

Magnetic excitations in the claringbullite series, $Zn_xCu_{4-x}(OD)_6FCl$ for $x = 0$ and 1

6.1 Introduction

Chapter 5 discussed the crystal structures and bulk magnetometry data for the $x = 0$ and $x = 1$ samples of the claringbullite series, $Zn_xCu_{4-x}(OD)_6FCl$, as well as the magnetic structure refinement of the $x = 0$ material. Claringbullite itself undergoes a crystallographic phase transition from $P6_3/mmc$ to $Pnma$ at low temperature, whilst $x = 1$ Zn-claringbullite retains its $P6_3/mmc$ symmetry down to $T = 1.5$ K. The magnetic susceptibility showed our claringbullite sample to have a magnetic transition at $T = 17$ K, whereas Zn-claringbullite ($x = 1$ sample) showed no signature of a transition to long-range order down to $T = 2$ K. This chapter will present inelastic neutron scattering (INS) measurements on claringbullite and the $x = 1$ Zn-doped sample, herein also referred to as Zn-claringbullite, using the same samples discussed in the previous chapter.

INS was used to measure the spin wave spectrum of claringbullite below the transition temperature, with the goal of determining the energy scales and the exchange interactions that govern the system. Since the crystal structures of the $x = 0$ and $x = 1$ samples have similar bonding geometries, the exchange interactions in

both samples were initially expected to be similar. Naively, it was hoped that determining the exchange interactions in claringbullite would allow those of Zn-claringbullite to be estimated. As will be detailed in this chapter, we found claringbullite to have a 3-dimensional magnetic system quite far from the 2-dimensional kagome of Zn-claringbullite, making it difficult to map the exchanges from one system to the other. Therefore, an attempt was made to estimate the exchange interactions for the two materials independently. Linear spin wave theory was used to analyse the INS data of claringbullite and led us to propose an exchange interaction model that captures the main features of the observed spin waves. For Zn-claringbullite, an analysis of the spin correlations in Q and E was used to determine the nature of the exchange interactions. The INS results and analyses are discussed for each sample separately and followed by a comparison of the two systems.

6.2 Inelastic neutron scattering on claringbullite

The energy range of the magnetic excitations of claringbullite were determined by an INS experiment on MERLIN, ISIS. Experiments on PANTHER and IN5 at the ILL, were then carried out to study the magnetic excitations in detail with targeted incoming energies, lower temperatures and longer counting times. Measurement conditions used on PANTHER and IN5 are listed in Table 6.1 for reference throughout this section.

6.2.1 Initial measurements - MERLIN

To get an overview of the excitation energies of claringbullite, a 5.17 g deuterated powder sample was measured on MERLIN, ISIS. Figure 6.1 shows data collected above and below $T_N = 17$ K at $T = 7$ and 55 K, with incident neutron energies $E_i = 17$ and 41 meV. With $E_i = 41$ meV the elastic line extends up to $\sim$4 meV and for $Q > 3$ Å intense phonons are seen to dominate $S(Q,E)$. At $T = 7$ K, there is an intense band centred at 11 meV and spin wave branches coming down at $Q = 1.2$ and 2.4 Å^{-1} that are gapped, a feature more easily seen in the PANTHER data (Section 6.2.2). At $T = 55$ K, the 11 meV branch remains and is most likely phonon scattering (Section 6.2.4 gives a more detailed analysis of its origin). At

high temperature, the spin waves become more diffuse and the gap closes. In the $E_i = 17$ meV data at $T = 7$ K, there is evidence of an additional magnetic signal below 3 meV that is much more intense than the $Q = 1.2$ Å^{-1} spin wave branch. Due to its low intensity, the high-energy excitation cannot be seen in Figures 6.1c and d. When temperature increases to $T = 55$ K, the low-energy magnetic scattering collapses. Although with $E_i = 17$ meV both magnetic responses could in principle be measured, longer counting times would be required as the magnetic scattering of the higher energy excitation is much weaker.

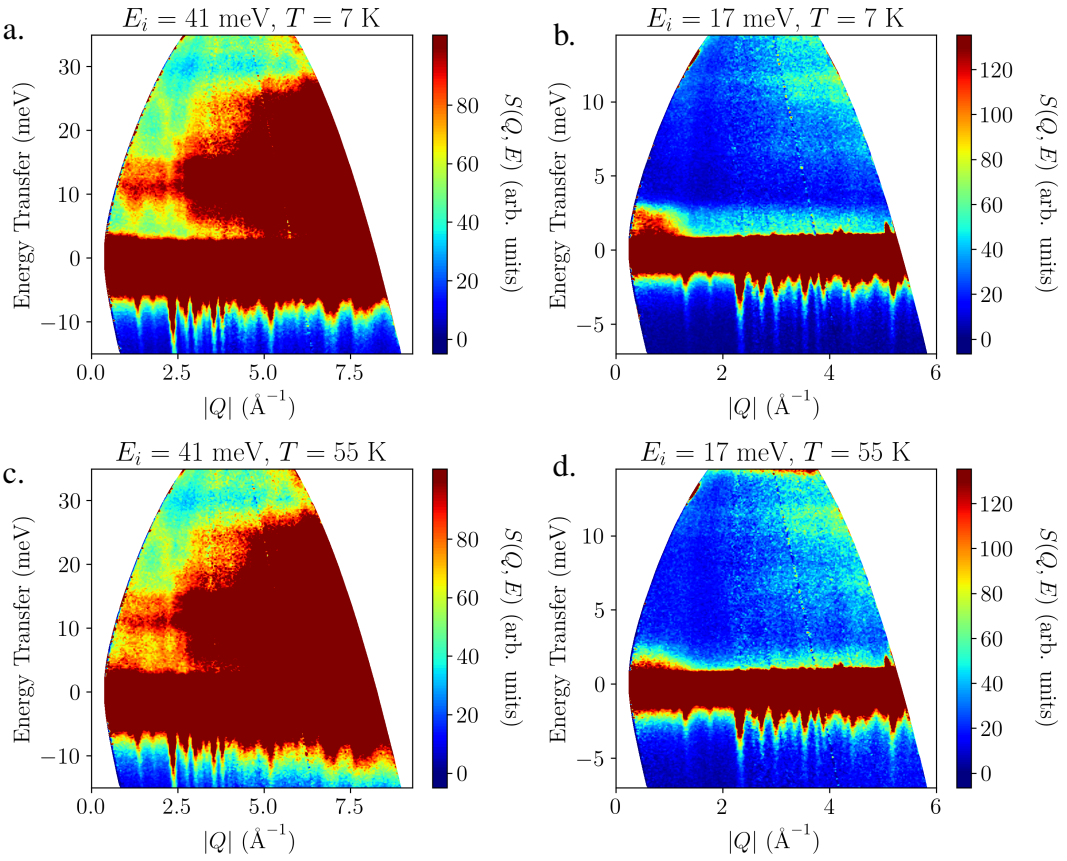

Figure 6.1: Claringbullite, $S(Q,E)$ measured on MERLIN. **Top.** $T = 7$ K and **bottom.** $T = 55$ K with **left.** $E_i = 41$ meV and **right.** $E_i = 17$ meV. At $T = 7$ K, there are two magnetic excitation responses: a band at 11 meV with gapped spin wave branches at $Q = 1.2$ and 2.4 Å^{-1}; and below 3 meV.

6.2.2 High-energy excitations on PANTHER

To investigate the high-energy excitation extending up to ~ 10 meV, measurements were made on the thermal-neutron time-of-flight spectrometer PANTHER. A 4.94 g sample was loaded into an annular aluminium cylinder with outer diameter 15 mm and inner diameter 12 mm, attached to a sample stick and inserted into a standard orange cryostat. A summary of the conditions for the data collected is given in Table 6.1.

T (K) \ E_i (meV)	3.55	5.11	10.43	19.2	35
1.6-1.8	IN5	IN5	IN5	PANTHER	PANTHER
25	IN5	IN5	IN5	PANTHER	PANTHER
100	-	-	-	PANTHER	PANTHER

Table 6.1: Summary of the measurement conditions used on IN5 and PANTHER for claringbullite.

The data reduction was done as described in Chapter 4. Empty can measurements were made for all incident energies at $T = 1.8$ K and subtracted from the sample data. Plots of the reduced $S(Q,E)$ data collected with an incident neutron energy of 35 and 19.2 meV at $T = 1.6,\ 25$ and 100 K are shown in Figure 6.2. The $E_i = 35$ meV data allows for a comparison with the $E_i = 41.10$ meV MERLIN data (Figures 6.1a and b). At $T = 1.8$ K, $S(Q,E)$ is again dominated by strong phonons for $Q > 3$ Å^{-1} and there is no low-Q scattering above ~ 17 meV (Figure 6.2a). Flat bands are seen at 11 and 14 meV, and their origin will be discussed in Section 6.2.4. As seen in the MERLIN data, there is an excitation at $Q \sim 1.2$ Å^{-1} that is gapped, which at $T = 25$ K (Figure 6.2c) becomes gapless. These features become clearer in the $E_i = 19.2$ meV data (discussed in the next paragraph). In Figure 6.2d at $T = 100$ K the $Q \sim 1.2$ Å^{-1} excitation has become completely diffuse. At this temperature there is intense scattering extending from the elastic line at low-Q, which represents neither magnetic nor phonon scattering. In neutron scattering experiments, this type of scattering can sometimes occur from the recoil of gaseous molecules. Attempts to explain this scattering with gases that may have been present during the experiment such as ^{4}He or air (N_2), were unsuccessful. The

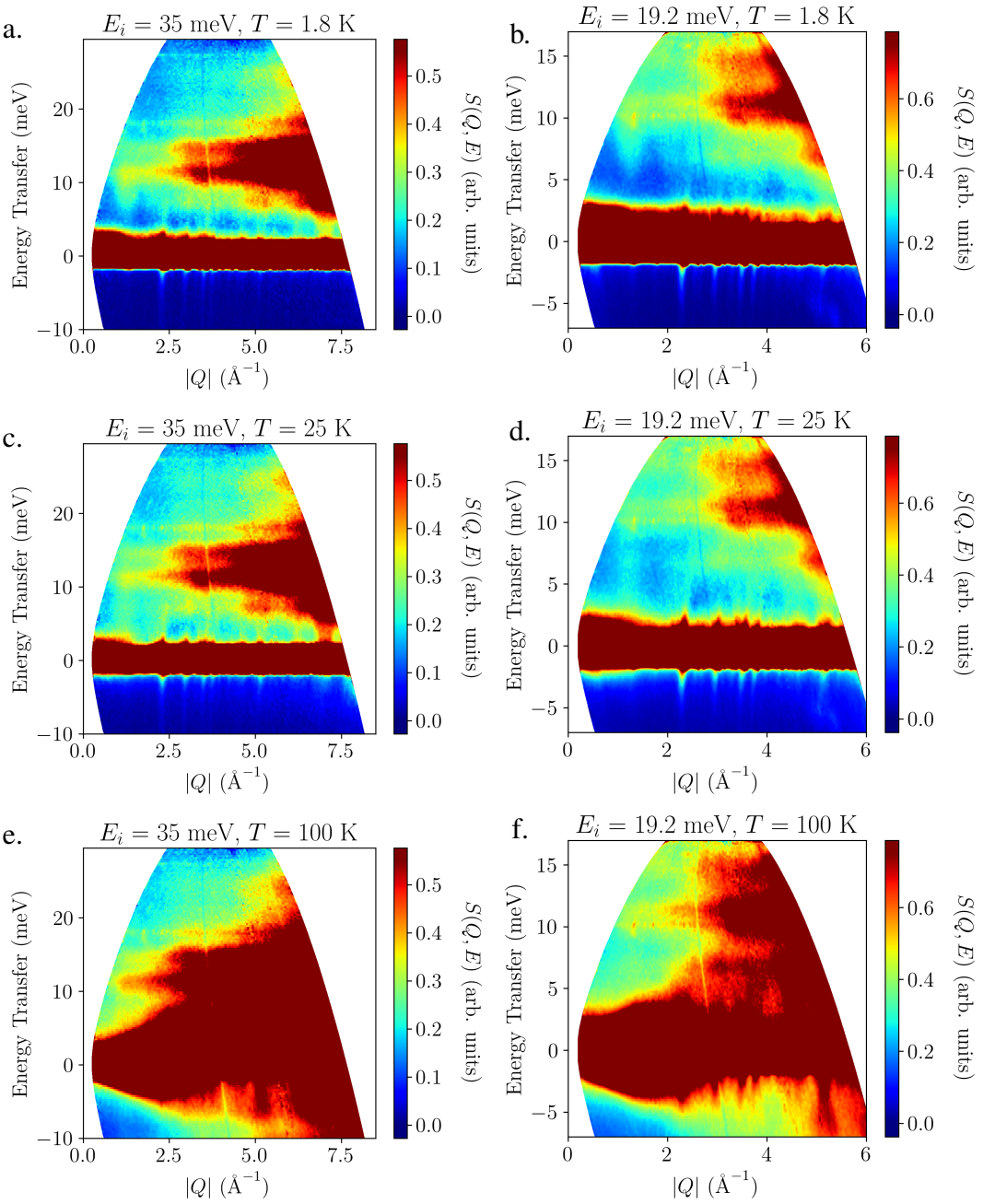

Figure 6.2: Claringbullite, $S(Q,E)$ from PANTHER measured with $E_i = 19.2$ meV (**left.**) and $E_i = 35$ meV (**right.**) at $T = 1.8$ K (**a.-b.**), $T = 25$ K (**c.-d.**) and $T = 100$ K (**e.-f.**).

observed scattering is most intense at low energy transfers and is not present in the high-energy high-Q region where phonons dominate, unlike true recoil gas scattering. It was concluded that this scattering arises from the sample, but its origin is unclear as it cannot be immediately attributed to magnetic or phonon excitations. This scattering caused issues in temperature subtractions, particularly with the $T = 25$ K

data where it interferes with the gapless column of scattering at $Q \sim 1.2$ Å^{-1}.

The $E_i = 35$ meV data indicated that there is no magnetic scattering above 17 meV, so the $E_i = 19.2$ meV data is more appropriate to analyse the high-energy magnetic excitation. At $T = 1.8$ K (Figure 6.2b) the elastic line extends from 0 to ~ 3 meV (dark red region). Acoustic phonons are seen at *e.g.* ~ 2.2 Å^{-1} and optical phonons appear as bands at *e.g.* 6 and 12 meV that have Q^2 dependent intensity. The spin wave centred at $Q = 1.25$ Å^{-1} is clearly gapped below 5 meV giving a bandwidth of 8.3 meV. Its centre is closest to the (−1, 1, 1) Bragg peak at 1.17 Å^{-1}, in agreement with the $\mathbf{k} = \mathbf{0}$ propagation vector observed in the neutron diffraction data on D20 (Section 5.5). Again, there is evidence of magnetic scattering at low Q in the tail of the elastic scattering, which can also be seen in the MERLIN data with $E_i = 17.08$ meV (Figure 6.1c).

At $T = 25$ K the magnetic inelastic scattering becomes more diffuse in Q and the energy gap closes, indicating the presence of strong short-range correlations. At $T = 100$ K no magnetic excitations are seen in $S(Q,E)$ (Figure 6.2f), showing that these correlations vanish. This behaviour is in agreement with the DC susceptibility measurements, which show an onset of magnetic correlations below $T = 150$ K (Section 5.4.1). Since the high-energy excitation persists up to $T = 25$ K, a temperature subtraction with the $T = 100$ K data is more appropriate, but care must be taken with an over-subtraction in the phonon region. $\chi''(Q,E)$ at $T = 100$ K (Fig-

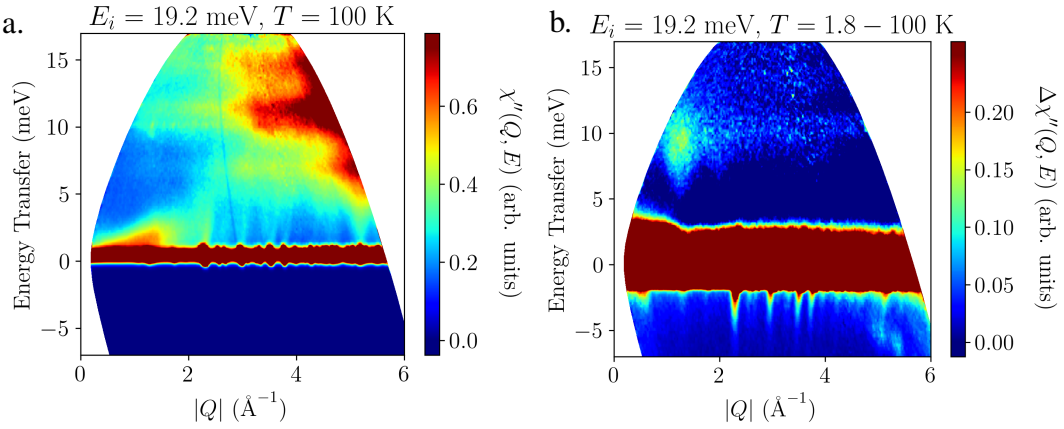

Figure 6.3: Claringbullite, PANTHER data. **a.** $\chi''(Q,E)$ at $T = 100$ K. **b.** Temperature subtraction $\Delta\chi''(Q,E,T = 1.8–100$ K).

ure 6.3a), obtained by dividing $S(Q,E)$ by the Bose population factor (see equation 4.19), was subtracted from $\chi''(Q,E)$ at $T = 1.8\ K$, that is almost equal to $S(Q,E)$ at this temperature (Figure 6.2b), to give Figure 6.3b. As discussed earlier for Figure 6.2e, at $T = 100$ K there is scattering extending up in energy transfer from the elastic line that cannot be assigned to magnetic or phonon scattering. This scattering causes a slight over-subtraction near the elastic line in the temperature subtraction (Figure 6.3b), but it does not affect the gapped high-energy excitation. Figure 6.3b reveals a magnetic excitation centred at ~ 1.2 Å^{-1} and a weak band at 10 meV. The origin of the latter will be discussed in Section 6.2.4.

The data collected on PANTHER and MERLIN for the claringbullite sample at $T = 1.8$ K, show a gapped spin wave excitation near $Q = 1.25$ Å^{-1} that becomes gapless and diffuse above T_N. Additional magnetic scattering at low Q in the tail of the elastic scattering was also observed, but could not be resolved in these data. To carry out a similar investigation of the behaviour of this lower energy magnetic scattering, data were collected on the IN5 spectrometer as detailed in the next section.

6.2.3 Low-energy excitations on IN5

To investigate the low-energy excitation, measurements were made on the cold-neutron time-of-flight spectrometer IN5 using the same sample and aluminium cylinder as for PANTHER. A summary of the data collected is in Table 6.1. The raw data were reduced in the same manner as those from PANTHER, except no empty can measurements were made so only a flat background was subtracted. Using $E_i = 10.43$ meV, the low-energy excitation at $T = 1.6$ K is most easily seen from a temperature subtraction in $\chi''(Q,E)$ (Figure 6.4a). It has many spurious features *e.g.* at 2 meV on the edge of the kinematic window and at 2 Å^{-1}, so the $E_i = 5.11$ and 3.55 meV data sets were combined in order to analyse the whole bandwidth of the low energy excitation (Figures 6.4c-e). $\chi''(Q,E)$ at $T = 25$ K is plotted in Figure 6.4b and it very clearly shows that the $Q = 1.2$ Å^{-1} excitation is gapless. The scattering at 2 meV extending from low-Q and also at 2 meV at $1.6 < Q < 2$ Å^{-1} is spurious scattering as it cannot be seen in Figures 6.4c-e which correspond to data

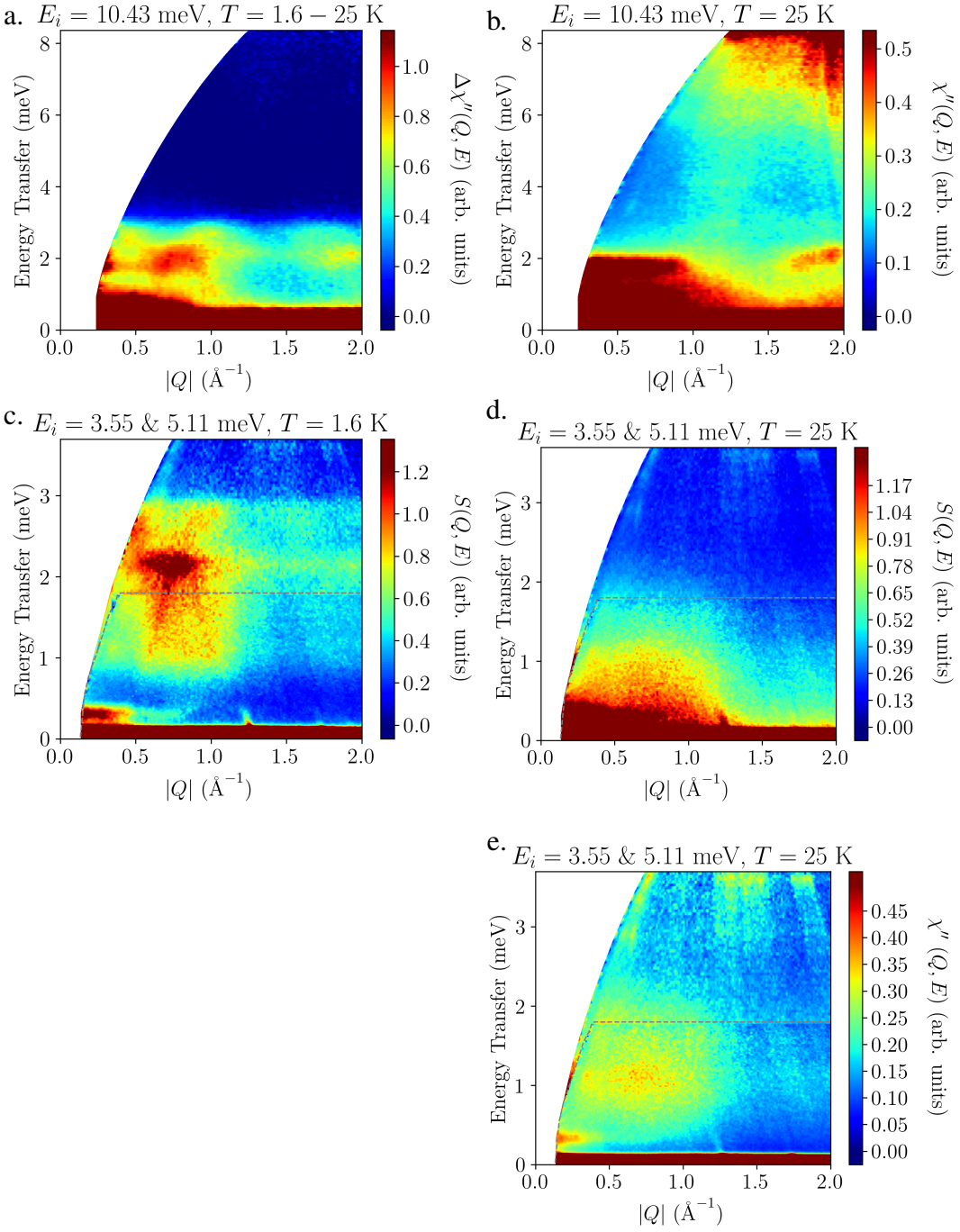

Figure 6.4: Claringbullite, IN5 data. **a.** $E_i = 10.43$ meV temperature subtraction of the dynamic susceptibility, $\Delta\chi''(Q,E)$=$\chi''(Q,E,T = 1.5$ K)$-\chi''(Q,E,T = 25$ K). **b.** $E_i =$ 10.43 meV $\chi''(Q,E)$ at $T = 25$ K. The gap between the two excitations clearly fills in. **c.** Combined E_i=3.55 and 5.11 meV $S(Q,E)$ at $T = 1.6$ K and **d.** $T = 25$ K. **e.** $\chi''(Q,E)$ at $T = 25$ K of combined E_i=3.55 and 5.11 meV data.

collected with lower incident neutron energies.

At $T = 1.6$ K, the low-energy magnetic excitation seen on MERLIN (Figure 6.1c) and hinted to in the PANTHER data (Figures 6.2a and b) is shown on IN5 to be gapped with strong features in both Q and E (Figure 6.4c). It is centred at 2.1 meV with branches extending above and below it, and two flat bands at 2.1 and 2.9 meV. The energy gap evidences anisotropy in the system, a characteristic seen in previous electron spin resonance (ESR) measurements on single crystals that were used to suggest the presence of easy-plane anisotropy [1]. In Figures 6.4c and e, the band-like intense feature at $E = 0.2$ meV and extending up to $Q \sim 1$ Å^{-1} is spurious scattering from the cryostat. Above T_N, at $T = 25$ K, the excitation collapses becoming diffuse and revealing short-range dynamic spin correlations, in agreement with the magnetic susceptibility measurements (see Chapter 5).

6.2.4 Results and analysis

The observations on IN5 and PANTHER, indicate that below the magnetic transition temperature claringbullite has two magnetic excitations, which are gapped from each other and have a zero-energy gap. For the discussion below, the data sets from all incident neutron energies on IN5 and PANTHER were combined.

The Q-dependence of the spectra was used to differentiate the magnetic excitations from the phonons. Figure 6.5a shows $S_Q(E) = \int_{Q-\delta Q}^{Q+\delta Q} S(Q,E)dQ$, integrated over $1.1 < Q < 1.3$ Å^{-1} and $1.6 < Q < 1.8$ Å^{-1} at $T = 1.8$ K, where the magnetic excitations are expected to be strongest. The additional intensity at $Q = 1.2$ Å^{-1} compared to $Q = 1.7$ Å^{-1} below 10 meV indicates magnetic scattering. Between 11 meV and 13 meV a band was seen in the $S(Q,E)$ spectra (Figure 6.2), but the $S_Q(E)$ intensity is nearly Q-independent. Further clarity can be gained by looking at the behaviour of this peak with temperature. $S_Q(E)$ integrated over $1.1 < Q < 1.4$ Å^{-1} at all temperatures are compared in Figure 6.5b. At $T = 1.8$ K there are two magnetic responses. The low-energy excitation has a 0.45 meV gap from zero-energy, peaks at 2.3 meV and extends up to 3.22 meV giving a bandwidth of 2.77 meV. It is separated from the high-energy excitation by a 1.78 meV gap, which appears to have non-zero intensity due to a background from multi-

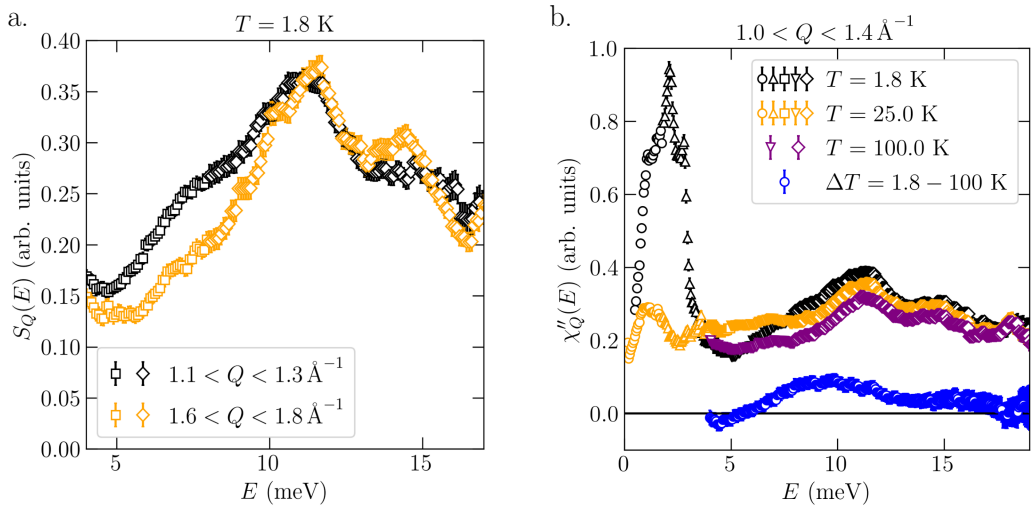

Figure 6.5: Claringbullite, PANTHER and IN5 combined data of $E_i = 3.55$, 5.11, 10.43, 19.2 and 35 meV. **a.** $T = 1.8$ K $S_Q(E)$ integrated over $1.1 < Q < 1.3$ Å^{-1} (black) and $1.6 < Q < 1.8$ Å^{-1} (orange). **b.** $\chi''_Q(E)$ integrated over $1.0 < Q < 1.4$ Å^{-1} at $T = 1.8$ (black), 25 (orange), 100 (purple) and 1.8–100 K (blue).

ple scattering events or incoherent scattering that can be explained by the $\sim 4\%$ H content found in the Rietveld refinements (Chapter 5). The high-energy excitation extends from 5 to 13.3 meV resulting in a bandwidth of 8.3 meV.

At $T = 25$ K, $\chi''_Q(E)$ shows the low-energy response becomes completely diffuse, whilst conserving the total area of the magnetic response. As seen in the $S(Q,E)$ spectra (Figure 6.2), above T_N the gap between the low- and high-energy excitations closes, and a vertical column of scattering remains. At $T = 100$ K, the intensity of $\chi''_Q(E)$ decreases further as the excitation becomes even more diffuse with increasing temperature. The shape of the peak at 11 meV stays constant with temperature indicating it is a phonon band, but its intensity decreases with increasing temperature, evidencing a broad magnetic response below the phonon peak. This behaviour is most easily visualised with a temperature subtraction (Figure 6.3). A temperature difference of $\chi''_Q(E)$ between the $T = 1.8$ and 100 K data is also plotted in Figure 6.5b. A slight over-subtraction is seen, due to the scattering arising from low-Q discussed earlier (see Figure 6.3a), but it clearly shows the high-energy broad magnetic response from 5 meV to 13.3 meV. Higher energy excitation bands were assigned to optical phonons: Figure 6.5a shows a peak appearing at

$\sim$14 meV with increasing Q, and Figure 6.5b shows that above 15 meV $\chi''(Q,E)$ remains similar with temperature.

Figure 6.6 shows $\chi''_E(Q) = \int_{E-\delta E}^{E+\delta E} \chi''(Q,E)dE$, integrated over different E ranges: in the gap at $4.0 < E < 5.0$ meV, through the spin wave excitation at $5 < E < 7$ meV, in the lowest energy excitation band at $11.0 < E < 12$ meV, and in the higher energy excitation bands at $13.5 < E < 14.5$ meV and $14.5 < E < 15.5$ meV. In each plot above 7 meV, the red line corresponds to the Q-dependence of incoherent phonons and follows the form

$$I_{ph}(Q) = a + bQ^2 \exp\left(\frac{-Q^2\langle u^2\rangle}{3}\right), \tag{6.1}$$

where a is a flat background term accounting for multiple scattering, b is a scaling factor for the phonon Q^2 contribution and the exponential term is the Debye-Waller factor [2]. The variables a, b and c were adjusted in each energy range. In Figure 6.6a taken at $T = 1.8$ K, no clear peak at low-Q is seen as the energy range is in the gap between the two excitations, but at $T = 25$ K there is a peak at $Q \sim 1.2$ Å^{-1} as the excitation becomes ungapped. At $T = 100$ K the spurious scattering seen in Figure 6.3a meant $\chi''_E(Q)$ could only be assessed for $Q > 2.5$ Å^{-1}. $\chi''_E(Q)$ does not overlap at all temperatures, but this is most likely an issue with the Bose factor correction in the $T = 100$ K data, which assumes that the phonon scattering is temperature independent. In Figure 6.6b there is a clear peak centred at $\sim$1.2 Å^{-1} corresponding to the spin wave excitation, which becomes more diffuse with temperature and disappears at 100 K in line with the $S(Q,E)$ spectra. In Figure 6.6c, up to 2 Å^{-1} there is a peak which loses intensity with increasing temperature indicating that the response is magnetic, and above 2 Å^{-1} the intensity stays similar with increasing temperature, so the subsequent modulations correspond to coherent phonon scattering superposed on the incoherent one. Going to higher energy transfers in Figures 6.6d and e, the intensity at all three temperatures is similar indicating no magnetic scattering at low temperature and the peak centred at 3 Å^{-1} is coherent phonon scattering. At high Q in Figure 6.6e, the $\chi''_E(Q)$ responses do not overlap at all temperatures, which again is probably due to an issue with the Bose

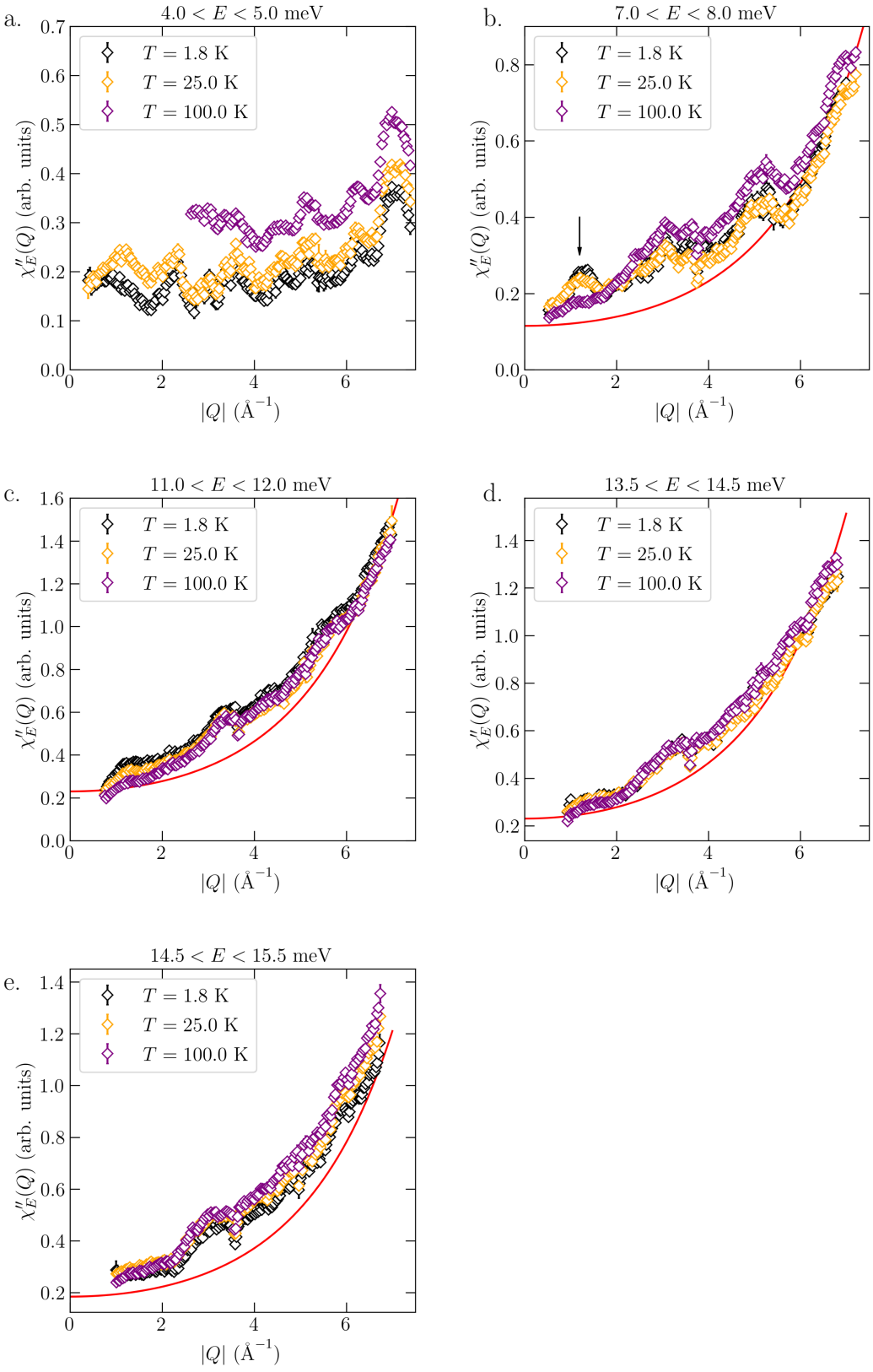

Figure 6.6: Claringbullite, PANTHER data. $\chi''_E(Q)$ integrated over different energy transfer ranges at $T = 1.8$ K (black), 25 K (orange) and 100 K (purple). **a.** $4.0 < E < 5.0$ meV. **b.** $7.0 < E < 8.0$ meV. The arrow indicates the peak corresponding to the magnetic scattering which at $T = 100$ K becomes completely diffuse. **c.** $11.0 < E < 12.0$ meV. **d.** $13.5 < E < 14.5$ meV. **e.** $14.5 < E < 15.5$ meV. The red lines show the phonon $\sim Q^2$ dependence (equation 6.1).

factor. $\chi''_Q(E)$ indicates that the excitation bands seen in Figure 6.3b correspond to phonons. The phonons in this sample change with temperature from $T = 1.8$ K to $T = 100$ K leading to an under-subtraction in $\chi''(Q,E)$.

The dispersion of the high-energy excitation was characterised using temperature subtracted data integrated over various energy ranges, $\Delta\chi''_E(Q)$, with a width of 0.5 meV. Figure 6.7a shows Gaussian fits (with a linear background) to two peaks and the results are in Figure 6.7b. The peaks are centred at $Q = 1.25(1)$ Å^{-1}, close to the (–1, 1, 1) Bragg peak, and at $Q = 1.91(2)$ Å^{-1}, close to the (0, 0, 2) Bragg peak. The peak centre of the $Q = 1.25$ Å^{-1} peak remains relatively constant with increasing energy transfer and the increase in the full-width half-maximum (FWHM) with increasing energy transfer indicates a dispersive excitation. The extracted peak areas confirm $\Delta\chi''_Q(E)$ plotted in Figure 6.5b. The second peak at $Q = 1.91$ Å^{-1} is much weaker and not clearly seen in the $\Delta\chi''(Q,E)$ spectrum (Figure 6.3b).

The E and Q dependence of the low-energy excitation was also investigated. $S_E(Q)$ integrated over various energy ranges is shown in Figure 6.8 at $T = 1.6$ K and 25 K. At low temperature, the excitation has two branches originating from $Q \sim 0.50$ and $\sim$1.18 Å^{-1}, best seen in the $1.2 < E < 1.3$ meV scan (Figure 6.8a), corresponding to the (1, 0, 0) and (0, 1, 1) magnetic Bragg peaks. These two dispersive branches seem to join each other at $Q = 0.76$ Å^{-1} and $E = 2.0$ meV with maximal intensity. Above 2.0 meV the excitations continue to disperse but the intensity decreases. At $T = 25$ K, we saw from the $S(Q,E)$ spectra (Figure 6.4d) that the excitation has collapsed. $\chi''_E(Q)$ (Figure 6.8b) shows that down to the lowest resolved energy transfers, $0.45 < E < 0.5$ meV, the intensity of the excitation and its peak centre remain similar at 0.73 Å^{-1}.

To characterise the low-energy excitation, $S_Q(E)$ integrated over 0.1 Å^{-1} widths between 0.5 and 2 Å^{-1} at $T = 1.6$ K is shown in Figure 6.9a. The excitation has several peaks in energy, with the most intense one at $\sim$ 2 meV, the centre of the excitation. The peak position changes as Q increases, showing a dispersive excitation with an energy gap. The zero-energy gap was determined using $\Delta\chi''_Q(E) = \chi''(E, T = 1.6\text{ K}) - \chi''(E, T = 25\text{ K})$, integrated over $0.8 < Q < 1.0$ Å^{-1}

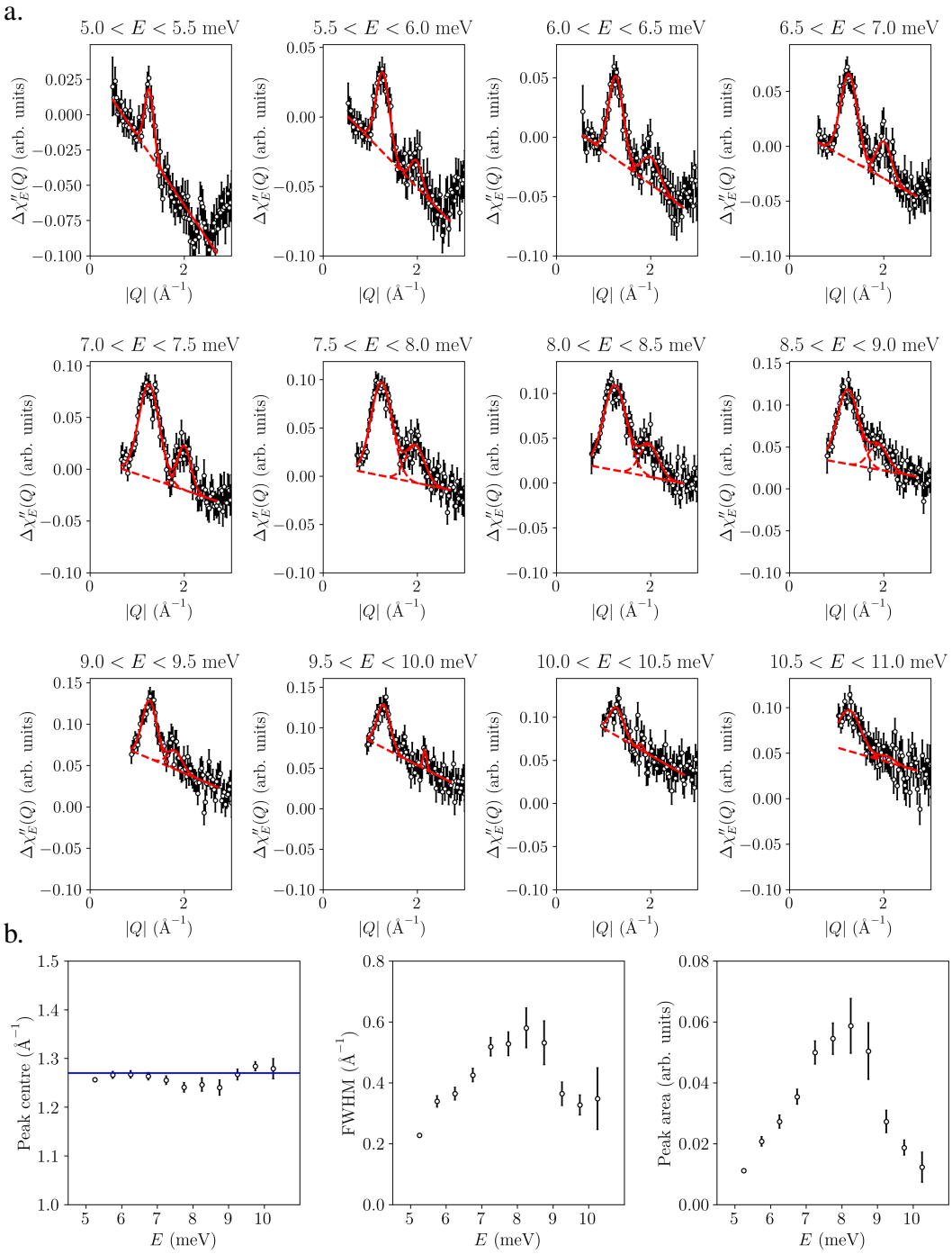

Figure 6.7: Claringbullite, PANTHER data collected with $E_i = 35$ meV. **a.** $\Delta\chi''_E(Q)$= $\chi''_E(Q,T = 1.8\text{ K})$–$\chi''_E(Q,T = 25\text{ K})$ (black). The red lines are Gaussian fits with a linear background. **b.** Results of Gaussian fits. The main spin wave branch has an average centre at 1.25(1) Å^{-1} (vertical blue line). The increase in the full-width half-maximum (FWHM) with increasing energy transfer indicates a dispersive excitation. The peak area of the excitation supports the observation in Figure 6.3b that it is most intense at ~ 8 meV.

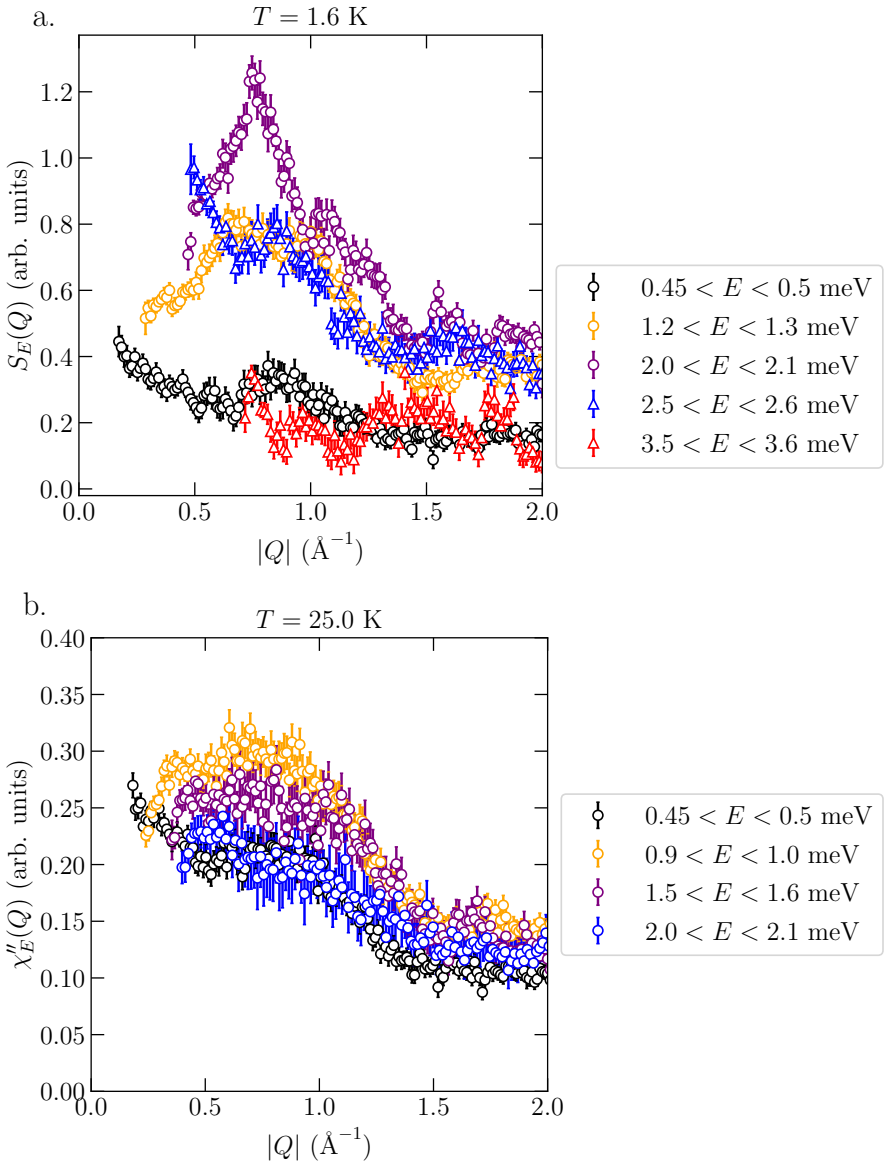

Figure 6.8: Claringbullite, IN5 data collected with $E_i = 3.55$ and 5.11 meV. **a.** $S_E(Q)$ integrated over energy transfer ranges between 0.45 and 3.5 meV at $T = 1.6$ K. The excitation is strongest at ~ 2 meV with a peak at 0.7 Å^{-1}. **b.** $\chi''_E(Q)$ integrated over energy transfer ranges between 0.45 and 2.0 meV at $T = 25$ K. The excitation has a similar shape and intensity as E increases.

being careful to avoid the low-energy spurious scattering. The linear part in energy was extrapolated, as shown in Figure 6.9b, to give a gap of 0.45 meV. Similarly the linear part of the excitation above 2.7 meV was extrapolated to 3.22 meV, allowing an estimate of the bandwidth of 2.77 meV.

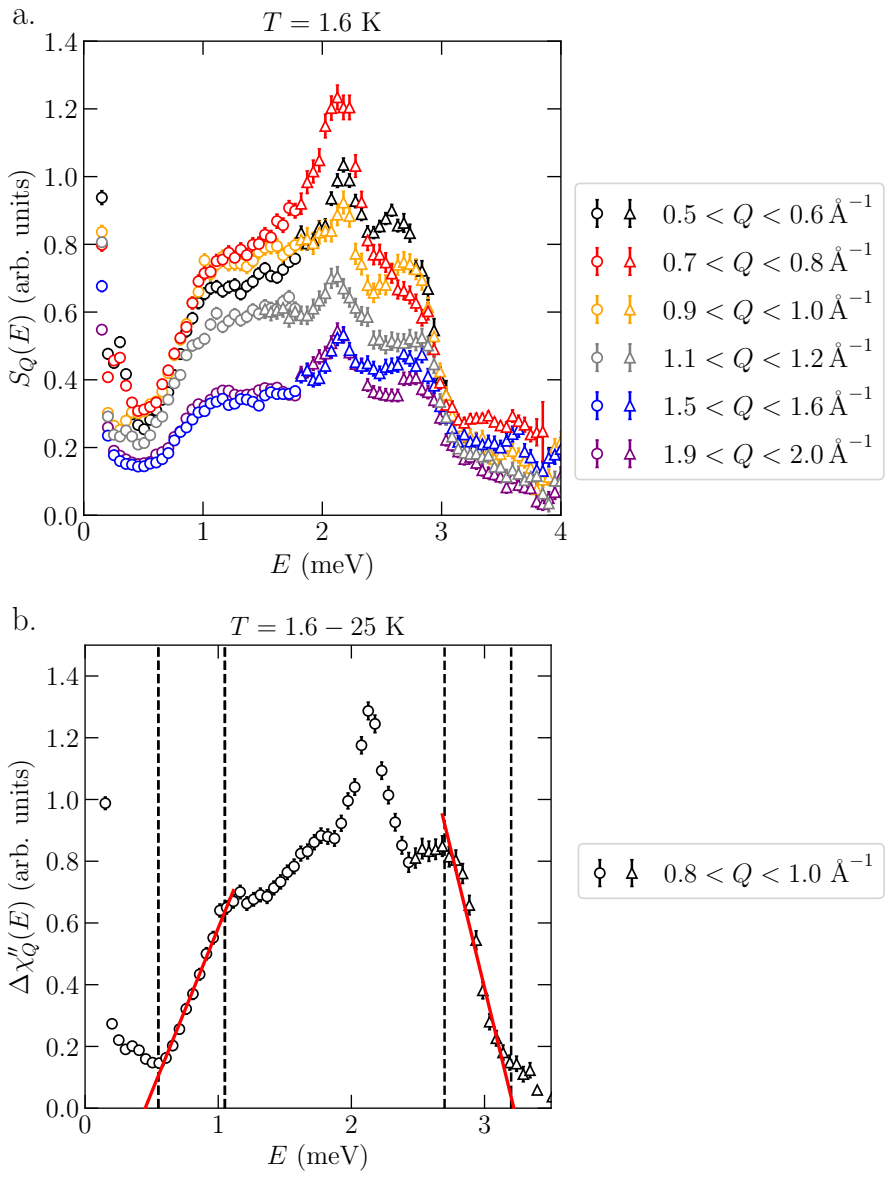

Figure 6.9: Claringbullite, combined data of $E_i = 3.55$ and 5.11 meV collected on IN5. **a.** $S_Q(E)$ at $T = 1.6$ K integrated over widths of 0.1 Å^{-1} from 0.5 to 2 Å^{-1}, clearly showing a dispersive excitation at low energy. **b.** $\Delta\chi''_Q(E)$ obtained from the subtraction $\chi''_Q(E, T = 1.6$ K$)$–$\chi''_Q(E, T = 25$ K$)$, integrated over $0.8 < Q < 1.0$ Å^{-1}. The red lines are linear extrapolation of the intensity of the magnetic excitation between 0.55 and 1.05 meV, and 2.7 and 3.2 meV (black dashed lines). They give low-energy gap of 0.45 meV and an upper limit of 3.22 meV (bandwidth of excitation is 2.77 meV).

In the absence of static magnetic order, above T_N, quasi-elastic scattering would be expected to dominate the magnetic scattering. This relaxation is commonly described by an exponential decay of the correlation function with time. The dynamic structure factor is the Fourier transform of the correlation function in space and time, and that of an exponential decay function is a Lorentzian [2]. To characterise the diffuse excitation, $S_Q(E)$ integrated over $0.7 < Q < 0.9$ Å^{-1} was fitted with the quasi-elastic Lorentzian function, appropriate for paramagnetic systems (Figure 6.10), as was done previously for kapellasite [3]. The quasi-elastic Lorentzian (QEL) function is given by

$$\chi''(E) = \frac{\chi'_Q E\Gamma}{E^2+\Gamma^2}, \tag{6.2}$$

where χ' is the real part of the total magnetic susceptibility, E is the energy and Γ is the line width [3]. Γ represents the characteristic decay time, τ, of the magnetisation correlation function and is given by

$$\Gamma = \hbar/\tau. \tag{6.3}$$

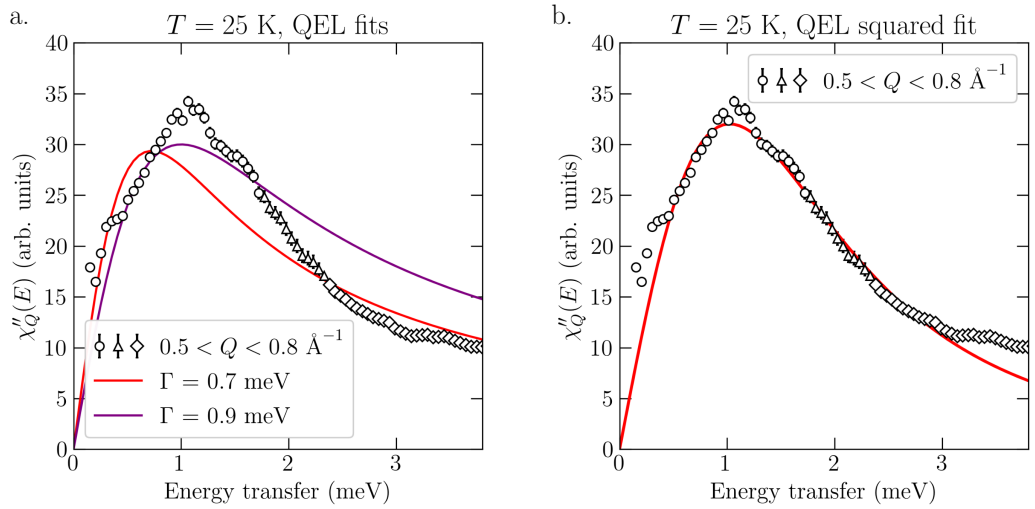

Figure 6.10: Claringbullite, IN5 combined data of $E_i = 3.55$, 5.11 and 10.43 meV at $T = 25$ K. $\chi''_Q(E)$ integrated between 0.5 and 0.8 Å^{-1}. At $E < 0.5$ meV there is spurious scattering (Figure 6.4d). **a.** The red and purple lines are two quasi-elastic Lorentzian functions with $\Gamma = 0.7$ and 0.9 meV, respectively. Neither fit represents the data well. **b.** The red line is a squared QEL fit between $0.3 < E < 3.0$ meV as described in the text.

Figure 6.10a shows two attempts to fit the energy dependence of the diffuse excitation with a QEL with a small and large Γ but neither describe the data well. This indicates that this excitation cannot simply be described with a single relaxation time.

An attempt was also made to fit this excitation with a damped harmonic oscillator (DHO) fit, as previously done for herbertsmithite [4], given by

$$\chi''(E) \propto \frac{4}{\pi} \frac{\Gamma E}{(E^2 - E_0^2)^2 + 4\Gamma^2 E^2}, \tag{6.4}$$

where Γ is the line width and corresponds to the relaxation rate of the excitations, and E_0 is the energy of the DHO mode. The least-squared fits did not give stable E_0 values, but pointed to overdamped excitations where $\Gamma > E_0$. This damping may arise from strong spin fluctuations [4] and an attempt was made to fit the data with a squared QEL that describes an overdamped collective spin excitation (or overdamped magnon) in the limit of the characteristic energy E_0 being much smaller than the line width, Γ:

$$\chi''(E) = \frac{2E\chi'\Gamma^3}{(E^2 + \Gamma^2)^2}, \tag{6.5}$$

where the terms are defined as in equation 6.2. The fit is shown in Figure 6.10b with $\Gamma = 1.77(1)$ meV and $\chi'_Q = 49.3(1)$. Up to 3 meV, the squared QEL function is a better description of $\chi''_Q(E)$ than the simple QEL. The tail of the excitation is not well fitted, but the $\chi''(Q,E)$ plot in Figure 6.4b shows there may be some contribution from the high-energy excitation. Figure 6.4e clearly shows that integrating over a narrower Q range will not isolate the tail of the low-energy excitation as there is other scattering for $E > 2.5$ meV at all Q values.

This section detailed a qualitative analysis of the magnetic excitations observed for claringbullite above and below its magnetic phase transition at $T_N = 17$ K. Below T_N, spin waves are seen that can be modelled using semi-classical linear spin wave theory to determine the exchange interactions, as will be described in Section

6.2.5. Above T_N, the non-Lorentzian E dependence of the magnetic excitations can be described by a squared quasi-elastic Lorentzian function indicating overdamped excitations and a correlated paramagnetic state. This state will be compared to the QSL state of the $x = 1$ Zn-doped variant, Zn-claringbullite, in Section 6.4.1.

6.2.5 Modelling the exchange interactions

It is often challenging to determine the defining exchange interactions of disordered magnetic phases, such as a quantum spin liquid (QSL), from powder inelastic neutron scattering (INS) spectra, and place it in a QSL phase diagram. An initial estimate of the sign and magnitude of the exchange interactions can be made using the Curie-Weiss temperature in a mean-field calculation, as will be done below for claringbullite. Often, a more precise determination of the exchanges requires complex analytical models that have been developed for a particular Hamiltonian [5]. However, materials with long-range magnetic order have spin wave excitations, which can be modelled using tools like linear spin wave theory (LSWT) to determine the exchange interactions. The key steps of the LSWT method were outlined in Chapter 1. While such analysis is typically done using single crystals, our group has previously accomplished this using powder INS data for the $S = 1/2$ kagome magnets vesignieite [6] and haydeeite [7]. In both cases the Hamiltonians were simple and included two parameters: the former had two exchanges, whereas the latter had one anisotropic symmetric exchange interaction with the degree of anisotropy being the second parameter.

Claringbullite and Zn-claringbullite have similar bonding geometries with kagome ∠Cu-O(D)-Cu superexchange angles of 115-121° and 117°, respectively. Therefore, their exchange interactions were hypothesised to be similar and by determining the exchanges from the magnetically ordered phase of claringbullite we aimed to place Zn-claringbullite in a spin-liquid phase diagram. However, we note some key points that indicate claringbullite deviates from an isotropic kagome system, which complicates the mapping of the exchange interactions from the $x = 0$ to the $x = 1$ sample:

- Aside from the orthorhombic distortion in claringbullite, which may lift the

degeneracy of exchange interactions from these of a symmetric kagome lattice, the system would not necessarily be 2-D. Depending on the spin couplings, claringbullite may have stronger 3-D exchange coupling than the 2-D kagome layers in Zn-claringbullite. Looking at the Cu-Cu distances of the $x = 0$ sample in Table 5.6, there is no clear distinction between those within the kagome triangles and those connecting to the interlayer Cu3, suggesting 3-D magnetic behaviour. The strength and sign of the exchange interactions for nearest-neighbour (n.n.) spins, are governed by the Cu-O(D)-Cu superexchange angles (also in Table 5.6) and comparison with the literature [8] indicates a clear separation between the antiferromagnetic exchanges in the kagome triangles and the ferromagnetic ones between both Cu1 and Cu2 with Cu3.

- The kagome component of the refined magnetic structure of claringbullite is not that of any regular magnetic order (RMO) on the kagome lattice described in [9] —a spin flip in the kagome triangle would be required to achieve a RMO.

- Claringbullite has strong anisotropy evidenced by the zero-energy gap seen in the inelastic spectra, and suggested by previous barlowite single crystal magnetometry measurements [10].

Nevertheless, determining the exchange interactions of claringbullite is interesting in its own right as it could help further our understanding of the coupling between kagome layers, the exchange model of clinoatacamite [11] and provide a comparison to the exchanges proposed for barlowite, $Cu_4(OH)_6FBr$, obtained from density functional theory (DFT) calculations and tenth order high-temperature series expansion analysis of the magnetic susceptibility [12, 13].

As detailed in Chapter 2, long-range magnetic order occurs as a result of exchange interactions that are able to select a coherent ground state from the frustrated possibilities. The sum of the exchange interactions can be determined using mean-field theory, where it is assumed that each magnetic atom couples to the resulting

magnetic field of all other magnetic atoms. For a Heisenberg model, the sum of the exchanges, J', can be related to the Curie-Weiss temperature [14] by

$$\theta_W = -\frac{2}{3}S(S+1)\sum_{ij} J'_{ij}. \tag{6.6}$$

The sum is taken over all ij indices independently and hence counts each bond twice, with opposite directions. The negative sign in equation 6.6 comes from the defined spin Hamiltonian in Chapter 2, where $J' > 0$ corresponds to antiferromagnetic exchange interactions. For a single n.n. isotropic symmetric exchange interaction J', equation 6.6 can be simplified so that for z nearest neighbours, the summation becomes zJ' [14]. The high temperature region of the magnetic susceptibility was used to determine $\theta_W = -136$ K (see Chapter 5). Assuming a kagome system with $S = 1/2$ and $z = 4$, gives an antiferromagnetic $J' = 68$ K≈ 5.9 meV. To be comparable to the results of linear spin wave theory described below, which uses a single counting of Cu-Cu bonds, a factor of 2 difference must be considered giving $J = 2J' \approx 11.7$ meV.

Linear spin wave theory is a common tool that can be used to estimate the strongest exchange interactions. Calculating the spin wave spectra for the regular kagome lattice with the $\mathbf{k} = \mathbf{0}$ and $\sqrt{3} \times \sqrt{3}$ structures, showed the bandwidth of the spin wave excitations to be $E \approx 2JS$ and for $S = 1/2$, $E = J$ [15–17]. Interestingly, if claringbullite were a kagome system then $E = 11.6$ meV, which is in good agreement with the top of the high-energy excitation. However, claringbullite may be best described as a 3-D system, as reasoned above, with corresponding complexity that would suggest that a more intricate combination of various exchanges. INS spectra of these were shown in Figures 6.2, 6.3 and 6.4 and are shown again in Figure 6.12. The main features of the excitations are the two responses at ~ 10 meV and ~ 2 meV, which are separated by a 1.8 meV finite energy gap and have a zero-energy gap of 0.45 meV.

To model the spin wave spectra of claringbullite, semi-classical linear spin wave theory was used as realised in the program SpinW [15]. The SpinW input consisted of the lattice parameters and space group of the primitive unit cell, the

lattice coordinates of the magnetic atoms, the directions of the spins determined from the magnetic structure and the exchange interactions. The Hamiltonian used was

$$\mathscr{H} = \sum_{<ij>} J_{ij}\mathbf{S}_i \cdot \mathbf{S}_j + \mathbf{D}_{ij} \sum_{<ij>} (\mathbf{S}_i \times \mathbf{S}_j), \tag{6.7}$$

where the sum is over pairs of sites ij (the brackets in the summation indicate single-counting of bonds) and $\mathbf{D}_{ij}$ represents the antisymmetric and anisotropic Dzyaloshinskii-Moriya interaction (DMI). The exchange model used and referred to throughout this section is shown in Figure 6.11. The reasoning behind this model will be explained below, but it is now important to introduce the exchange interaction labels: the n.n. exchange interactions in the kagome triangles are approximated to be equal to J_1; there are three 'tripod' exchange interactions from Cu3 to Cu1 and Cu2 (J_{t1}, J_{t2} and J_{t3}); an exchange between the kagome layers J_c; and three second

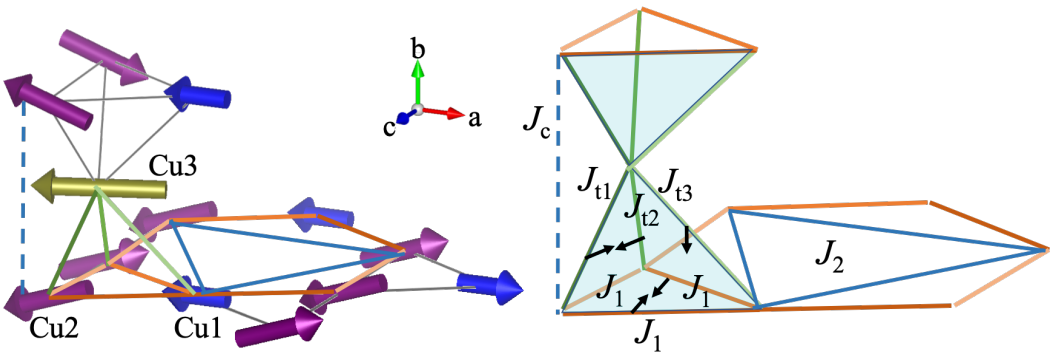

Figure 6.11: Claringbullite magnetic structure refined from D20 data at $T = 1.7$ K (**left.**) and redrawn with relevant exchange interactions on the **right.**. The black arrows indicate the directions of the DMI vectors parallel to the b and c directions. The exchanges with the corresponding Cu-Cu distances are given in Table 6.2.

J_i	d (Å)
J_{t1}	2.801
J_{t2}	3.104
J_{t3}	3.169
J_1	3.317 - 3.353
J_c	4.354 - 4.797
J_2	5.768 - 5.798

Table 6.2: Claringbullite Cu-Cu distances corresponding to the exchange interactions shown in Figure 6.11.

n.n. exchanges in the kagome layers approximated to be equal to J_2. The approximations are based on similar Cu-Cu bond distances (see Table 6.2) and Cu-O(D)-Cu superexchange pathways. The directions of the DMI vectors on J_{t1}, J_{t2}, J_{t3} and two of the three J_1 interactions are also illustrated in Figure 6.11.

The previous DFT calculations and tenth order high-temperature series expansion (HTSE) fitting to inverse susceptibility data, were used to calculate the exchange interactions for barlowite with *Cm* symmetry (space group no. 8) [12]. At low temperature, barlowite and claringbullite crystallise in the *Pnma* space group and have similar magnetic structures that may be described in the Γ_7 irreducible representation using Kovalev's notation [18]. Our claringbullite sample and the *Cm* barlowite structure have similar ∠Cu-O(H/D)-Cu superexchange angles in the kagome triangles: 115 - 121° in claringbullite and 117° in barlowite [12]. Therefore, despite the magnetic moments in our claringbullite sample being slightly smaller than those previously reported for barlowite [19], the exchange interactions in the two materials are expected to be similar. For the *Cm* barlowite structure, DFT and HTSE calculations led to the proposal of the following exchange couplings: a single antiferromagnetic $J_1 \approx 11.3$ meV; two ferromagnetic 'tripod' exchanges ($J_{t1} \approx -17.1$ meV and $J_{t2} = J_{t3} \approx -2.76$ meV); a weak $J_c \approx 0.43$ meV; and a Cu3-Cu3 exchange (1.38 meV) involving two J_{t1} pathways [12]. This exchange model involves five parameters, which is a sizeable refinement phase space and highlights the fact that the magnetic structure is expected to be the consequence of many competing interactions.

As aforementioned, there is evidence of strong anisotropy in claringbullite and the most common type of anisotropic exchange in related kagome systems, such as herbertsmithite [20], is the DMI. The relative magnitude of the symmetric exchange and the antisymmetric DMI can be expressed in terms of the gyromagnetic ratio, g, and its difference with the free electron value, $\sim (\Delta g/g)J$ [21]. Previous magnetisation measurements on single crystals of barlowite indicated $|\mathbf{D}|/J_1 \approx 0.006 - 0.1$ [12, 22]. In other Cu-based frustrated systems, the DMI has been found to be $\sim 8\%$ in herbertsmithite [23] and 16% in the triangular antiferromagnet Cs_2CuCl_4 [24].

The exchange model suggested using the previously mentioned DFT and HTSE calculations in the literature [12], led to a Hamiltonian that was not diagonalizable in SpinW, suggesting different relative magnitudes of these exchanges or the necessity of other further-neighbour ones. Simplifying it to exclude the weak Cu3-Cu3 exchange and/or J_c did not help to stabilise the magnetic structure, but in later calculations J_c was found to improve the simulated spectra and so was kept in the exchange models.

Stabilising the magnetic structure was found to be extremely challenging and the phase space of five parameters (four symmetric exchange values and the magnitude of the antisymmetric DMI) was too large to be probed solely based on SpinW calculations due to the computational resources required. To probe this exchange phase space and determine regions where the experimental magnetic structure was stabilised, a new Monte Carlo-like program, Serendipity, was developed and applied [25]. Serendipity uses a symmetry analysis of the crystal structure above T_{N} to generate a set of possible isotropic exchange interactions and DMIs to incorporate into a model. Many possible exchange value combinations were generated and their eigenvectors of the symmetric exchange matrix were tested against the experimental structure and the Weiss temperature. Those that were compatible with these requirements were then tested against their ability to stabilise the observed magnetic structure with respect to possible magnetic phases associated with the various irreducible representations of $G_{\mathbf{k}}$. The dimensionality of the phase space resulting from around 106 trial exchange combinations per model makes its stability region challenging to visualise and so the results were filtered into clusters, such as $J_1 > 0$, $J_2 > 0$, $|J_{t1}| > |J_{t2}| > |J_{t3}|$ and $J_c > 0$. Each model-type was trialled in SpinW against the INS data and used to guide the SpinW calculations to regions of phase space where the experimentally observed magnetic structure was stable.

The magnetic structure used as the basis for Serendipity included the ordered magnetic moment sizes refined from the D20 data, whereas linear spin wave theory considers an "intrinsic" spin $S = 1/2$ rather than the ordered moment sizes. As claringbullite is an insulator, it is expected that the electrons are well-localised and

behave as $S = 1/2$ spins. However, it may be important to consider the fact that the ordered magnetic moments are significantly reduced from the full 1 μ_B, likely due to quantum fluctuations, and such a reduction in the intrinsic spin length could lead to a change in both the energies and intensities of some spin wave modes. For this study $S = 1/2$ was used and exchange interactions were trialled and compared with the experimental data. Qualitatively this was done by inspection of the calculated $S(Q,E)$ spectra and quantitatively by using $S_Q(E)$ and $S_E(Q)$ integrated over various Q and E ranges.

A requirement of LSWT is that the magnetic structure is an energy minimum of equation 6.7. Therefore, the classical optimisation *optmagsteep* in SpinW [15] was used to relax the structure determined by diffraction, creating a minimal model whereby Cu1 was rotated by $\sim 90°$ in the $a-c$ plane, Cu2 was rotated by $\sim 96°$ out of the kagome plane and Cu3 was rotated by $\sim 10°$ in the $a-c$ plane (17° was refined from the D20 data). The ferromagnetic canting of Cu3 was further stabilised by $|\mathbf{D}| = 0.05J_{t3}$ along the b direction. It was found that $|\mathbf{D}|/J_{t3}$ had to be slightly larger than $|\mathbf{D}|/J_i$ parallel to the b direction (see Figure 6.11) to prevent Cu3 from rotating out of the $a-c$ plane. The inclusion of the DMI introduced a zero-energy gap, in some cases with an appropriate size of ~ 0.5 meV. Further refinements of the size of the DMI, can only be done when more accurate exchanges are determined.

As the parameter phase space was sizeable, it was efficient to use a Monte Carlo script for SpinW [26] to test a range of exchange values predicted by Serendipity. This script calculated spin wave spectra and compared them to the experimental data using two $S_Q(E)$ scans integrated over $0.63 < Q < 0.83$ Å^{-1} and $1.1 < Q < 1.3$ Å^{-1}. A goodness-of-fit value, χ^2, was used to assess the best results. The number of Monte Carlo cycles was determined by doubling the number of possible values for each parameter in an energy range E with step size dE and multiplying out the possibilities for all parameters. Typically only two or three parameters were refined against each other, with each exchange being allowed to refine in a 2 meV range with a 0.1 meV step size — for a two-parameter refinement, for example, the number of Monte Carlo cycles was 1600.

The condition in SpinW that the Hamiltonian must be diagonalizable, led to the conclusion that further neighbour exchanges outside the tetrahedra were required. The Cu2 spins in the magnetic structure (Figure 6.11) form antiferromagnetic chains along b, which can freely rotate in the a-c plane. Our diffraction refinements indicated the rotation angle to be 18° out of the kagome plane, which likely results from a combination of competing symmetric exchanges and a DMI. Models with a further neighbour exchange in the kagome plane were explored to stabilise the rotation angle of the Cu2 spins. Trials were made with second n.n. exchanges, J_2, third n.n., J_3, and exchanges across the diagonals of the kagome hexagons, J_d. Inclusion of J_3 and/or J_d did not result in spectra similar to the experimental data, whereas J_2 improved the calculations. Models outputted from Serendipity with both ferro- and antiferromagnetic J_2 were trialled, but only the latter was found to stabilise the structure. Furthermore, an in-plane DMI parallel to the c direction of $0.03J_i$ between Cu2 and Cu1/Cu3 was used to help stabilise the structure (see Figure 6.11). It was also found that the bandwidth of the low-energy response relies on the different magnitudes of J_{t1}, J_{t2} and J_{t3} so three distinct values were required.

The calculated spin wave spectra of one of the exchange models that best describes the observed data, though not a unique solution, is shown in Figure 6.12. This is an eight parameter model as the in and out-of-plane DMI had to be slightly different to stabilise the Cu3 and Cu2 spin canting in and out of the $a-c$ plane, respectively. The calculated spectra with $E_i = 35$ meV clearly indicates two magnetic responses at high and low energy, as observed in the experimental data. The excitations at ~ 18 meV are not clearly seen in the experimental data, but it should be noted that most of the predicted intensity lies outside the experimentally accessible kinematic window. Looking at the data simulated with $E_i = 19.2$ meV, shows a magnetic excitation centred at $Q \approx 1.2$ Å^{-1} that extends from ~ 5 to 13 meV as seen in the experimental spectra. This is separated by a gap from a lower energy magnetic response. Although the low energy response is ~ 0.5 meV lower than the experimental data, it comprises of two bands with spin wave branches coming out from above and below it. Importantly the low-energy response is more intense

than the higher energy one as seen in experiment. Based on the crystal structure the Curie-Weiss temperature was calculated by

$$\theta_{\mathrm{W}} = -\frac{S(S+1)}{3}\left[\frac{4}{16}\sum_{<i=1,j>} J_{ij}\mathbf{S}_i\cdot\mathbf{S}_j + \frac{8}{16}\sum_{<i=2,j>} J_{ij}\mathbf{S}_i\cdot\mathbf{S}_j + \frac{4}{16}\sum_{<i=3,j>} J_{ij}\mathbf{S}_i\cdot\mathbf{S}_j\right], \quad (6.8)$$

where the summations are taken over the mean fields of each Cu atom (Cu1, Cu2 and Cu3 indicated by $i = 1,\ 2$ and 3, respectively) in the primitive orthorhombic unit cell containing 16 Cu atoms. For the best exchange model (see Figure 6.12), $\theta_{\mathrm{W}} = -95$ K in close agreement with -136 K, determined from DC susceptibility (Chapter 5), particularly considering that many further neighbour exchanges around the F^- ion have not been taken into account.

In this model, the exchange coupling between kagome planes J_c is $\sim 30\%$ of J_1. Halving its value results in the spectra shown in Figure 6.13. This comparison shows that J_c has an effect on all magnetic excitations: reducing J_c causes the bandwidth of the magnetic excitation at ~ 10 meV to decrease and the low-energy excitation to lose intensity relative to the high-energy excitation, whilst moving up in energy transfer. It should be noted that models from Serendipity with ferromagnetic J_c were also trialled as the Cu1 and Cu2 spins in consecutive kagome layers are aligned parallel with respect to the a direction. However, these led to spectra that were less representative of the experimental data.

The 'tripod' exchanges were mainly found to affect the excitation at ~ 2 meV. An example is shown in Figure 6.13, where J_{t3} has been reduced by 1 meV compared to Figure 6.12. The width in both Q and E of the ~ 10 meV excitation largely remains the same, whereas the ~ 2 meV excitation has a smaller bandwidth and a higher intensity.

The examples shown here evidence the intricacies of the exchange interactions, and the complexity of a model with so many parameters. However, these calculations do show that the main features of the experimental data can be captured with a model of six exchanges and reasonable DMI values. Numerous attempts to fur-

ther refine these exchanges were made, and a better model has not been found to date. These results highlight the importance of the interlayer exchange, as well as a further neighbour interaction within the kagome layers, in understanding the magnetic behaviour of claringbullite. It is possible that further neighbour exchanges are present, but this model has already pushed the limits of what can be learnt from these powder INS data. A better, more accurate model, would likely be dependent on future single crystal INS data. The fact that the exchange models from Serendipity were unable to stabilise a model of $S = 1/2$ spins in SpinW with the relative spin orientation angles found from diffraction, signifies the possible limitations in using semi-classical linear spin wave theory for frustrated systems with significantly reduced moment sizes.

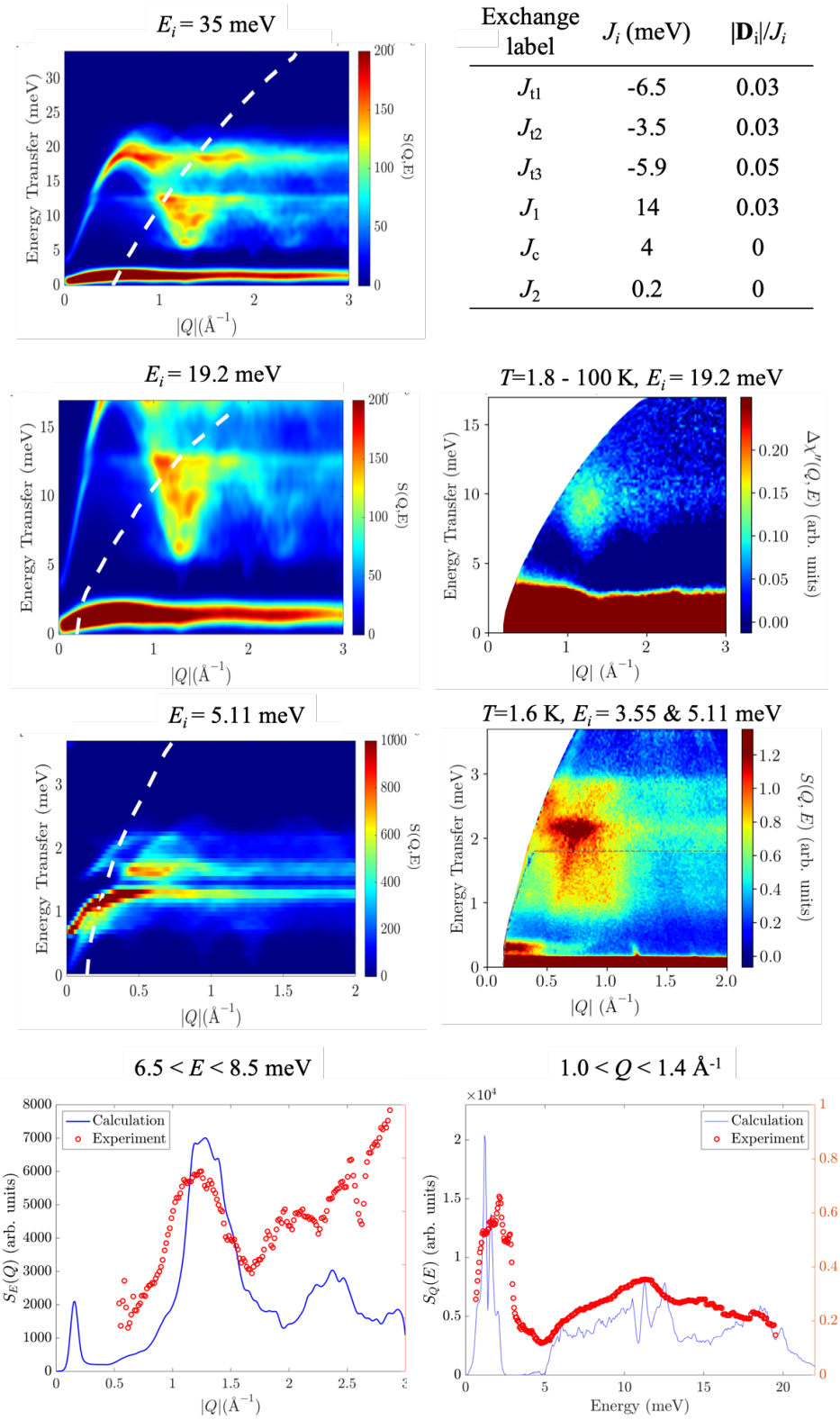

Exchange label	J_i (meV)	$\lvert\mathbf{D}_i\rvert/J_i$
J_{t1}	-6.5	0.03
J_{t2}	-3.5	0.03
J_{t3}	-5.9	0.05
J_1	14	0.03
J_c	4	0
J_2	0.2	0

Figure 6.12: Claringbullite calculated spin wave spectra (**left.**) with the corresponding exchange interactions in the table, that represent the best reproduction of the experimental data (**right.**). The directions of the DMI are shown in Figure 6.11. The dashed white lines indicate the kinematic windows for the corresponding incident neutron energies. $S_E(Q)$ and $S_Q(E)$ scans of the calculated (blue) and experimental (red) data are shown at the **bottom.** This exchange model provides the best reproduction of the experimental features.

Exchange label	J_i (meV)	$\|\mathbf{D}_i\|/J_i$
J_{t1}	-6.5	0.03
J_{t2}	-3.5	0.03
J_{t3}	-5.9	0.05
J_1	14	0.03
J_c	2	0
J_2	0.2	0

Exchange label	J_i (meV)	$\|\mathbf{D}_i\|/J_i$
J_{t1}	-6.5	0.03
J_{t2}	-3.5	0.03
J_{t3}	-4.9	0.05
J_1	14	0.03
J_c	4	0
J_2	0.2	0

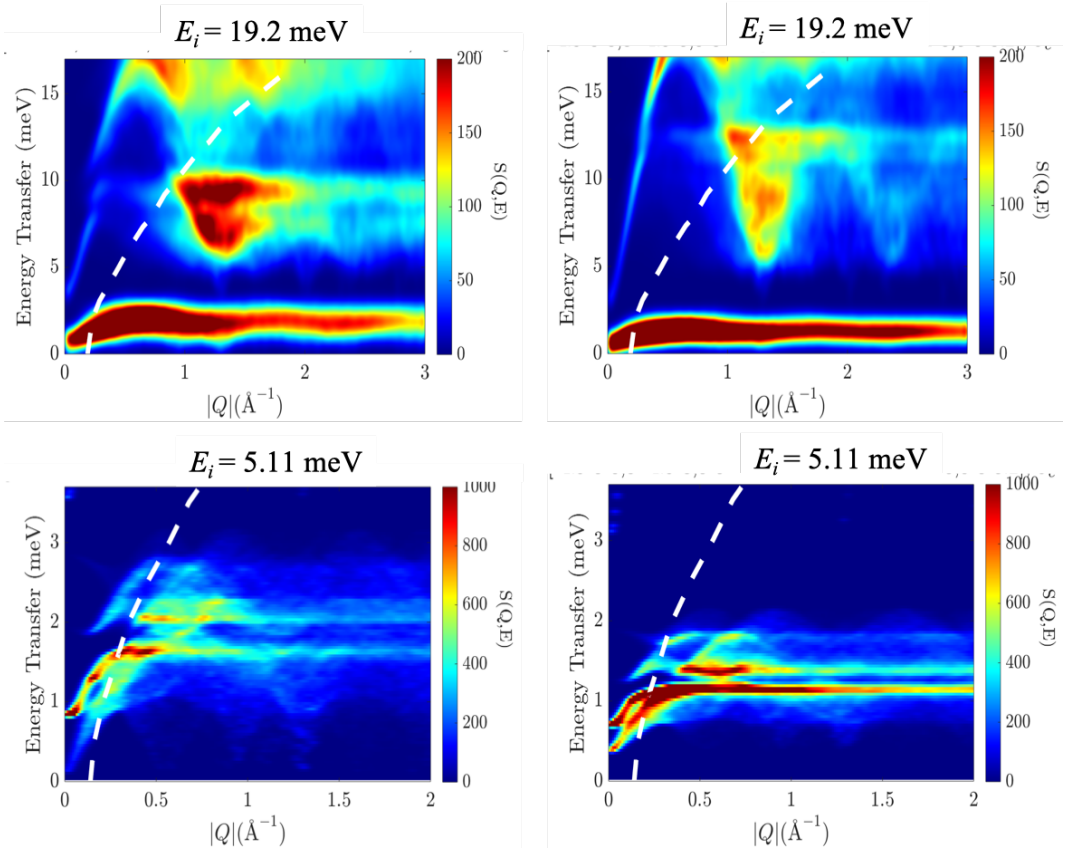

Figure 6.13: Claringbullite calculated spin wave spectra for the exchange interactions in the tables that trial changing J_c and J_{t3} from the values refined in Figure 6.12. The directions of the DMI are shown in Figure 6.11. The dashed white lines are the kinematic windows for the corresponding incident neutron energies. (**Left.**) The J_c value has been halved with respect to the best model (*i.e.* $J_c = 2$ meV), shown in Figure 6.12, which affects the bandwidth of the ∼10 meV excitation, the energy transfer value of the ∼ 2 meV excitation and their relative intensities. (**Right.**) The J_{t3} value has been increased by 1 meV to $J_{t3} = -4.9$ meV with respect to Figure 6.12, which mainly affects the bandwidth of the ∼ 2 meV excitation.

6.3 Inelastic neutron scattering measurements on Zn-claringbullite

The susceptibility results (Section 5.4) show that the Zn-claringbullite sample does not have a magnetic phase transition down to $T = 2$ K and that its magnetic properties are governed by short-range correlations. As for the $x = 0$ sample, the best way to probe its excitations is through INS. Since the two samples have similar crystal structures, the exchange interactions are also expected to be similar, which would cause the magnetic excitations to be in the same energy window. To measure the excitation spectra, data were collected on the cold-neutron time-of-flight spectrometer LET at the ISIS Neutron and Muon source, summarised in Table 6.3. The INS results with a quantitative analysis will be given, followed by a more quantitative analysis giving the signs of the exchange interactions in this system.

T (K)	E_i (meV)			
1.7 50.0	1.64	2.82	5.96	20.03

Table 6.3: Summary of INS data collection conditions for Zn-claringbullite measured on LET with incident neutron energies E_i at two temperatures T.

6.3.1 Magnetic excitations on LET

For the experiment on LET, the same 7.00 g deuterated sample measured on D2B was loaded into an 8 mm vanadium can. Plots of the reduced $S(Q,E)$ collected with the three higher incident energies are shown in Figure 6.14. The data collected with $E_i = 1.64$ meV are included in Appendix C and were not used in the analysis due to the poor statistics. At $T = 1.7$ K with $E_i = 20.03$ meV (Figure 6.14a), the data are dominated by phonons for $Q > 2$ Å^{-1} and there is a magnetic excitation at $Q \sim 1.3$ Å^{-1} extending up to ~ 10 meV. This is most easily seen in a temperature subtraction in $\chi''(Q,E)$ between the $T = 1.7$ and 50 K data, shown in Figure 6.17. Similar to claringbullite, there is evidence of magnetic scattering in the tail of the elastic line below 2 Å^{-1}, clearly seen in Figure 6.14c. This excitation shows a gapless smooth continuum centred at ~ 0.7 Å^{-1} and extending up to 2 meV. Both

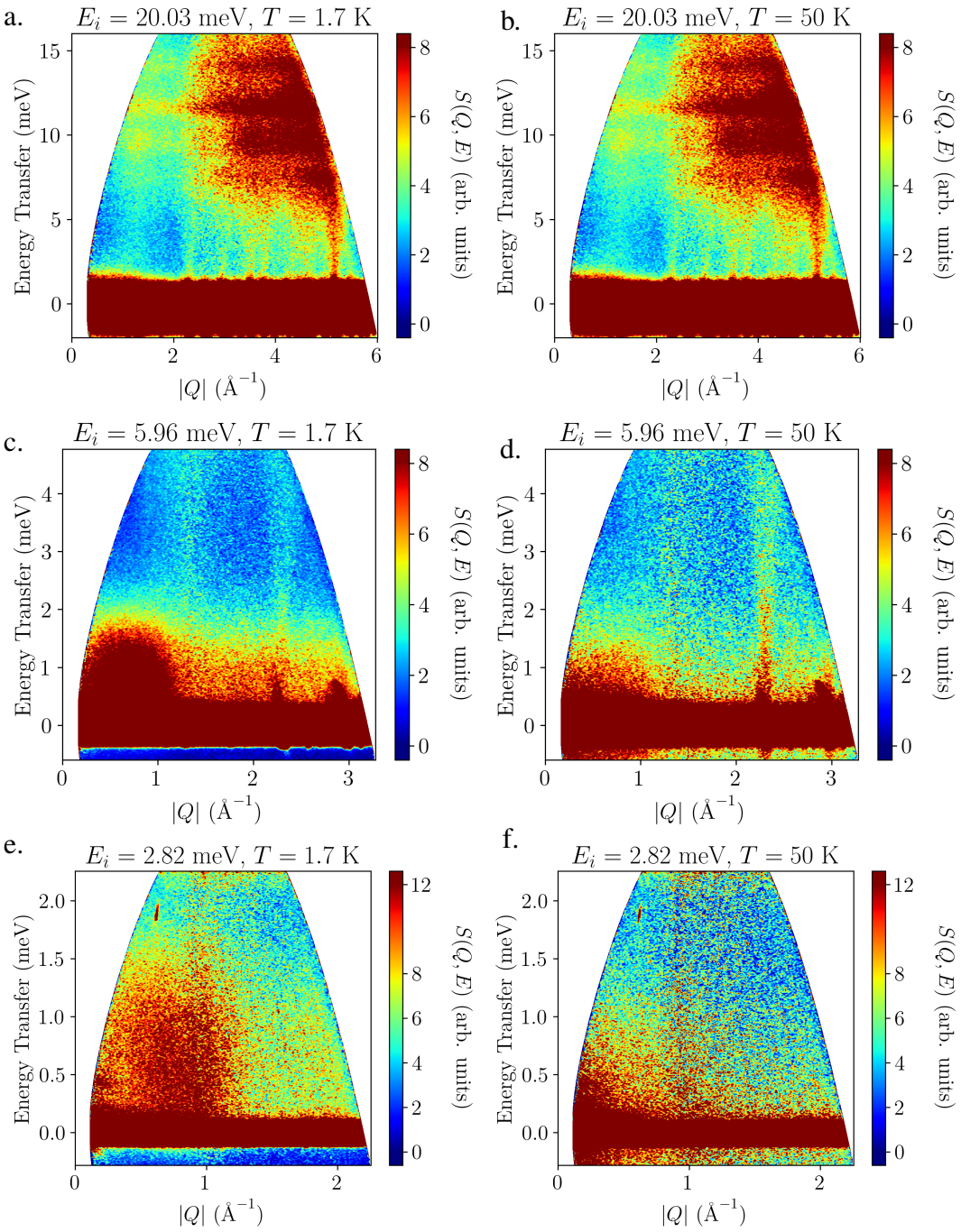

Figure 6.14: Zn-claringbullite, $S(Q,E)$ from LET with incident neutron energies of $E_i = 20.03$ meV, $E_i = 5.96$ meV and $E_i = 2.82$ meV (**top.-bottom.**) at temperature of $T = 1.7$ K (**left.**) and $T = 50$ K (**right**).

high- and low-energy excitations become more dissipated in Q and energy at higher temperatures, but persist up to at least $T = 50$ K (right column of Figure 6.14) indicating strong short-range correlations. $S_Q(E)$ and $S_E(Q)$ at high and low temperatures were used to distinguish the magnetic excitations from the phonon contribution.

6.3.2 Results and analysis

Starting with the high-energy excitation, Figure 6.15a shows $S_Q(E)$ at $T = 1.7$ K obtained by integrating over two Q ranges: between 1.2 and 1.4 Å^{-1} where the inelastic magnetic excitation is observed, and in the range $1.6 < Q < 1.8$ Å^{-1} where there is no visible magnetic excitation or acoustic phonon (see Figure 6.14a). Below 11 meV there is less intensity in the lower Q range, indicating that up to and including the first peak at ~ 10 meV there is a magnetic excitation and the second peak at ~ 12 meV is a phonon. The behaviour of the excitation centred at ~ 1.3 Å^{-1} with temperature is shown in Figure 6.15b. When temperature increases, $\chi''_Q(E)$ loses intensity below 11 meV, whereas the second peak changes little, confirming the magnetic origin of the contribution below 11 meV.

Similar to undoped claringbullite, the magnetic excitations and phonons are at

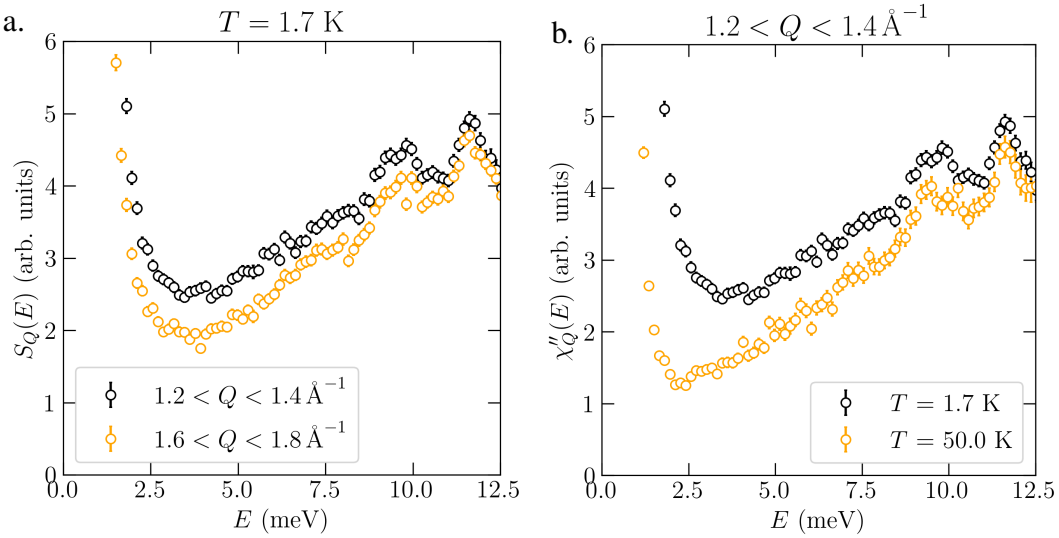

Figure 6.15: Zn-claringbullite, LET data with $E_i = 20.03$ meV. **a.** At $T = 1.7$ K, $S_Q(E)$ integrated over $1.2 < Q < 1.4$ Å^{-1} (black) and $1.6 < Q < 1.8$ Å^{-1} (orange). **b.** $\chi''_Q(E)$ integrated over $1.2 < Q < 1.4$ Å^{-1} at $T = 1.5$ (black) and 50 K (orange).

very similar energies, particularly the bands at 10 and 12 meV. $\chi''_E(Q)$ obtained by integrating $\chi''(Q,E)$ over various energy ranges are shown in Figure 6.16 at both high and low temperatures. Up to 10 meV the excitation peak is clearly seen at ~ 1.3 Å^{-1} and loses some intensity with temperature, whereas the phonon contributions above $Q = 2$ Å^{-1} have similar intensities. Between 11 and 12 meV (Figure 6.16c) and similarly between 13.5 and 14.5 meV (Figure 6.16d), the change in in-

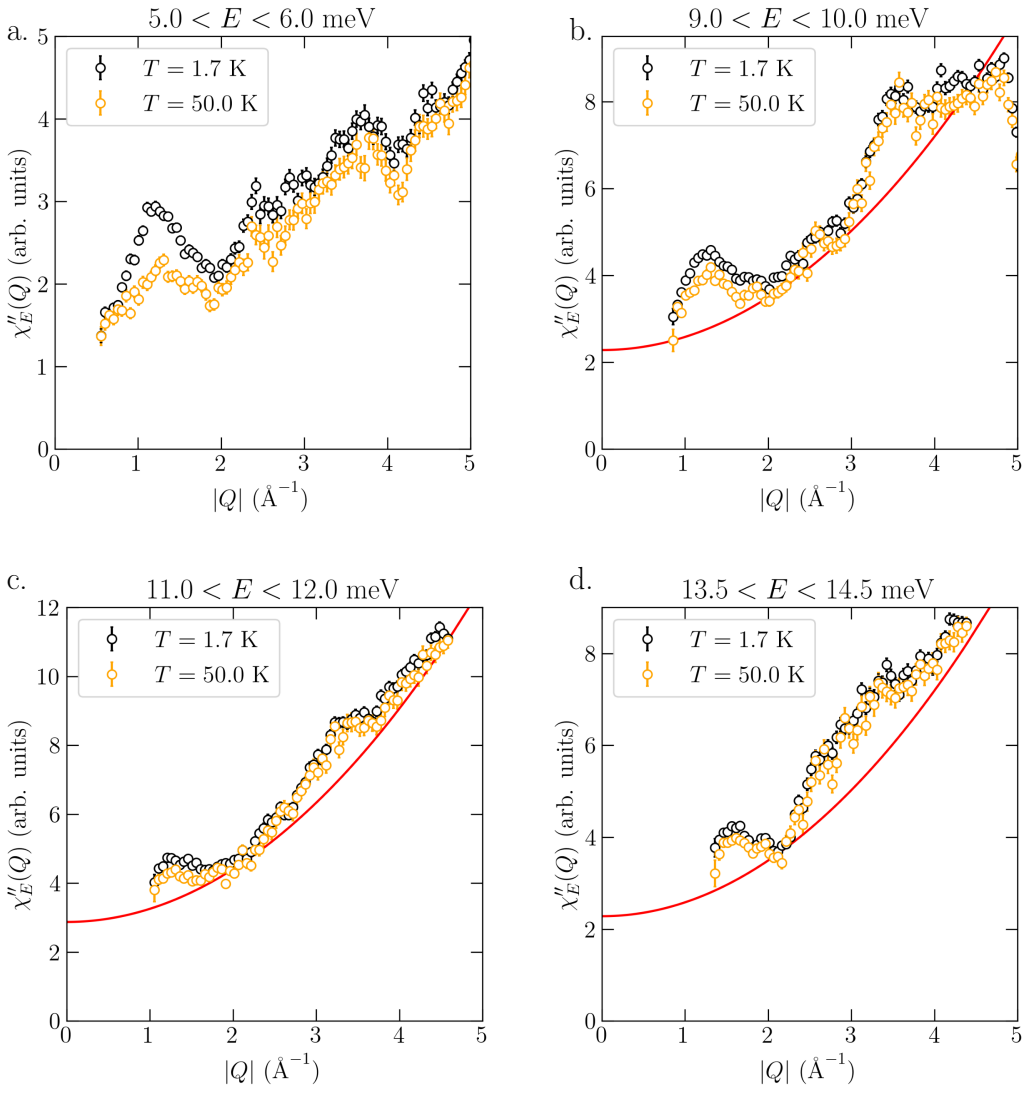

Figure 6.16: Zn-claringbullite, LET $E_i = 20.03$ meV data. $\chi''(Q,E)$ integrated over various energy ranges at 1.7 K (black) and 50 K (orange). **a.** $5.0 < E < 6.0$ meV and **b.** $9.0 < E < 10.0$ meV, showing the peak of the magnetic excitation centred at ~ 1.3 Å^{-1}. **c.** $11.0 < E < 12.0$ meV. **d.** $13.5 < E < 14.5$ meV. The red lines show the incoherent phonon $\sim Q^2$ dependence (equation 6.1).

tensity between 1 Å^{-1} and 2 Å^{-1} does not show clear evidence of a magnetic contribution. From these $\chi''_E(Q)$ plots it was concluded that there is no clear magnetic contribution to the excitations above $\sim$ 10 meV.

The magnetic scattering close to $Q = 1.3$ Å^{-1} arises from short-range correlations in the system and its centre can be used to identify the type of short-range correlations present. The centre of the excitation was determined using temperature subtracted data, $\Delta\chi''(Q,E)$, shown in Figure 6.17. The temperature subtraction served to remove the phonon contributions (both optical and acoustic), but it should be noted that some magnetic intensity is lost since the excitation persists beyond $T = 50$ K. $\Delta\chi''(Q,E)$ was integrated between different energy transfer ranges to obtain $\Delta\chi''_E(Q)$ and was fitted with a Gaussian function and flat background (Figure 6.18). Figure 6.18 shows the peak centre is at 1.29(3) Å^{-1}, independent of energy. The FWHM changes little in Q, indicating a non-dispersive excitation with an average value of 1.00(5) Å^{-1}. The average FWHM results in a correlation length of 6.3(3) Å that is $\sim$ 1.1 kagome hexagons. The peak area decreases with increasing energy transfer as expected from $\Delta\chi''(Q,E)$(Figure 6.17).

A similar analysis can be done for the low-energy diffuse excitation, most clearly seen in Figures 6.14c and e. $S_E(Q)$ was obtained by integrating over dif-

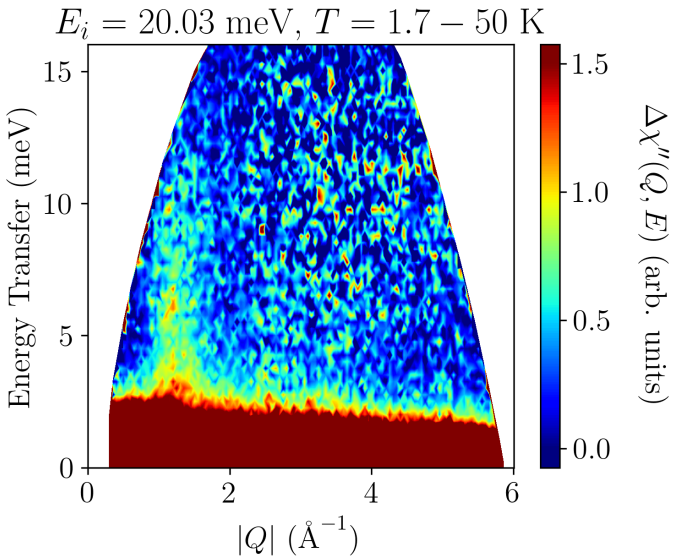

Figure 6.17: Zn-claringbullite LET $E_i = 20.03$ meV data. $\Delta\chi''(Q,E)$ at $T = 1.7 - 50$ K showing magnetic scattering centred at $Q = 1.29$ Å^{-1} and extending up to $\sim$ 10 meV.

ferent energy transfer ranges with a 0.2 meV width and also fitted with a Gaussian function and a flat background term (Figure 6.19). The extracted peak centres have an average value of 0.685(4) Å^{-1} and the peak areas increase as $E \to 0$, as is also seen from the $S(Q,E)$ spectra. The FWHM in Q decreases slightly with increasing energy up to ~ 0.8 meV, after which it stays relatively constant. The average value is 0.75(2) Å^{-1} giving a correlation length of 8.4(2) Å that is ~ 1.2 kagome hexagons, which is similar to the result from the high-energy excitation. From the

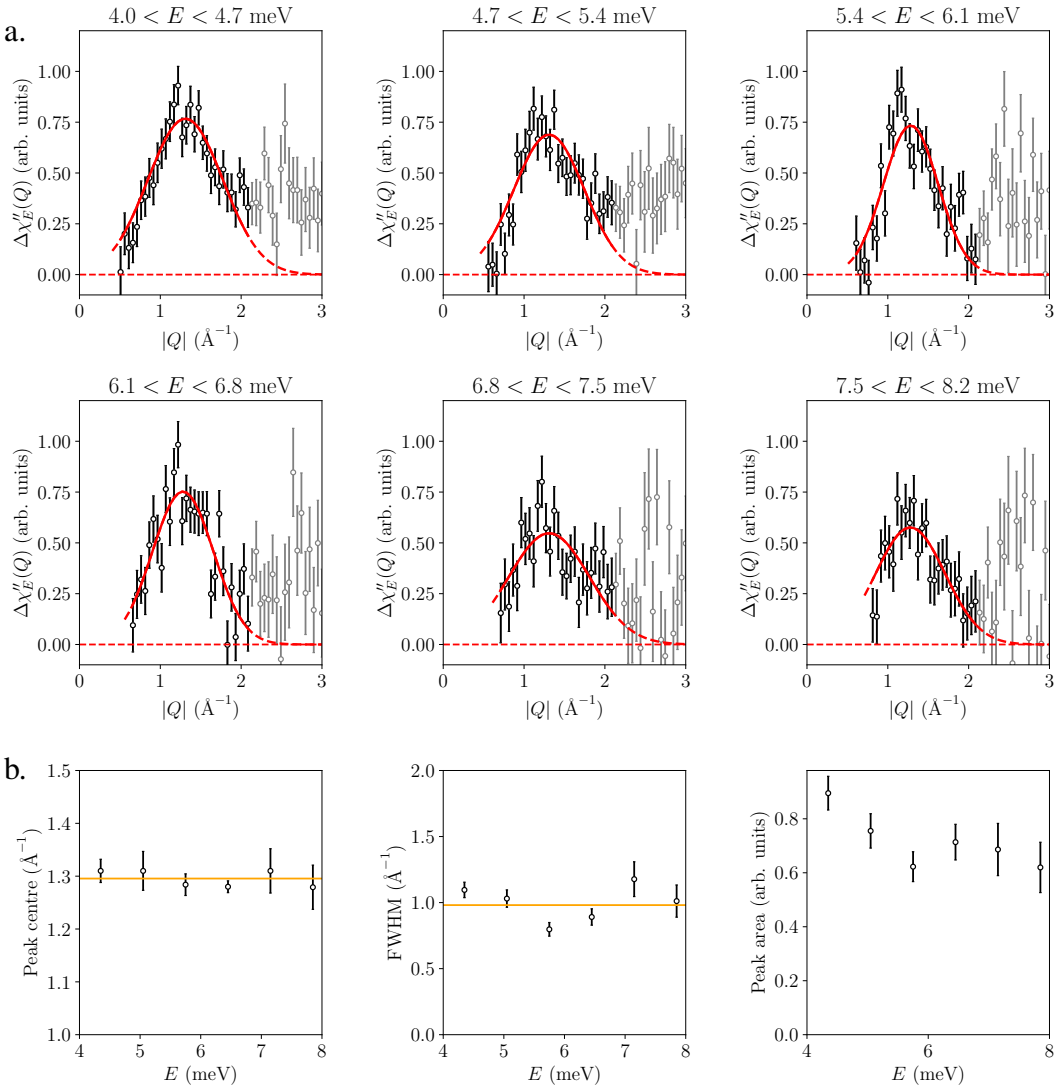

Figure 6.18: Zn-claringbullite. **a.** $\Delta\chi''_E(Q)$ from a temperature subtraction $T = 1.7$–50 K of LET $E_i = 20.03$ meV data (grey). The range used for the fits is in black. The solid red lines are Gaussian fits with a flat background (dashed line). **b.** Results from the Gaussian fits. The average peak centre is 1.29(3) Å^{-1} (horizontal orange line). The average FWHM is 1.00(5) Å^{-1} (horizontal orange line) and the peak area decreases with increasing energy.

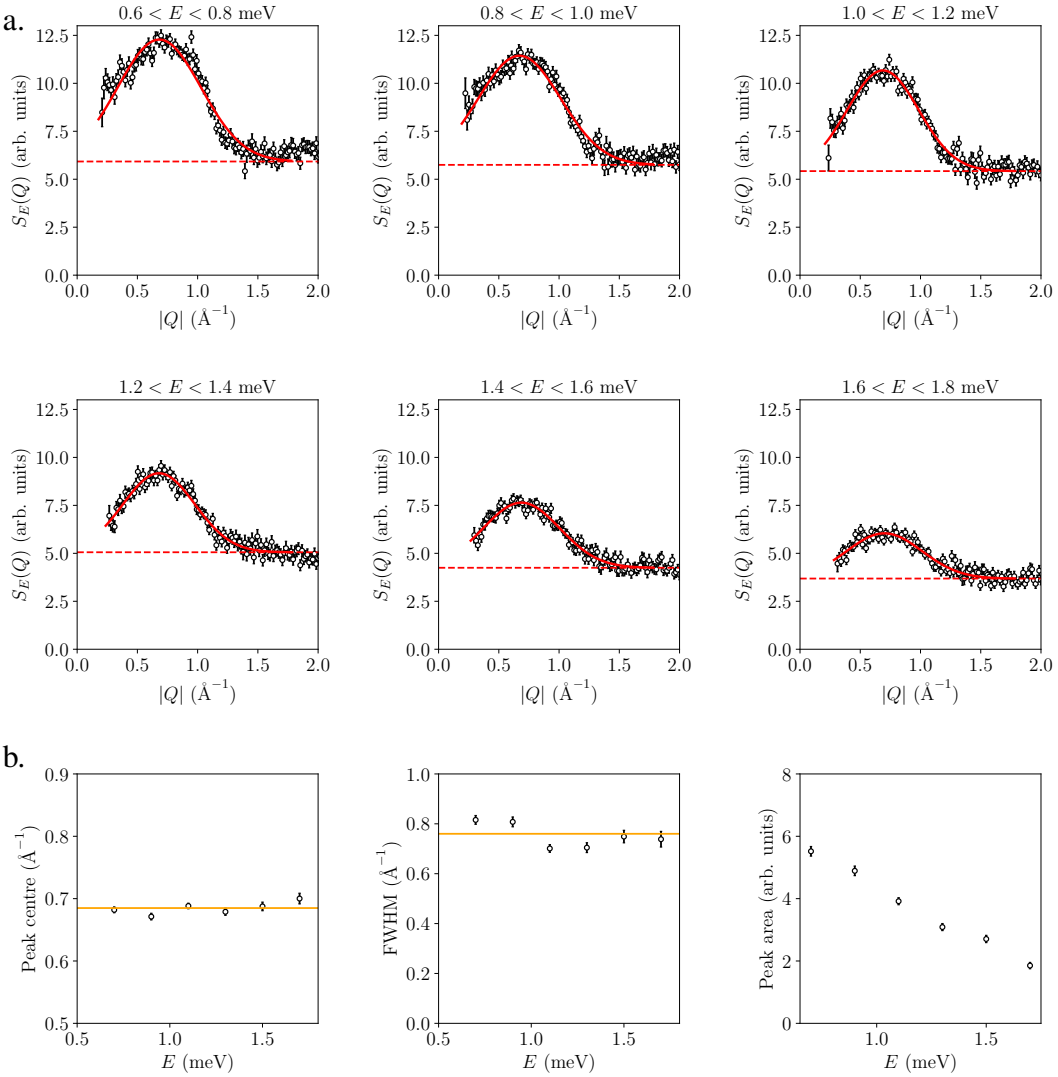

Figure 6.19: Zn-claringbullite, LET $E_i = 5.96$ meV data. **a.** $S_Q(E)$ integrated over successive energy transfer ranges with a width of 0.2 meV. The red lines are Gaussian fits with a flat background term (dashed line). **b.** The average peak centre (orange line) is 0.685(4) Å^{-1}. The average FWHM is 0.75(2) Å^{-1}. The peak area decreases with increasing energy transfers as expected from the $S(Q,E)$ plots in Figure 6.14.

Gaussian fits, both excitations indicate short-range correlations in the system of similar distances.

The classical phase diagram for the kagome lattice, considering first, second, third and across-hexagon diagonal exchange interactions, has been calculated by Messio *et. al.*, and is found to be dominated by the so-called "regular magnetic orders (RMOs)" [9]. To identify the type of short-range correlations present in the $x = 1$ system, the Q positions of the excitations were compared to those of the

RMOs. Table 6.4 lists the expected Q positions of structures with $\mathbf{k} = \mathbf{0}$, $\mathbf{k} = (\frac{1}{2}, 0, 0)$ and $\mathbf{k} = (\frac{1}{3}, \frac{1}{3}, 0)$. The magnetic excitations centred at $Q = 0.68$ and 1.29 Å^{-1} are closest to the positions predicted for $\mathbf{k} = \mathbf{0}$. In general, this propagation vector either corresponds to a ferromagnetic state or an antiferromagnetic $\mathbf{k} = \mathbf{0}$ structure on the kagome lattice. The latter is the case for Zn-claringbullite as the magnetic susceptibility results show a strong antiferromagnetic mean field.

$\mathbf{k} = \mathbf{0}$		$\mathbf{k} = (\frac{1}{2}, 0, 0)$		$\mathbf{k} = (\frac{1}{3}, \frac{1}{3}, 0)$	
$h\ k\ l$	$\lvert Q \rvert$ (Å^{-1})	$h\ k\ l$	$\lvert Q \rvert$ (Å^{-1})	$h\ k\ l$	$\lvert Q \rvert$ (Å^{-1})
0 0 1	0.69	$\frac{1}{2}$ 0 0	0.55	$\frac{1}{3}$ $\frac{1}{3}$ 0	0.63
0 1 0	1.09	$\frac{1}{2}$ 0 1	0.88	$\frac{1}{3}$ $\frac{1}{3}$ 1	0.93
1 0 1	1.29	$-\frac{1}{2}$ 1 0	0.94	$\frac{2}{3}$ $\frac{2}{3}$ 0	1.26
0 0 2	1.37	$-\frac{1}{2}$ 1 1	1.17	$\frac{2}{3}$ $\frac{2}{3}$ 1	1.43

Table 6.4: Expected reflections for the propagation vectors $\mathbf{k} = \mathbf{0}$, $\mathbf{k} = (\frac{1}{2}, 0, 0)$ and $\mathbf{k} = (\frac{1}{3}, \frac{1}{3}, 0)$, with lattice parameters $a = b = 6.659$ Å, $c = 9.173$ Å, $\alpha = \beta = 90°$ and $\gamma = 120°$. In Zn-claringbullite, short-range correlations are observed at $Q = 0.68$ and 1.29 Å^{-1}.

It is notable that the excitation spectrum of the $x = 1$ sample at $T = 1.7$ K is extremely similar to that of the $x = 0$ sample at $T = 25$ K, in its cooperative paramagnetic state. The crystallographic studies showed the diamagnetic doping away from $x = 0$ to be primarily on the interlayer sites, therefore the similarities between these spectra suggests that the low-energy response at $Q = 0.68$ Å^{-1} is due to the kagome layers. The high-energy excitation is present in both samples, evidencing strong coupling between the spins within the kagome plane.

The energy dependence of the magnetic scattering centred at 0.682 Å^{-1} was obtained by $S_Q(E)$ integrated over $0.6 < Q < 0.8$ Å^{-1} of combined $E_i = 2.82$ meV and $E_i = 5.96$ meV data (Figure 6.20). It appears to be quasielastic, gapless and relaxational. The maximum peak intensity is close to the lowest energy transfers resolved, making it difficult to fit with a QEL function (equation 6.2) as illustrated in Figures 6.20a and b for two different values of Γ. A larger Γ improves the description of the peak maximum but a smaller Γ is better able to describe the tail. These fits show that a QEL cannot accurately represent the experimental data, indi-

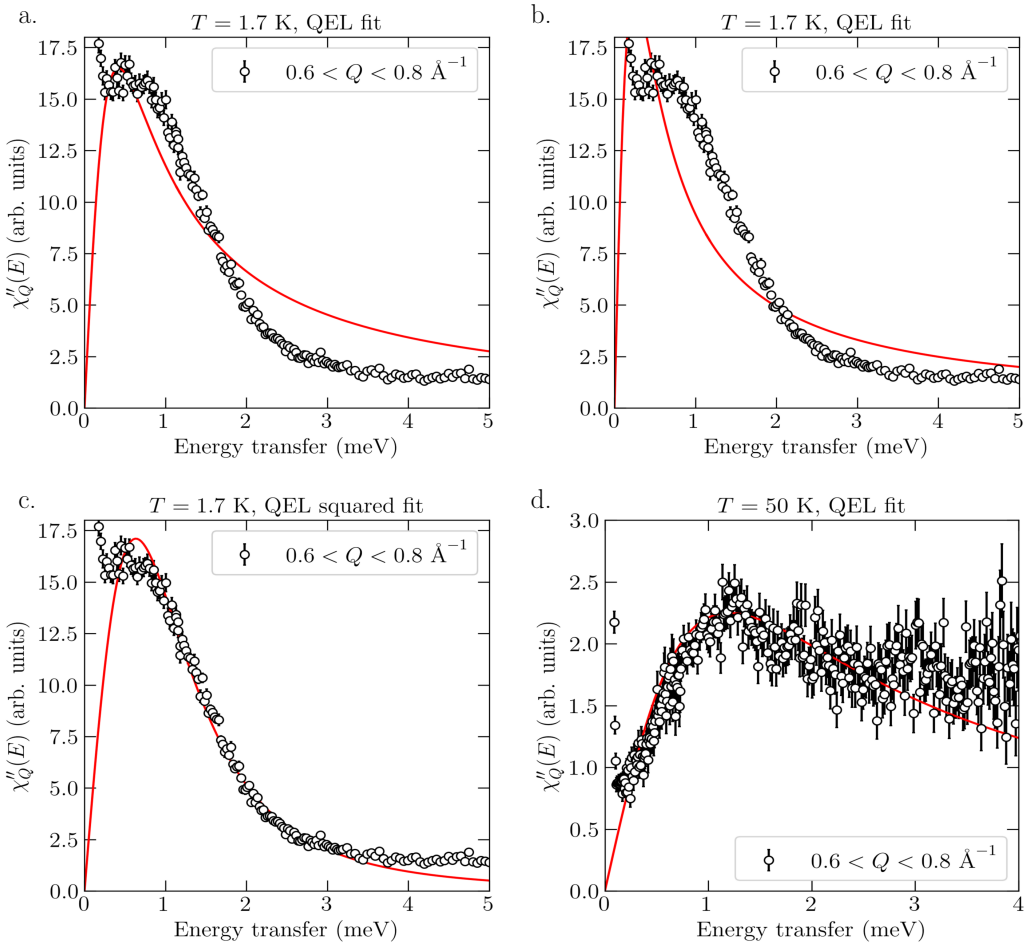

Figure 6.20: Zn-claringbullite, LET combined data of $E_i = 2.82$ and 5.96 meV. **a.** $T = 1.7$ K. $\chi''_Q(E)$ integrated over $0.6 < Q < 0.8$ Å^{-1} (black). The red line is a QEL function (equation 6.2) with $\Gamma = 0.43$ meV. **b.** Same data as in (**a.**) with a QEL function with $\Gamma = 0.25$ meV. **c.** Same data as in **a.** with a squared QEL function (equation 6.5) with $\Gamma = 1.09(1)$ meV. **d.** $T = 50$ K. $\chi''_Q(E)$ integrated over $0.6 < Q < 0.8$ Å^{-1} with a QEL fit as described in the text.

cating that this excitation is not governed by a single relaxation time and additional correlations are present [3]. An attempt was also made to fit this excitation with a squared quasi-elastic Lorentzian function (equation 6.5) and the fit is shown in Figure 6.20c with $\Gamma = 1.09(1)$ meV and $\chi'_Q = 26.3(3)$. This function describes an overdamped excitation in the limit of the characteristic energy being much smaller than the line width Γ. The tail of the data for $E > 3$ meV is not well-described, possibly due to the background arising from incoherent scattering of protons in the sample. The fit suggests that the excitation is gapless down to the lowest accessible

energy transfer of 0.27 meV. However, local-probe techniques such as μSR or NMR would be required to determine the size of a gap smaller than this.

At 50 K, the diffuse excitation persists so a similar analysis was done. $\chi''_Q(E)$ was integrated over $0.5 < Q < 1.0$ Å^{-1}and the QEL fit is shown in Figure 6.20d. It describes the data well up to 3 meV, giving $\Gamma = 1.28(2)$ meV so $\tau = 5.14(8) \cdot 10^{-13}$ s. The observation that the QEL function is a much better representation of the $T = 50$ K data indicates the presence of more "classical" spin fluctuations described by a single relaxation time, similar to those expected in a paramagnet. On the other hand, the insufficiency of the QEL at low temperature suggests that in this region quantum fluctuations are important.

6.3.3 Short-range order

The inelastic neutron scattering results of Zn-claringbullite ($x = 1$ sample) show that the magnetic system is dominated by short-range magnetic correlations down to $T = 1.7$ K. A zeroth- and first-moment analysis [27, 28] was used to determine the spin-spin correlations and the sign of the dominant exchange interactions in Zn-claringbullite. The exchange interactions that are relevant to this analysis are shown in Figure 6.21, with the corresponding Cu-Cu distances given in Table 6.5.

The Q-dependence of the zeroth moment of the diffuse magnetic scattering,

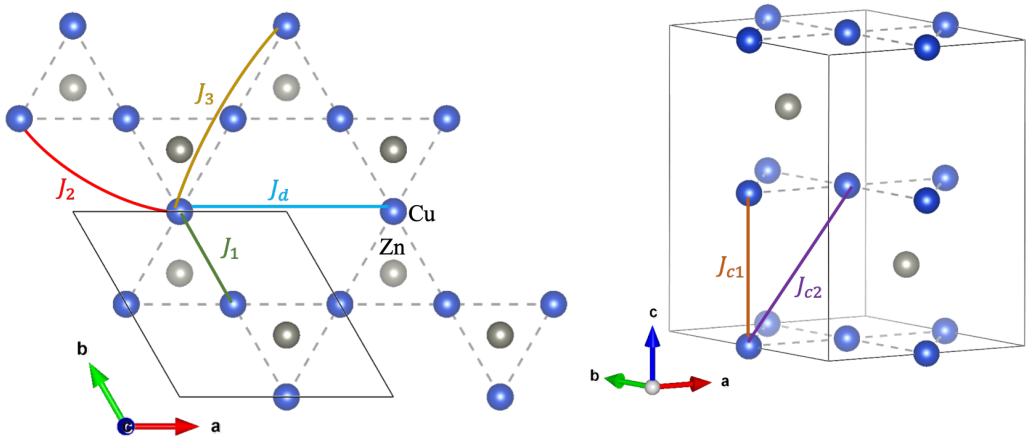

Figure 6.21: Zn-claringbullite structure determined from the D2B data Rietveld refinement at $T = 1.5$ K (Chapter 5), showing only the kagome Cu (blue) and interlayer Zn (grey) atoms, with the exchange interactions defined in Table 6.5.

i	d_i (Å)	J_i
1	3.33	J_1
c1	4.60	J_{c1}
c2	5.68	J_{c2}
2	5.77	J_2
3	6.66	J_3
d	6.66	J_d

Table 6.5: Zn-claringbullite Cu-Cu bond distances, d_i, for bond i with the associated exchange interaction, J_i. The distances were determined from the D2B data Rietveld refinement at $T = 1.5$ K (Chapter 5).

was analysed to determine the nature of the spin correlations using the reverse Monte Carlo (RMC) technique [28]. For an isotropic paramagnet, it is given by

$$S_{\text{mag}}(Q) = \int_{-\infty}^{\infty} S(Q,E)dE \tag{6.9}$$

$$= \frac{2}{3}|gf(Q)|^2 S(S+1)\left(1+\frac{1}{N}\sum_{i,j}\langle \mathbf{S}_i \cdot \mathbf{S}_j\rangle \frac{\sin(Qd_{ij})}{Qd_{ij}}\right), \tag{6.10}$$

where N is the number of spins in the system, $f(Q)$ is the magnetic form factor and $\langle \mathbf{S}_i \cdot \mathbf{S}_j\rangle$ are the spin correlations between spins separated by a distance d_{ij}. The diffuse magnetic scattering was separated from the incoherent phonons and normalised to absolute units by doing a Rietveld refinement on the elastic scattering, as described in Chapter 4. $S_{\text{mag}}(Q)$ was calculated by integrating over the magnetic diffuse scattering in $S(Q,E)$ in the range $0.1 < E < 12.0$ meV and SPINVERT [28] was used to fit the range $0.11 < Q < 1.98$ Å^{-1} to exclude the first coherent phonon near $Q = 2$ Å^{-1}. The program SPINVERT only accepts unit cells with orthogonal axes as input, so the $P6_3/mmc$ unit cell was converted to its maximal subgroup $Cmcm$ with $a = 11.5359$ Å, $b = 6.6603$ Å and $c = 9.1741$ Å, containing 12 Cu^{2+} atoms. The RMC fit was run with 1000 moves per spin for 10 independent cycles to assess the consistency of the results. Box sizes of $6 \times 6 \times 6$, $10 \times 10 \times 10$ and $12 \times 12 \times 12$ unit cells were trialled and it was found that it was unnecessary to

use a larger box than the $10 \times 10 \times 10$ supercell (containing 12000 spins) as the refinement began to over-fit the data at low Q. For the $10 \times 10 \times 10$ supercell, three fits are shown as an example in Figure 6.22a indicating consistent results for each independent run. The refined effective magnetic moment from SPINVERT, $\mu_{\text{eff}} = 1.705(1)\ \mu_{\text{B}}$, is in good agreement with the spin-only value of 1.73 μ_{B}, which gives confidence to these results.

The program SPINCORREL [28] was used to calculate the average spin correlations over ten independent cycles. For each box size up to a Cu-Cu distance $d_{3,d} = 6.660$ Å, they are compared in Figure 6.22b and reach a plateau after the

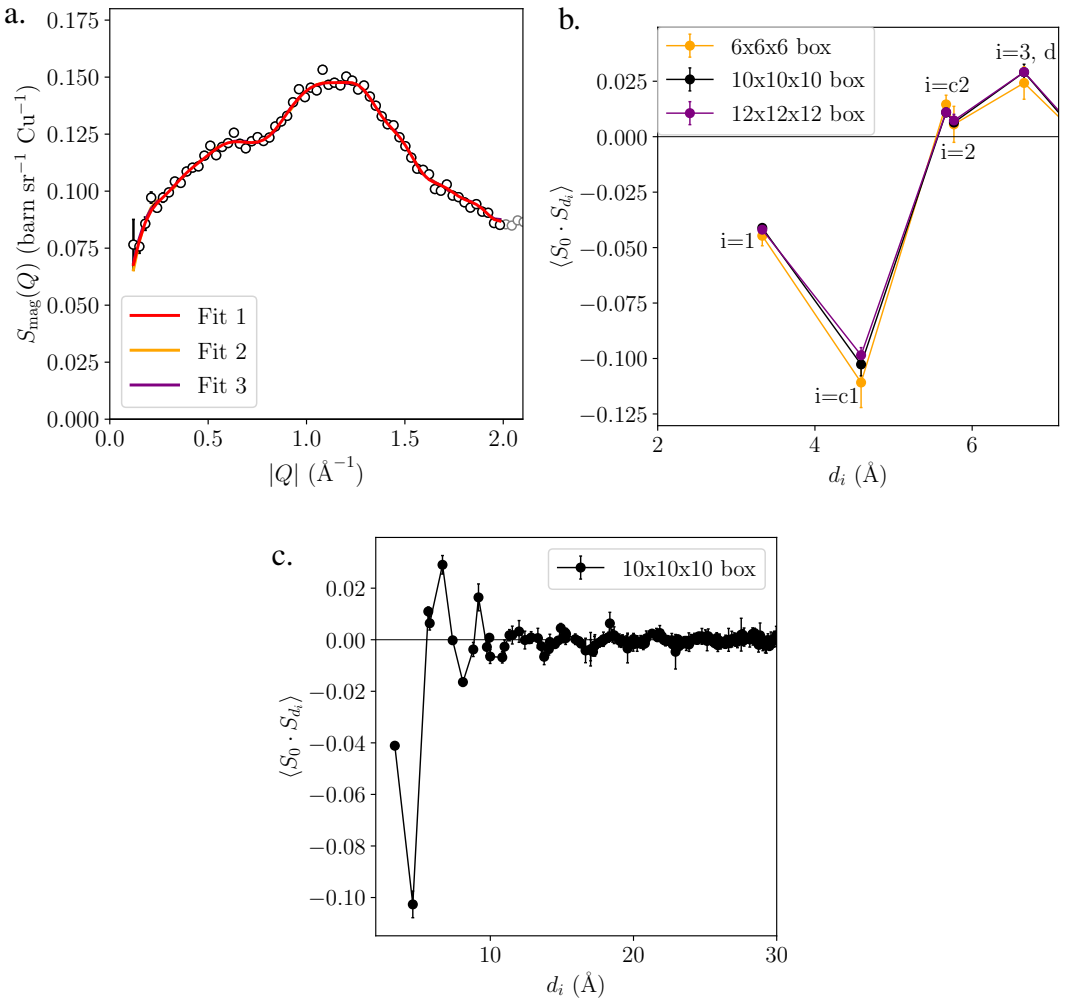

Figure 6.22: Zn-claringbullite LET data. **a.** $S(Q,E)$ integrated between 0.1 and 12.0 meV as a function of Q. The full data set is shown in grey and the black region was used for the RMC fits (Fit 1, 2 and 3). **b.** Spin pair correlation function up to $d_i = 6.66$ Å for different box sizes. **c.** Spin pair correlation function for the $10 \times 10 \times 10$ box size.

$10 \times 10 \times 10$ supercell. For the $10 \times 10 \times 10$ supercell, the spin correlations up to $d_i = 20$ Å are plotted in Figure 6.22c. The most significant correlation is for the interlayer distance, $d_{c1} \approx 4.56$ Å, and is negative, indicating antiferromagnetic coupling between kagome layers. The first neighbour correlation in the kagome plane is also antiferromagnetic, as expected from the large negative Weiss temperature. For $d_i \geq 8.8$ Å the correlations become increasingly smaller and average to around zero.

The first moment of the magnetic scattering for powder averaged data [27], is given by

$$\langle E \rangle = \int_{-\infty}^{\infty} S_{\text{mag}}(Q,E) E dE = \frac{2}{3} \left| \frac{g}{2} f(Q) \right|^2 \frac{1}{N} \sum_{r,d} J_{\mathbf{d}} \langle \mathbf{S_r} \cdot \mathbf{S_{r+d}} \rangle \left(\frac{\sin Qd}{Qd} - 1 \right), \tag{6.11}$$

where the sum is taken over all Cu-Cu bond distances $d = |\mathbf{d}|$ and all spins, $\mathbf{S_{r+d}}$. $J_{\mathbf{d}}$ are the exchange interactions, and $\langle \mathbf{S_r} \cdot \mathbf{S_d} \rangle$ are the spin correlations. The magnetic form factor, $|f(Q)|^2$ is given by

$$|f_{Cu^{2+}}(Q)|^2 = (A\mathrm{e}^{-as^2} + B\mathrm{e}^{-bs^2} + C\mathrm{e}^{-cs^2} + D)^2 \tag{6.12}$$

for the magnetic atom Cu^{2+}, where $s = |Q|/4\pi$, $A = 0.0232$, $a = 34.9686$, $B = 0.4023$, $b = 11.5640$, $C = 0.5882$, $c = 3.8428$ and $D = -0.0137$ [29]. The data were normalised to absolute units as for SPINVERT. The Cu-Cu distances up to a separation of 6.66 Å (3rd n.n. distance) were taken into account (see Table 6.6 and Figure 6.21). The 3rd n.n., J_3, and the kagome diagonal, J_d, have the same distance and cannot be differentiated in this type of analysis. Equation 6.11 thus becomes

$$\langle E \rangle \propto |f(Q)|^2 \frac{1}{N} \sum_i A_i \left(\frac{\sin Qd_i}{Qd_i} - 1 \right), \tag{6.13}$$

where the number of atoms $N = 3$ and the bond energies A_i are:

$$A_1 = 12J_1\langle \mathbf{S}_0 \cdot \mathbf{S}_{d_1} \rangle, \tag{6.14}$$

$$A_{c1} = 6J_{c1}\langle \mathbf{S}_0 \cdot \mathbf{S}_{d_{c1}} \rangle, \tag{6.15}$$

$$A_{c2} = 24J_{c2}\langle \mathbf{S}_0 \cdot \mathbf{S}_{d_{c2}} \rangle, \tag{6.16}$$

$$A_2 = 12J_2\langle \mathbf{S}_0 \cdot \mathbf{S}_{d_2} \rangle, \tag{6.17}$$

$$A_3 = 12J_3\langle \mathbf{S}_0 \cdot \mathbf{S}_{d_3} \rangle + 6J_d\langle \mathbf{S}_0 \cdot \mathbf{S}_{d_3} \rangle. \tag{6.18}$$

For this analysis $S(Q,E)$ was multiplied by E and integrated between 0.1 and 12.0 meV, consistent with the zeroth-moment analysis, and equation 6.13 was used to fit the data using least-squares minimisation. Figure 6.23a shows each bond energy contribution plotted separately and it is evident that the curve yielded by $i = 1$ (1st n.n. with J_1) best represents the position of the first peak, but not the peak amplitude. Figure 6.23b shows combinations of different terms to improve the fit, and since the curves yielded by $i = 2$ and $i = c2$ are very similar (see Figure 6.23a), A_2 and A_{c2} were set to be equal. Least squares minimisation quickly results in highly correlated refined variables when the number of parameters is more than about three, but Figure 6.23b shows that three parameters are not adequate to fit the peak near $Q = 1.2$ Å^{-1}. The best fit was found to require at least four A_i parameters and is shown by the blue curve in Figure 6.23b. These fits indicate that contributions from longer bonds are important at low Q. The A_i values for the best fit are shown in Figure 6.23c.

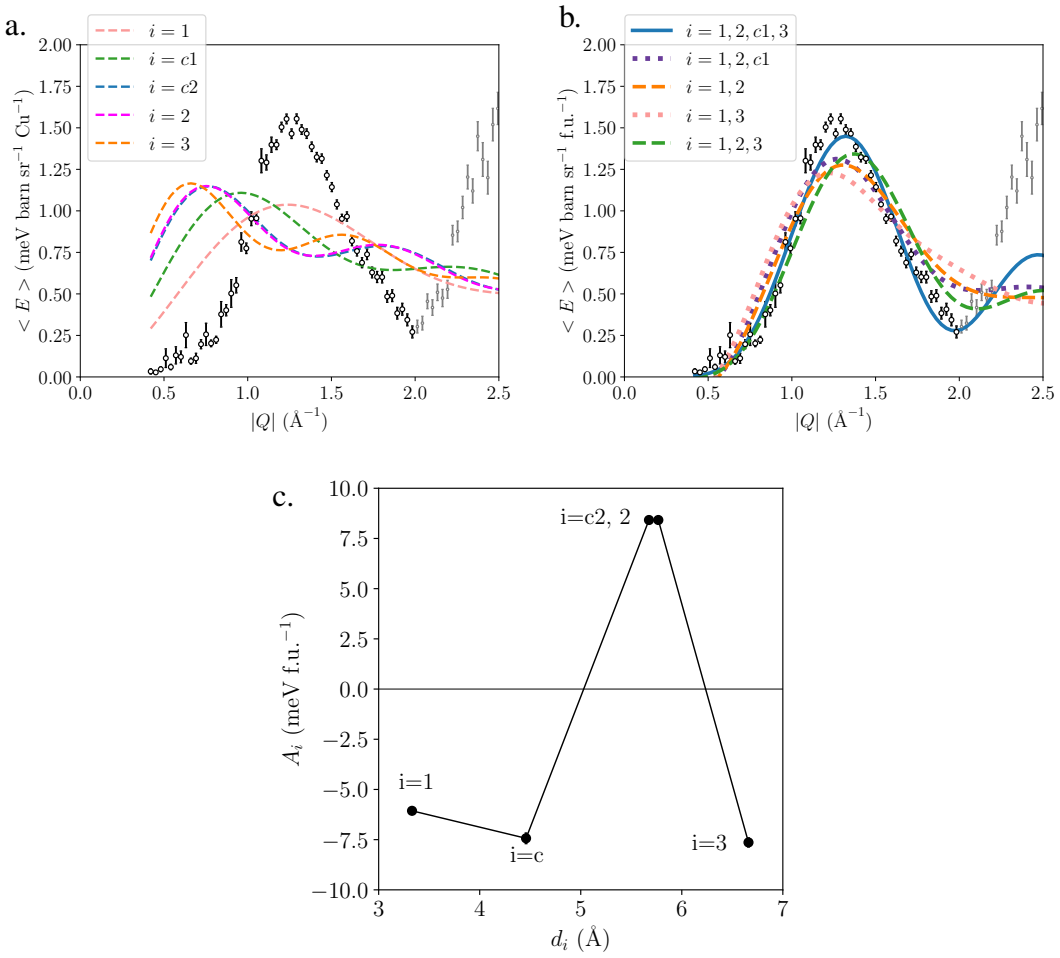

Figure 6.23: Zn-claringbullite LET data at $T = 1.5$ K. First moment of $S(Q,E)$ obtained by integrating over combined data with $E_i = 2.82, 5.96$ and 20.03 meV, between 0.1 and 12 meV (black) and normalised per formula unit. The first moment sum rule (equation 6.13) was used for the fits. **a.** Separate terms for the unique Cu-Cu bond distances in Table 6.6. **b.** Different models attempted. The best fit (blue) required all four A_i parameters ($A_2 = A_{c2}$) with a reduced χ^2 value of 8.41. **c.** Bond energies, A_i, resulting from the best fit in **b.**.

Due to the limited Q range in the first moment, it was not possible to accurately refine the bond energies. However, their signs can be used to determine whether the exchange interactions are ferro- or antiferromagnetic. Combining the signs of the spin correlations with those of the bond energies results in the exchange signs shown in Table 6.6. They indicate a largely antiferromagnetic system, in agreement with the large negative Weiss temperature of –261 K.

i	d_i (Å)	J_i	Sign of J_i
1	3.33	J_1	+
c1	4.60	J_{c1}	+
c2	5.68	J_{c2}	+
2	5.77	J_2	+
3, d	6.66	$2J_3 + J_d$	–

Table 6.6: Zn-claringbullite Cu-Cu bond distances, d_i, for bond i are given with the associated exchange interaction, J_i and the resulting sign of J_i from the spin correlations and bond energies determined in the zeroth- and first-moment analyses. $J_i > 0$ indicates an antiferromagnetic exchange interaction.

The Q positions of the magnetic excitations suggest $\mathbf{k} = \mathbf{0}$ type short-range correlations in Zn-claringbullite. Assuming a dominant first neighbour interaction and negligible interlayer couplings, a $J_3 - J_d$ classical phase diagram for the kagome lattice can be constructed [9]. For $J_1 = 1$ and $J_2 = 0$ this is shown in Figure 6.24a, indicating that for a system to have $\mathbf{k} = \mathbf{0}$ type order, J_3 and/or J_d must be ferromagnetic. For a small antiferromagnetic J_2 this would still be the case (see Figure 6.24b). The consistency between the nature of the exchange couplings and the characteristic wave vector of the inelastic magnetic excitations, lends confidence to the results of the zeroth- and first-moment analyses.

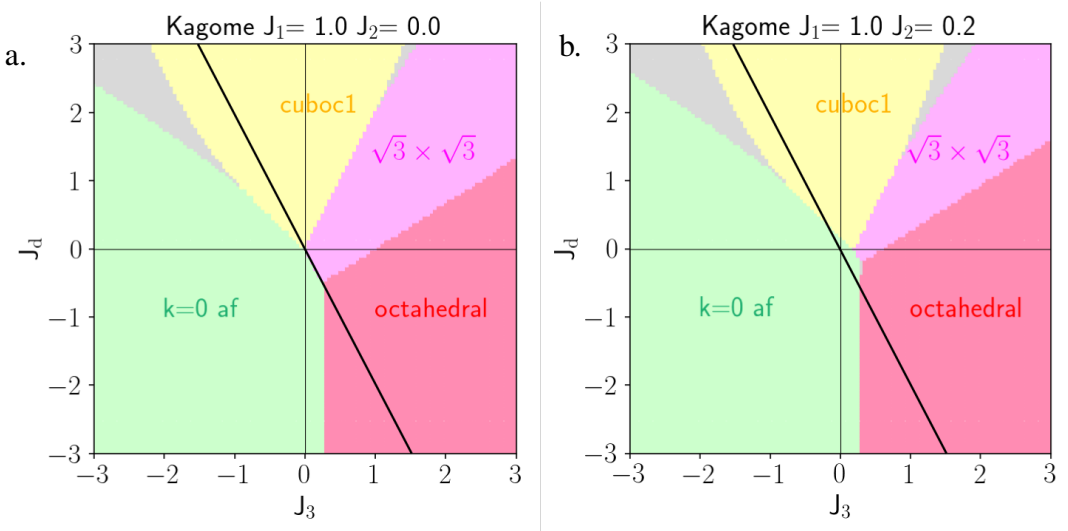

Figure 6.24: Classical phase diagrams for $J_3 - J_d$ on a regular kagome lattice with $J_1 = 1$ and **a.** $J_2 = 0$ or **b.** $J_2 = 0.2$. The grey regions are spiral states. The black lines show the relation $2J_3 + J_d = 0$.

6.4 Discussion

This chapter has presented the results of the INS experiments for claringbullite and Zn-claringbullite separately. From the low-temperature crystal structures of the two samples, the systems seem to be fundamentally different in that Zn-claringbullite can be considered an undistorted kagome system and claringbullite a distorted pyrochlore system. Despite these differences, the magnetic excitations seen in the INS data of the $x = 0$ correlated paramagnetic state ($T = 25$ K) and of the $x = 1$ spin-liquid state ($T = 1.7$ K) are similar, so a quantitative comparison will be given in Section 6.4.1. Section 6.4.2 will then compare our results for Zn-claringbullite with herbertsmithite and the literature report of Zn-doped barlowite [30].

6.4.1 Comparing claringbullite to its Zn-doped variant

For a quantitative comparison between the $x = 0$ and $x = 1$ systems of the claringbullite series, $Zn_xCu_{4-x}(OD)_6FCl$, the data were normalized to the nuclear Bragg peaks and placed on an absolute scale per formula unit (normalization details in Chapter 4). The two excitations were compared using $\chi''_Q(E)$ and $\chi''_E(Q)$ of claringbullite at $T = 25$ and 100 K, and of Zn-claringbullite at $T = 1.7$ and 50 K.

The Q dependence of the correlations was compared using $\chi''_E(Q)$ integrated between $5.0 < E < 6.0$ meV and $1.0 < E < 1.5$ meV, as shown in Figures 6.25a

and b, respectively. The solid lines are Gaussian fits with an incoherent phonon background and uncorrelated magnetic scattering given by

$$\chi''_E(Q) = |f_{Cu^{2+}}(Q)|^2[h\exp\left(-\frac{1}{2}\frac{(Q-Q_c)^2}{\sigma^2}\right)+d] + eE(a+b\,Q^2\exp(-cQ^2)), \quad (6.19)$$

where $f_{Cu^{2+}}(Q)$ is the Cu^{2+} magnetic form factor. The first part of the equation describes a Gaussian function and Q-independent uncorrelated magnetic scattering (apart from the magnetic form factor) given by d. For the Gaussian curve, h is the peak height, Q_c is the peak centre and σ is related to the FWHM through $\sqrt{8\ln 2}\sigma$. The second part of the equation describes the incoherent phonon Q dependence as was given in equation 6.1. The pre-factor eE is the linear dependence of the incoherent phonons on energy transfer, E, and e is refined in the fits shown in Figures 6.25c and d. The results of the Gaussian fits are given in Tables 6.7 and 6.8.

At higher energy transfer the peaks in both samples are centred at $Q \approx 1.2$ Å^{-1}, with similar FWHM, indicating similar correlations in both materials. The background of the $x = 0$ sample, is approximately twice that of the $x = 1$ material and is attributed to incoherent phonon scattering (second part of equation 6.19), as it does not change with temperature for each sample. The Rietveld refinements in Chapter 5 indicated a 96% deuteration level in both materials, resulting in incoherent scattering cross-sections of 44.3 barn and 42.9 barn for the $x = 0$ and $x = 1$ samples, respectively. As a comparison, a deuteration level of 90% in the $x = 0$ sample, would lead to its incoherent scattering cross section to be approximately twice that of the $x = 1$ material.

A comparison of the peak areas of $x = 0$ at $T = 25$ K with $x = 1$ at $T = 1.7$ K, suggests that the number of Cu atoms that contribute to the higher energy response is the same. This strongly evidences that in both materials, the excitation near $Q = 1.2$ Å^{-1} is a result of correlations from the kagome layers. When temperature increases to $T = 100$ K, the correlated magnetic scattering in the undoped claringbullite sample gets destroyed by the thermal fluctuations and no peak is observed.

The temperature dependence of Zn-claringbullite indicates that the correlations persist up to at least $T = 50$ K, with half the peak area at higher temperature.

At lower energy transfer (Figure 6.25b), there are three contributions to the scattering: incoherent phonons for which eE is determined from Figures 6.25c and d; uncorrelated magnetic scattering ($d \neq 0$ in equation 6.19) evidenced by the

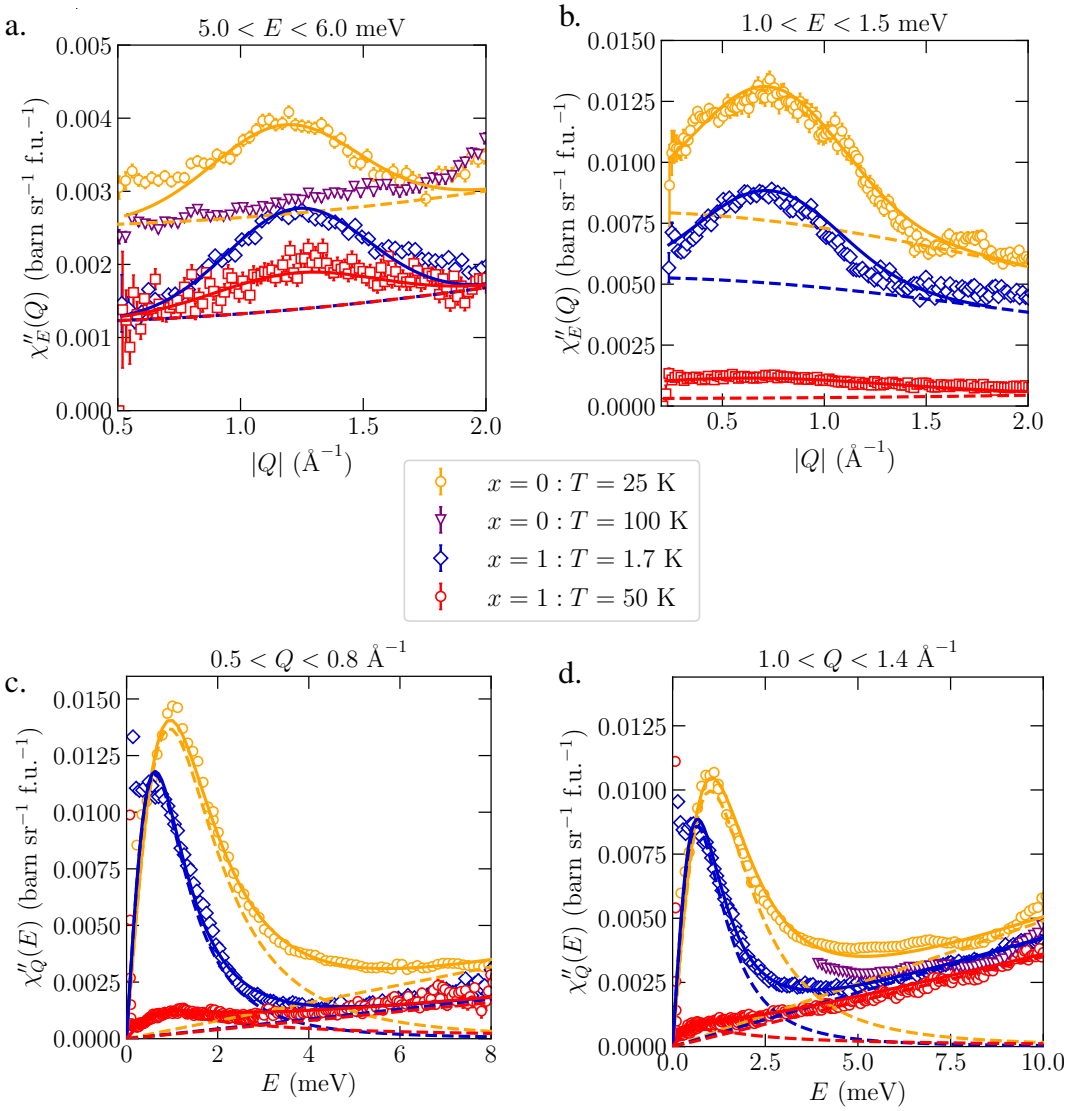

Figure 6.25: Claringbullite ($x = 0$ sample) at $T = 25$ K (orange) and Zn-claringbullite ($x = 1$ sample) at $T = 1.7$ K (blue) and $T = 50$ K (red). $\chi''_E(Q)$ integrated over **a.** $5.0 < E < 6.0$ meV and **b.** $1.0 < E < 1.5$ meV. The solid lines are Gaussian fits with a flat background (dashed lines). The peak centres are similar between the two samples, with values of ~ 0.7 Å^{-1} and ~ 1.2 Å^{-1}. $\chi''_Q(E)$ integrated over **c.** $0.5 < E < 0.8$ Å^{-1}and **d.** $1.0 < E < 1.4$ Å^{-1}. The solid lines are squared quasi-elastic Lorentzian fits with a line going through $\chi''_Q(E) = 0$ (dashed lines show the separate functions).

Sample	T (K)	Peak height	Position (Å^{-1})	FWHM (Å^{-1})	Area (meV Å^{-1})
$x = 0$	25	0.00128(2)	1.200(5)	0.706(11)	0.001053(19)
$x = 1$	1.7	0.00149(2)	1.253(4)	0.709(9)	0.01166(18)
$x = 1$	50	0.000753(24)	1.258(13)	0.824(1)	0.000621(21)

Table 6.7: Refined parameters from the Gaussian fits in Figure 6.25a for the $x = 0$ and $x = 1$ samples of the claringbullite series, $Zn_xCu_{4-x}(OD)_6FCl$, over $5 < E < 6$ meV.

Sample	T (K)	Peak height	Peak position (Å^{-1})	FWHM (Å^{-1})	Area (meV Å^{-1})
$x = 0$	25	0.00700(7)	0.750(2)	0.847(19)	0.00538(17)
$x = 1$	1.7	0.0040(3)	0.750(4)	0.745(34)	0.00321(2)
$x = 1$	50	0.000856(7)	0.683(21)	1.88(5)	0.00172(3)

Table 6.8: Refined parameters from the Gaussian fits in in Figure 6.25b for the $x = 0$ and $x = 1$ samples of the claringbullite series, $Zn_xCu_{4-x}(OD)_6FCl$, over $1.0 < E < 1.5$ meV.

change in "background" with temperature; and correlated magnetic scattering indicated by the peaks. The peak centres and FWHM are similar, suggesting that the low-energy response arises from similar correlations in the two samples. The correlated and uncorrelated magnetic contributions are 1.6 and 1.5 times more intense for claringbullite than for Zn-claringbullite, respectively. This suggests that the same atoms contribute to both the correlated and uncorrelated scattering. The zeroth-moment analysis on Zn-claringbullite indicated that the strongest correlations are between the kagome layers. Therefore, it is likely that these are the main contributor to the low-energy magnetic scattering in Zn-claringbullite. The additional intensity in the low-energy excitation of claringbullite, likely arises from the correlations between the kagome planes being strengthened by the additional exchange pathways provided by the interlayer Cu3.

At $T = 50$ K, $\chi''_E(Q)$ of Zn-claringbullite has completely collapsed and the peak area decreases by a factor of two. This is similar to the behaviour of the excitation near $Q = 1.2$ Å^{-1}, indicating that the correlations contributing to the two magnetic responses have a similar temperature dependence.

The energy dependence of the excitations was compared through $\chi''(Q,E)$ integrated between $0.5 < Q < 0.8$ Å^{-1} and $1.0 < Q < 1.4$ Å^{-1}, shown in Figures 6.25c

and d, respectively. In Sections 6.2.4 and 6.3.2, it was demonstrated that both excitations can be described by a squared QEL function, which describes over-damped excitations. The refined line widths are plotted in Figures 6.26a and b for the lower and higher Q ranges (Figures 6.25c and d), respectively. In Figures 6.25c and d, an additional line $\chi''_Q(E) = eE$ has been used to describe the high-energy behaviour. A linear behaviour can arise from both magnetic and phonon scattering, so this does not distinguish between the two. However, the temperature dependence of this scattering can be used to determine the magnetic contribution to the scattering, as it should lose intensity with temperature. At low Q (Figure 6.25c), claringbullite has a peak maximum at $E = \Gamma/\sqrt{3} = 0.940(3)$ meV, whereas Zn-claringbullite peaks at 0.624(2) meV. For Zn-claringbullite, $\chi''_Q(E)$ remains similar at $E \geq 5$ meV when temperature increases from $T = 1.7$ to 50 K, suggesting an absence of magnetic scattering above 5 meV. At higher Q (Figure 6.25d), the correlated scattering of claringbullite becomes completely diffuse by $T = 100$ K at $E \geq 5$ meV, evidenced by Figure 6.25a. Therefore, the intensity that remains in $\chi''_Q(E)$ at $T = 100$ K can be attributed to phonons. The line widths, Γ, determined at both lower and higher Q ranges (Figures 6.26a and b), suggest that claringbullite does not follow the same linear temperature dependence as Zn-claringbullite. Since Γ is inversely propor-

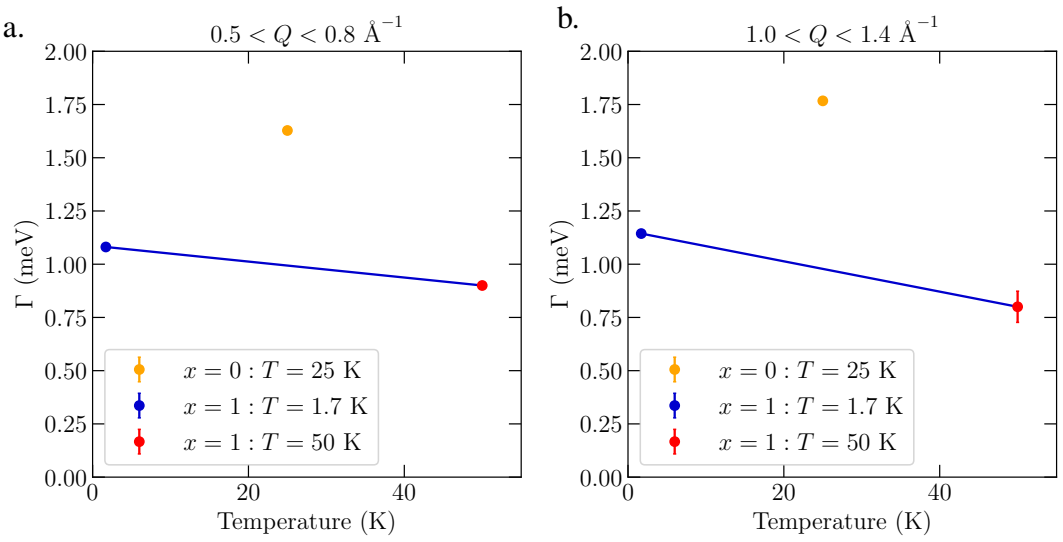

Figure 6.26: Line widths refined in **a.** Figure 6.25c and **b.** Figure 6.25d for claringbullite ($x = 0$ sample) at $T = 25$ K (orange) and Zn-claringbullite ($x = 1$ sample) at $T = 1.7$ K (blue) and $T = 50$ K (red). The error bars for some points are too small to be seen.

tional to the relaxation time of the excitations, these results indicate that the excitations of Zn-claringbullite have a longer relaxation time than those of claringbullite.

Figure 6.25c shows that as temperature increases $\chi''_Q(E)$ of the $x = 1$ sample, decreases more at low than at high E in agreement with $\chi''_E(Q)$ in Figure 6.25b. However, at $E > 5$ meV $\chi''_Q(E)$ remains similar, strongly suggesting that the scattering above 5 meV has a phonon origin rather than a magnetic one. At higher Q (Figure 6.25d), the behaviour at low-energy is similar as it corresponds to the tail of the low energy response, whereas at high E $\chi''_Q(E)$ loses some intensity with temperature. For claringbullite, this implies that the scattering observed at $T = 100$ K originates from phonons and the additional scattering at $T = 1.7$ K is the magnetic contribution. For Zn-claringbullite at $T = 50$ K, there is a phonon and magnetic contribution at high E evidenced by the peak in Figure 6.25a.

Zn-claringbullite and herbertsmithite are both hydroxide materials formed of Cu kagome planes, where one of the Cl^- ions in the latter is replaced by the electronegative F^- ion in the former. As previously mentioned, the result of this is an *AA* stacking of the kagome layers in Zn-claringbullite as opposed to the *ABC* layering in herbertsmithite. Due to their structural similarities, it is interesting to note that previous characterisations of the energy dependence of the magnetic excitations in herbertsmithite, indicated them to be well-described by a damped harmonic oscillator (DHO) fit (see equation 6.4), evidencing underdamped excitations with $\Gamma \approx 0.19$ meV$< E_0 \approx 0.290$ meV [4]. This indicates a different type of magnetic behaviour in Zn-claringbullite, for which we find overdamped excitations (Figures 6.25c and d).

6.4.2 Zn-claringbullite as a new candidate quantum spin liquid

The inelastic neutron scattering (INS) spectra of Zn-claringbullite showed diffuse magnetic excitations with two responses and a detailed discussion of their likely origins was provided in Section 6.4.1. The absence of a magnetic phase transition in the magnetic susceptibility (Chapter 5), as well as the absence of magnetic Bragg peaks in the INS data indicated that Zn-claringbullite is a good quantum spin liquid candidate. Broadly, quantum spin liquids can be classified by whether their excita-

tions have a gap to zero energy or not, making the determination of a gap important [31]. The squared QEL fits (Section 6.3.2) indicated Zn-claringbullite to be gapless at least down to 0.27 meV. Local probe measurements such as NMR may be able to determine whether Zn-claringbullite is truly gapless, which would help in the classification of its ground state.

In the literature, INS and NMR measurements on barlowite and Zn-barlowite [30] were used to indicate gapped magnetic excitations in both samples. For Zn-barlowite, a gap of 0.65 meV has been previously suggested using NMR measurements [32] and literature INS data show a similar gap size at $Q \approx 1$ Å^{-1} [30]. Despite the findings of gapped magnetic excitations in Zn-barlowite [30], they are visually similar to the INS spectra of the Zn-claringbullite presented in our work for which we find gapless ($E \geq 0.27$ meV) excitations. The similarities between the INS spectra of Zn-barlowite and Zn-claringbullite are likely due to the two materials being isostructural and a determination of a possible gap in Zn-claringbullite will indicate whether it hosts the same type of QSL state as found in Zn-barlowite.

The Q positions of the excitations in the INS data of Zn-claringbullite indicated that the short-range order ($8.3 - 9.5$ Å) is likely $\mathbf{k} = \mathbf{0}$, corresponding to the Γ point in the trigonal Brillouin zone. The $Q = 0.68$ Å^{-1} and 1.29 Å^{-1} peaks are indexed by the (0, 0, 1) and (1, 0, 1) expected reflections for $\mathbf{k} = \mathbf{0}$, respectively, implying the presence of spin correlations between kagome layers. This suggests a 3-D magnetic system rather than a 2-D one as initially hypothesised. The model-free zeroth- and first-moment analyses also pointed to $\mathbf{k} = \mathbf{0}$ type short-range order, but determining the exchange parameters from these analyses was not possible due to coherent phonons limiting the accessible Q range of the magnetic scattering. Experimentally this could be improved using polarised neutron scattering, as the magnetic scattering can be separated from the phonon one. This type of analysis would also be further improved by INS measurements on single crystals, as the spatial component of the excitations could be used to indicate the important Cu-Cu bond distances in different crystallographic directions.

A key finding in this work is that the spin correlations between kagome lay-

ers are the strongest and are negative, indicating a predominant antiparallel spin alignment and implying a degree of coupling between the kagome layers. In the geometrically similar parent material, claringbullite, it was found that the best exchange models determined in Section 6.2.5 have an inter-kagome coupling of $J_c/J_1 \approx 14-30\%$ that is stronger than the second n.n. exchange in the kagome layers, J_2. In claringbullite, this is supported by shorter Cu-Cu distances between kagome layers compared to the J_2 pathway. The relative distances of these pathways are the same in Zn-claringbullite, further highlighting the importance of the inter-kagome exchange path in understanding the magnetic behaviours of these materials. Previous calculations using the coupled-cluster method, found that for a $S = 1/2$ layered kagome system, such as Zn-claringbullite, an inter-kagome coupling of up to 15% of the n.n. J_1 will not destroy a QSL state in favour of a long-range ordered one (irrespective of the sign of J_c) [33]. While we assumed that the inter-kagome exchange interaction J_c is negligible to allow a comparison with the pre-existing classical phase diagram of the kagome lattice, it will be interesting to determine whether Zn-claringbullite fits into the QSL region of the previously reported J_c/J_1 phase diagram [33].

It is now interesting to compare the excitations observed for Zn-claringbullite with those previously observed for herbertsmithite, which is perhaps the best realisation of the $S = 1/2$ Heisenberg model on the kagome lattice [34, 35]. Its Hamiltonian has dominant nearest-neighbour exchange couplings, but includes small Dzyaloshinskii-Moriya interactions [20] as well as $\sim 10\%$ symmetric exchange anisotropy [36]. Similar to Zn-claringbullite, the powder [34] and single crystal [35] INS data of herbertsmithite indicated two magnetic responses centred at $Q \approx 0.67$ Å^{-1} and $Q \approx 1.3$ Å^{-1}, which extend up to ~ 2 meV [35] and ~ 25 meV [34], respectively. Although part of the low-energy magnetic scattering was initially attributed to 15% Cu impurity spins on the interlayer sites [22], a variational Monte Carlo study showed it to be an intrinsic kagome response within the nearest-neighbour RVB model [37]. In our analysis of Zn-claringbullite, both magnetic responses are attributed to the kagome layers through comparison with the parent

material claringbullite. The percentage of impurity spins has to be determined in future studies using anomalous x-ray diffraction, for example, that is an element- and site-specific technique. Depending on their abundance, correlations involving impurity spins may have to be considered as part of the spin model that describes the observed magnetic excitations. Furthermore, unlike herbertsmithite that is a good approximation of a nearest-neighbour model [35], the correlations in Zn-claringbullite extend beyond this as shown by the FWHM of the Gaussian fits to $S_E(Q)$ and the analysis of the zeroth-moment of $S(Q,E)$. In Zn-claringbullite, the stronger spin correlations between kagome layers than within them, leads us to believe that the QSL flavour is different to that of herbertsmithite.

6.5 Future work

This chapter detailed the use of powder INS data and semi-classical spin wave theory, to propose an exchange interaction model in claringbullite. Attempting to determine the exchange interactions was challenging for two reasons: (*i.*) the magnetic structure of claringbullite is complicated and its low orthorhombic symmetry suggests that many competing interactions are relevant in the spin wave excitations, and (*ii.*) the use of powder averaged data meant that the directional spin wave information in reciprocal space was lost, so the effect of an exchange interaction on each excitation mode could not be determined uniquely. INS experiments on single crystals of claringbullite will be key in determining more accurate exchange interactions, and will help to understand the effect of Zn-doping on the exchange interactions by comparison with Zn-claringbullite.

The spin-liquid state in Zn-claringbullite was measured down to $T = 1.6$ K. Local probe techniques such as NMR and μSR can be used to reveal any trace glassiness and use of a dilution fridge would allow measurement of the spin fluctuations down to mK temperatures. Although we suggest that Zn-claringbullite hosts a QSL ground state, the determination of its exchange interactions will be key in placing it in a quantum spin liquid phase diagram. In the absence of single crystal INS data, one way to achieve this is by writing a Monte Carlo code to fit the first

moment, instead of using a least-squares approach. Furthermore, polarised neutron scattering experiments on these powder samples would allow the magnetic scattering to be isolated from the phonon one and the Q range would not be limited by coherent phonons.

6.6 Conclusions

This chapter presented the characterisation of the ground states of the $S = 1/2$ KAFM Zn-claringbullite and its parent material claringbullite. INS measurements showed the undoped claringbullite to have two gapped spin wave excitations below T_N, which became diffuse and ungapped above T_N. On the other hand, the INS measurements of Zn-claringbullite showed a continuum of diffuse excitations down to the lowest measured temperature, indicating the existence of a quantum spin liquid ground state. The excitations were found to be similar in Q position and E bandwidth to the excitations observed for the undoped claringbullite sample above T_N. The short-range correlations are reminiscent of $\mathbf{k} = \mathbf{0}$ fluctuations as determined by their Q positions and supported by the model-free zeroth- and first-moment analyses. Although these analyses did not provide exchange interaction values, they indicated a largely antiferromagnetic system in agreement with the large negative Weiss temperature of −206 K.

Attempts to simulate the experimentally observed spin wave excitations of claringbullite were made using linear spin wave theory in SpinW [15] and the newly developed Monte Carlo-like program Serendipity [25]. An exchange energy model was proposed that captures some of the main features of the data and builds on the literature exchange models of barlowite [12, 38]. Our work shows the requirement of additional further-neighbour exchange in the kagome layers as well as a sizeable inter-kagome exchange, J_c, to stabilise the experimental magnetic structure of claringbullite (that is similar to that of barlowite [19]). The importance of the exchange pathway between kagome layers in understanding the magnetic behaviour of the Zn-doped claringbullite family, is also highlighted by (*i.*) indexing the Zn-claringbullite excitations with the (0, 0, 1) and (1, 0, 1) expected reflections of the

$\mathbf{k} = \mathbf{0}$ characteristic wave vector and (*ii.*) by determining the inter-kagome correlations to be strongest from the radial spin correlation function of Zn-claringbullite.

Although the effect of each exchange interaction in claringbullite could not be directly related to specific spin wave branches, some patterns were found. For example, altering the magnitude of the inter-kagome J_c interaction was found to mainly affect the energy transfer of the ~ 2 meV excitation, along with a decrease in the ~ 10 meV excitation bandwidth. Moreover, it was discovered that the 'tripod' exchanges mainly affect the ~ 2 meV excitation, which was key in preferring a model of three distinct 'tripod' values rather than two as previously suggested [12]. The magnitude of J_c relative to the nearest-neighbour exchange in the kagome layers, J_1, was found to be of the order of $J_c/J_1 \approx 14-30\%$ to simulate spectra that resembled the experimental data, which is much larger than the value of $\sim 3\%$ previously suggested [12]. These studies provide insights into the exchange models that can both stabilise the observed magnetic structure and adequately describe the main features of the inelastic excitations observed in experiment, which are: the overall bandwidth of the two magnetic responses; their Q positions; the finite energy gap between them; and the zero-energy gap. Further investigation and refinement of these exchange models require future single crystal INS data.

The comparison of the correlations in claringbullite and Zn-claringbullite discussed in Section 6.4.1, indicated that the ~ 10 meV excitations likely originates from the kagome layers, whilst the ~ 2 meV response largely originates from inter-kagome correlations. This conclusion is supported by the sizeable inter-kagome exchange J_c found for undoped claringbullite, as well as the inter-kagome correlation in Zn-claringbullite being the strongest.

The spin models suggested for the Zn-doped claringbullite family include further-neighbour couplings within and between the kagome layers, suggesting a different QSL flavour in Zn-claringbullite to herbertsmithite [35]. These findings may be important in elucidating the magnetic behaviour of the Zn-doped barlowite family and could also be useful in understanding the magnetic excitations of clinoatacamite [11], the parent material of herbertsmithite.

Bibliography

[1] X. Y. Yue, Z. W. Ouyang, J. F. Wang, Z. X. Wang, Z. C. Xia, and Z. Z. He, Phys. Rev. B **97**, 054417 (2018).

[2] G. L. Squires, *Introduction to the Theory of Thermal Neutron Scattering*, 3rd ed. (Cambridge University Press, Cambridge, 2012).

[3] B. Fåk, E. Kermarrec, L. Messio, B. Bernu, C. Lhuillier, F. Bert, P. Mendels, B. Koteswararao, F. Bouquet, J. Ollivier, A. D. Hillier, A. Amato, R. H. Colman, and A. S. Wills, Phys. Rev. Lett. **109**, 037208 (2012).

[4] G. J. Nilsen, M. A. De Vries, J. R. Stewart, A. Harrison, and H. M. Rønnow, J. Phys. Condens. Matter **25**, 106001 (2013).

[5] L. Clark and A. H. Abdeldaim, Annu. Rev. Mater. Res. **51**, 495 (2021).

[6] D. Boldrin, B. Fåk, E. Canévet, J. Ollivier, H. C. Walker, P. Manuel, D. D. Khalyavin, and A. S. Wills, Phys. Rev. Lett. **121**, 107203 (2018).

[7] D. Boldrin, B. Fåk, M. Enderle, S. Bieri, J. Ollivier, S. Rols, P. Manuel, and A. S. Wills, Phys. Rev. B **91**, 220408 (2015).

[8] L. F. Jones, C. A. Kilner, and M. A. Halcrow, Polyhedron **26**, 1977 (2007).

[9] L. Messio, C. Lhuillier, and G. Misguich, Phys. Rev. B **83**, 184401 (2011).

[10] T.-H. Han, E. D. Isaacs, J. A. Schlueter, and J. Singleton, Phys. Rev. B **93**, 214416 (2016).

[11] A. S. Wills, T. G. Perring, S. Raymond, B. Fåk, J.-Y. Henry, and M. Telling, J. Phys. Conf. Ser. **145**, 012056 (2009).

[12] H. O. Jeschke, F. Salvat-Pujol, E. Gati, N. H. Hoang, B. Wolf, M. Lang, J. A. Schlueter, and R. Valentí, Phys. Rev. B **92**, 094417 (2015).

[13] D. Guterding, R. Valentí, and H. O. Jeschke, Phys. Rev. B **94**, 125136 (2016).

[14] D. I. Khomskii, *Basic Aspects of The Quantum Theory of Solids* (Cambridge University Press, Cambridge, 2010).

[15] S. Toth and B. Lake, J. Phys. Condens. Matter **27**, 166002 (2015).

[16] B. Fåk and S. Toth, *Tutorial 7: k=0 Kagome antiferromagnet*, (Feb. 2016) https://spinw.org/tutorials/07tutorial.

[17] B. Fåk and S. Toth, *Tutorial8: sqrt(3) x sqrt(3) Kagome antiferromagnet*, (Feb. 2017) https://spinw.org/tutorials/08tutorial.

[18] K. Tustain, E. E. McCabe, A. M. Arevalo-Lopez, A. S. Gibbs, S. P. Thompson, C. A. Murray, C. Ritter, and L. Clark, Chem. Mater. **33**, 9638 (2021).

[19] K. Tustain, G. J. Nilsen, C. Ritter, I. Da Silva, and L. Clark, Phys. Rev. Mater. **2**, 111405 (2018).

[20] M. Rigol and R. R. P. Singh, Phys. Rev. B **76**, 184403 (2007).

[21] T. Moriya, Phys. Rev. **120**, 91 (1960).

[22] T. H. Han, M. R. Norman, J. J. Wen, J. A. Rodriguez-Rivera, J. S. Helton, C. Broholm, and Y. S. Lee, Phys. Rev. B **94**, 060409 (2016).

[23] A. Zorko, S. Nellutla, J. van Tol, L. C. Brunel, F. Bert, F. Duc, J.-C. Trombe, M. A. de Vries, A. Harrison, and P. Mendels, Phys. Rev. Lett. **101**, 026405 (2008).

[24] R. Coldea, D. A. Tennant, K. Habicht, P. Smeibidl, C. Wolters, and Z. Tylczynski, Phys. Rev. Lett. **88**, 137203 (2002).

[25] A. S. Wills, Private communication (2022).

[26] D. Boldrin, Private communication (2021).

[27] M. B. Stone, Y. Chen, J. Rittner, H. Yardimci, D. H. Reich, C. Broholm, D. V. Ferraris, and T. Lectka, Phys. Rev. B **65**, 064423 (2002).

[28] J. A. M. Paddison, J. Ross Stewart, and A. L. Goodwin, J. Phys. Condens. Matter **25**, 454220 (2013).

[29] A.-J. Dianoux and G. Lander, *Neutron Data Booklet*, 2nd (2003), pp. 5–1.

[30] Y. Wei, Z. Feng, W. Lohstroh, D. H. Yu, D. Le, C. d. Cruz, W. Yi, Z. F. Ding, J. Zhang, C. Tan, L. Shu, Y.-C. Wang, H.-Q. Wu, J. Luo, J.-W. Mei, F. Yang, X.-L. Sheng, W. Li, Y. Qi, Z. Y. Meng, Y. Shi, and S. Li, arXiv:1710.02991v3 (2020).

[31] C. Broholm, R. J. Cava, S. A. Kivelson, D. G. Nocera, M. R. Norman, and T. Senthil, Science **367**, eaay0668 (2020).

[32] Z. Feng, Z. Li, X. Meng, W. Yi, Y. Wei, J. Zhang, Y.-C. Wang, W. Jiang, Z. Liu, S. Li, F. Liu, J. Luo, S. Li, G.-q. Zheng, Z. Y. Meng, J.-W. Mei, and Y. Shi, Chin. Phys. Lett. **34**, 077502 (2017).

[33] O. Götze and J. Richter, EPL **114**, 67004 (2016).

[34] M. A. de Vries, J. R. Stewart, P. P. Deen, J. O. Piatek, G. J. Nilsen, H. M. Rønnow, and A. Harrison, Phys. Rev. Lett. **103**, 237201 (2009).

[35] T.-H. Han, J. S. Helton, S. Chu, D. G. Nocera, J. A. Rodriguez-Rivera, C. Broholm, and Y. S. Lee, Nature **492**, 406 (2012).

[36] T. Han, S. Chu, and Y. S. Lee, Phys. Rev. Lett. **108**, 157202 (2012).

[37] C. Zhang and T. Li, Phys. Rev. B **102**, 195106 (2020).

[38] T.-H. Han, J. Singleton, and J. A. Schlueter, Phys. Rev. Lett. **113**, 227203 (2014).

Chapter 7

Crystallographic and bulk magnetisation studies of the averievite series, $Zn_xCu_{5-x}(VO_4)_2O_2CsCl$ for x = 0, 1 and 2

7.1 Introduction

Although there has been an extensive materials search for model $S = \frac{1}{2}$ kagome magnets, no material has yet matched the simplicity of the KAFM theoretical model with equilateral triangles, and is without interplanar coupling and dilution of the kagome ions. This has stimulated experimentalists to search for new candidate QSL materials. This chapter presents the synthesis and characterisation of a series of compounds $Zn_xCu_{5-x}(VO_4)_2O_2CsCl$, where the parent material ($x = 0$) averievite was found in volcanic exhalations of the Great Tolbachik fissure eruption in Russia, 1975 [1]. Averievite is an oxide material containing a Cu^{2+} pyrochlore slab structure, where the slab layers are well separated by $CuVO_3$ and CsO_2 groups (Figure 7.1a). Alternatively, averievite's structure can be viewed as a Cu^{2+} kagome lattice sandwiched by two $Cu^{2+} - V^{5+}$ honeycomb lattices. The pyrochlore slab formed

by the magnetic atoms is shown in Figure 7.1b. Due to the electronic interactions of the honeycomb Cu^{2+} sites with the kagome lattice, averievite magnetically orders at $T_N = 24$ K [2]. Our goal was to suppress the magnetic ordering by deliberate doping of the honeycomb Cu^{2+} sites with diamagnetic Zn (Figure 7.1) to make an $x = 2$ sample, herein also referred to as Zn_2-averievite, representing the optimum stoichiometry for a $S = \frac{1}{2}$ kagome antiferromagnet.

This chapter will present neutron and x-ray diffraction data collected on $Zn_xCu_{5-x}(VO_4)_2O_2CsCl$ for $x = 0$, 1 and 2, as well as bulk magnetometry and elemental analysis using scanning electron microscopy with energy dispersive x-ray analysis for the two latter samples. As will be shown, undoped averievite undergoes a crystallographic as well as magnetic transition. We find that the $x = 1$ (Zn_1-averievite) and $x = 2$ (Zn_2-averievite) samples retain equilateral kagome triangles down to $T = 1.5$ K, which are rotated in the plane thereby distorting the kagome hexagons. Importantly, for the continuing search for model kagome QSLs, the DC magnetic susceptibility data collected on Zn_2-averievite suggest that no magnetic transition occurs down to $T = 2$ K.

7.2 Synthesis

7.2.1 Preliminary work

Previous studies on the averievite series, $Zn_xCu_{5-x}(VO_4)_2O_2CsCl$, were based on powder samples for $0 \leq x \leq 1$ where the maximum level corresponds to half the honeycomb Cu sites being replaced by Zn [2]. These samples were prepared using a solid state method, whereby the reagents were heated for 12 h, cooled to room temperature, pressed into a pellet and heated using the same temperature cycle for 12 h [2]. We followed this method and then adapted it to a one-step process: the ground reagents were pressed into a pellet and heated for 24 h before cooling. PXRD patterns of samples from the two methods showed similar purity and crystallinity so we opted for the one-step synthesis.

Laboratory PXRD patterns showed the products from both syntheses to have an insoluble CuO impurity that could not be removed post-synthesis, so attempts

were made to minimise it prior to heating. Botana *et al.* used a reagent ratio of $(5-x)$ CuO : x ZnO : 1 V_2O_5 : 1.048 CsCl, with a CsCl stoichiometric excess due to its volatility and we followed these ratios. To remove the CuO from the product, a CsCl series was attempted by varying the initial reagent amounts but this did not show any improvement. A series where the variable was the time spent grinding the reagents to homogenise the mixture, proved it to be a key factor in sample purity. Manual grinding in a pestle and mortar required a minimum of 20 min and to avoid this laborious process a ball mill was used.

Synthesis of the Zn-doped variants was initially attempted by replacing stoichiometric amounts of CuO with ZnO as in the literature [2]. Samples doped to the $x = 1$ level, contained large amounts of CuO ($\sim$ 15%), so a different method was developed to improve purity. In this method, stoiberite, $Cu_5(VO_4)_2O_2$, was synthesised first and CsCl was added in a second step. The synthesis of stoiberite is well-established in the literature [3]. Synthesising stoiberite as a first step was also attempted for the $x = 0$ sample and although laboratory PXRD showed the main phase to be averievite with $\sim$ 2% CuO, the DC magnetic susceptibility data showed a small ferromagnetic signal at room temperature suggesting a related impurity. Similar magnetometry studies on an $x = 0$ sample synthesised *via* the one-step method showed no ferromagnetic signal at room temperature and its magnetic susceptibility agreed with the literature value [2].

The alternate synthesis (CsCl added to stoiberite) was unsuccessful for $x = 2$ because $Zn_2Cu_3(VO_4)_2O_2$ is not a thermodynamically stable product, so the one-step $x = 0$ synthesis was adapted by replacing stoichiometric amounts of CuO with ZnO. Initial Rietveld refinements of the PXRD patterns after 24 h heating showed a $\sim$ 10% CuO impurity, so the product was re-ground, re-pelletised and re-heated as detailed below. Reducing the CuO impurity this way was also attempted for a one-step synthesis of Zn_1-averievite, but did not effectively reduce it.

7.2.2 Final synthesis

The final synthesis for averievite, $Cu_5(VO_4)_2O_2CsCl$, was as follows. V_2O_5 (Sigma-Aldrich, 0.25 g, 1.37 mmol), CuO (Sigma-Aldrich, 0.547 g, 6.87 mmol) and CsCl

(Alfa-Aesar, 0.243 g, 1.44 mmol) were pulverised using the Pulverisette 0 (Fritsch) agate ball mill with an amplitude of 1.5 mm for 10 min. The powder was pressed into 5 mm pellets and heated in an open alumina crucible at 500 °C for 24 h, cooled to 450 °C at 0.5 ° min^{-1} and then furnace cooled to room temperature. To synthesise Zn_2-averievite ($x = 2$), stoichiometric amounts of CuO were replaced with ZnO (Alfa-Aesar). The powder was pelletised and heated at 500 °C for 48 h, cooled to 450 °C at 0.5 ° min^{-1} and then furnace cooled to room temperature.

For Zn_1-averievite ($x = 1$), stoiberite was synthesised and used as a precursor: V_2O_5 (Sigma-Aldrich, 0.25 g, 1.37 mmol), CuO (Sigma-Aldrich, 0.437 g, 5.50 mmol) and ZnO (Alfa Aesar, 0.112 g, 1.38 mmol) were pulverised for 10 min and pelletised. The pellets were placed into capped alumina crucibles, heated to 800 °C at 60 °C h^{-1}, held for 72 h and cooled to room temperature at 60 °C h^{-1}. For the final product, the stoiberite pellet was manually ground with CsCl in a 1:1.048 ratio for 20 min and re-pelletised. The pellet was heated in an open alumina crucible at 500 °C for 24 h, cooled to 450 °C at 0.5 ° min^{-1} and then furnace cooled to room temperature.

7.3 Structural studies

Laboratory PXRD was initially used in transmission geometry to characterise all samples. It was previously found that averievite goes through structural distortions at $T = 310$ K and 127 K. To observe any peak splitting and verify the crystal structures of the $x = 0$, 1 and 2 samples, data with a higher resolution was required, so synchrotron diffraction data were obtained on the 11-BM beamline at the Advanced Photon Source, USA ($\lambda = 0.457794$ Å). Neutron diffraction experiments down to $T = 1.5$ K were performed to determine more accurate positions for the light atoms, O and Cl, that can be difficult using PXRD due to their small structure factors. Measurements were made on the time-of-flight high-resolution diffractometer HRPD, ISIS as well as the constant wavelength high-flux diffractometer D2B, ILL. A summary of the data collection conditions is given in Table 7.1. The literature crystal structure of averievite will first be presented and then the results of scanning elec-

tron microscopy with energy dispersive x-ray analysis will be discussed, followed by the findings from the structural refinements.

Sample \ T (K)	1.5	25	50	75	100	300
$x = 0$	HRPD	HRPD	HRPD	HRPD	HRPD/ 11-BM	D2B/ 11-BM
$x = 1$	HRPD	-	-	-	HRPD/ 11-BM	-
$x = 2$	HRPD	-	-	-	HRPD/ 11-BM	D2B

Table 7.1: Summary of powder neutron and synchrotron x-ray data collected on HRPD, 11-BM ($\lambda = 0.457794$ Å and 0.457841 Å) and D2B ($\lambda = 1.595226$ Å) for the averievite series, $Zn_xCu_{5-x}(VO_4)_2O_2CsCl$.

7.3.1 Literature crystal structure of averievite

Averievite, $x = 0$, is reported to crystallise in the trigonal $P\bar{3}m1$ structure at $T =$ 400 K, with a trigonal-monoclinic transition at $T = 310$ K. At $T = 295$ K its crystal structure is described in the monoclinic $P12_1/c_1$ space group [2]. The literature lattice parameters can be found in Table 7.2. The trigonal structure is formed of two crystallographically inequivalent Cu^{2+} (or Zn^{2+}) sites: one forms the kagome planes, Cu_k, whilst the other, Cu_h, caps the triangles (Figure 7.1). Cu_h has a trigonal bipyramidal coordination to three equatorial oxygens (VO_4 basal oxygens) and two apical oxygens (an axial VO_4 oxygen and an intra-kagome one lying in the centre of the kagome triangles). Cu_k forms $CuVO_3$ layers which are separated by CsO_2

	Temperature / K	
	400	295
Space group	$P\bar{3}m1$	$P12_1/c1$
a (Å)	6.369326	8.373335
b (Å)	6.369326	6.366556
c (Å)	8.375817	11.01280
α (°)	90.0000	90.0000
β (°)	90.0000	90.0221
γ (°)	120.0000	90.0000

Table 7.2: Lattice parameters of undoped averievite at $T = 295$ K and 400 K reported in the literature [2].

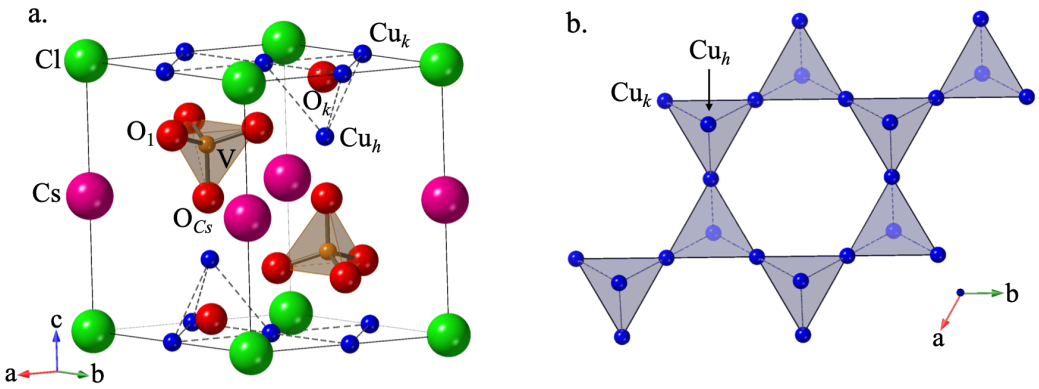

Figure 7.1: Averievite. **a.** $P\bar{3}m1$ crystal structure of averievite at $T = 310$ K with lattice parameters and atomic positions from the literature [2]. **b.** Cu^{2+} pyrochlore slab structure, where Cu_k forms a kagome plane and each kagome triangle is capped by Cu_h, which forms a $Cu^{2+} - V^{5+}$ honeycomb lattice.

and the Cl^- ions lie in the centre of the kagome hexagons.

7.3.2 Scanning electron microscopy with energy dispersive x-ray analysis

Scanning electron microscopy with energy dispersive x-ray analysis (SEM-EDX) was carried out on the Zn_1 and Zn_2-averievite samples for two reasons: (*i.*) to image the crystallites and rule out the presence of an impurity phase, and (*ii.*) to get a good estimate of the sample stoichiometries. For these measurements, a few mg of each sample were dusted onto conductive carbon tape stuck onto a metal base and placed on a rotating metal disk in a sample chamber that was evacuated.

For the EDX, a Co standard was used as a reference material for the spectra and measurements were made on various parts of the sample to reduce statistical errors. Four spectra were collected for the Zn_1-averievite and three for Zn_2-averievite. Figure 7.2 shows the measured weight % of each element for both samples with standard deviations, compared to the nominal stoichiometric weight %. The values for oxygen were calculated according to the nominal stoichiometries. For the $x = 1$ sample, the calculated Zn value has a 7.29% difference from the measured one, falling just outside the standard deviation ($\pm 5.26\%$), whereas Cu and V are within error. For the $x = 2$ sample, the calculated values for Zn, Cu and V are all within

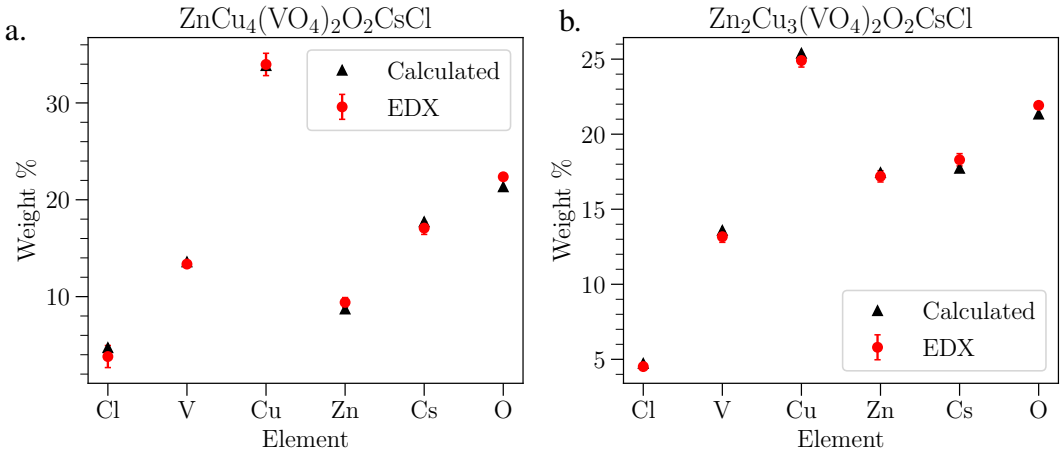

Figure 7.2: Weight % of elements for **a.** Zn_1-averievite and **b.** Zn_2-averievite measured by EDX (red) with error bars representing the standard deviation and the calculated values for the nominal stoichiometry are shown by the black markers.

the standard deviation error. Atomic percentages were used to quantify the ratio of chemical elements present relative to V. For Zn_1-averievite the nominal ratios of V:Zn:Cu are 1:0.5:2 and EDX gave 1:0.548:2.039. For Zn_2-averievite the nominal V:Zn:Cu ratios are 1:1:1.5 and the measured ones are 1:1.017:1.517. These results indicate that the stoichiometries of both the $x = 1$ and 2 samples are close to the nominal ones and can be fixed to the nominal ones in the structural refinements.

SEM images of Zn_1- and Zn_2-averievite are shown in Figures 7.3 and 7.4, respectively. Both materials have 2-dimensional crystallites with diameters up to a few μm and no amorphous impurity phase can be seen in either sample.

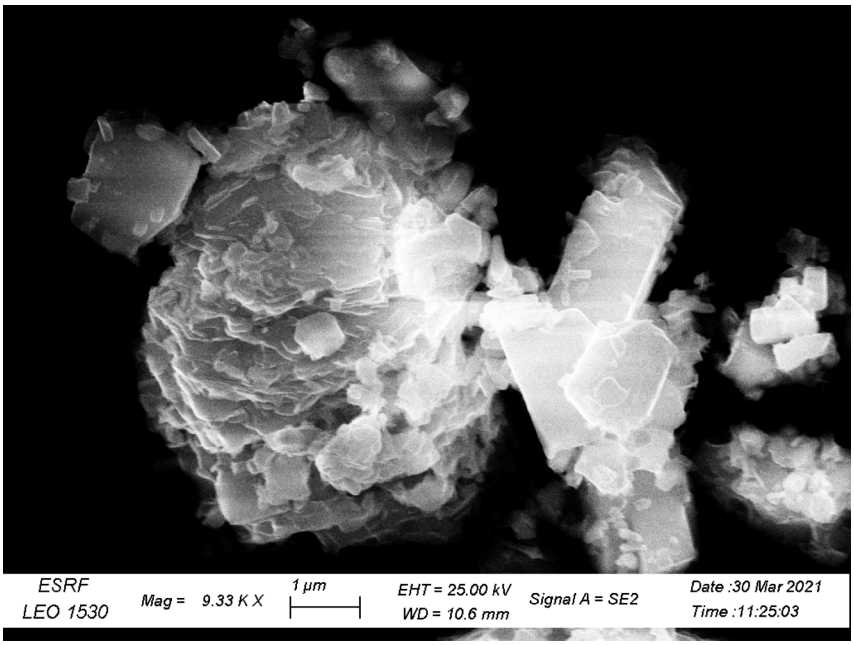

Figure 7.3: SEM image of Zn_1-averievite showing platelets of various sizes up to a few µm and no amorphous impurity phase.

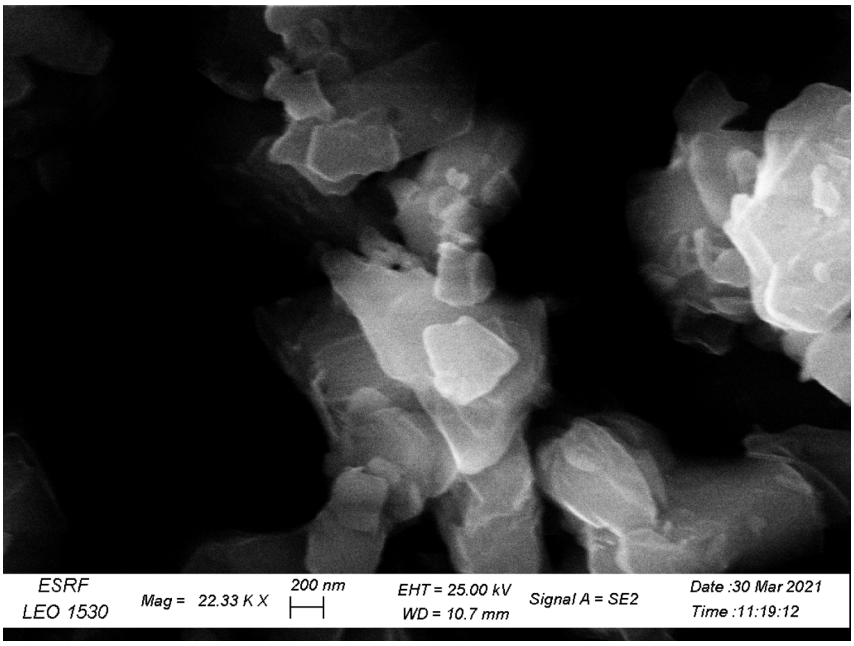

Figure 7.4: SEM image of Zn_2-averievite showing 2-dimensional crystallites up to $\sim$ 1 µm in diameter and no amorphous impurity phase.

7.3.3 Laboratory x-ray diffraction

Laboratory powder x-ray diffraction (PXRD) was carried out in flat-plate mode with a Mo source ($\lambda = 0.7093$ Å) on a Stoe Stadi-P diffractometer in Debye-Scherrer geometry. Data were collected for all samples at room temperature to check their purity. Pawley refinements using TOPAS [4] showed all samples to crystallise in the higher symmetry space group, $P\bar{3}m1$, as all peaks can be indexed by the main phase or CuO. The diffraction peak that evidenced the structure to be $P12_1/c1$ in the literature [2] had too low intensity in our lab data to be differentiated from the background, so we collected synchrotron data on 11-BM at the APS.

7.3.4 Crystal structure refinements of averievite: synchrotron and neutron diffraction on 11-BM, D2B and HRPD

The experimental conditions for the synchrotron and neutron diffraction data collected for undoped averievite are given in Table 7.1. For the synchrotron measurements, averievite was loaded into 0.8 mm kapton capillaries and measured at $T = 100$ K and 300 K with $\lambda = 0.457794$ Å and $\lambda = 0.457841$ Å, respectively. Assuming a packing density of ~ 0.6 the sample absorption for both wavelengths is $\mu R = 1.42$ and a correction was applied in the refinements. The sample for the 11-BM measurements was taken from the 7.45 g batch synthesised for the D2B and HRPD experiments to ensure sample consistency across measurements. Crystallographic refinements were done using TOPAS [4].

Neutron diffraction data on D2B were collected on the 7.45 g sample packed into an 8.5 mm cylindrical vanadium can. A Pawley refinement in TOPAS [4] showed that the diffraction pattern measured at room temperature could not be successfully indexed in the $P\bar{3}m1$ trigonal space group, unlike the x-ray lab data, indicating it had gone through the trigonal-monoclinic phase transition reported in the literature to be at $T = 310$ K [2]. The maximal monoclinic subgroup $C2/m$ (no. 12) did not index all observed peaks. In agreement with the literature, the peaks of the main phase could all be indexed in the $P12_1/c1$ space group [2] and impurity peaks were successfully indexed as CuO. The final refinement in $P12_1/c1$ is shown

in Appendix D. The D2B diffraction profile was described using a pseudo-Voigt function with eight spherical harmonics to help fit the low-Q data. Isotropic displacement parameters, U_{iso}, were restrained to be equal for the O atoms and the Cu kagome sites. In the literature, the Cs is found to be disordered over two sites [2]. Indeed our refinements show that when it occupies the 2b site with full site occupancy, U_{iso} refines to an unphysically large value, suggesting positional disorder. Moving it to the 4e site with half occupancy reduces U_{iso} to 0.0787(25) Å^2, which is still quite large. Refining the anisotropic displacement parameters (ADPs) on this site results in ellipsoids elongated along the a-axis and suggests positional disorder on the Cs site. Refinement of ADPs on the other sites, led to unphysical values so the isotropic values were used in the final refinement.

The Rietveld refinement of the synchrotron data at $T \approx 300$ K was initialised using the results of the fit to the D2B data, as the latter has a lower resolution. The results of the two refinements are in agreement with each other, indicating a $P12_1/c1$ crystal structure. In the literature, the second crystallographic phase transition is reported to occur below $T = 127$ K, but this lower symmetry phase has not been characterised [2]. At $T = 100$ K, our synchrotron data evidenced new

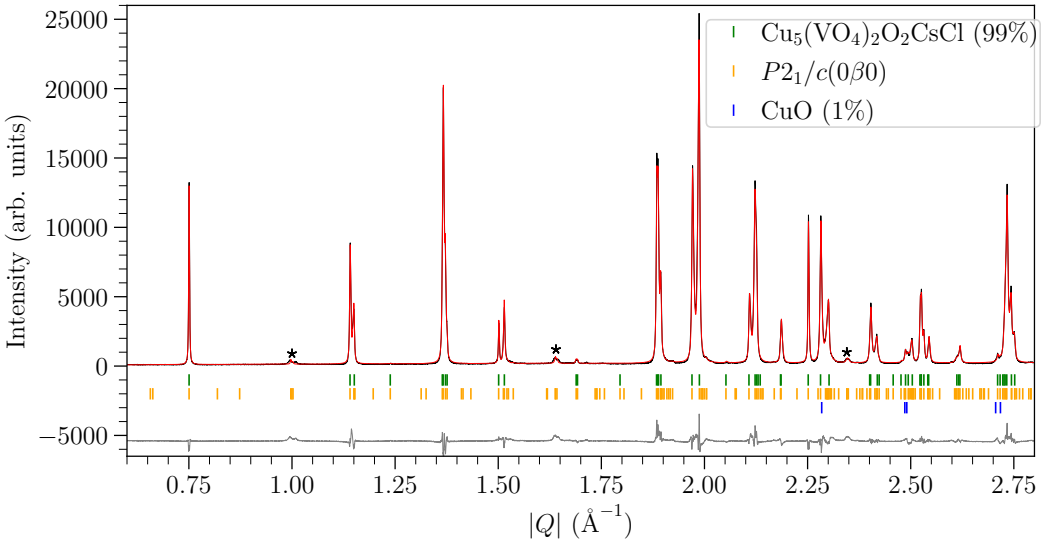

Figure 7.5: Averievite, $T = 100$ K. Rietveld refinement (red) of 11-BM diffraction data (black, $\lambda = 0.457794$ Å) with the difference plot (grey). The peak positions of the main averievite phase ($P12_1/c1$) and of CuO are shown by green and blue ticks, respectively. The orange tick marks correspond to the $P12_1/c1(0\frac{1}{3}0)$ modulated averievite phase.

peaks that could not be indexed even in the lowest symmetry space group $P1$. They were successfully indexed with the propagation vector $\mathbf{k} = (0, \frac{1}{3}, 0)$, indicating a phase transition to a modulated crystal structure with a commensurate propagation vector. The diffraction pattern was fitted with a Rietveld refinement of averievite in space group $P12_1/c1$ with lattice parameters a, b, c and β, and a Pawley fit with lattice parameters $a' = a$, $b' = 3b$, $c' = c$ and $\beta' = \beta$. A CuO impurity phase was also included. The profile parameters for the two averievite phases were set to be equal and the refinement is shown in Figure 7.5.

To observe any further crystallographic phase transitions, HRPD data were collected between $T = 1.5$ K and 100 K on the same 7.45 g sample as on D2B, loaded into a slab-can made of an Al-alloy that had vanadium windows framed by steel. The data were corrected for absorption of the main phase material using the Mantid software [5], so no further correction was applied in the refinements. The diffraction patterns measured are shown in Figure 7.6 and no new peaks are observed as temperature is decreased, indicating no further crystallographic transition below $T = 100$ K. Therefore, the $T = 1.5$ K data with minimal atomic displace-

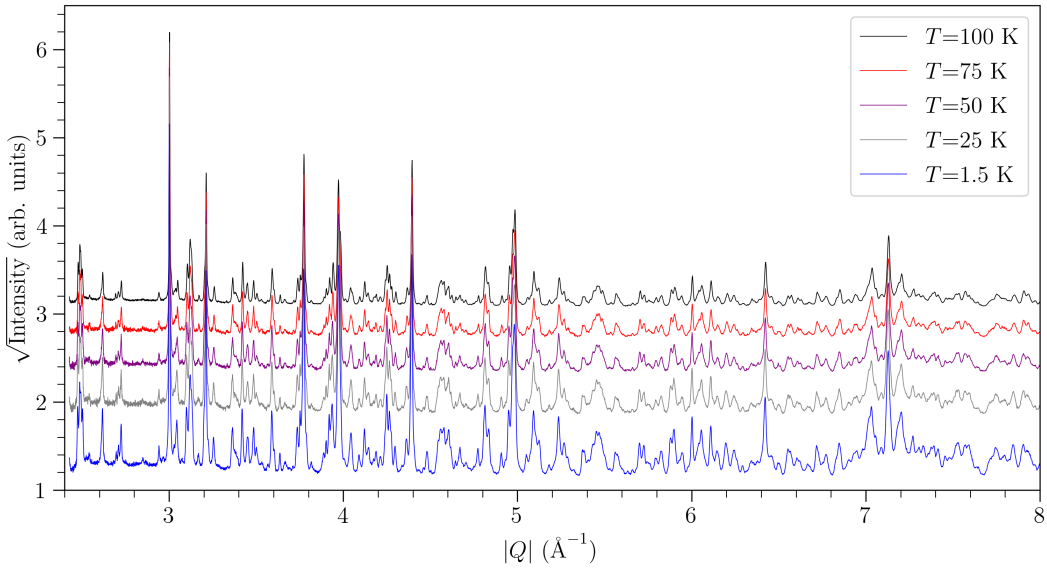

Figure 7.6: Averievite, HRPD neutron diffraction data at $T = 1.5$, 25, 50, 75 and 100 K. The data are presented as the square root of the intensity to facilitate comparison of the data sets at higher Q where the peak intensity is lower. No new peaks or peak splittings are seen as temperature decreases, indicating no further crystallographic transition below $T = 100$ K.

ment parameters was used for a Rietveld refinement that initialised the refinements at higher temperatures. The diffractometer constants and instrumental profile parameters were determined using standard Si and CeO_2 data sets. At $T = 1.5$ K the peaks of the main phase can be indexed in the $P12_1/c1$ space group and extra peaks were attributed to a CuO impurity phase. The peaks corresponding to the modulation below $Q = 1.8$ Å^{-1} are beyond the Q range of the HRPD back-scattering bank and the peaks at $Q = 2.84$, 3.07 and 3.28 Å^{-1} are difficult to differentiate from the background. The 30° bank has an approximate Q range of $0.7 < Q < 8$ Å^{-1}, but the modulation peaks cannot be observed above the background and the 90° bank has a lower Q limit of ~ 1.9 Å^{-1}.

The diffraction profile on HRPD was modelled using a convolution of the instrument profile and a time-of-flight psuedo-Voigt function with eight spherical harmonics accounting for *hkl*-dependent peak anisotropy. Atomic positions and isotropic displacement parameters were stably refined within $P12_1/c1$ for all atoms apart from vanadium (with U_{iso} fixed to be equal for Cu_{k1} and Cu_{k2}, and that of the oxygens restrained to be equal), due to its extremely low coherent scattering length of $b_{coh} = -0.5824$ fm making it almost invisible to neutrons. Unfortunately, anisotropic displacement parameters could not be stably refined. The refinement at $T = 1.5$ K is shown in Figure 7.7 with the resulting crystal structure in Figure 7.8. The atomic positions and displacement parameters are given in Appendix D.

The Cu-Cu distances and $\angle$Cu$-(\mu_2$-O$)-$Cu bond angles are expected to be the most important exchange pathways in averievite and are given in Table 7.3. The superexchange angles indicate AFM nearest-neighbour interactions in the kagome triangles according to the Goodenough-Kanamori rules [6]. As the kagome triangles are isosceles (within error) with a distortion of only $\sim 2\%$, the n.n. exchange interactions are likely to be approximately equal. The superexchange angles between the kagome Cu atoms and the honeycomb Cu_h ones are near the 95° crossover angle from ferro- to antiferromagnetic exchange interactions, suggesting these exchanges may be close to zero. In addition, these angles indicate that the Cu_k-Cu_h exchanges will be much weaker than the Cu_k-Cu_k ones.

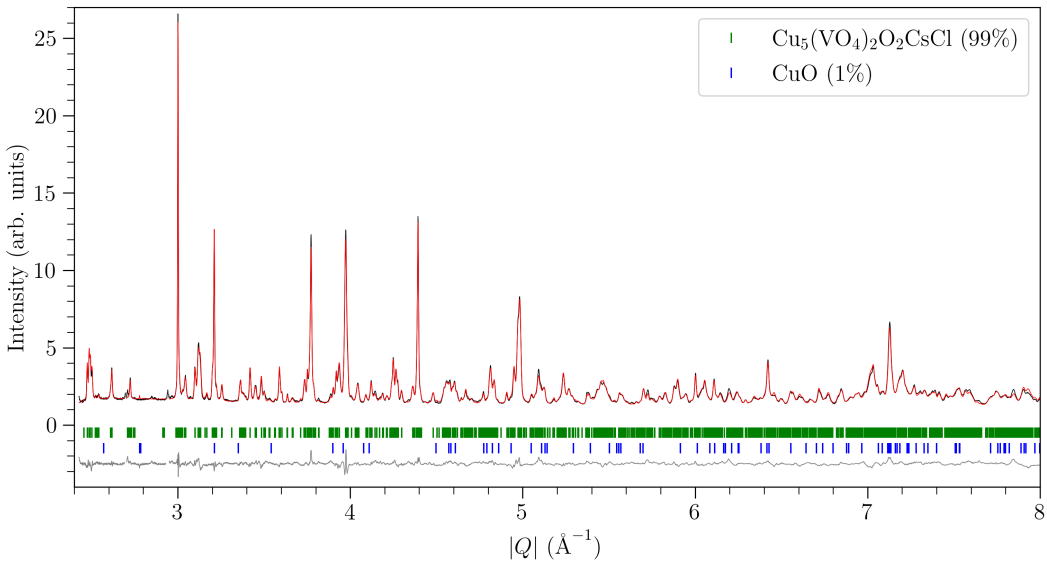

Figure 7.7: Averievite, $T = 1.5$ K. Rietveld refinement (red) of HRPD neutron diffraction data (black) with the difference plot (grey). The refinement showed a $\sim 1\%$ CuO impurity in the sample. The peak positions of the main averievite phase and of CuO are shown by green and blue ticks, respectively. The excluded regions are Bragg peaks from the aluminium sample can.

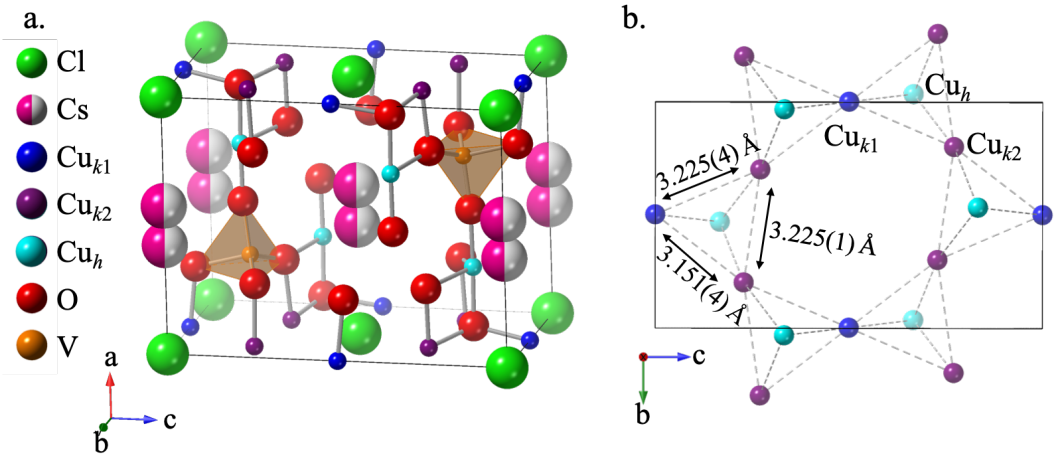

Figure 7.8: Averievite. **a.** Crystal structure refined in the $P12_1/c1$ space group from neutron diffraction data collected at $T = 1.5$ K using HRPD with lattice parameters $a = 8.37298(5)$ Å, $b = 6.38326(10)$ Å, $c = 10.92442(18)$ Å and $\beta = 90.1878(12)°$. **b.** A pyrochlore slab layer viewed from the top, showing the distorted kagome planes.

Cu - Cu	Distance (Å)
Cu_{k1} - $Cu_{k2(1)}$	3.151(4)
Cu_{k1} - $Cu_{k2(2)}$	3.225(4)
$Cu_{k2(1)}$ - $Cu_{k2(2)}$	3.2251(10)
Cu_{k1} - Cu_h	2.919(4)
$Cu_{k2(1)}$ - Cu_h	2.913(4)
$Cu_{k2(2)}$ - Cu_h	2.935(4)

Cu_{k2} - Cu_{k2} Cu_{k1} - Cu_{k2}	Angle	Cu_{k2} - Cu_h Cu_{k1} - Cu_h	Angle	Average
$\angle$ $Cu_{k2(1)}$ - O_k - $Cu_{k2(2)}$	118.9(3)°	$\angle$ $Cu_{k2(1)}$ - O_k - Cu_h	100.8(3)°	96.04°
$\angle$ Cu_{k1} - O_k - $Cu_{k2(1)}$	114.7(3)°	$\angle$ $Cu_{k2(1)}$ - O_1 - Cu_h	91.27(18)°	
$\angle$ Cu_{k1} - O_k - $Cu_{k2(2)}$	117.0(3)°	$\angle$ $Cu_{k2(2)}$ - O_k - Cu_h	100.4(3)°	96.68°
		$\angle$ $Cu_{k2(2)}$ - O_2 - Cu_h	92.96(19)°	
		$\angle$ Cu_{k1} - O_k - Cu_h	99.9(3)°	95.55°
		$\angle$ Cu_{k1} - O_{Cs} - Cu_h	91.19(17)°	

Table 7.3: Averievite Cu-Cu distances in the tetrahedra of the pyrochlore slabs and Cu-O-Cu superexchange angles, from crystallographic structure refinements in $P12_1/c1$ using data collected at $T = 1.5$ K on HRPD. From each Cu_k1 and Cu_k2 there are two possible superexchange pathways to Cu_h, so the average angle was calculated.

7.3.5 Crystal structure refinements of Zn_2-averievite: synchrotron and neutron diffraction on 11-BM, D2B and HRPD

For a full-view picture of the crystallographic structures in the averievite series, it is useful to now discuss the diffraction results of Zn_2-averievite ($x = 2$ sample) as the results allow us to also understand the structure of Zn_1-averievite ($x = 1$ sample). To the best of our knowledge, this is the first reported synthesis and characterisation of Zn_2-averievite. Neutron diffraction patterns were collected on a 7.82 g sample at room temperature on D2B and at $T = 1.5$ and 100 K on HRPD, in an 8.5 mm cylindrical vanadium can and Al-alloy slab-can (as described for undoped averievite), respectively. At all temperatures, Pawley refinements in TOPAS [4] indicated that the majority of the peaks can be indexed in the trigonal space group $P\bar{3}m1$ (no. 164), with extra peaks being attributed to CuO and an unidentified impurity phase that cannot be assigned to any other starting materials. Inspection of the HRPD data at $T = 1.5$ and 100 K showed no peak splitting or peak width increase at low temperature, indicating no phase transition below $T = 100$ K. Therefore, the structural refinement was first done at $T = 1.5$ K with minimal thermal effects.

At $T = 1.5$ K, the HRPD profile was described by a convolution of the instrument profile with a time-of-flight pseudo-Voigt function, modified for *hkl*-dependent peak anisotropy with eight spherical harmonics. A Rietveld refinement in $P\bar{3}m1$ showed the (3 0 l) family of peaks to be missing intensity that could not be attributed to preferred orientation (up to eight spherical harmonics were tried to model preferred orientation). In fact, the diffraction pattern shows the family of (0 0 l) peaks to be more asymmetric than the rest. Such asymmetry can arise from anisotropic microstrain in the sample and is especially evident on the most intense peak, the (0 0 4) peak. To describe this microstrain and hence the *hkl*-dependent peak shapes, Stephen's anisotropic peak broadening model for the trigonal crystal system was used [7]. This is a phenomenological model where each crystallite is treated as having slightly different lattice parameters. Therefore, the lattice parameters can be treated as a multi-dimensional distribution throughout the sample,

leading to parameters that can be varied to fit *hkl*-dependent peak shapes. For the (0 0 4) peak an additional Q-dependent shift and circles convolution was required. Such an approach has previously been used in Sr-vesignieite to describe strain/size effects in the (0 0 l) direction [8].

In $P\bar{3}m1$, the refined isotropic displacement parameters for the kagome Cu_k site was about three times the value reported in other kagome antiferromagnets such as kapellasite and haydeeite [9]. Anisotropic displacement parameters (ADPs) were stably refined for all atoms except vanadium. The latter were fixed to the values refined from the synchrotron data collected at $T = 100$ K. For the Cu kagome site and the basal oxygens of the VO_4 group, O_h, the ADPs were large in the *ab* plane indicating displacive disorder. In an attempt to model this disorder, the Cu kagome site was moved off the 3*e* position to the 6*g* one with half site occupancy and O_h was moved off the 6*i* to the 12*j* position, whilst also refining their ADPs. It was expected that the site disorder would compensate the ADPs for both sites, but the Cu_k ADP remained large in the *ab* plane and r_{wp} remained at 3.4. On splitting the O_h site, the ADP tilted so that it was out of the *ab* plane. The large ADP on Cu_k shows that there is disorder around this site and this model is an average of the crystal structure. The Rietveld refinement for this structure along with the lattice parameters, atomic coordinates and anisotropic displacement parameters can be found in Appendix D.

An alternative way to describe the data is by allowing a static rotation of equilateral kagome triangles in the *ab* plane. This is achieved by lowering the symmetry from $P\bar{3}m1$ to $P3$ (no. 143) and results in distorted kagome hexagons. In this space group, all sites apart from Cs are fully occupied and the inversion symmetry from $P\bar{3}m1$ was imposed on the O, Zn and V sites, since there is no physical reason to remove it or improvement in the refinement without it. The V position was very unstable, refining onto the O_{Cs}, so was fixed to the position refined at $T = 100$ K using the synchrotron data. The Cs position refined very close to ($\frac{1}{2}$, 0, 0), so was fixed to this position and its ADP was refined to account for positional disorder. For the other atoms, the refined ADPs were constrained to be equal for sites related by the forced inversion symmetry. This led to unphysical values for the O_{Cs1}

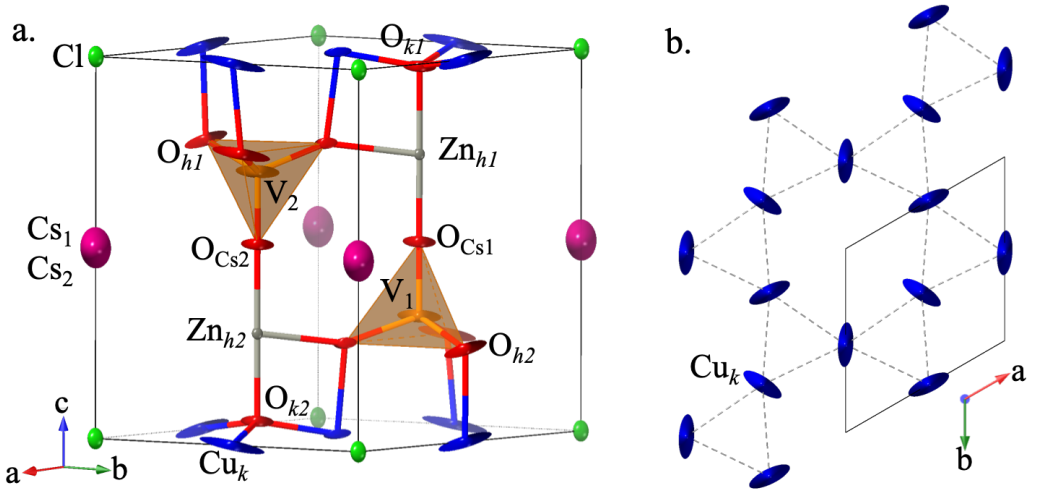

Figure 7.9: Zn_2-averievite. **a.** Crystallographic structure refined in space group $P3$ from data collected at $T = 1.5$ K using HRPD (Figure 7.10) with the anisotropic displacement ellipsoids at 50% probability. **b.** Kagome planes formed by equilateral Cu triangles rotated in the *ab* plane, therefore distorting the hexagons.

and O_{Cs2} sites, so their ADPs were fixed to be equal to those of O_{k1} and O_{k2} as they all have 3.. site symmetry. This model provides a more concise description of the Cu disorder in the kagome plane and the resulting structure with the ADPs is shown in Figure 7.9. The Rietveld refinement is shown in Figure 7.10 and the lattice parameters, atomic coordinates and anisotropic displacement parameters are given in Appendix D. The ellipsoids representing the displacements of the Cu and O atoms are elongated in the *a*/*b* directions as they partially account for the displacive disorder in the powder averaged structure.

At $T = 1.5$ K in $P3$, the difference Fourier map showed missing intensity around the Zn and O_{h1}/O_{h2} sites. For the Zn site this could be due to partial Cu-Zn antisite disorder, but the Zn and Cu nuclear coherent scattering lengths ($b_{\text{coh,Zn}} =$ 5.680 fm and $b_{\text{coh,Cu}} = 7.485$ fm [10]) are too similar to allow a stable refinement of site occupancies. The missing intensity could also be due to local symmetry lowering, as a result of the displacive disorder that affects the O_{h1}/O_{h2} atoms. The distortion in the coordination environment around Zn, may cause it to move off the high-symmetry $1a/1b$ position. Placing the Zn atoms on a $3d$ site with Zn_1 at $(\frac{1}{3},\ y,\ z)$, results in $y = 0.67005(206) \approx \frac{2}{3}$ and the difference Fourier map no longer shows missing intensity around Zn. The proximity of $(\frac{1}{3},\ 0.67005,\ z)$ to the

1*b* position, allows the powder averaged structure to be modelled with Zn on the higher symmetry site.

Refinements in the lower symmetry space group $C12_1/m1$ (no. 12) did not improve the fits - the same intensity issues appear at the same peaks and could not be attributed to preferred orientation. Therefore, there was no evidence to support a lower symmetry space group than $P3$. In all diffraction patterns there is evidence of an unidentified impurity phase, most visible in the synchrotron data. The peak intensities are comparable to those of the CuO impurity suggesting it is of the order of a few % of the sample.

The analysis of the room temperature D2B data, indicated the same intensity issues in the $(3\ 0\ l)$ family of peaks (see Appendix D for the refinement in space group $P3$). This suggests that the displacive disorder is present from $T = 300$ K down to $T = 1.5$ K. Although this can be modelled with a static rotation of the kagome triangles, the refined ADPs down to $T = 1.5$ K are similar suggesting that the disorder has a dynamic aspect. To determine any local symmetry lowering, NMR measurements would be useful.

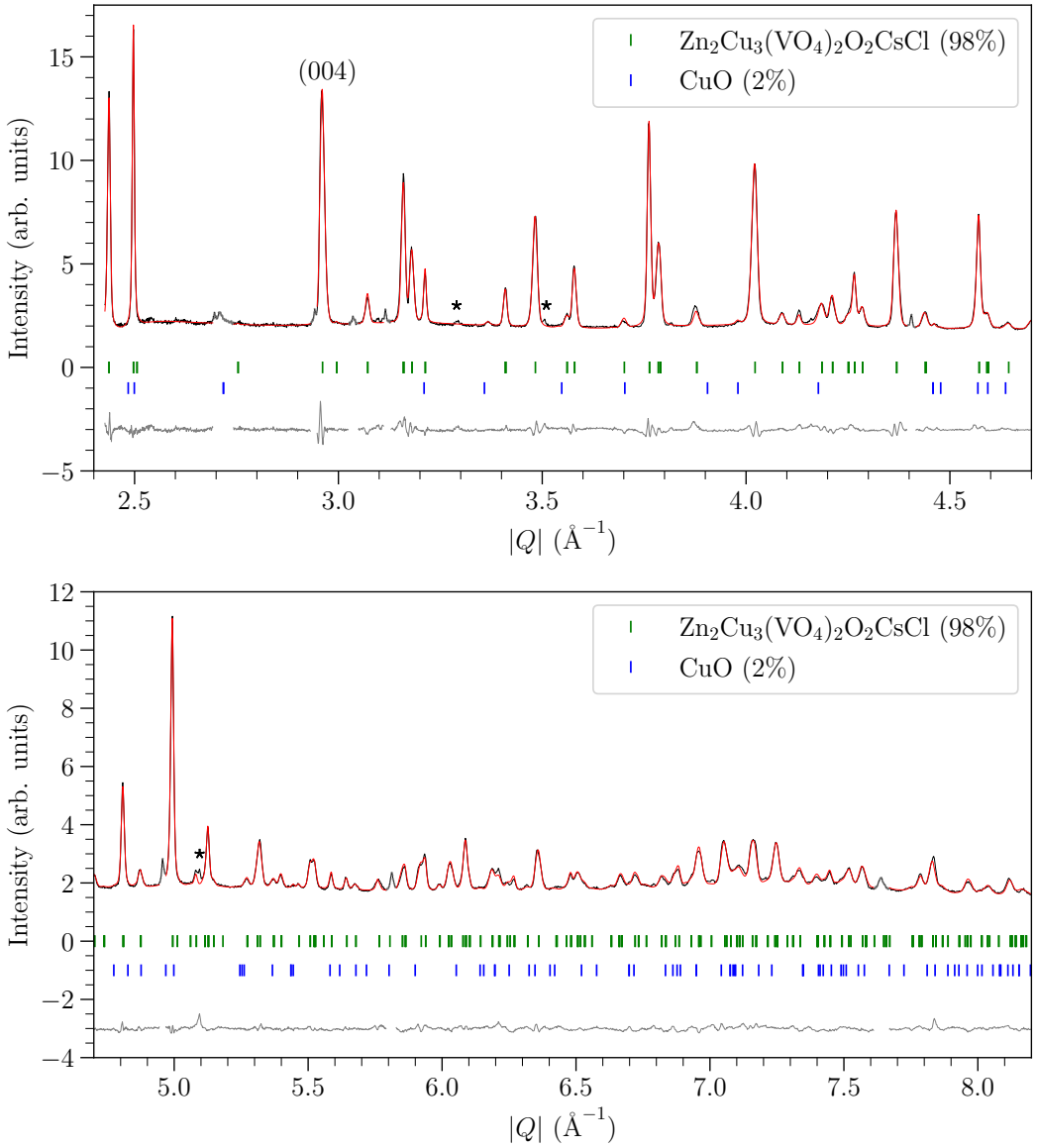

Figure 7.10: Zn_2-averievite Rietveld refinement in the $P3$ space group (no. 143) on data collected at $T = 1.5$ K on the back-scattering bank of HRPD with 82 parameters ($r_{wp} = 3.12$ and $\chi^2 = 3.15$). There is a $\sim 2\%$ CuO impurity shown by the blue ticks and unidentified impurity peaks are marked by asterisks. The regions not included in the refinement are scattering from the aluminium sample can. **Top.** Low-Q range and **bottom.** high-Q range.

7.3.6 Crystal structure refinements of Zn_1-averievite: synchrotron and neutron diffraction on 11-BM, D2B and HRPD

Neutron diffraction data for Zn_1-averievite were collected on a 8.06 g sample on HRPD at $T = 1.5$ and 100 K, packed in an Al-alloy slab-can (as described for undoped averievite). At $T = 100$ K, synchrotron data on 11-BM was acquired on a sample taken from the batch prepared for the HRPD measurements. All data can be indexed in the $P\bar{3}m1$ space group (no. 164) and inspection of the HRPD diffraction patterns at both temperatures does not evidence new peaks or peak splitting, indicating no crystallographic phase transition at low temperature.

The synchrotron data at $T = 100$ K has additional peaks to the main phase indicating impurities of the order of a few % (see Appendix D for the Rietveld refinement). The most distinct extra peaks were successfully indexed using CuO and $ZnCu_4(VO_4)_2O_2$, which were used as precursors in the synthesis. A Pawley refinement on lab PXRD data of $ZnCu_4(VO_4)_2O_2$ (shown in Appendix D), was used to determine appropriate lattice parameters for the synchrotron refinement.

The HRPD data at $T = 1.5$ K could be refined in the $P\bar{3}m1$ space group, but showed similar intensity issues in the (3 0 l) family of peaks as seen in Zn_2-averievite. Therefore, similarly to the $x = 2$ sample, the final refinement was done in the $P3$ space group (no. 143), which allows for a rotation of the kagome triangles and VO_4 groups in the ab plane. The $(0\ 0\ 4)$ peak is less asymmetric in the $x = 1$ sample than the $x = 2$, but its shape still indicates anisotropic microstrain. In Zn_1-averievite, there are Cu atoms on half the honeycomb sites that may couple the pyrochlore slab layers leading to less microstrain in the c direction than in the $x = 2$ sample, where the planes are believed to be largely decoupled. A good description of the $(0\,0\,4)$ peak was achieved using Stephen's anisotropic peak broadening model for the trigonal crystal system [7]. The final refinement is shown in Figure 7.11 and lattice parameters, atomic positions and displacement parameters are given in Appendix D, Table D.7. The ADPs indicate similar disorder in the Cu atoms forming the kagome lattice as in Zn_2-averievite.

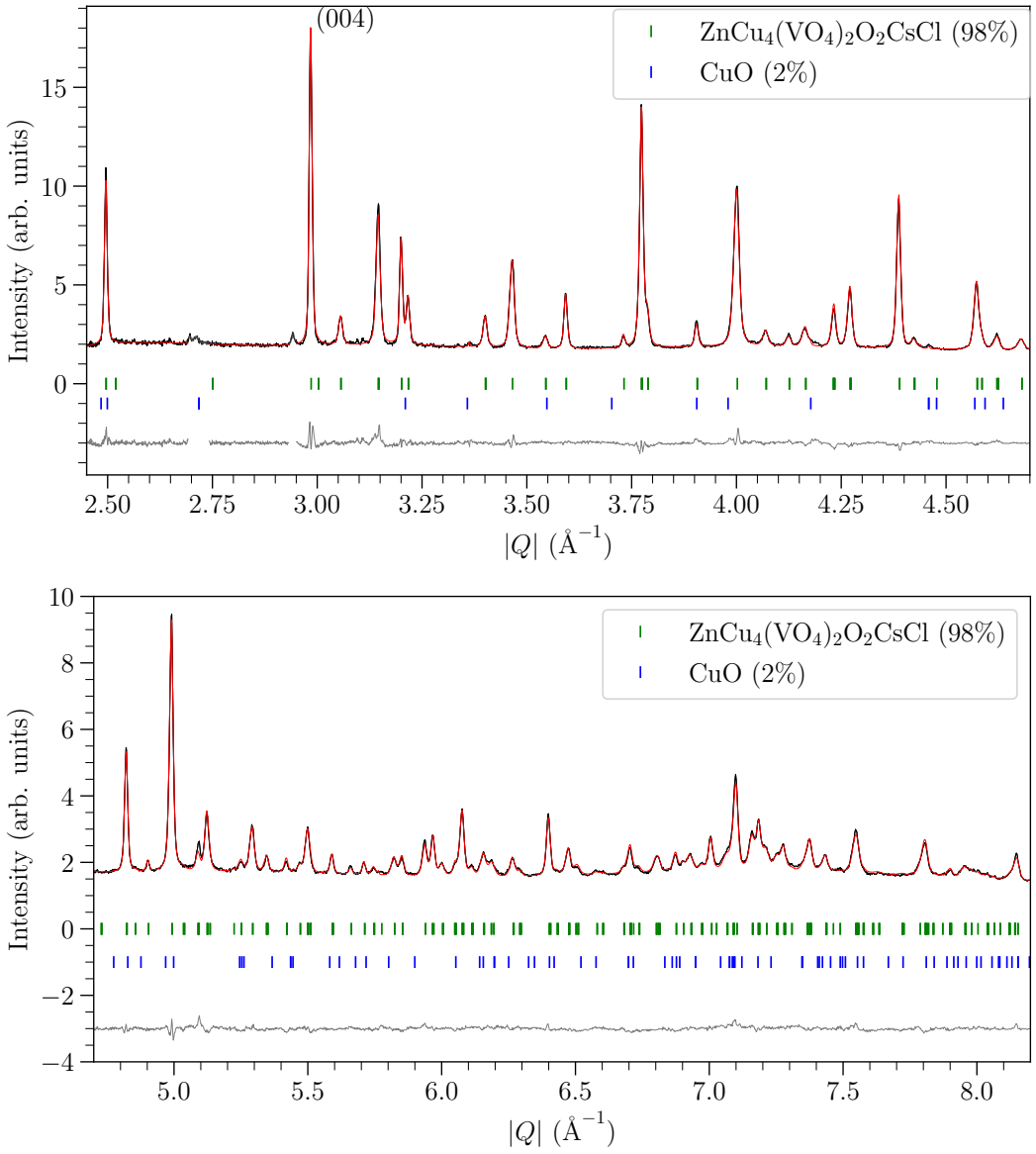

Figure 7.11: Zn_1-averievite Rietveld refinement in the $P3$ space group (no. 143) on data collected at $T = 1.5$ K on the back-scattering bank of HRPD with 79 parameters ($r_{wp} = 2.71$ and $\chi^2 = 1.92$). There is a $\sim 2\%$ CuO impurity shown by the blue ticks. The regions not included in the refinement are scattering from the sample can. **Top.** Low-Q range and **bottom.** high-Q range.

7.4 SQUID magnetometry

In addition to determining the crystal structures of averievite and its Zn-doped variants, we aimed to explore their magnetic ground states. Previous magnetometry measurements showed that undoped averievite has a transition to long-range magnetic order at $T_N = 24$ K and that doping $Zn_xCu_{5-x}(VO_4)_2O_2CsCl$ with Zn to the $x = 1$ level completely suppresses this transition [2]. This section presents the results of our magnetometry measurements on our samples of $Zn_xCu_{5-x}(VO_4)_2O_2CsCl$ for $x = 0$, 1 and 2. DC magnetometry was collected using both a Quantum Design PPMS in VSM mode and a Quantum Design MPMS XL DC-SQUID, described in Chapter 4. Data were collected as a function of temperature, T, in various external magnetic fields, H, and at constant T as a function of H. Field-cooled (FC) measurements were made by cooling the sample to base temperature in a magnetic field and collecting data on heating in the same field. The diamagnetic contribution in each sample was subtracted using Pascal's constants for the nominal structural formulas [11].

7.4.1 DC susceptibility of averievite

Field-cooled (FC) and zero-field cooled (ZFC) measurements were made on a 0.2900 g sample of averievite in a 1000 G field. Figure 7.12a shows the molar magnetic susceptibility, χ, which indicates a phase transition at $T = 23$ K and an upturn at $T = 7$ K, in close agreement with the literature [2]. The upturn at low temperature possibly indicates ferromagnetic correlations growing stronger below $T = 7$ K. The first derivative of the susceptibility, $d\chi/dT$, clearly shows a magnetic transition at $T = 23$ K, but does not indicate another phase transition down to $T = 2$ K (Figure 7.12b). The inverse susceptibility (Figure 7.12c) is only linear down to $T = 200$ K, indicating that at lower temperatures short-range correlations become increasingly stronger before the antiferromagnetic transition at $T_N = 23$ K. A linear extrapolation of the χ^{-1} data between 200 and 320 K resulted in a Weiss temperature $\theta_W = -180(1)$ K, which corresponds to an antiferromagnetic mean field in the sample. The inverse of the slope gives a Curie constant of 0.513(1) emu K mol^{-1} Cu^{-1}, from which an effective magnetic moment, μ_{eff}, of 2.02 μ_B Cu^{-1} is calculated. Cal-

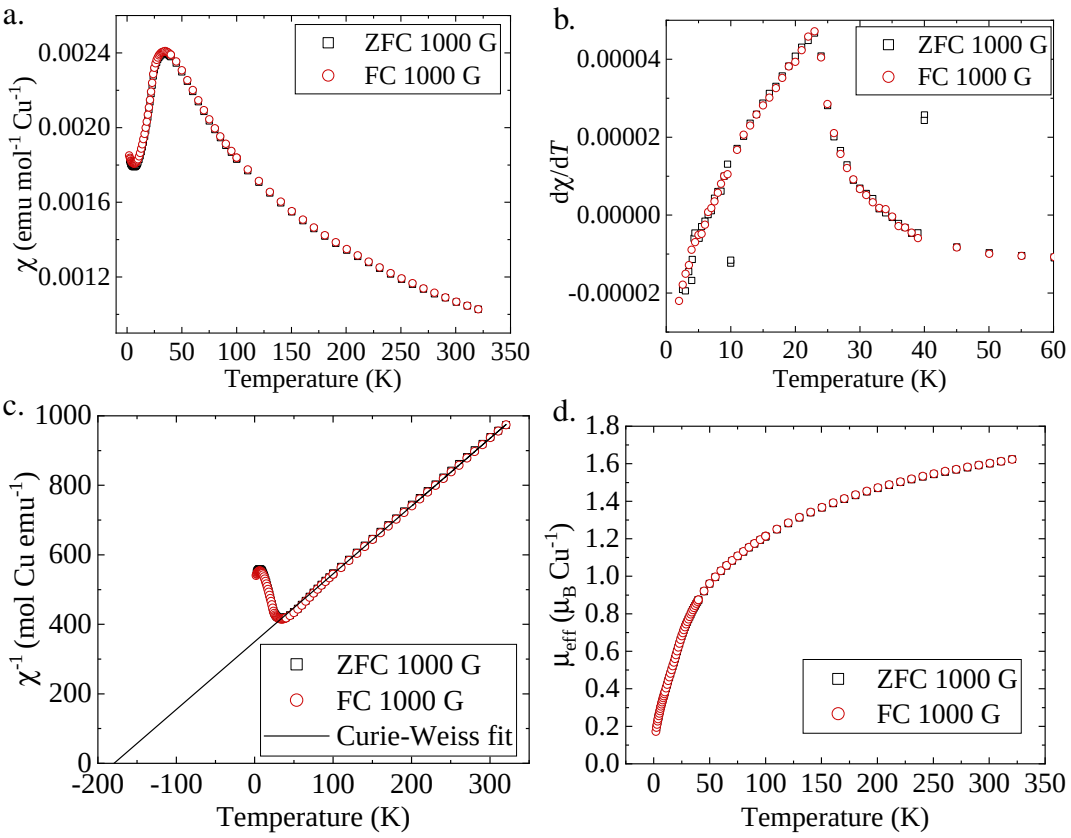

Figure 7.12: Averievite. **a.** Field cooled (black) and zero field cooled (red) magnetic susceptibility, χ, collected in a field of 1000 G. **b.** First derivative of χ showing a clear magnetic phase transition at $T = 23$ K. **c.** Inverse magnetic susceptibility with a linear Curie-Weiss fit (black line) between 200 K and 320 K that gives $\theta_W = -180(1)$ K. **d.** Effective magnetic moment, μ_{eff}, as a function of temperature, T, calculated using $\mu_{\text{eff}} = \sqrt{8\chi T}$.

culating the μ_{eff} from $\sqrt{8\chi T}$ is shown in Figure 7.12d as a function of temperature. At high temperature this value reaches 1.62 μ_{B} Cu^{-1}, which is slightly lower than

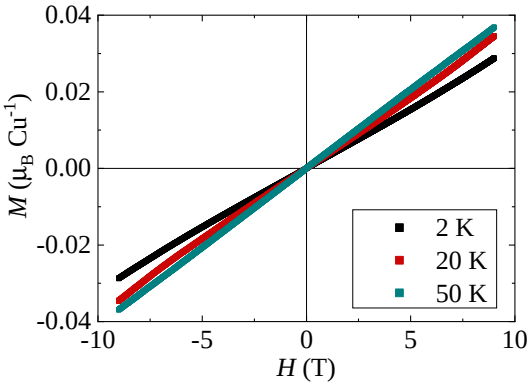

Figure 7.13: Averievite. magnetisation, M, as a function of field, H, at $T = 2, 20$ and 50 K. No hysteresis is seen down to $T = 2$ K.

the spin-only value for $S = \frac{1}{2}$ ions of 1.73 μ_B Cu^{-1} (assuming $g = 2$), but remains unsaturated at $T = 320$ K.

Magnetisation, M, as a function of field, H, was measured on a 0.03125 g sample. Data at $T = 2, 20$ and 50 K are shown in Figure 7.13. No hysteresis is seen down to $T = 2$ K, indicating an absence of an ordered ferromagnetic contribution.

7.4.2 DC susceptibility of Zn_1-averievite

Magnetometry data were collected on a 0.2907 g sample of Zn_1-averievite and the susceptibility as a function of temperature is shown in Figure 7.14a. At low temperature, there is a hint of downwards curvature and the first derivative, shown in Figure 7.14b, reveals a transition at $T = 3.5$ K. This is in contrast to the literature that states the magnetic transition has been suppressed when doping $Zn_xCu_{5-x}(VO_4)_2O_2CsCl$

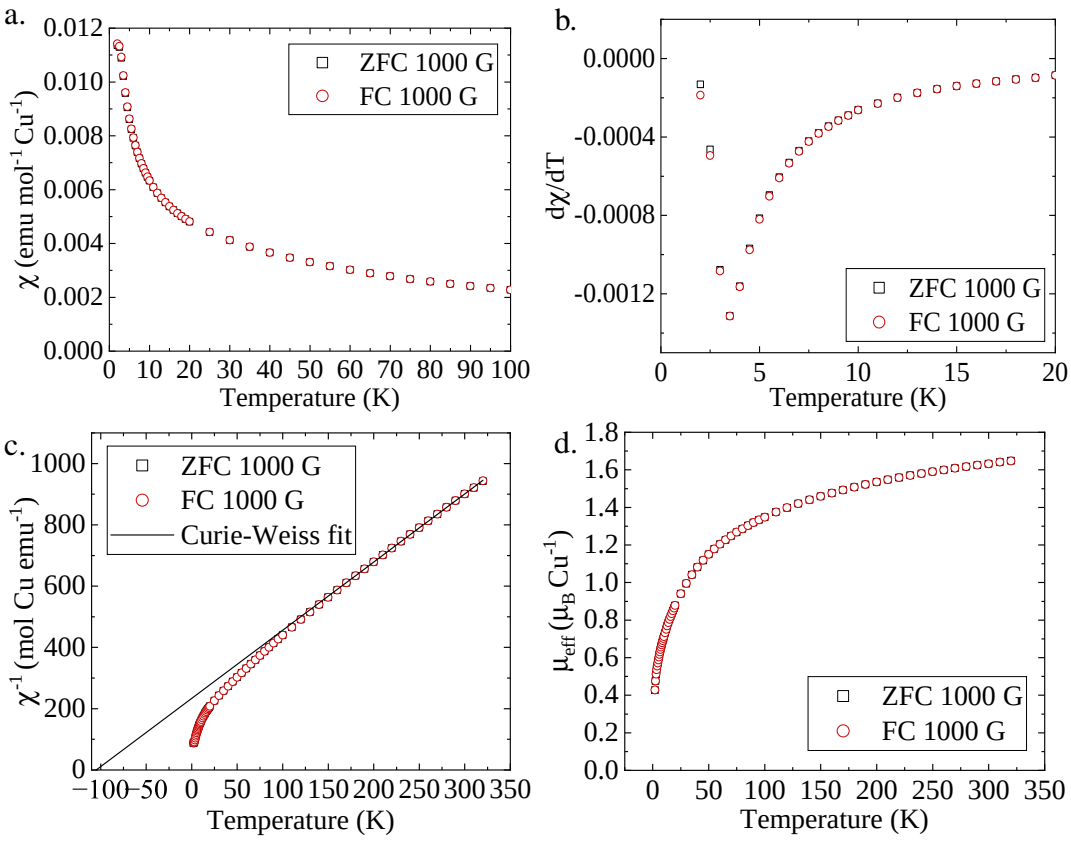

Figure 7.14: Zn_1-averievite. **a.** Field cooled (black) and zero field cooled (red) magnetic susceptibility, χ, collected in a field of 1000 G. **b.** First derivative of χ showing a clear magnetic phase transition at $T = 3.5$ K. **c.** Inverse magnetic susceptibility with a linear Curie-Weiss fit (black line) between 200 K and 320 K that gives $\theta_W = -105(1)$ K. **d.** Effective magnetic moment, μ_{eff}, as a function of temperature, T, calculated using $\mu_{\text{eff}} = \sqrt{8\chi T}$.

to the $x = 1$ level [2]. The inverse susceptibility as a function of temperature is shown in Figure 7.14c and a linear extrapolation of the data between 150 and 320 K gives a Weiss temperature of $-105(1)$ K. The slope gives a Curie constant of 0.449(1) emu K mol^{-1} Cu^{-1} and $\mu_{\text{eff}} = 1.90\ \mu_{\text{B}}$ Cu^{-1}. Calculating μ_{eff} using $\sqrt{8\chi T}$ is shown in Figure 7.14d and similarly to the $x = 0$ sample it does not saturate at the highest measured temperature.

7.4.3 DC susceptibility of Zn_2-averievite

DC susceptibility measurements were made on a 0.06817 g sample of Zn_2-averievite. Field cooled and zero-field cooled data in a field of 1000 G are shown in Figure 7.15. The magnetic susceptibility indicates no magnetic transition down to $T = 2$ K, further evidenced by $d\chi/dT$. When comparing the susceptibility of Zn_2-averievite to that of the $x = 0$ and $x = 1$ Zn-doped samples, it becomes clearer that Zn_1-averievite has a transition at low temperature (Figure 7.15a). The inverse susceptibility data of Zn_2-averievite was extrapolated between $T = 160$ and 320 K to give a Weiss temperature of $-109(1)$ K and a Curie constant of 0.487(2) emu K mol^{-1} Cu^{-1} (see Figure 7.15b). From the Curie constant, the effective magnetic moment is $\mu_{\text{eff}} = 1.97\ \mu_{\text{B}}$ Cu^{-1}. The effective magnetic moment μ_{eff} was also calculated using $\sqrt{8\chi T}$ as shown in Figure 7.15c and similarly to the $x = 0$ and 1 samples does not saturate at $T = 320$ K, reaching a value of 1.71 μ_{B} Cu^{-1}, close to the spin-only value for $S = \frac{1}{2}$ ions of 1.73 μ_{B} Cu^{-1}.

Magnetisation, M, as a function of field, H, at $T = 2$ K is shown in Figure 7.16. M does not saturate in the highest measured field and a Brillouin function describing the paramagnetic magnetisation is not sufficient to model the data. In fact, the magnetisation seems to be linear for fields larger than ~ 7 T. A similar observation was made in the magnetisation of herbertsmithite [12], which was modelled by a phenomenological expression [13] to separate the intrinsic kagome contribution from possible defect Cu spins on the interlayer sites. This is given by

$$M = nM_{\text{sat}}\tanh\left(\frac{gS\mu_{\text{B}}H}{k_{\text{B}}(T+\theta)}\right) + \chi_{\text{kag}}H, \tag{7.1}$$

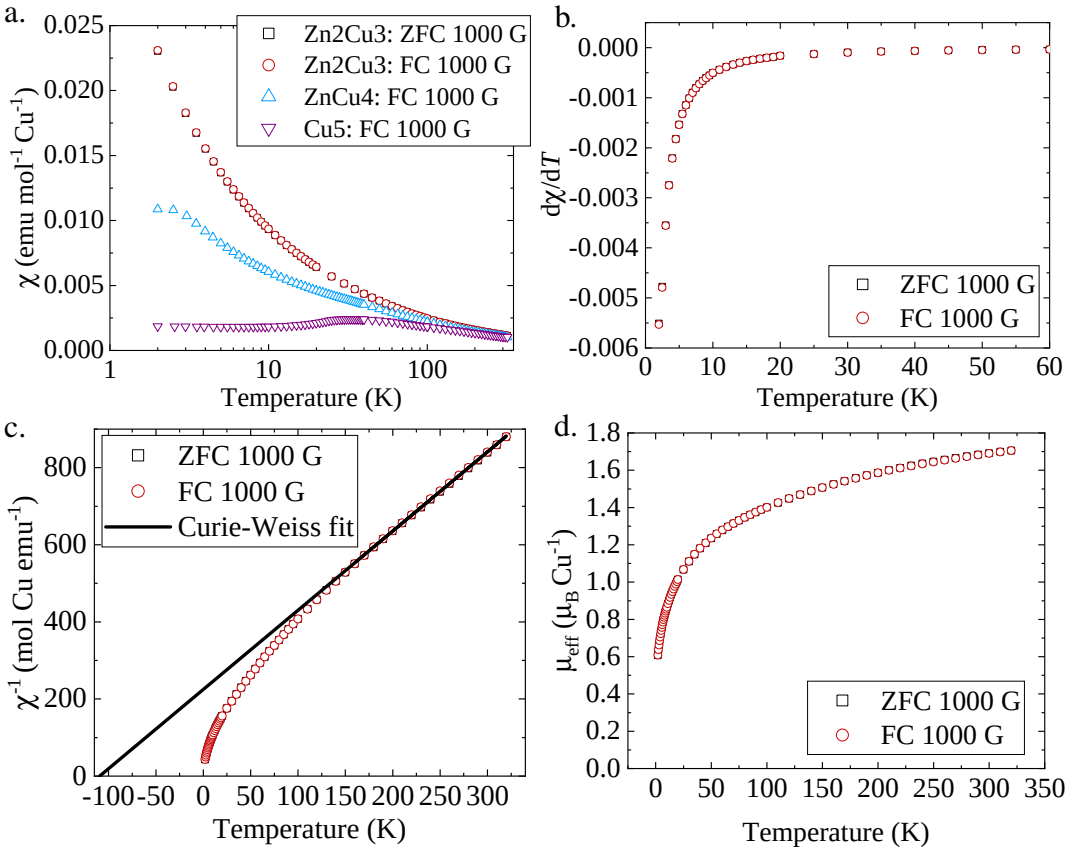

Figure 7.15: Zn_2-averievite. **a.** Field cooled (black) and zero field cooled (red) magnetic susceptibility, χ, on a log(T) scale collected in a field of 1000 G. The FC measurements of averievite (purple) and Zn_1-averievite (blue) are plotted for comparison. **b.** Inverse magnetic susceptibility with a linear Curie-Weiss fit (black line) between 160 K and 320 K that gives $\theta_W = -109(1)$ K. **c.** Effective magnetic moment, μ_{eff}, as a function of temperature, T, calculated using $\mu_{\text{eff}} = \sqrt{8\chi T}$.

where $S = \frac{1}{2}$ and M_{sat} is the saturated magnetisation of 1 mole of Cu^{2+} spins given by $N_A g \mu_B S$. The first part of the equation accounts for the defect spin magnetisation, M_{defect}, using an adapted Brillouin function that describes paramagnetic-like spins with a weak coupling given by the energy scale of θ. Assuming that the magnetic defects behave as $S = 1/2$ spins, the percentage of defect spins in the sample is given by n. The second part of equation 7.1 accounts for the intrinsic magnetisation of the kagome lattice. It is assumed that the kagome exchange interactions are much larger than the applied field and that the intrinsic kagome susceptibility, χ_{kag}, is constant with increasing field, up to at least 9 T in the case of Zn_2-averievite.

Figure 7.16 shows the magnetisation per Cu, normalized to the saturated magnetisation of 1 mole of $S = \frac{1}{2}$ spins and fitted with equation 7.1. In the absence

of local susceptibility data that would give a more accurate value of χ_{kag}, this was treated as a free parameter. Furthermore, we are not aware of other studies that have investigated the defect spins in Zn_2-averievite and their coupling strengths, so θ was also freely refined. The Landé g-factor was fixed to $g = 2.27$, derived from $\mu_{eff} = 1.97\ \mu_B\ Cu^{-1}$. The refined values of n and θ are $\sim 6.3\%$ and ~ 0.4 K, respectively. Fixing θ to zero results in a very similar χ^2 value as allowing it to freely refine, and restraining it to higher values significantly worsens the fit. The separate magnetisations of the kagome spins and that attributed to defect (or orphan) Cu^{2+} spins is shown in Figure 7.16. Assuming that the behaviour of the defect Cu^{2+} spins is paramagnetic-like, this analysis gives a minimum of $\sim 6\%$ of defect Cu^{2+} spins out of the total Cu^{2+} in the sample.

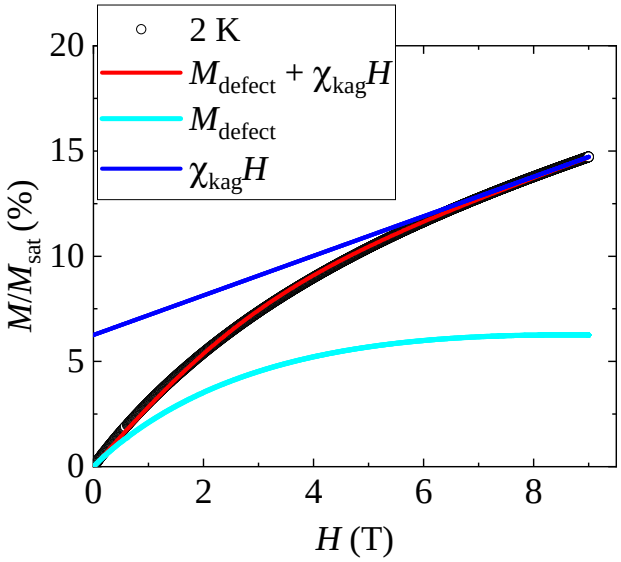

Figure 7.16: Zn_2-averievite magnetisation at $T = 2$ K as a function of field, H (black), normalized to 1 mole of Cu^{2+} spins. The red line is a fit using equation 7.1, the blue line is the kagome magnetisation that depends on the susceptibility, χ_{kag} and the cyan line is the magnetisation of defect Cu^{2+} spins.

7.5 Magnetic structure refinement of averievite on WISH

A neutron diffraction study as a function of temperature was done on undoped averievite ($x = 0$) on the cold-neutron time-of-flight diffractometer WISH at ISIS. The cold neutrons allowed for measurement of higher d-spacings with sufficient flux to observe the magnetic Bragg peaks of the $S = \frac{1}{2}$ moments. The same sample was used as for HRPD (same 10 mm Al-alloy slab-can) and D2B, and measurements were made in a standard 'orange' cryostat.

Data were collected with high statistics at $T = 1.5$ K and above T_N at $T = 40$ K ($\sim$ 2.5 h collection time), and at intermediate temperatures with lower statistics ($\sim$ 15 min collection time). The crystal structure was refined at $T = 1.5$ K using a multi-bank refinement and for the highest-resolution bank (bank 5) is shown in Appendix D. It was assumed that the crystal structure is the average one and the modulation was not taken into account. Due to the low intensity of the magnetic Bragg peaks, the easiest way to observe them is through temperature subtractions between low temperature data and that collected at $T = 40$ K. Temperature difference plots are shown in Figures 7.17a and b for banks 1 and 2, respectively, indicating four magnetic Bragg peaks at $Q = 0.37$, 0.69, 1.21 and 1.61 Å^{-1}. These can be indexed with the propagation vector $\mathbf{k} = (\frac{1}{2}, 0, 0)$ in the $P12_1/c1$ space group.

Representation analysis was employed through the program SARAh to determine the irreducible representations (irreps) for the $P12_1/c1$ structure and the basis vectors for the magnetic structure [14]. The crystal structure has three Cu sites: the honeycomb site Cu$_h$ at (0.72862, 0.53568, 0.16828) and the two sites that make up the kagome lattice, Cu$_{k1}$ and Cu$_{k2}$, at (0, 0, 0.5) and (0, 0.80048, 0.23059). The decomposition of the magnetic representation over irreps of $\mathrm{G}_{\mathbf{k}}$ in Kovalev's notation [15] for these sites is:

$$\mathrm{Cu}_h : \Gamma_{Mag} = 3\Gamma_1^1 \oplus 3\Gamma_2^1 \oplus 3\Gamma_3^1 \oplus 3\Gamma_4^1, \tag{7.2}$$

$$\mathrm{Cu}_{k1} : \Gamma_{Mag} = 3\Gamma_1^1 \oplus 0\Gamma_2^1 \oplus 3\Gamma_3^1 \oplus 0\Gamma_4^1, \tag{7.3}$$

$$\mathrm{Cu}_{k2} : \Gamma_{Mag} = 3\Gamma_1^1 \oplus 3\Gamma_2^1 \oplus 3\Gamma_3^1 \oplus 3\Gamma_4^1. \tag{7.4}$$

The simplest possibility was initially considered where the second-order mag-

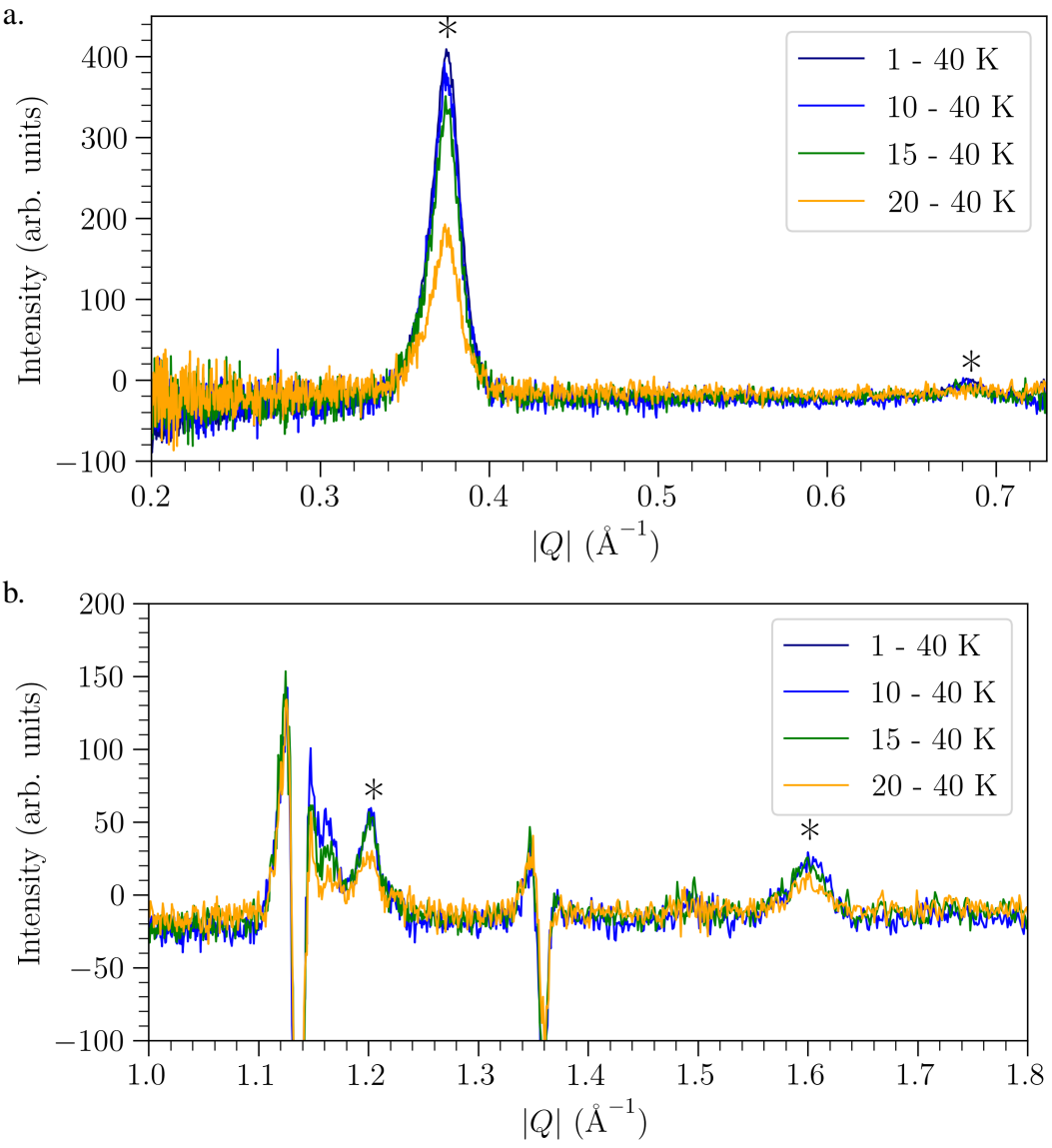

Figure 7.17: Averievite, WISH data. Plots of temperature differences of (**a.**) bank 1 and (**b.**) bank 2 data. The asterisks indicate the magnetic Bragg peaks.

netic transition involves only one irrep and consequently irreps common to all three Cu sites: Γ_1 and Γ_3. For both these irreps, each Cu site has three basis vectors shown in Appendix D. For Cu_h the basis vectors give antiferromagnetic correlations along the three unit cell directions. For Cu_{k1} and Cu_{k2}, Γ_1 (Γ_3) gives ferromagnetic (antiferromagnetic) correlations along b and anti-ferromagnetic (ferromagnetic) ones along c.

There were only four Bragg peaks from which to determine the magnetic structure and a maximum of nine degrees of freedom to refine. Attempting to refine all nine mixing coefficients in either Γ_1 or Γ_3 led to the refinements diverging. In an attempt to minimise the number of refined mixing coefficients, collinear structures along the a, b and c directions were trialled, but these led to zero intensity being predicted at the $Q = 0.37$ Å^{-1} and/or 1.61 Å^{-1} peak positions. However, confining the spins to the kagome $b-c$ plane allowed for a good description of the peak intensities.

In Γ_1, the most intense peak near $Q = 0.37$ Å^{-1} is only sensitive to the moments along b of Cu_h and Cu_{k2}. As it is the most intense peak, the component of the moments along b must be larger than in the other directions. To satisfy this, either the Cu_{k2} moments must be the largest (~ 2 times that of Cu_{k1}) or the Cu_h moments are the largest with similar sized moments forming the kagome lattice. The superexchange angles between kagome spins are similar, ranging between 114.7° and 118.9°, and the distortion away from equilateral triangles is only $\sim 2\%$, supporting similar sized moments in the kagome triangles. Freely refining the spins in the $b-c$ plane resulted in a structure that has a net directional component along b (see Appendix D for this magnetic structure in Γ_1), suggesting stronger ferro- than antiferromagnetic correlations between spins. This disagrees with the superexchange angles in the kagome triangles and the large negative Weiss temperature determined from the susceptibility data, $\theta_W = -180(1)$ K.

In Γ_3, the peak centred at $Q = 0.37$ Å^{-1} is sensitive to the component of the moments along c of Cu_{k1} and Cu_{k2}. Freely refining Cu_{k1} and Cu_{k2} in the $b-c$ plane results in them forming a general $q = 0$ structure with different moment sizes, which

are smaller than the Cu_h ones. As the angle of rotation in the $b-c$ plane cannot be reliably refined with such few Bragg peaks, a $q = 0$ structure with spin angles of 90°, 135° and 135° can be formed with the following restrictions: Cu_{k1} was fixed to the c direction and the mixing coefficients of Cu_{k2} were constrained to be equal in the b and c directions. The refined mixing coefficients are given in Table 7.4 and the fit is shown in Figure 7.18 with the resulting structure in Figure D.13. The moment sizes of Cu_{k1}, Cu_{k2} and Cu_h are 0.30, 0.47 and 0.60 μ_B, respectively. Attempting to restrain the moment of Cu_{k1} to be of equal magnitude to Cu_{k2}, led to too much intensity predicted at the 1.61 $Å^{-1}$ peak.

Atom	Coordinates	Basis vector, ψ_i	C_i
Cu_{k1}	(0, 0, 0.5)	ψ_1	0
		ψ_2	0
		ψ_3	–0.30(1)
Cu_{k2}	(0, 0.80048, 0.23059)	ψ_1	0
		ψ_2	–0.33(1)
		ψ_3	–0.33(1)
Cu_h	(0.72862, 0.53568, 0.16828)	ψ_1	0
		ψ_2	–0.215(8)
		ψ_3	–0.56(1)

Table 7.4: The refined mixing coefficients, C_i, for each basis vector of Atom 1 of the three Cu sites (Cu_{k1}, Cu_{k2} and Cu_h) corresponding to the refinements shown in Figure 7.18. Tables detailing the basis vectors and other atom coordinates can be found in Appendix D.

Atom	Moment size (μ_B)
Cu_{k1}	0.30
Cu_{k2}	0.47
Cu_h	0.60

Table 7.5: The refined moment sizes of the three Cu sites (Cu_{k1}, Cu_{k2} and Cu_h) from the refinements shown in Figure 7.18.

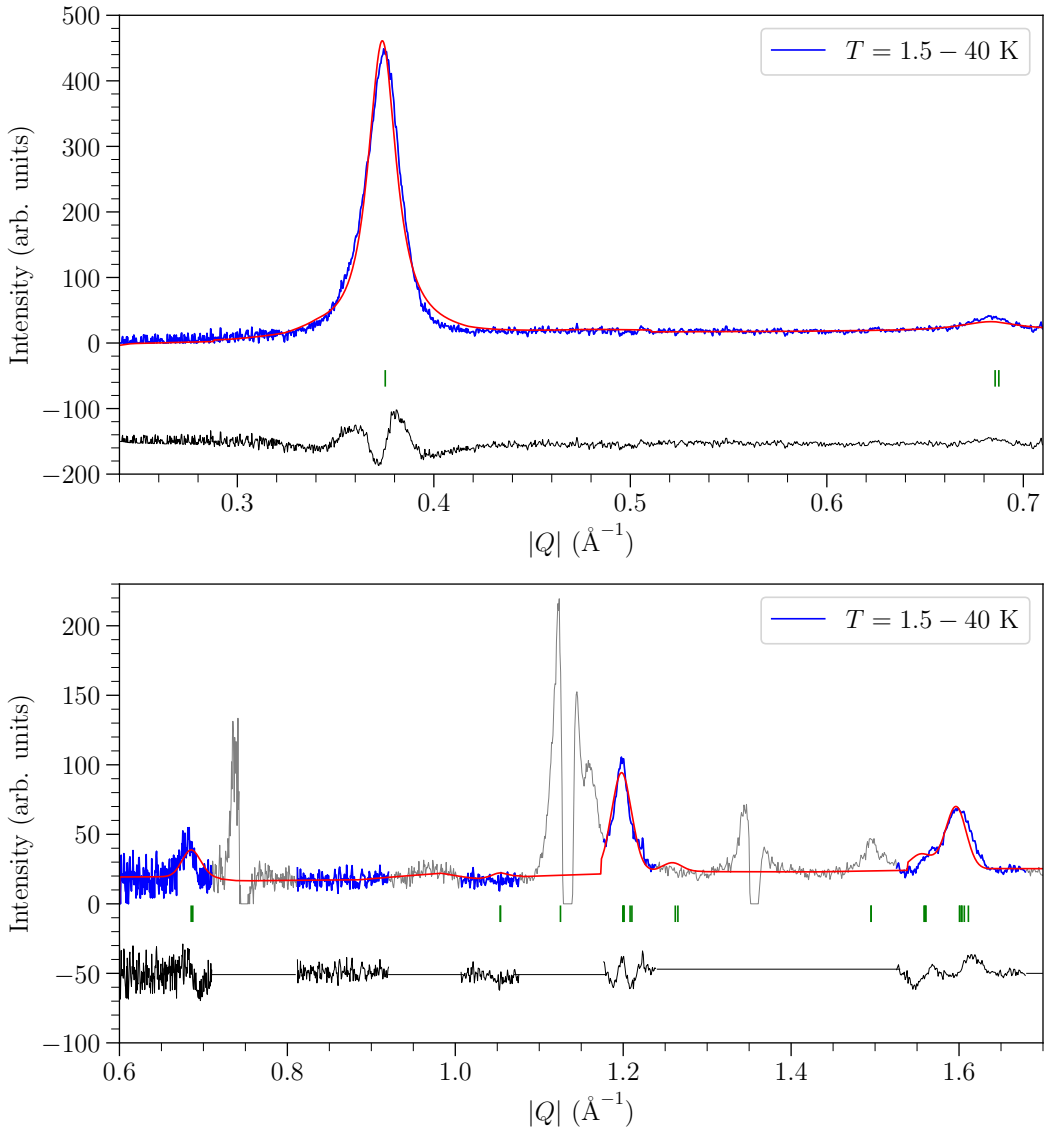

Figure 7.18: Averievite WISH data obtained from the temperature subtraction $T = 1.5$–40 K, with a magnetic structure refinement (red) in Γ_3. The grey regions arise from the subtraction of nuclear peaks and were excluded from the refinements. The green tick marks indicate the magnetic Bragg peak positions and the difference plot is shown in black. (**Top.**) Bank 1. (**Bottom.**) Bank 2.

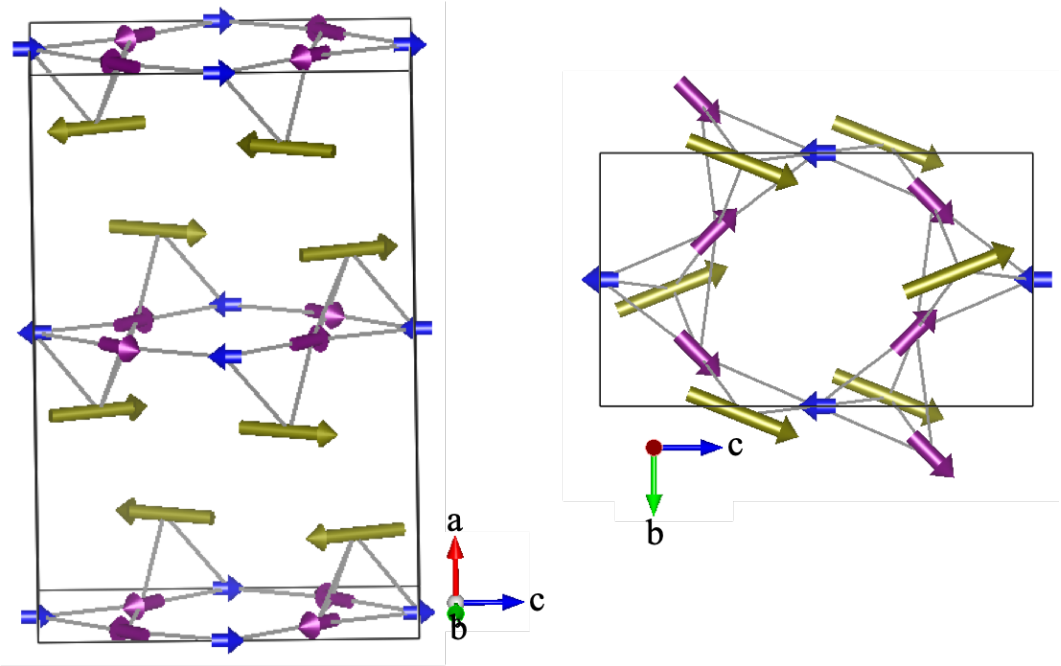

Figure 7.19: Averievite magnetic structure viewed from the side and from the top, refined from WISH data in Γ_3 of space group $P12_1/c1$. The magnetic moments are 0.60 μ_B for Cu_h (yellow), 0.30 μ_B for Cu_{k1} (blue) and 0.47 μ_B for Cu_{k2} (purple).

7.6 Sublattice magnetisation of averievite

The diffraction data collected on WISH were used to extract the integrated intensities, I, of the $(\frac{1}{2}, 0, 0)$ magnetic Bragg peak near $Q = 0.37$ Å^{-1}, as a function of temperature. These are proportional to the square of the sublattice magnetisation M and are expected to follow a power law near the critical temperature, T_{N} [16], given by

$$I \propto M^2 \propto \left(\frac{T_{\mathrm{N}} - T}{T_N}\right)^{2\beta}, \tag{7.5}$$

where β is a critical exponent. I was determined using single peak fits with a pseudo-Voigt function in TOPAS [4]. The background was modelled as a polynomial at $T = 100$ K and scaled for $T < T_N$. T_{N} was fixed to 23 K as determined from $d\chi/dT$ (Section 7.4.1), though its maximum error is estimated to be 1 K. A fit of equation 7.5 yielded $\beta = 0.34(1)$ (Figure 7.20). This value is close to those of the ordered 3-D Ising and XY universality classes ($\beta = 0.327$ and 0.346, respectively) [17–19]. Importantly, these results indicate 3-D correlations in averievite ($d = 3$) rather than 2-D ones.

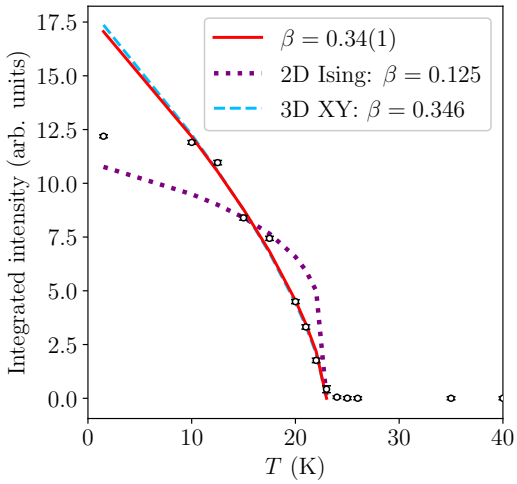

Figure 7.20: Averievite, WISH data. Integrated intensities of the $(\frac{1}{2}, 0, 0)$ magnetic Bragg peak as a function of temperature, T (black open circles). The red line is a fit to equation 7.5 with $T_{\mathrm{N}} = 23$ K. The dotted and dashed lines show the power law behaviour for the ordered 2-D Ising and 3-D XY universality classes, respectively.

7.7 Discussion

The structural analyses of the averievite series of materials, for which Zn_2-averievite is synthesised and characterised here for the first time, indicated a suppression of the monoclinic distortion with Zn-doping as previously reported for the $x = 0$ and $x = 1$ materials [2]. The structure of undoped averievite below its second phase transition at $T = 127$ K has not been previously determined, but was suggested to arise from an ordering of the Cs site [2]. Averievite crystallises in the monoclinic space group $P12_1/c1$ down to $T = 127$ K and our diffraction pattern collected at $T = 100$ K (synchrotron data) showed new peaks compared to the $T = 300$ K data, which could be indexed by the $\mathbf{k} = (0,\ \frac{1}{3},\ 0)$ propagation vector. $P12_1/c1$ does not have many symmetry elements to break, namely there is a 2_1 screw axis and a glide plane. However, the symmetry of this single propagation vector suggests the breaking of three-fold symmetry. As previously suggested [2], this could arise from the Cs site ordering onto a position along a and moving perpendicular to the modulation vector that points in the b direction. Another possibility is inspired by the analyses of the Zn_1- and Zn_2-averievite diffraction patterns. These indicated displacive disorder in the kagome layers, which was described by a static rotation of the Cu triangles in the ab plane. It is therefore possible that the kagome triangles in undoped averievite, are rotated in an extreme version of the displacive disorder found in Zn_1- and Zn_2-averievite.

The determination of the magnetic structure of averievite is important in trying to describe its magnetic excitations. Unfortunately, the number of magnetic Bragg peaks was limited and therefore the number of degrees of freedom that could be reliably refined was correspondingly limited. Several magnetic structures were capable of describing the observed data, but the $\angle$Cu-(μ_2-O)-Cu superexchange angles in the kagome triangles suggest antiferromagnetic exchange couplings making it likely that the relative spin orientations represent an antiferromagnetic structure and one corresponding to irrep Γ_3 is proposed. This is a coplanar magnetic structure where the Cu_{k1} and Cu_{k2} kagome spins form a $q = 0$ structure, with relative spin angles of 90°, 135° and 135°, and the capping Cu_h spins mainly point along the c axis

with antiferromagnetic canting in the *bc* plane. Three different moment sizes were required to describe the data with the relative magnitudes being $Cu_h > Cu_{k2} > Cu_{k1}$ and these could be further refined with future single crystal measurements.

It is interesting to note that when doping with Zn to the $x = 1$ level, the Weiss temperature becomes more positive (from −180 K to −105 K) suggesting that the honeycomb Cu_h spins have an antiferromagnetic mean field. The exchange couplings between Cu_h-Cu_h and Cu_h-Cu_k, likely have an energy scale of the Weiss temperature difference. The $x = 1$ and $x = 2$ samples have similar Weiss temperatures of −105 K and −109 K, respectively. The slight decrease in the Weiss temperature of Zn_2-averievite could indicate that when the honeycomb positions are only half occupied by Cu, their mean field is slightly ferromagnetic.

The synthesis of three samples in the averievite series provides an opportunity of comparison between different ground states. The magnetometry results showed a suppression of magnetic order with Zn-doping. Contrary to what has been reported in the literature [2], our data shows that Zn_1-averievite has a magnetic transition at $T = 3.5$ K. This indicates that a spin liquid-like state is unlikely. However, the DC susceptibility below $T = 3.5$ K does not clearly show bifurcation between the field-cooled and zero field-cooled data, as may be expected from a spin glass. To confirm whether Zn_1-averievite has a glassy state, μSR experiments have been planned in collaboration with Dr G. Simutis, Dr F. Bert and Prof. P. Mendels. A comparison of the $x = 1$ and $x = 2$ averievite magnetic susceptibilities, indicates that the two materials have different magnetic behaviours. Whilst it is clear that Zn_2-averievite does not have a magnetic transition down to $T = 2$ K, the susceptibility of the $x = 1$ sample at low temperature is lower than of the $x = 2$ material as it goes through the transition at $T = 3.5$ K.

The presence of Cu/Zn antisite disorder is a common issue when doping such layered materials and has been observed in other kagome antiferromagnets [9, 20–22]. In the case of herbertsmithite, extensive efforts have gone in to accurately parameterizing this disorder as defect spins may have an effect on the low-energy magnetic excitations [23]. For Zn_2-averievite, SEM-EDX indicated a stoichiometry

close to the nominal one and the magnetisation data were used to give a lower bound of $\sim 6.3\%$ Cu spins occupying honeycomb sites. A measure of the local susceptibility of Zn_2-averievite, would give a more accurate intrinsic kagome susceptibility that could be used to fit the magnetisation data.

7.8 Future work

To determine the origin of the modulation in the crystal structure of averievite, the first step would be an analysis of the synchrotron data measured at $T = 100$ K using difference Fourier maps. However, the synthesis and diffraction studies of single crystals would make the structure determination more straightforward as it would allow the structure to be probed in various spatial directions.

Local probe measurements such as NMR on Zn_1-averievite and Zn_2-averievite would help to determine whether the displacive disorder in fact leads to local symmetry lowering. This would be particularly important to determine in Zn_2-averievite that we suggest has equilateral triangles and distorted hexagons, as the crystal structure is used as the basis for interpreting its magnetic ground state and excitations.

Scanning electron microscopy combined with energy dispersive x-ray analysis (SEM-EDX) was used to get a good estimate of the elemental composition of the $x = 1$ and $x = 2$ Zn-doped samples. It showed the two samples to have almost nominal stoichiometries. For Zn_2-averievite, the magnetisation data gave an estimate of the percentage of Cu that sits on the honeycomb sites, but the possible dilution of the kagome layers could not be quantified. A more accurate determination of the sample stoichiometries and extent of antisite disorder can be made using anomalous x-ray diffraction. In this technique, the x-ray energy is tuned to match the absorption edges of the elements in the sample providing both the sample stoichiometry and the element site position.

7.9 Conclusions

This chapter has presented crystallographic studies and magnetometry measurements on the averievite series of materials, $Zn_xCu_{5-x}(VO_4)_2O_2CsCl$ for $x = 0$, 1 and 2, as well as the magnetic structure refinement of the parent compound. For

$x = 0$ averievite, we find the crystal structure at room temperature agrees with the literature [2]. For the previously undetermined crystal structure below $T = 127$ K, we find a commensurately modulated crystal structure with $\mathbf{k} = (0,\ \frac{1}{3},\ 0)$. We propose that this either arises from an ordering of the Cs in the *a* direction, in agreement with the previous suggestion [2], or from displacive disorder in the kagome triangles, similar to that found in our Zn-doped samples. Displacive disorder in both the $x = 1$ and $x = 2$ materials was found from the analyses of neutron diffraction data, but it is more prominent in the kagome planes of Zn_2-averievite as Cu_k in Zn_1-averievite refines to the high-symmetry (0.5, 0, 0) position, within error. Using SEM-EDX, we find both Zn_1-averievite and Zn_2-averievite to have a stoichiometry close to the nominal one, with the latter having a minimum of $\sim 7\%$ Cu defects from DC susceptibility.

The magnetic structure of averievite is important in the determination of its exchange interactions. The number of degrees of freedom that could be reliably refined was limited and symmetry analysis was used to stabilise the refinement. Several magnetic structures were capable of describing the observed data, so the $\angle$Cu-(μ_2-O)-Cu superexchange angles in the kagome triangles were used to favour a structure in Γ_3 over Γ_1. The magnetic structure suggested here comprises of two kagome sites forming a $q = 0$ structure with moments smaller than the Cu_h ones. However, single crystal data will be required to further refine the magnetic structure. The order parameter of averievite indicates 3-D spin correlations rather than 2-D ones, suggesting strong correlations between the kagome and honeycomb Cu_h spins, as well as between pyrochlore slabs. Importantly, the $\angle Cu_{k1,k2}$-(μ_2-O)-Cu_h superexchange angles suggest weak coupling between the kagome layers and the honeycomb spins.

Bulk magnetometry showed a suppression of magnetic order with increased Zn doping and indicated three different ground states. The $x = 2$ sample was found to have a large negative Weiss temperature, indicating an antiferromagnetic mean field, and no magnetic transition down to $T = 2$ K despite a build-up of spin correlations below $T = 160$ K, evidencing strong frustration in the system. Despite the

crystallographic distortion in the kagome hexagons of Zn_2-averievite, the absence of magnetic order indicates that the frustration still survives in this geometry and that the material presented is a good candidate quantum spin liquid.

Bibliography

[1] L. P. Vergasova, G. L. Starova, S. K. Filatov, and V. V. Ananev, Dokl. Earth Sci. **359A**, 450 (1998).

[2] A. S. Botana, H. Zheng, S. H. Lapidus, J. F. Mitchell, and M. R. Norman, Phys. Rev. B **98**, 054421 (2018).

[3] T. Hillel and Y. Ein-Eli, J. Power Sources **229**, 112 (2013).

[4] A. Coelho, *Topas Academic Version 4.1.* 2007.

[5] O. Arnold, J. Bilheux, J. Borreguero, A. Buts, S. Campbell, L. Chapon, M. Doucet, N. Draper, R. Ferraz Leal, M. Gigg, V. Lynch, A. Markvardsen, D. Mikkelson, R. Mikkelson, R. Miller, K. Palmen, P. Parker, G. Passos, T. Perring, P. Peterson, S. Ren, M. Reuter, A. Savici, J. Taylor, R. Taylor, R. Tolchenov, W. Zhou, and J. Zikovsky, Nuclear Instruments and Methods in Physics Research Section A: Accelerators, Spectrometers, Detectors and Associated Equipment **764**, 156 (2014).

[6] J. B. Goodenough, Scholarpedia **3**, 7382 (2008).

[7] P. W. Stephens, J. Appl. Cryst. **32**, 281 (1999).

[8] D. Boldrin, "Synthesis and Study of Quantum Kagome Magnets", Ph.D. thesis (University College of London, 2015).

[9] R. H. Colman, A. Sinclair, and A. S. Wills, Chem. Mater. **22**, 5774 (2010).

[10] V. F. Sears, Neutron News **3**, 26 (1992).

[11] G. A. Bain and J. F. Berry, J. Chem. Educ. **85**, 532 (2008).

[12] F. Bert, A. Olariu, A. Zorko, P. Mendels, J. C. Trombe, F. Duc, M. A. de Vries, A. Harrison, A. D. Hillier, J. Lord, A. Amato, and C. Baines, J. Phys.: Conf. Ser. **145**, 012004 (2009).

[13] E. Kermarrec, "Nouveaux états quantiques de spin induits par frustration magnétique sur le réseau kagome", Ph.D. thesis (2012).

[14] A. S. Wills, Phys. B **278**, 680 (2000).

[15] O. V. Kovalev, *Representations of the Crystallographic Space Groups: Irreducible Representations, Induced Representations and Corepresentations*, edited by H. T. Stokes and D. M. Hatch, 2nd ed. (Gordon and Breach, London, 1993).

[16] M. F. Collins, *Magnetic Critical Scattering* (Oxford University Press, 1989).

[17] L. D. Sanjeewa, V. O. Garlea, M. A. McGuire, C. D. McMillen, H. Cao, and J. W. Kolis, Phys. Rev. B **93**, 224407 (2016).

[18] F. L. Pratt, P. J. Baker, S. J. Blundell, T. Lancaster, M. A. Green, and M. Kurmoo, Phys. Rev. Lett. **99**, 017202 (2007).

[19] B. Thielemann, C. Rüegg, K. Kiefer, H. M. Rønnow, B. Normand, P. Bouillot, C. Kollath, E. Orignac, R. Citro, T. Giamarchi, A. M. Läuchli, D. Biner, K. W. Krämer, F. Wolff-Fabris, V. S. Zapf, M. Jaime, J. Stahn, N. B. Christensen, B. Grenier, D. F. McMorrow, and J. Mesot, Phys. Rev. B **79**, 020408 (2009).

[20] F. Bert, S. Nakamae, F. Ladieu, D. L'Hôte, P. Bonville, F. Duc, J. C. Trombe, and P. Mendels, Phys. Rev. B **76**, 132411 (2007).

[21] M. A. De Vries, D. Wulferding, P. Lemmens, J. S. Lord, A. Harrison, P. Bonville, F. Bert, and P. Mendels, Phys. Rev. B **85**, 014422 (2012).

[22] H. Yoshida, Y. Muraoka, T. Sörgel, M. Jansen, and Z. Hiroi, Phys. Rev. B **73**, 020408 (2006).

[23] M. A. de Vries, J. R. Stewart, P. P. Deen, J. O. Piatek, G. J. Nilsen, H. M. Rønnow, and A. Harrison, Phys. Rev. Lett. **103**, 237201 (2009).

Chapter 8

Magnetic excitations in the averievite series, $Zn_xCu_{5-x}(VO_4)_2O_2CsCl$ for x = 0, 1 and 2

8.1 Introduction

Chapter 7 analysed the crystal structures and bulk magnetometry data of the averievite series, $Zn_xCu_{5-x}(VO_4)_2O_2CsCl$ for $x = 0$, 1 and 2, as well as the magnetic structure of undoped averievite. X-ray synchrotron and neutron diffraction data were used to show that undoped averievite crystallises in the monoclinic $P12_1/c1$ space group (no. 14) with a commensurate modulation at low temperature described by the propagation vector $\mathbf{k} = (0,\ \frac{1}{3},\ 0)$. Both Zn_1-averievite ($x = 1$ sample) and Zn_2-averievite ($x = 2$ sample) were modelled in the trigonal $P3$ space group (no. 143), where equilateral kagome triangles are rotated in the ab plane thereby distorting the kagome hexagons. The magnetic susceptibility of averievite showed a magnetic phase transition at $T_N = 23$ K in agreement with the literature [1]. For Zn_1-averievite, a magnetic transition was seen in $d\chi/dT$ at $T = 3.5$ K and Zn_2-averievite indicated no magnetic transition down to $T = 2$ K. The magnetometry results of Zn_2-averievite, together with its almost ideal kagome lattice, make it a good candidate in the search of experimental materials hosting quantum spin liquid ground states. To this end, the magnetic excitations of Zn_2-averievite as well

as of the $x = 0$ and $x = 1$ samples were measured using powder inelastic neutron scattering (INS).

It was thought that since the distortion in the kagome triangles of undoped averievite is very small ($\sim$2%), the Cu-Cu couplings would have a similar energy scale to those in Zn_2-averievite and could be used to place Zn_2-averievite in a quantum spin liquid phase diagram. As will be detailed in this chapter, determining the exchange interactions in averievite was a difficult task due to the limitations in determining an accurate magnetic structure, discussed in Chapter 7. The results and analyses of the INS measurements will be presented for each sample separately, followed by a comparison between them.

8.2 Inelastic neutron scattering on averievite

8.2.1 Overview

The magnetic excitations of the ground state of averievite were measured by inelastic neutron scattering (INS). An initial experiment on the thermal-neutron time-of-flight (TOF) spectrometer MERLIN, ISIS, was used to determine the energy scale of the magnetic excitations. As these measurements were made with quite high incident neutron energies, E_i, lower incoming neutron energies, as well as longer counting times, were required to determine the presence of a gap. Therefore, data were also collected on the cold-neutron TOF spectrometer IN5 at the ILL. The measurements revealed spin wave excitations at $Q = 0.37$, 1.16 and 1.97 Å^{-1}, extending up to $\sim$ 11 meV. A summary of the data collection conditions on IN5 is given in Table 8.1 for reference throughout this section.

8.2.2 Initial measurements on MERLIN

A $\sim$ 5 g sample, from the $\sim$ 7 g measured on WISH and HRPD, was loaded into an aluminium cylinder and placed in a top-loading closed-cycle refrigerator. It was measured with $E_i = 17,\ 38$ and 100 meV at $T = 7$ and 50 K, above and below $T_N = 23$ K. The $E_i = 38$ and 100 meV data are included in Appendix E. At $T = 7$ K, the data collected with the two higher incident neutron energies show the existence of dispersive spin waves up to 11 meV and no magnetic scattering at higher energy

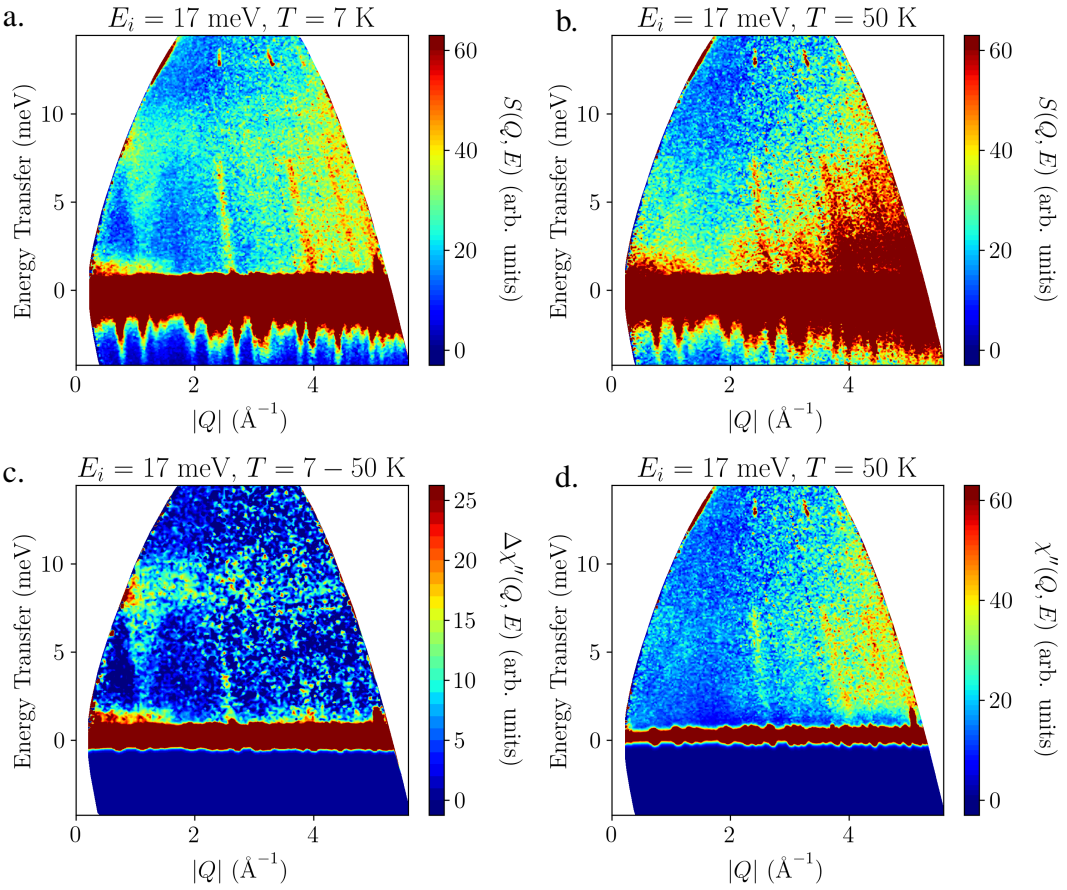

Figure 8.1: Averievite, MERLIN data measured with E_i =17 meV. **a.-b.** $S(Q,E)$ at $T = 7$ K and $T = 50$ K. **c.** Temperature subtraction in $\chi''(Q,E)$ between the $T = 7$ and 50 K data. **d.** $\chi''(Q,E)$ at $T = 50$ K.

transfers. The spin waves are better seen with $E_i = 17$ meV (Figure 8.1a) and become diffuse above T_N (Figure 8.1b).

The high-temperature $S(Q,E)$ was divided by the Bose population factor and the resulting $\chi''(Q,E)$ is shown in Figure 8.1d. A temperature subtraction in $\chi''(Q,E)$ can be used to isolate the magnetic scattering as shown in Figure 8.1c. A spin wave branch at $Q = 1.16$ Å^{-1} is clearly seen in $\Delta\chi''(Q,E)$ and appears to be gapless down to at least $E = 1.7$ meV. The magnetic scattering below 1.7 meV cannot be seen with this incident neutron energy and longer counting times would be needed for better statistics. To investigate the magnetic scattering and a possible gap below this, data were collected with lower incident neutron energies on IN5.

8.2.3 Spin wave excitations on IN5

A 2.83 g sample, from the ~ 7 g measured on WISH and HRPD, was loaded into an annular aluminium cylinder with outer diameter 15 mm and inner diameter 13 mm, attached to a sample stick and inserted into a standard orange cryostat. A summary of the data collection conditions can be found in Table 8.1. Empty can measurements were made with all incident energies at $T = 1.5$ K and subtracted from the sample data.

T (K) \ E_i (meV)	3.55	5.11	10.43	20.45
1.5	IN5	IN5	IN5	IN5
40-43	IN5	-	-	IN5
60	-	IN5	IN5	-
120	-	-	-	IN5

Table 8.1: Summary of averievite INS measurements on IN5 at the ILL, with incident neutron energies E_i at temperatures T.

Figures 8.2a-c show $S(Q,E)$ collected with an incident neutron energy of $E_i = 20.45$ meV. At $T = 1.5$ K, the spin wave branch seen on MERLIN at $Q = 1.16$ Å^{-1} is clearly seen extending up to ~ 11 meV. For $Q > 4$ Å^{-1}, the intense scattering above 2 meV corresponds to incoherent phonons that have a $\sim Q^2$ dependence. When temperature is increased above $T_N = 23$ K to $T = 43$ K, the spin waves collapse into diffuse scattering that at low Q is centred at ~ 1 Å^{-1} (Figure 8.2b). As temperature is further increased to $T = 120$ K, the magnetic scattering becomes more diffuse and the phonon intensity dominates the spectrum (Figure 8.2c).

The magnetic scattering was separated from the incoherent phonons by a temperature subtraction in $\chi''(Q,E)$. At $T = 1.5$ K, $\chi''(Q,E)$ is equal to $S(Q,E)$ (Figure 8.2a) and $\chi''(Q,E)$ at $T = 120$ K is shown in Figure 8.2d. The temperature subtraction is shown in Figure 8.2e, where the intense scattering above the elastic line extending to about $E = 2.5$ meV and $Q = 2.1$ Å^{-1} is spurious. The spin wave excitations are clearly seen extending up to about 10 meV and the branch at 1.97 Å^{-1} is more evident than in the MERLIN data.

To fully characterise the magnetic excitations, data were collected with lower

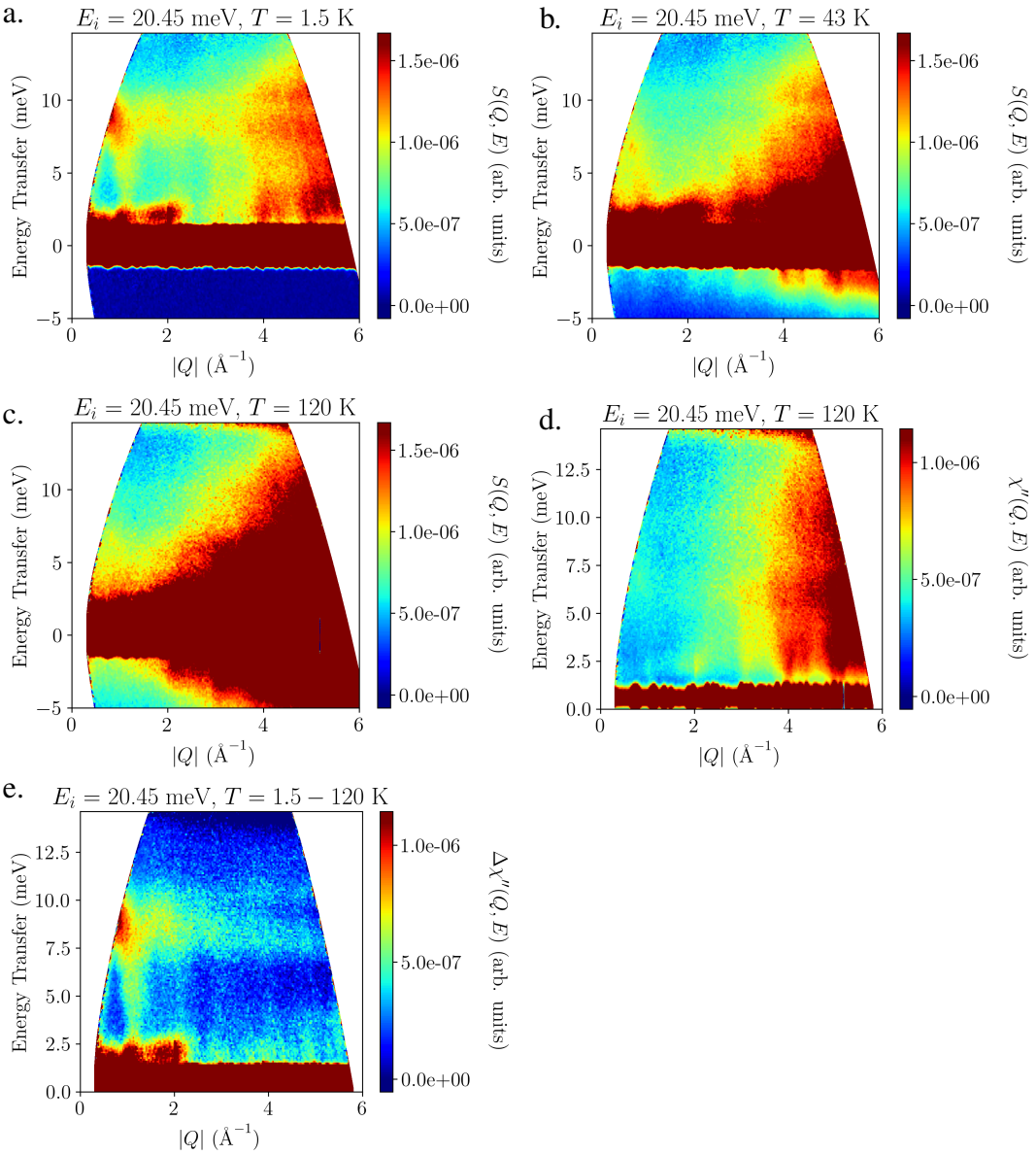

Figure 8.2: Averievite, IN5 data measured with E_i =20.45 meV. **a.-c.** $S(Q,E)$ at $T = 1.5$ K, $T = 43$ K and $T = 120$ K. **d.** $\chi''(Q,E)$ measured at $T = 120$ K. **e.** Temperature subtraction in $\chi''(Q,E)$ between the $T = 1.5$ and 120 K data.

incident neutron energies. At $T = 1.5$ K, the $E_i = 10.43$ meV data (Figure 8.3a) show the same spin wave branches as seen with $E_i = 20.45$ meV and unfortunately has spurious scattering in the range $1.7 < Q < 2.2$ Å^{-1} at $E = 2$ meV, originating from the cryostat. Nevertheless, there is a hint of additional scattering on the edge of the kinematic window at low Q extending up to ~ 4 meV. This is more clearly seen in a combined plot of the $E_i = 3.55$ and 5.11 meV data at $T = 1.5$ K (Figure 8.3c), which reveal a spin wave branch at 0.37 Å^{-1}. The gap of the 1.16 Å^{-1} branch

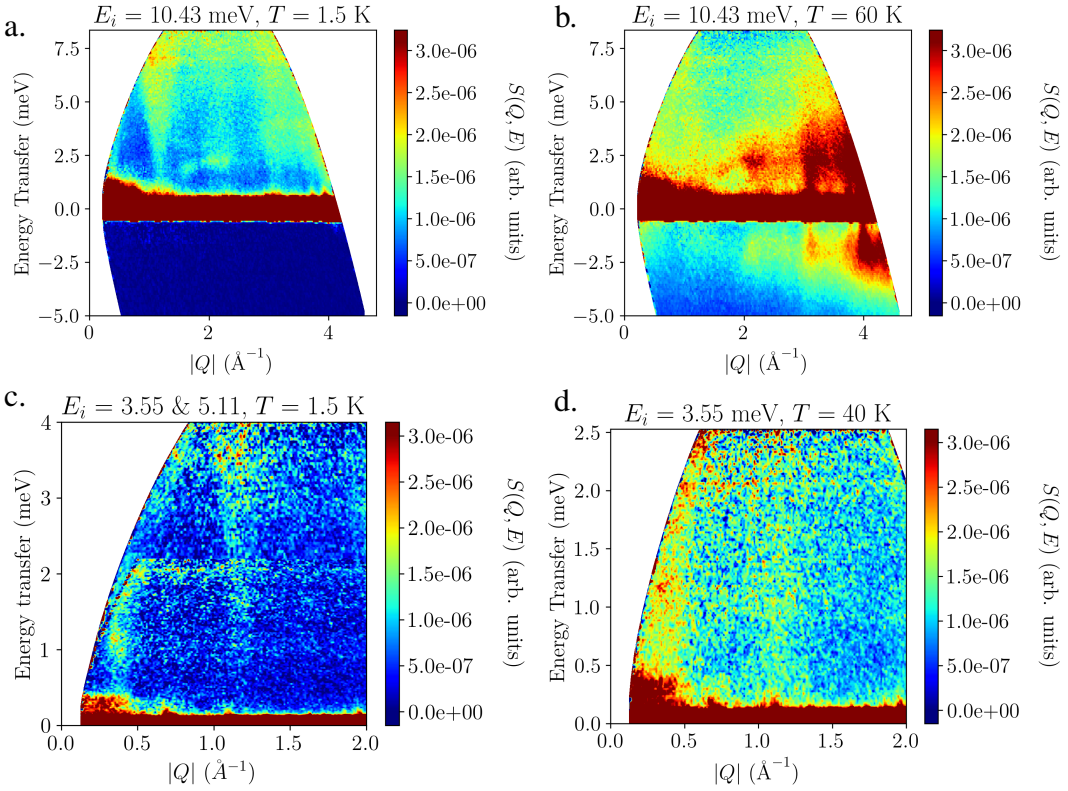

Figure 8.3: Averievite, $S(Q,E)$ measured on IN5 with $E_i = 10.43$ meV at **a.** $T = 1.5$ K and **b.** $T = 60$ K. **c.** Combined data with $E_i = 3.55$ and 5.11 meV at $T = 1.5$ K. **d.** $S(Q,E)$ with E_i =3.55 meV at $T = 40$ K.

is estimated to be ~ 0.4 meV as will be further discussed in Section 8.2.4. The data collected with $E_i = 3.55$ and 5.11 meV at $T > 1.5$ K are not at the same temperature, so a similar data combination could not be done and the former are shown at $T = 40$ K in Figure 8.3d. The magnetic excitations have become diffuse and two vertical columns of magnetic scattering centred at the same Q positions (0.37 Å^{-1} and 1.16 Å^{-1}) are observed, indicative of strong short-range correlations. This is in agreement with the magnetic susceptibility data, which showed antiferromagnetic correlations building up below $T = 200$ K well before the magnetic transition.

8.2.4 Analysis

The spin wave excitations at $T = 1.5$ K were characterised using their E and Q dependencies. The Q positions of the spin wave branches were determined by integrating $\Delta\chi''(Q,E)$ over various E ranges as shown in Figure 8.4. $\Delta\chi''_E(Q)$ was fitted with two Gaussian peaks and a flat background, giving peak centres at 1.16(1) Å^{-1}

and 1.97(5) Å^{-1}. The branch near $Q = 1.16$ Å^{-1} is close to the magnetic Bragg peaks at $Q = 1.13$ Å^{-1} and $Q \approx 1.2$ Å^{-1}in the $P12_1/c1$ space group. These include: the $(\frac{3}{2}, 0, 0)$ at $Q = 1.13$ Å^{-1}; and the $(-\frac{3}{2}, 1, 1)$, $(\frac{1}{2}, 1, 1)$ and $(-\frac{3}{2}, 0, 2)$ near $Q \approx 1.2$ Å^{-1}, in order of increasing Q. The peak at 1.16 Å^{-1} seems to move to

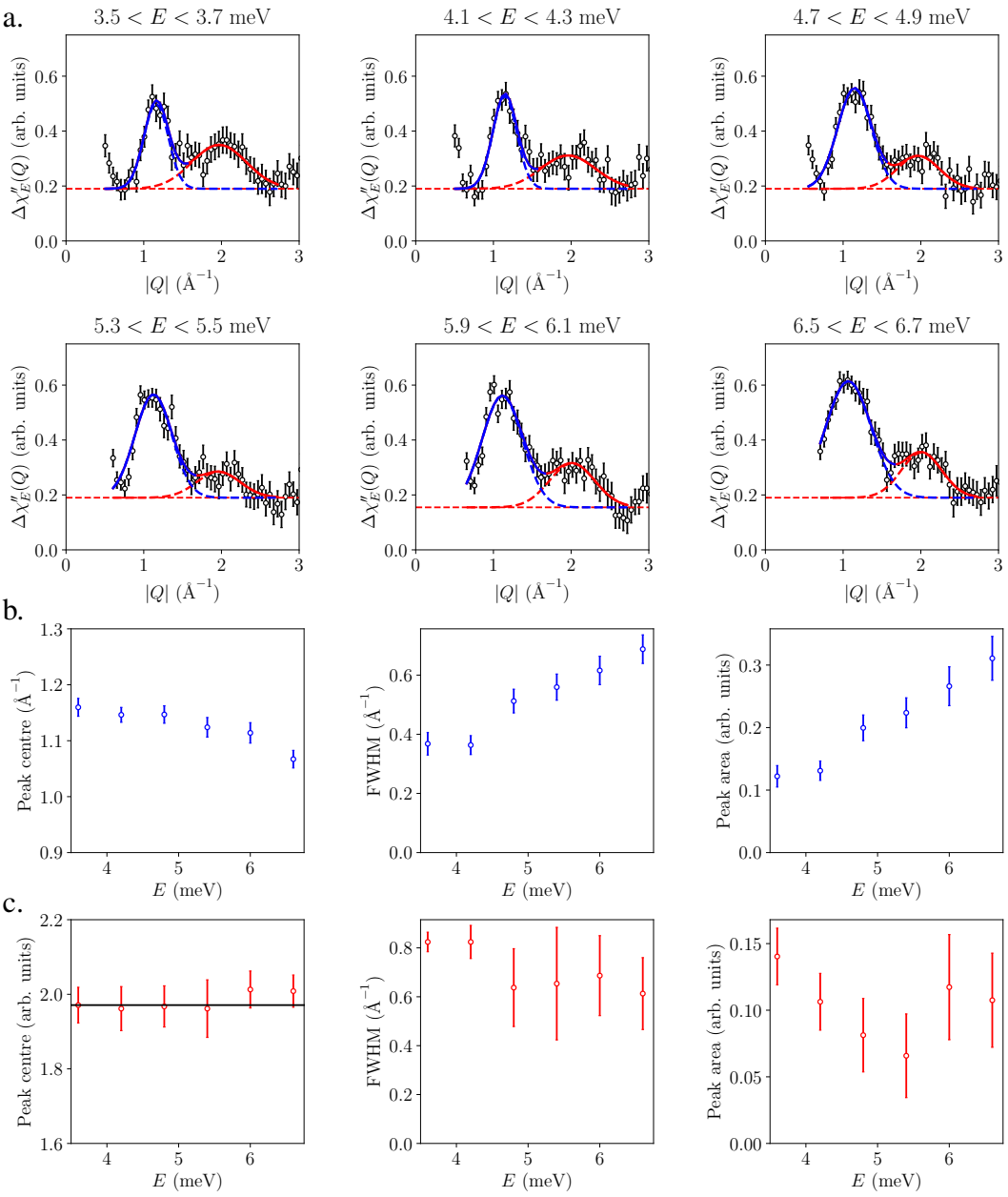

Figure 8.4: Averievite IN5 data with $E_i = 20.45$ meV at $T = 1.5$ K. **a.** $\Delta\chi''_E(Q)$ obtained by integrating $\Delta\chi''(Q, E, T = 1.5 - 100$ K) over various energy ranges (black) fitted with two Gaussians (red and blue solid lines) and a flat background (dashed red line). Parameters obtained from the Gaussian fits for **b.** the peak near $Q = 1.16$ Å^{-1} and **c.** the peak near $Q = 1.97$ Å^{-1}. The horizontal black line shows the average peak centre.

lower Q with increasing energy transfer, indicating that the intensity in the powder average disperses to lower Q. Its FWHM increases with increasing E, giving further support for its dispersive character. The peak area increases with increasing energy until the branch approaches the optical band at ~ 6 meV (see Figure 8.2e).

The peak at higher Q is found to be centred at 1.97(5) Å^{-1}, which is near the ($-\frac{7}{2}$, 0, 1) and ($\frac{5}{2}$, 0, 1) magnetic Bragg peaks. Its centre stays relatively constant as the energy increases and its FWHM also seems to stay relatively constant up to 6.6 meV, probably due to the powder averaging of the spin wave intensity.

A similar analysis was used for the spin wave branch at lower Q observed in the data collected with $E_i = 3.55$ and 5.11 meV (Figure 8.3c). $S(Q,E)$ was integrated over various energy ranges to obtain $S_E(Q)$ and fitted with two Gaussian functions and a flat background as shown in Figure 8.5. The peak at lower Q has an average centre at 0.37(1) Å^{-1} and this stays constant within error between 0.5 and 1.5 meV. This spin wave branch emerges from the ($\frac{1}{2}$, 0, 0) magnetic Bragg peak in the space group $P12_1/c1$. Between 0.5 and 1.5 meV the FWHM also changes little, but its peak area increases with increasing E. The other peak was found to be centred at Q =1.16(2) Å^{-1}, in good agreement with the value determined from the $E_i = 20.45$ meV data. In the energy range $0.7 < E < 1.5$ meV, its peak area seems to stay relatively constant.

The magnetic scattering can also be analysed using its energy dependence, by integrating $\Delta\chi''(Q,E)$ over various Q ranges to obtain $\Delta\chi''_Q(E)$. $\Delta\chi''(Q,E)$ was integrated over the 1.16 Å^{-1} and 1.97 Å^{-1} branches, as well as at lower and higher Q ranges as shown in Figure 8.6a. As expected, $\Delta\chi''_Q(E)$ is most intense at the position of the 1.16 Å^{-1} spin wave branch. The magnetic scattering near the Q =1.97 Å^{-1} branch is weaker and comparable to $0.6 < Q < 0.8$ Å^{-1}. At higher Q the magnetic contribution is only in the optical band above $\sim$6 meV.

To confirm the magnetic origin of the 1.16 Å^{-1} spin wave branch, $\chi''_Q(E)$ at $T = 1.5$, 43 and 120 K integrated over $0.9 < Q < 1.3$ Å^{-1} is shown in Figure 8.6b. At the lowest measured temperature, the excitation has maximum intensity at ~ 8.7 meV with a bandwidth of $\sim$11 meV. Above T_N at $T = 43$ K, the peak

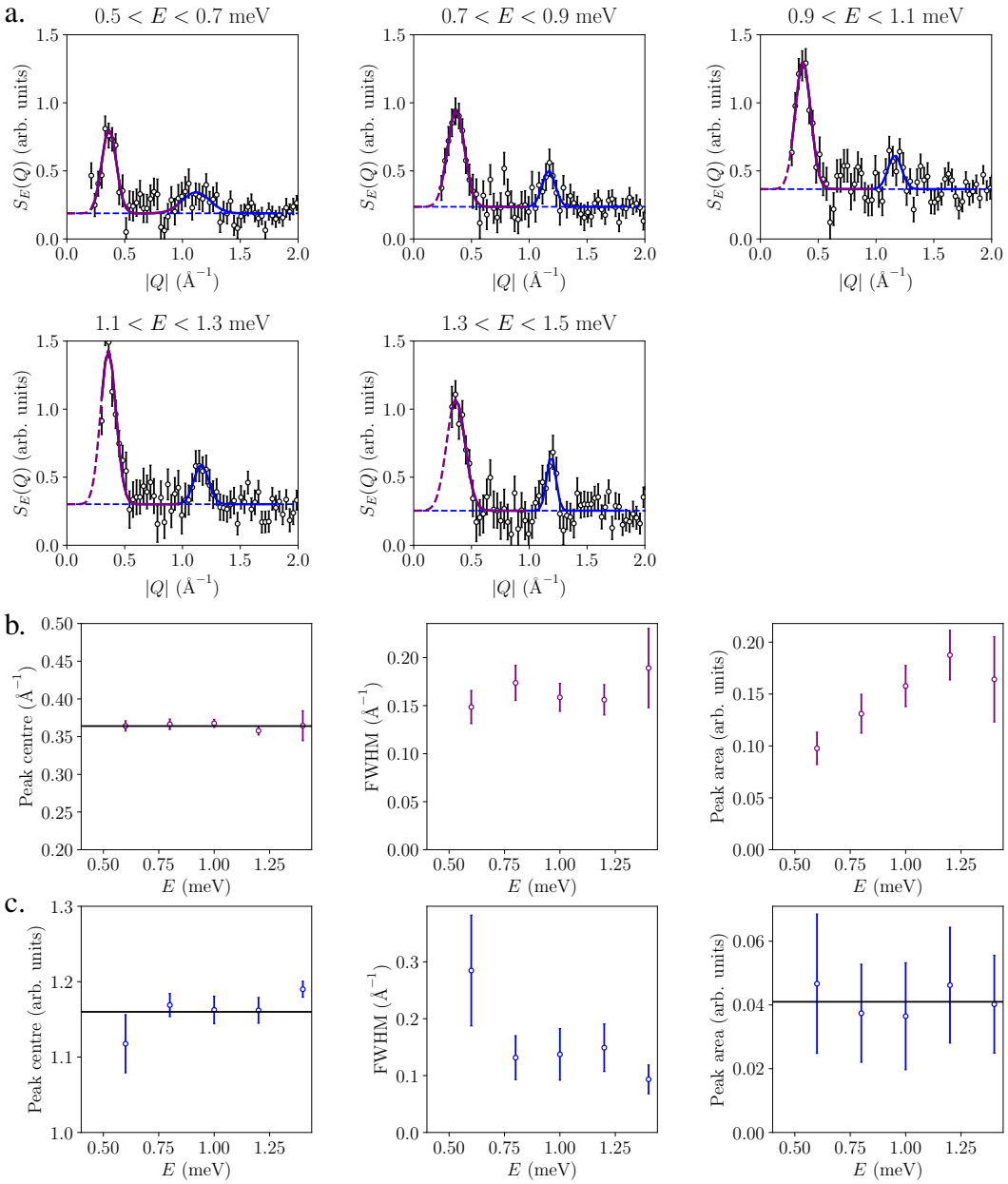

Figure 8.5: Averievite IN5 data with $E_i = 3.55$ meV at $T = 1.5$ K. **a.** Energy integrated $S(Q,E)$ (black) fitted with two Gaussians (purple and blue solid lines) and a flat background (blue dashed line). **b.** Parameters obtained from the Gaussian fits for the peak near $Q = 0.37$ Å^{-1}. The black line shows the average peak centre. **c.** Parameters obtained from the Gaussian fits for the peak near $Q = 1.16$ Å^{-1}. The black lines show the average peak centre and average peak area.

in $\chi''_Q(E)$ disappears as the system goes through the magnetic phase transition into a correlated paramagnetic state. At $T = 120$ K, $\chi''_Q(E)$ loses intensity across the whole E range, becoming almost flat in energy, as the magnetic correlations are

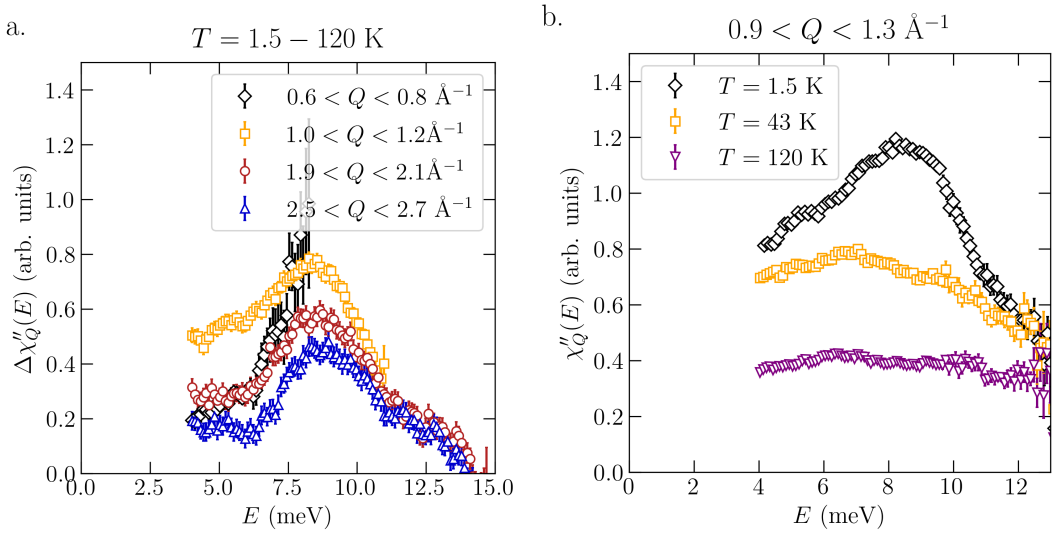

Figure 8.6: Averievite IN5 data with $E_i = 20.45$ meV, excluding the spurious scattering above the elastic line. **a.** $\Delta\chi''_Q(E)$ obtained by integrating $\Delta\chi''(Q,E,T = 1.5 - 120$ K) over various Q ranges. **b.** $\chi''(Q,E)$ integrated over $1.9 < Q < 1.3$ Å^{-1} at $T = 1.5$ K (black), $T = 43$ K (orange) and $T = 120$ K (purple).

further weakened and the scattering becomes more diffuse.

The results of the Gaussian fits were used to estimate the size of a hypothetical gap. For the spin wave branch centred at $Q = 0.37$ Å^{-1}, the spurious scattering extending up to 0.66 meV prevents the determination of a gap smaller than this. For the branch near $Q = 1.16$ Å^{-1}, the peak areas from the Gaussian fits in Figures 8.4

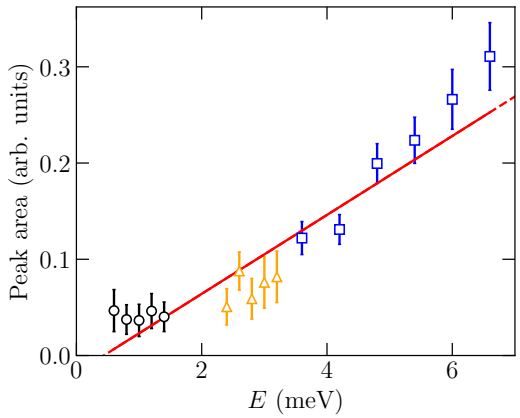

Figure 8.7: Averievite IN5 data at $T = 1.5$ K collected with $E_i = 3.55$ (black), 5.11 (orange) and 20.45 meV (blue). Peak areas of the peak near 1.16 Å^{-1} as a function of energy, obtained from the Gaussian fits shown in Figures 8.4, 8.5 and Appendix E. The red line is a linear fit as explained in the text.

and 8.5, were combined with the results of Gaussian fits for the $E_i = 5.11$ meV data (Appendix E). A linear fit of the peak areas was used to estimate an energy gap of at most 0.4(2) meV (see Figure 8.7).

Thus far, a qualitative description of the magnetic excitation spectra of undoped averievite has been given and the next section will detail attempts to simulate the observed spin waves at $T = 1.5$ K using a preliminary exchange interaction model.

8.2.5 Exchange interactions

The aim of measuring the spin wave excitations of undoped averievite was to determine the dominant exchange interactions and use them to approximate those of the $x = 1$ and $x = 2$ Zn-doped samples. Semi-classical linear spin wave theory in SpinW was used to calculate spin wave spectra [2]. The INS spectra indicated spin waves with branches at $Q = 0.37$, 1.16 and 1.97 Å^{-1} with a bandwidth of 11 meV. Unlike the two magnetic responses seen in claringbullite (Chapter 6), it seems that a single response dominates the spin wave spectra of averievite. Each Cu_h-O-Cu_k pathway has an average superexchange angle of $\sim 96°$, which is close to the 95° crossover angle between ferro- and antiferromagnetic exchange [3] suggesting the exchanges could be close to zero. Despite this weak coupling between the Cu_h and Cu_k spins, the magnetic structure refinements and magnetic susceptibility data (Chapter 7) indicated that all magnetic moments order with a single phase transition and therefore all spins contribute to the observed spin wave excitations. The magnetic structures compatible with the experimentally observed magnetic Bragg peaks (see Chapter 7), indicated that the magnetic moment of the honeycomb Cu_h may be about twice as large as the kagome ones (assuming the kagome Cu moments are similar to each other) with values of 0.60 μ_B, 0.30 μ_B and 0.47 μ_B for Cu_h, Cu_{k1} and Cu_{k2}, respectively. Therefore, to a first approximation, exchange models including only Cu_h were built. The Cu_h spins point along the c direction with a canting in the bc plane and were approximated to be collinear along c.

A simple model with two exchange parameters was considered and is shown in Figure 8.8: J_4 couples the Cu_h spins from one pyrochlore slab to the next (inter-

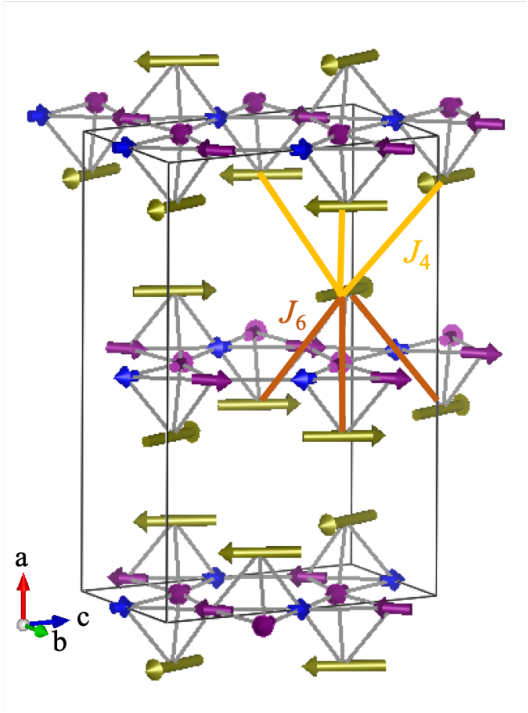

J_i	Cu_h-Cu_h distance
J_4	5.41(5)
	5.42(4)
	5.42(4)
J_6	5.72(5)
	5.72(5)
	5.73(5)

Figure 8.8: Averievite magnetic structure with three magnetic sites: Cu_h (yellow), Cu_{k1} (blue) and Cu_{k2} (purple). The magnetic moments were refined from WISH data. The exchanges are those used in SpinW with a list of the corresponding Cu-Cu distances.

slab exchange); and J_6 couples them within each slab layer through the pathway Cu_h-O-Cu_k-O-Cu_h (intra-slab coupling). Averievite has a Weiss temperature of ~ -180 K evidencing an antiferromagnetic mean field. Since the Weiss temperature becomes more positive with Zn-doping, a reasonable assumption is that the mean field and dominant coupling between the Cu_h spins is antiferromagnetic. The magnetic structure shows the Cu_h spins are antiparallel between pyrochlore slab layers, so the largest antiferromagnetic exchange was set to be $J_4 = 5.28$ meV, with a small ferromagnetic intra-slab exchange $J_6 = -0.88$ meV. The spin wave spectrum was convoluted with the instrumental resolution of $E_i = 20.45$ meV ($dE = 0.4$ meV and $dQ = 0.06$ Å^{-1}), and the result is shown in Figure 8.9b. These exchange interactions capture the bandwidth and Q positions of the observed spin waves, as well as the spin wave stiffness of the branches near $Q = 1.16$ and 1.95 Å^{-1} (see Figure 8.9c). However, the spin wave stiffness of the $Q = 0.37$ Å^{-1} branch does not match the experimental data (Figure 8.9d). This indicates that additional exchanges, likely the ones in the kagome plane, play a role in the excitations. This is further exem-

plified by the magnon density of states shown in Figure 8.9e, where the intensity of the calculated $S_Q(E)$ is lower than the experimental one in most of the energy range. The contribution of J_4 and J_6 to the Weiss temperature can be calculated by

$$\theta_W = -\frac{1}{3}S(S+1)[3J_4 + 3J_6] \approx -38\ K, \tag{8.1}$$

which is about half the difference between the Weiss temperatures of averievite and Zn_2-averievite ($|\Delta\theta_W| = 70$ K). This suggests that additional antiferromagnetic interactions involving Cu_h need to be taken into account. From the magnetic structure refinement of the WISH data (Chapter 7), the kagome Cu spins were refined with angles of 90°, 135° and 135°. Finding exchanges that stabilise these exact angles is a difficult task, particularly considering that they arise from refinements with a limited number of degrees of freedom and may not be accurate (see Chapter 7 for further details). Easier to stabilise is a structure where the kagome spins are at 120° to each other. Considering a dominant first neighbour antiferromagnetic exchange in the kagome layer, with a weaker second neighbour exchange (also in the kagome layer) gives a powder averaged spectrum with the most intense branch at $Q = 1.2$ Å^{-1} and no branch at $Q = 0.37$ Å^{-1}. A suitable exchange between kagome spins that gave a branch at $Q = 0.37$ Å^{-1} could not be found. Combining the kagome exchanges with J_4 and J_6 resulted in the $Q = 1.2$ Å^{-1} branch being the most intense, whilst it can be seen from the Q dependence in Figure 8.9c that the $Q = 0.37$ Å^{-1} branch is the most intense. A more precise magnetic structure from single crystal measurements, may enable a better estimate of the kagome exchanges by comparison to the powder averaged data presented here. Inelastic neutron scattering measurements on single crystals would also make this task easier.

Analysis of the energy dependence of the spin wave branch near $Q = 1.16$ Å^{-1}, indicated a zero-energy gap of at most 0.4(2) meV. The most likely origin of such a hypothetical gap is an anisotropic Dzyaloshinskii-Moriya interaction (DMI). This may also be expected to stabilise the antiferromagnetic canting of the Cu_h spins in the *bc* plane, but is not symmetrically allowed on all J_4 and J_6 exchanges.

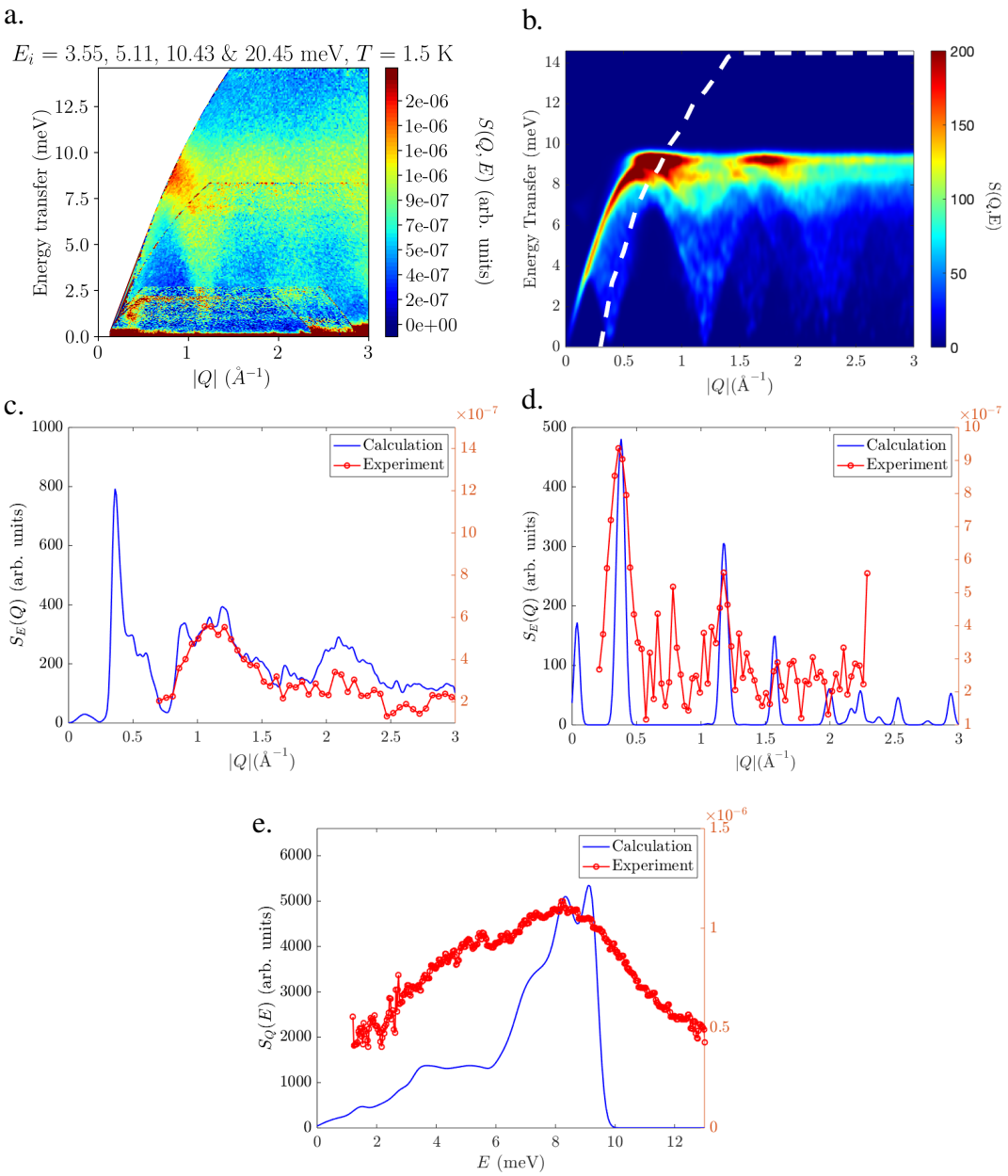

Figure 8.9: Averievite SpinW results. **a.** Combined data collected on IN5 with $E_i = 3.55$, 5.11, 10.43 and 20.45 meV. **b.** Calculated spin wave spectrum with $J_4 = 5.28$ meV and $J_6 = -0.88$ meV corresponding to the exchanges in Figure 8.8. The white dashed line is the kinematic window for $E_i = 20.45$ meV. **c.** Energy integrated $S(Q,E)$ over $4.9 < E < 5.1$ meV from the $E_i = 20.45$ meV data (red) with the calculation in blue. **d.** Energy integrated $S(Q,E)$ over $0.7 < E < 0.9$ meV from the $E_i = 3.55$ meV data (red, $dQ = 0.02$ Å^{-1}) with the calculation in blue. **e.** $S(Q,E)$ integrated over $1.0 < Q < 1.4$ Å^{-1} from the $E_i = 5.11,\ 10.43$ and 20.45 meV data (red) with the calculation in blue.

8.3 Inelastic neutron scattering on Zn_1-averievite

8.3.1 Overview

Inelastic neutron scattering (INS) measurements on Zn_1-averievite were made using the cold neutron time-of-flight (TOF) spectrometer IN5 and the thermal neutron TOF spectrometer PANTHER. A summary of the data collection conditions can be found in Table 8.2. For these measurements, a 7.93 g sample (also measured on HRPD) was loaded into an annular aluminium cylinder with outer and inner diameters of 15 mm and 10 mm, respectively. The raw data were reduced as detailed in Chapter 4 and an empty can measurement was subtracted. The sample environment was a standard orange cryostat as for undoped averievite.

T (K) \ E_i (meV)	3.55	12.5	19.2	20.45
1.5	IN5	PANTHER	PANTHER	IN5
15	IN5	PANTHER	PANTHER	IN5
50	-	PANTHER	PANTHER	-
100	-	PANTHER	PANTHER	-

Table 8.2: Summary of Zn_1-averievite INS measurements on PANTHER and IN5 at the ILL, with incident neutron energies E_i at temperatures T.

8.3.2 High-energy excitations on PANTHER

INS data were collected on PANTHER with incident neutron energies $E_i = 12.5$ and 19.2 meV (summarised in Table 8.2). The reduced $S(Q,E)$ spectra are shown in Figure 8.10. At $T = 1.5$ K with $E_i = 19.2$ meV, the strongest intensities in $S(Q,E)$ are from the elastic scattering centred at $E = 0$ and the phonon scattering at $Q > 2.5$ Å^{-1}. There is a diffuse magnetic excitation centred at $0.75(3)$ Å^{-1} and extending up to ~ 10 meV. With a lower incident neutron energy, $E_i = 12.5$ meV, it is clearer that there are two contributions centred at $Q \approx 0.4$ and 1.0 Å^{-1} (see Figure 8.10b). To better resolve these two excitations, measurements were made with lower E_i on the cold neutron TOF spectrometer IN5 and the results are discussed in the next section. As temperature increases the magnetic scattering becomes more diffuse, but persists up to at least $T = 100$ K (Figures 8.10c-h). This is consistent

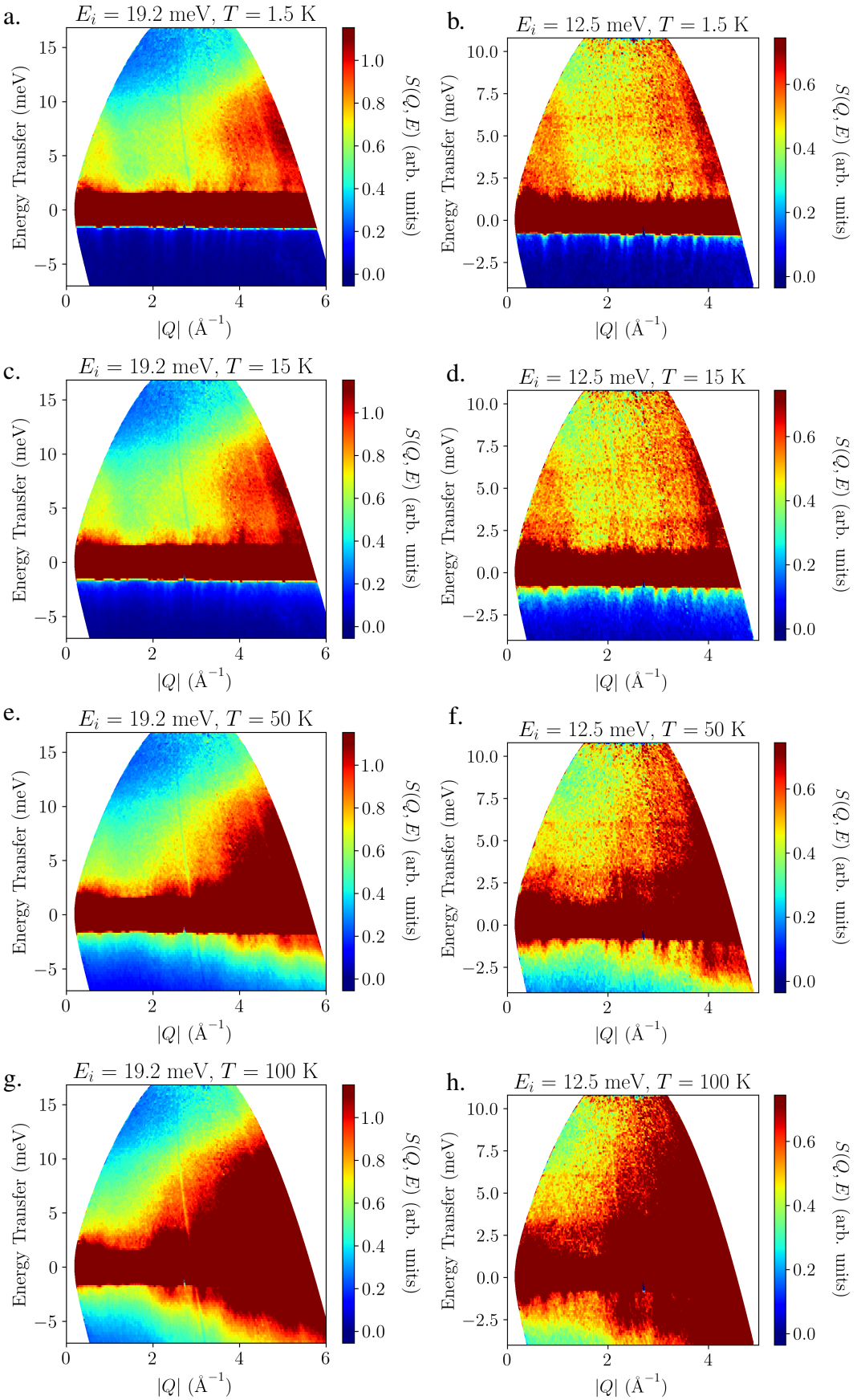

Figure 8.10: Zn_1-averievite $S(Q,E)$ collected on PANTHER with **left.** E_i =19.2 meV and **right.** E_i =12.5 meV at T = 1.5, 15, 50 and 100 K (**top.-bottom.**).

with the magnetic susceptibility data, which shows an onset of antiferromagnetic correlations below $T = 200$ K (Chapter 7).

8.3.3 Low-energy excitations on IN5

To better resolve the two excitations observed using PANTHER and determine the presence of a possible energy gap, measurements were made on IN5 with $E_i = 3.55$ meV at $T = 1.5$ and 15 K (Figure 8.11). At both temperatures, there are two horizontal bands at $E = 1.1$ meV and $E = 2$ meV, which are due to unidentified spurious scattering and the monitor used on IN5, respectively. At $T = 1.5$ K, there are two columns of magnetic scattering at $Q \approx 0.4$ and 1.0 Å^{-1}. The square-like intense feature extending up from the elastic line up to $E \approx 0.5$ meV and $Q \approx 0.5$ Å^{-1}, is spurious scattering from the cryostat. At $T = 15$ K, the excitations are slightly more diffuse, but the two columns of scattering can still be clearly seen. The magnetic susceptibility measurements (Chapter 7) indicated an onset of magnetic order below $T = 3.5$ K and the two excitations in Figure 8.11a are reminiscent of spin waves. To investigate the possibility of long-range magnetic order at $T = 1.5$ K, the elastic line of $S(Q,E)$ was inspected but no magnetic Bragg peaks were seen. This may suggest a spin glass-like system, despite the magnetic susceptibility data (Chapter 7) not clearly evidencing bifurcation between the field-cooled and zero field-cooled data, as may be expected from a spin glass. The ground state of Zn_1-averievite will be further investigated using μSR measurements, which can

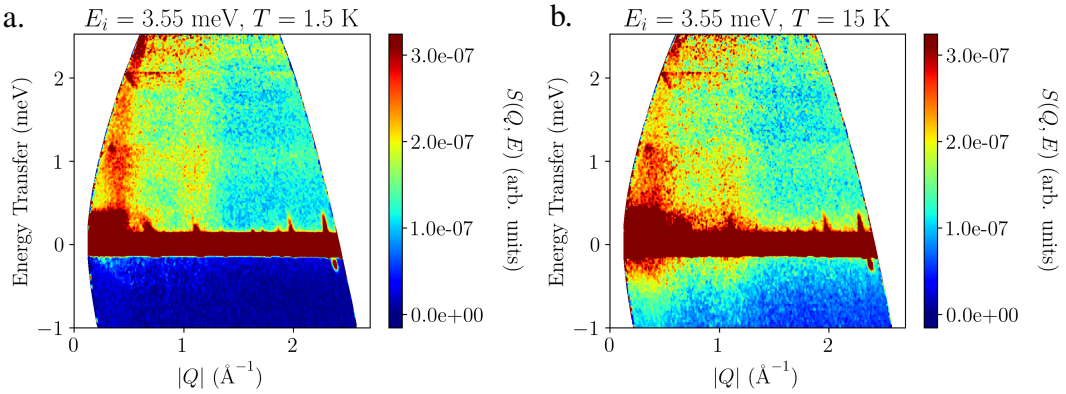

Figure 8.11: Zn_1-averievite $S(Q,E)$ measured on IN5 with E_i =3.55 meV at **a.** $T = 1.5$ K and **b.** $T = 15$ K.

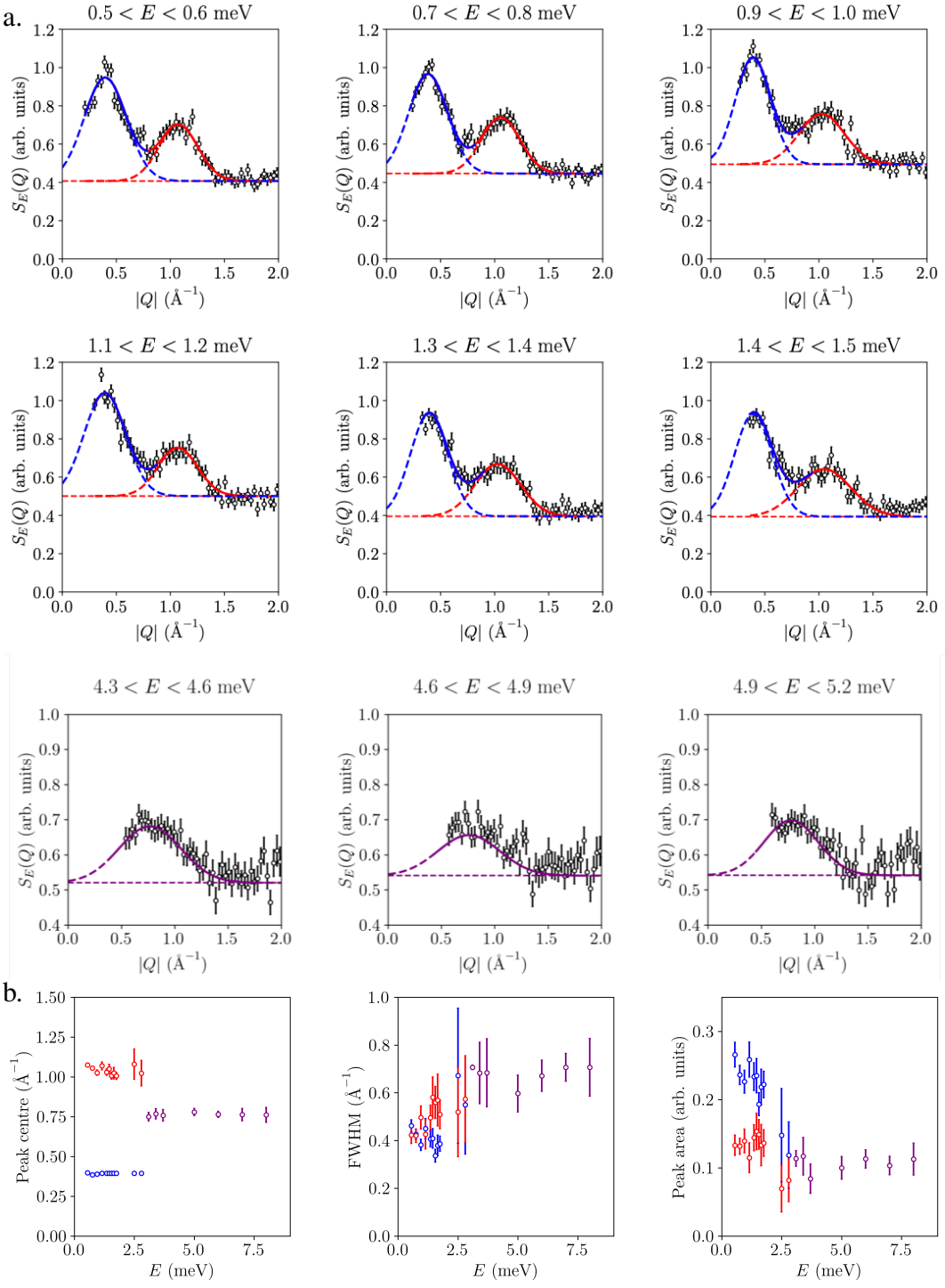

Figure 8.12: Zn_1-averievite, IN5 ($E \leq 1.5$ meV) and PANTHER data obtained with $E_i = 3.55$ and 12.5 meV, respectively, at $T = 1.5$ K. **a.** $S_E(Q)$ obtained by integrating $S(Q,E)$ over various energy ranges (black) fitted with Gaussians and a flat background (solid lines). Separate components shown by the dashed lines. **b.** Parameters obtained from Gaussian fits.

differentiate between static and dynamic fields from fluctuating magnetic moments.

8.3.4 Analysis

The magnetic scattering of Zn_1-averievite was characterised using its Q and E dependence. Energy integrated $S_E(Q)$ scans of the $E_i = 3.55$ and 12.5 meV data were fitted with two Gaussian functions and a flat background up to $E = 3.1$ meV. For $E > 3.1$ meV, the kinematic window edge prevents an accurate characterisation of the peak at lower Q and $S_E(Q)$ was fitted with a single Gaussian and flat background. Some of these fits are shown in Figure 8.12a and the rest can be found in Appendix E. The results from all fits are shown in Figure 8.12b.

Using the energy transfer range $0.5 \leq E \leq 1.0$ meV, the peak at lower Q was determined to be centred at 0.393(2) Å^{-1}. For $E > 1.0$ meV, the lower Q limit of the kinematic window prevents an accurate determination of its peak centre, so this was fixed to 0.39 Å^{-1} to assess its FWHM and area. The peak at higher Q is on average centred at $Q = 1.05(9)$ Å^{-1}, though it appears to move to lower Q with increasing E. These peak positions cannot be indexed by the propagation vectors of the regular magnetic orders on a kagome lattice. However, they can be indexed by the characteristic wave vector $\mathbf{k} = (1/3,\ 0,\ 0)$ corresponding to a spiral state, where the pitch of the spiral is $2\pi/|\mathbf{k}|$. The $Q = 0.39$ Å^{-1} position corresponds to the $(1/3,\ 0,\ 0)$ expected reflection and the $Q = 1.05$ Å^{-1} position is near the $(-1/3,\ 1,\ 0)$ and $(-2/3,\ 0,\ 1)$ reflections at $Q = 1.02$ and 1.07 Å^{-1}, respectively.

For the single Gaussian fits, the peak centre stays relatively constant with an average at 0.76(3) Å^{-1}, halfway between the two peaks resolved at lower energy transfer. As expected from fitting a single Gaussian to two peaks, the average FWHM increases. In the energy ranges that the two peaks can be resolved, the FWHM and peak area decrease for the peak near 0.39 Å^{-1}, whereas the opposite is observed for the peak near $Q = 1.05$ Å^{-1}. The average FWHM for the peaks at lower and higher Q, are 0.6(2) Å^{-1} and 0.5(2) Å^{-1}, respectively. From the FWHM, similar correlation lengths are found with values of 10(3) Å and 13(5) Å. These length scales indicate short-range correlations of approximately two kagome hexagons.

It is now interesting to look at the changes in the magnetic scattering with

temperature. Figure 8.13a shows $\chi''_E(Q)$ obtained by integrating $\chi''(Q,E)$ over $4.0 < E < 4.5$ meV at all measured temperature. The intensity of $\chi''_E(Q)$ remains very similar between $T = 1.5$ and 15 K, as can be seen in the $S(Q,E)$ spectra (Figures 8.10 and 8.11). At $T = 50$ and 100 K, $\chi''_E(Q)$ loses intensity as the thermal fluctuations become stronger than the spin-spin correlations and the magnetic scattering becomes increasingly diffuse.

A similar observation is made using $\chi''_Q(E)$, obtained by integrating $\chi''(Q,E)$

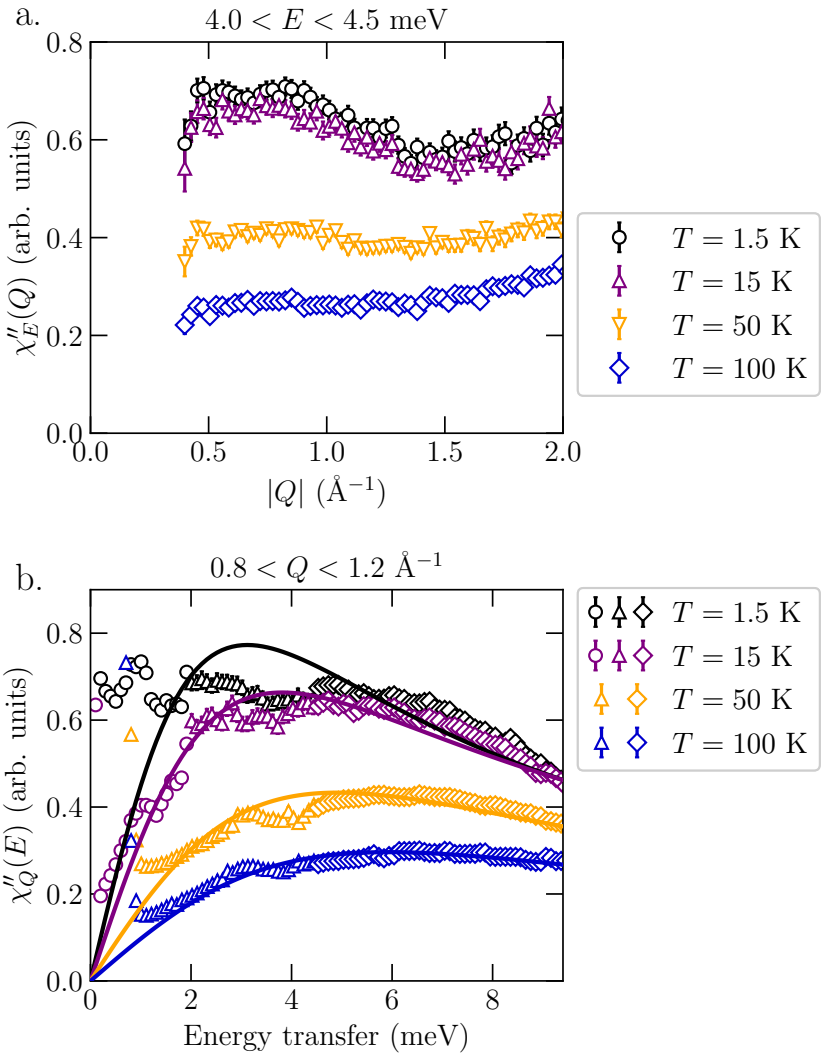

Figure 8.13: Zn_1-averievite IN5 and PANTHER data at $T = 1.5$ K (black), $T = 15$ K (purple), $T = 50$ K (orange) and $T = 100$ K (blue). **a.** $E_i = 20.45$ meV. $\chi''(Q,E)$ integrated over $4.0 < E < 4.5$ meV. **b.** Combined data collected with $E_i = 3.55$ (circles), 12.5 (triangles) and 19.2 meV (diamonds). $\chi''(Q,E)$ integrated over $0.7 < Q < 0.9$ Å^{-1}. The solid lines are quasi-elastic Lorentzian fits at each temperature.

over $0.8 < Q < 1.2$ Å^{-1} (Figure 8.13b). If the system does not have a transition to long-range order down to $T = 1.5$ K, quasi-elastic scattering would be expected to dominate. Therefore, an attempt was made to fit $\chi''_Q(E)$ with a quasi-elastic Lorentzian (QEL) function as shown in Figure 8.13b. The QEL describes excitations with a single relaxation time, such as those in an uncorrelated paramagnet. It is evident that at $T = 1.5$ K, a QEL function does not accurately describe $\chi''_Q(E)$ at low E indicating additional correlations at this temperature. However, at $T \geq 15$ K the QEL function is a good description of $\chi''_Q(E)$, meaning that below $T = 15$ K the excitation is more complex than a simple relaxational one. This agrees with the magnetic susceptibility (Chapter 7) that indicated a transition at $T = 3.5$ K, but the nature of the ground state remains an open question.

8.3.5 Zeroth- and first-moment analyses

The inelastic magnetic scattering observed in the INS measurements of Zn_1-averievite at $T = 1.5$ K, can be used to determine the spin-pair correlation function. This can then be used to indicate whether the exchanges are ferro- or antiferromagnetic. The exchange interactions up to the interlayer distance of ~ 8.42 Å are shown in Figure 8.14 with the corresponding distances in Table 8.3.

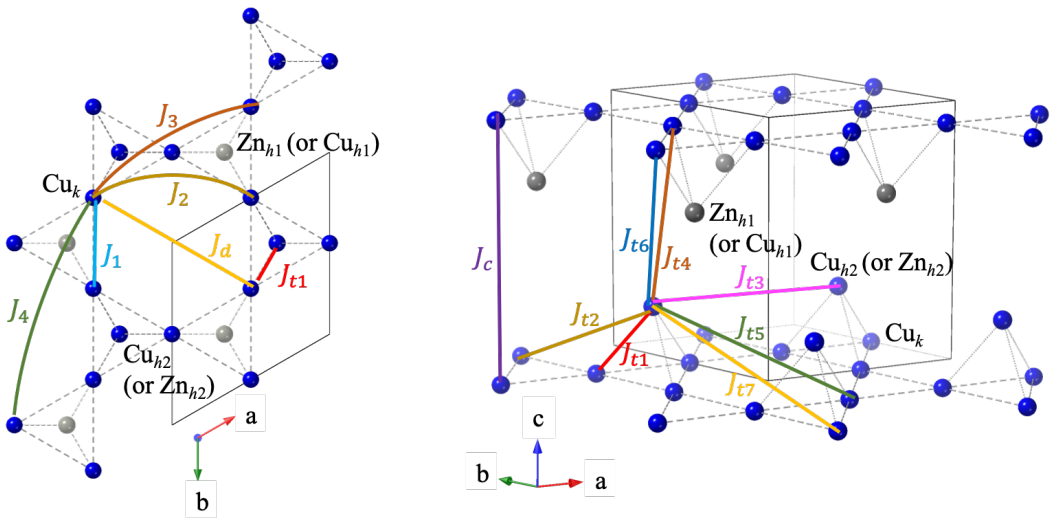

Figure 8.14: Zn_1-averievite Cu and Zn atoms in the $P3$ space group (no. 143) from the refinement of HRPD data collected at $T = 1.5$ K (Chapter 7). The exchange interactions correspond to the Cu-Cu distances in Table 8.3.

i	d_i (Å)	J_i
$t1$	2.90	J_{t1}
1	3.14	J_1
$t2$	5.30	J_{t2}
2	5.44	J_2
3, d, t3	6.28	$J_{3,d,t3}$
$t4$	6.42	J_{t4}
$t5$	6.92	J_{t5}
$t6$	7.80	J_{t6}
$t7$	8.22	J_{t7}
4	8.31	J_4
c	8.42	J_c

Table 8.3: Zn_1-averievite approximate Cu-Cu bond distances, d_i, for bonds i are given with the associated exchange interaction label, J_i, and correspond to Figure 8.14. These were determined from the refinement results using HRPD data at $T = 1.5$ K.

The spin-pair correlations were calculated by fitting the zeroth moment, $S_{\text{mag}}(Q)$, using reverse Monte Carlo (RMC) modelling in SPINVERT [4]. For an isotropic paramagnet, $S_{\text{mag}}(Q)$ is given as

$$S_{\text{mag}}(Q) = \int_{-\infty}^{\infty} S(Q,E)dE \tag{8.2}$$

$$= \frac{2}{3}|gf(Q)|^2 S(S+1)\left(1+\frac{1}{N}\sum_{i,j}\langle \mathbf{S}_i \cdot \mathbf{S}_j\rangle \frac{\sin(Qd_{ij})}{Qd_{ij}}\right), \tag{8.3}$$

where N is the number of spins in the magnetic unit cell, $f(Q)$ is the magnetic form factor and $\langle \mathbf{S}_i \cdot \mathbf{S}_j\rangle$ are the spin correlations between spins separated by a distance d_{ij}. The magnetic scattering was isolated from $S(Q,E)$ by subtracting the incoherent phonons, as detailed in Chapter 4. $S_{\text{mag}}(Q)$ was obtained by integrating the phonon-subtracted $S_{\text{mag}}(Q,E)$ between 0.5 and 10.0 meV. The magnetic form factor for Cu^{2+} is

$$f_{Cu^{2+}}(Q) = A\mathrm{e}^{-as^2} + B\mathrm{e}^{-bs^2} + C\mathrm{e}^{-cs^2} + D, \tag{8.4}$$

where $s = |Q|/4\pi$, $A = 0.0232$, $a = 34.9686$, $B = 0.4023$, $b = 11.5640$, $C = 0.5882$, $c = 3.8428$ and $D = -0.0137$ [5]. As SPINVERT only takes unit cells with orthogonal axes, the $P3$ unit cell was transformed to an orthogonal basis with

$a = 10.87707$ Å, $b = 6.27988$ Å, $c = 8.41825$ Å and eight Cu sites. The HRPD Rietveld refinements (Chapter 7) indicated a large anisotropic displacement parameter for the Cu sites, which was accounted for in SPINVERT as an isotropic one with a value of $U_{\text{iso}} = 0.0869$ Å^2. The RMC fit was run with 1000 moves per spin for ten independent cycles to ensure consistency in the results. Supercells made of $6\times6\times6$, $8\times8\times8$ and $10\times10\times10$ unit cells were trialled and it was found that the largest supercell was over fitting the data. As an example, three independent fits to the zeroth moment using an $8\times8\times8$ supercell are shown in Figure 8.15a. The program SPINCORREL was used to calculate the spin-pair correlations, $\langle \mathbf{S}_i \cdot \mathbf{S}_j \rangle$, for the three aforementioned supercells, which are shown in Figure 8.15b. The results converge with increasing box size and for the fits in Figure 8.15a, the spin correlations up to $d_i = 20$ Å are shown in Figure 8.15c. The strongest spin correlation is for the shortest bond distance ($d_{t1} \approx 2.90$ Å) and is positive, suggesting ferromagnetic coupling between the Cu_k and the capping Cu_1 spins. All other spin correlations are at least half in strength and for distances greater than $d_{t5} \approx 6.92$ Å, they become increasingly smaller and average to around zero.

An analysis of the first moment can be used to obtain the relative bond energy strengths. The first moment for powder averaged data [6] is calculated using

$$\langle E \rangle = \int_{-\infty}^{\infty} S_{\text{mag}}(Q,E) E dE = \frac{2}{3} |gf(Q)|^2 \frac{1}{N} \sum_i A_i \left(\frac{\sin Q d_i}{Q d_i} - 1 \right), \tag{8.5}$$

where $N = 4$ and the bond energies, A_i, corresponding to the notation in Table 8.3 are:

$$A_i = 6J_i \langle \mathbf{S}_0 \cdot \mathbf{S}_{d_i} \rangle, \text{ for } i = t1,\ t2,\ t4,\ t5,\ t6,\ t7, \tag{8.6}$$

$$A_i = 12J_i \langle \mathbf{S}_0 \cdot \mathbf{S}_{d_i} \rangle, \text{ for } i = 1,\ 2, \tag{8.7}$$

$$A_{3,d,t3} = 12J_3 \langle \mathbf{S}_0 \cdot \mathbf{S}_{d_3} \rangle + 6J_d \langle \mathbf{S}_0 \cdot \mathbf{S}_{d_3} \rangle + 6J_{t3} \langle \mathbf{S}_0 \cdot \mathbf{S}_{d_{t3}} \rangle, \tag{8.8}$$

$$A_c = 8J_c \langle \mathbf{S}_0 \cdot \mathbf{S}_{d_c} \rangle, \tag{8.9}$$

$$A_4 = 24J_4 \langle \mathbf{S}_0 \cdot \mathbf{S}_{d_4} \rangle. \tag{8.10}$$

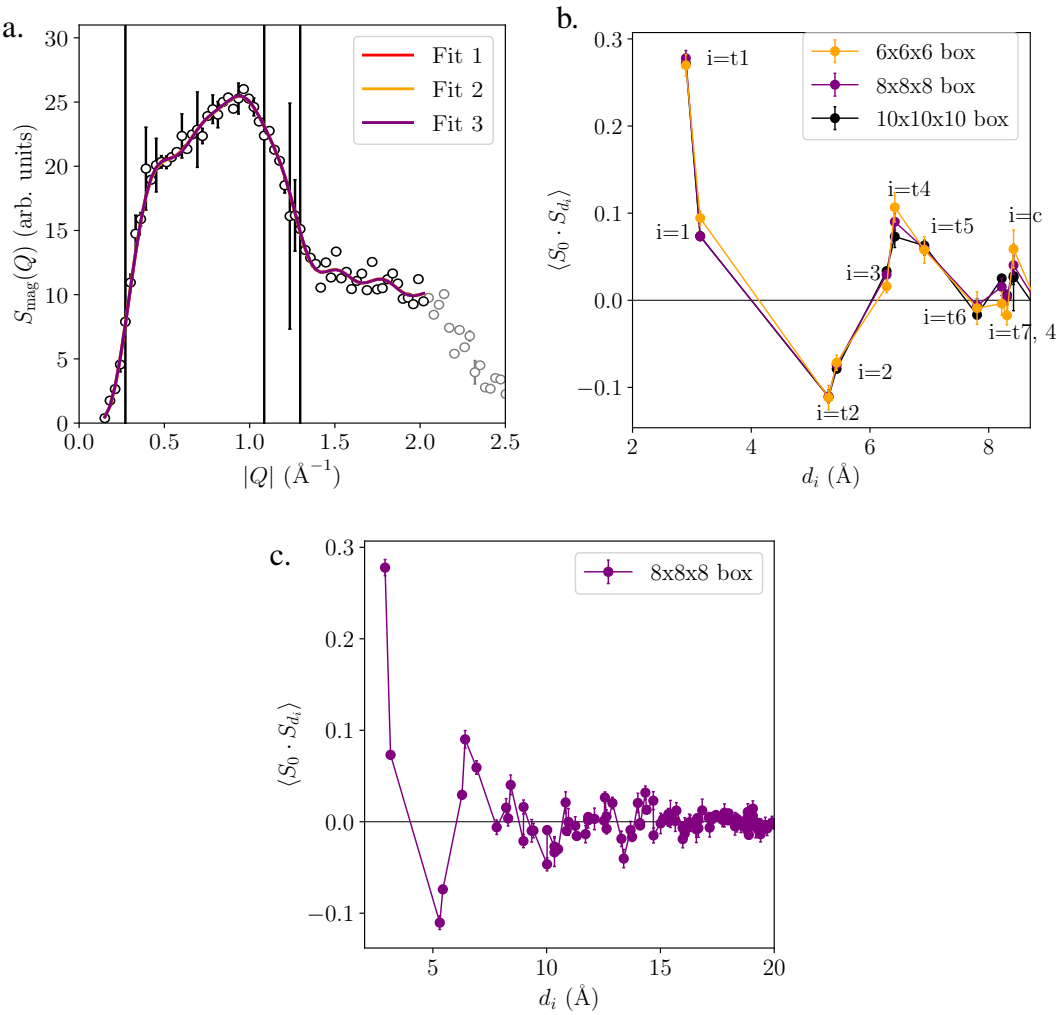

Figure 8.15: Zn_1-averievite, IN5 data. **a.** Zeroth moment calculated by integrating $S(Q,E)$ over $0.5 < E < 10$ meV and normalised as described in the text (grey). The range fitted in SPINVERT is shown in black ($Q < 2$ Å^{-1}), with three independent fits. **b.** Radial spin correlation function for the $6 \times 6 \times 6$, $8 \times 8 \times 8$ and $10 \times 10 \times 10$ supercells up to $d_c = 8.41825$ Å. **c.** Radial spin correlation function for the $8 \times 8 \times 8$ supercell.

In practice, the first moment was obtained by multiplying the the incoherent phonon-subtracted $S_{\mathrm{mag}}(Q,E)$ by E and integrating between 0.5 and 10.0 meV. A weighted least-squares fit was done up to $Q = 2.0$ Å^{-1} using equation 8.5 and considering the distances, d_i, given in Table 8.3. Some of the separate bond energy contributions are shown in Figure 8.16a. The peak positions of $\langle E \rangle$ are closest to the $i = 2$ and $i = t2$ curves, *i.e.* for Cu-Cu distances of 5.3-5.4 Å, but additional bond energy contributions are required to improve the fit at low Q. Combinations of different variables are shown in Figure 8.16b and the best fits were achieved using

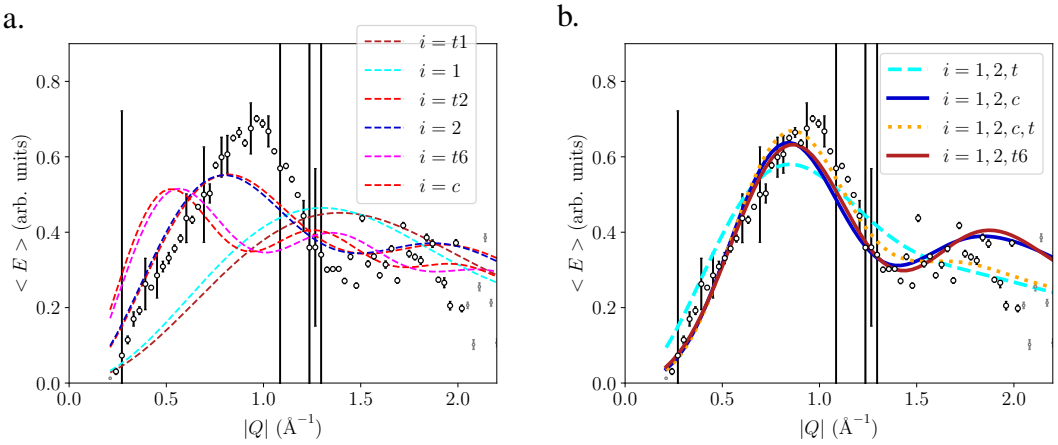

Figure 8.16: Zn_1-averievite, IN5 and PANTHER data. First moment calculated by integrating $S(Q,E)$ over $0.5 < E < 10$ meV and normalised as described in the text. **a.** Some of the separate bond energy contributions to the first moment contributions (equations 8.6-8.10). **b.** Various combinations of different i, as discussed in the text.

A_1, A_2 and a bond energy corresponding to distances of ~ 8 Å. This indicates that further neighbour interactions are important in the description of the first moment. However, the peak near $Q = 1$ Å^{-1} is not well described even with four parameters. Attempting refinements with more variables led to an unphysical curve for $Q > 2$ Å^{-1}, as well as high correlations between the refined parameters and large standard errors. Therefore, the determination of accurate bond energies is hindered by the limited Q range. In future studies, this could be improved by measuring the magnetic scattering using polarised neutrons, to experimentally isolate it from the coherent phonons that in our data are present above $Q = 2$ Å^{-1}.

The spin correlations suggest that the coupling between the capping Cu_{h1}/Cu_{h2} spins and the kagome Cu_k spins (see Figure 8.14) is ferromagnetic. It is notable that the Weiss temperature becomes slightly more negative on doping with Zn from the $x = 1$ to the $x = 2$ level possibly suggesting a ferromagnetic mean field for the capping Cu atoms. In addition, the crystal structure has average $\angle$$Cu_k$-O-$Cu_{h1}$/$Cu_{h2}$ superexchange angles of 95°, which is the crossover between ferro- and antiferromagnetic exchange for Cu-(μ_2-O)-Cu pathways according to the Goodenough-Kanamori rules [3]. These results suggest that J_{t1} is weak and ferromagnetic.

8.4 Inelastic neutron scattering on Zn_2-averievite

8.4.1 Overview

For Zn_2-averievite inelastic neutron scattering measurements were made on the cold neutron time-of-flight spectrometer IN5 and a summary of the data collection conditions is given in Table 8.4. For these measurements, a 2.63 g sample (part of the batch measured on HRPD and D2B) was loaded into an annular aluminium cylinder with a 15 mm outer diameter and 13 mm inner diameter. The sample environment was a standard orange cryostat as for the $x = 0$ and 1 samples.

T (K) \ E_i (meV)	3.55	5.11	20.45
1.5	IN5	IN5	IN5
15	IN5	-	IN5
60	IN5	-	IN5
120	IN5	IN5	IN5

Table 8.4: Summary of Zn_2-averievite INS measurements on IN5 with incident neutron energies E_i at temperatures T.

8.4.2 Diffuse excitations on IN5

The raw data were reduced as described in Chapter 4. The reduced $S(Q,E)$ plots collected with incident neutron energies $E_i = 20.45$ and 3.55 meV are shown in Figure 8.17. The $E_i = 20.45$ meV data shows the full bandwidth of the magnetic scattering. At $T = 1.5$ K (Figure 8.17a), the strongest intensities are from the elastic line (centred at $E = 0$) and the phonon scattering for $Q > 2.5$ Å^{-1}, which has a Q^2 dependence. $S(Q,E)$ shows diffuse magnetic scattering centred at $\sim$0.76 Å^{-1} that extends up to $\sim$ 10 meV. As temperature increases the magnetic scattering becomes more diffuse, but persists up to the highest measured temperature, $T = 120$ K. This indicates strong short-range correlations, in agreement with the magnetic susceptibility that showed downward curvature below $T = 200$ K indicative of antiferromagnetic correlations (Chapter 7). The magnetic excitation seen at $T = 1.5$ K can be isolated from the phonon scattering through a temperature subtraction in $\chi''(Q,E)$ with the $T = 120$ K data. $\chi''(Q,E)$ at $T = 120$ K was obtained from

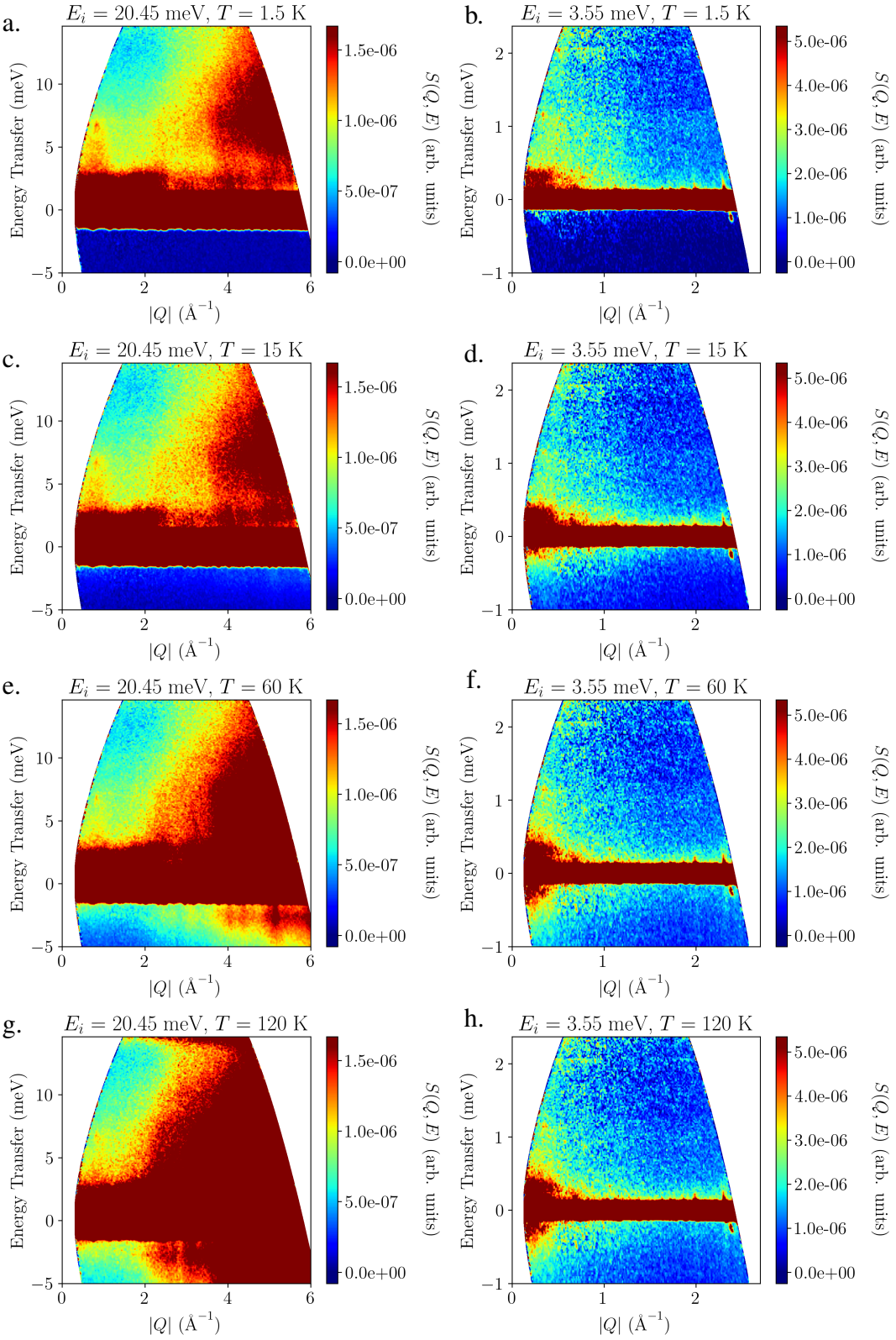

Figure 8.17: Zn_2-averievite measured on IN5. $S(Q,E)$ collected with $E_i = 20.45$ (**left.**) and $E_i = 3.55$ meV (**right.**) at $T = 1.5$, 15, 60 and 120 K (**top.-bottom.**).

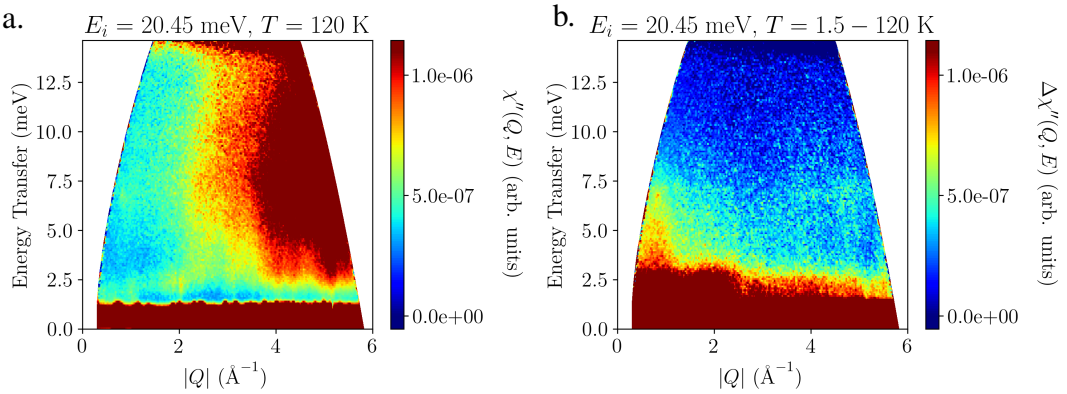

Figure 8.18: Zn_2-averievite, IN5 $E_i = 20.45$. **a.** $\chi''(Q,E)$ at $T = 120$ K. **b.** Temperature subtraction $\Delta\chi''(Q,E,T = 1.5 - 120$ K).

$S(Q,E)$ using the fluctuation-dissipation theorem and is shown in Figure 8.18a, with the subtraction from the $T = 1.5$ K data in Figure 8.18b. The intense scattering up to $E \approx 3$ meV is not from the sample, as confirmed by inspecting $S(Q,E)$ collected with lower incident energies.

$S(Q,E)$ measured with $E_i = 5.11$ meV is included in Appendix E as it has spurious scattering at low Q and $E \approx 1.9$ meV, which was confirmed to not be from the sample by inspecting the data collected with $E_i = 3.55$ meV (Figure 8.17). The data collected with $E_i = 3.55$ meV has spurious scattering above the elastic line in the range $0.1 < Q < 0.8$ Å^{-1} from the cryostat. There are two horizontal bands at $E = 1.1$ meV and $E = 2$ meV (difficult to see in $S(Q,E)$ but obvious in E and Q scans), which are due to unidentified spurious scattering and the monitor used on IN5, respectively. At $T = 1.5$ K, gapless diffuse magnetic scattering is observed up to $Q \approx 1.5$ Å^{-1}. As temperature increases, the magnetic scattering appears to become more intense near $Q = 0.2$ Å^{-1}, which is more obvious when looking at the negative energy transfer region due to the spurious scattering above the elastic line.

8.4.3 Analysis

The centre of the diffuse magnetic scattering can be used to determine the characteristic wave vector of the short-range correlations in Zn_2-averievite. The Q dependence of the magnetic scattering was determined using temperature subtracted data, $\Delta\chi''(Q,E)$ (Figure 8.18b), integrated over various energy ranges. $\Delta\chi''_E(Q)$ was fitted with a Gaussian function and a flat background as shown in Figure 8.19a. The

peak centre stays relatively constant with an average value of 0.76(4) Å^{-1}. The peak area also stays relatively constant between 3.6 meV and 6.2 meV, while the FWHM slightly increases. The average FWHM is 0.7(1) Å^{-1}, giving a correlation length of 9(1) Å that is $\sim$ 1.5 kagome hexagons. This indicates that this system is not limited to nearest neighbour dimers and further neighbour spin correlations are important.

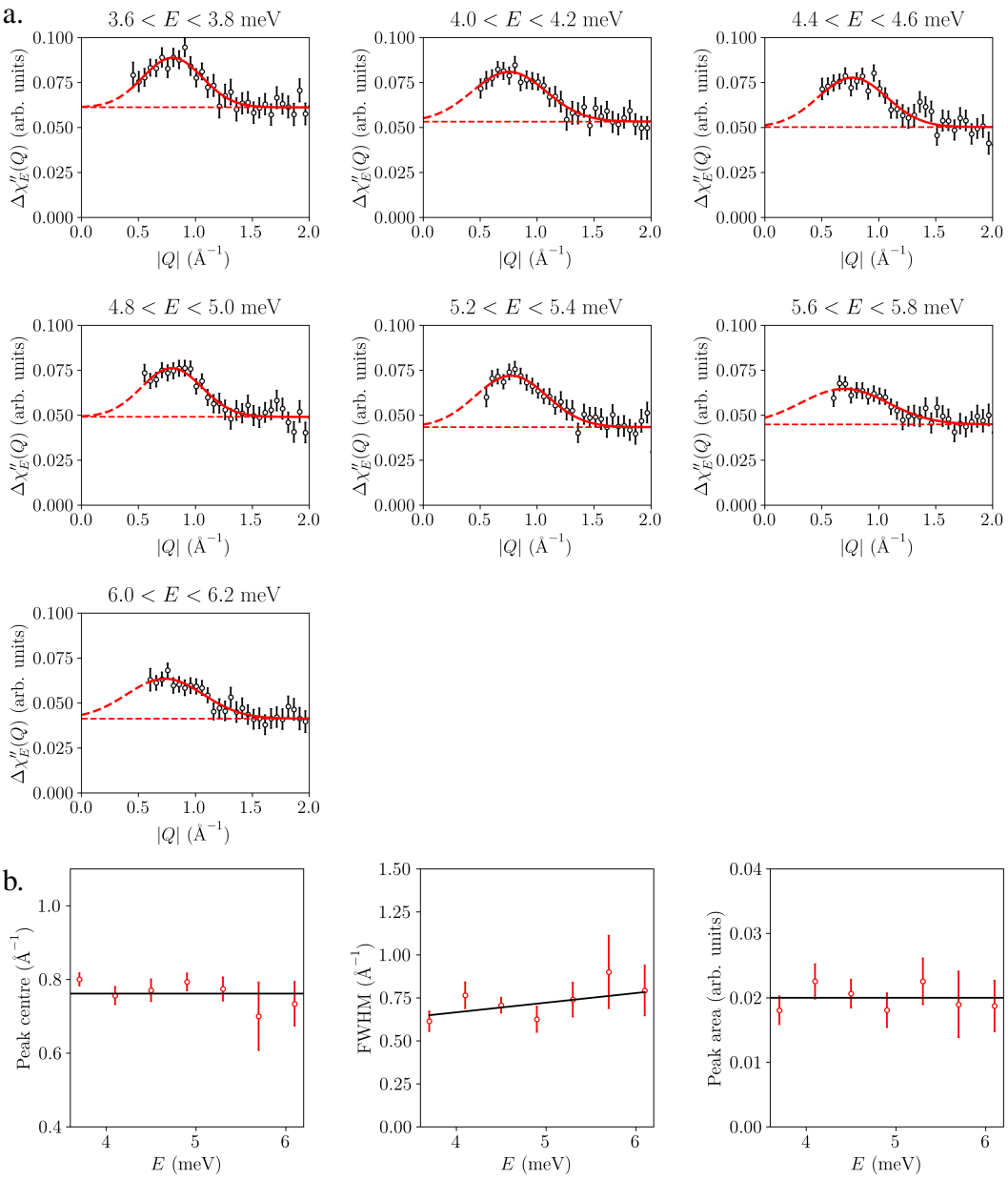

Figure 8.19: Zn_2-averievite IN5 data, $E_i = 20.45$ meV. **a.** $\Delta\chi''_E(Q)$ obtained by integrating $\Delta\chi''(Q,E) = \chi''(Q,E,T = 1.5 - 120$ K) over energy transfers ranges with width 0.2 meV. The red lines are Gaussian fits with a flat background term that is shown by the dashed lines. **b.** Results from the Gaussian fits.

Table 8.5 shows the Q positions expected for the propagation vectors of the regular magnetic orders on a kagome lattice: $\mathbf{k} = \mathbf{0}$, $\mathbf{k} = (\frac{1}{2},\ 0,\ 0)$ and $\mathbf{k} = (\frac{1}{3},\ \frac{1}{3},\ 0)$ [7]. The excitation centred at $Q = 0.76$ Å^{-1} is close to the expected (0, 0, 1) peak in $\mathbf{k} = \mathbf{0}$, which corresponds to the Γ point in the trigonal Brillouin zone.

$\mathbf{k} = \mathbf{0}$		$\mathbf{k} = (\frac{1}{2},0,0)$		$\mathbf{k} = (\frac{1}{3},\frac{1}{3},0)$	
$h\ k\ l$	$\lvert Q\rvert$ (Å^{-1})	$h\ k\ l$	$\lvert Q\rvert$ (Å^{-1})	$h\ k\ l$	$\lvert Q\rvert$ (Å^{-1})
0 0 1	0.74	$\frac{1}{2}$ 0 0	0.60	$\frac{1}{3}$ $\frac{1}{3}$ 0	0.67
0 1 0	1.16	$\frac{1}{2}$ 0 1	0.94	$\frac{1}{3}$ $\frac{1}{3}$ 1	1.00
1 0 1	1.38	$-\frac{1}{2}$ 1 0	1.01	$\frac{2}{3}$ $\frac{2}{3}$ 0	1.34
0 0 2	1.49	$-\frac{1}{2}$ 1 1	1.25	$\frac{2}{3}$ $\frac{2}{3}$ 1	1.53

Table 8.5: Characteristic wave vectors for the propagation vectors $\mathbf{k} = \mathbf{0}$, $\mathbf{k} = (\frac{1}{2},0,0)$ and $\mathbf{k} = (\frac{1}{3},\frac{1}{3},0)$, with lattice parameters $a = b = 6.279882$ Å, $c = 8.418249$ Å, $\alpha = \beta = 90°$ and $\gamma = 120°$.

The temperature dependence of the magnetic excitations was investigated using $\chi''_E(Q)$ obtained by integrating $\chi''(Q,E)$ over $3.8 < E < 4.2$ meV (Figure 8.20a). The red line shows the Q-dependence of incoherent phonons given by

$$I_{\text{ph}}(Q) = a + bQ^2 \exp\left(\frac{-Q^2\langle u^2\rangle}{3}\right), \tag{8.11}$$

where a is a flat background term accounting for multiple scattering, b is a scaling factor for the phonon Q^2 contribution and the exponential term is the Debye-Waller factor [8]. The peak at 0.76 Å^{-1} loses intensity as temperature increases, but can still be seen up to $T = 120$ K indicating that the magnetic correlations persist up to at least this temperature. At $T = 1.5$ K, there appears to be a second peak near $Q = 2.2$ Å^{-1} that loses little intensity at $T = 15$ K and its origin is likely coherent phonon scattering. The peaks at $Q > 2.7$ Å^{-1} are also due to coherent phonons. At $T = 60$ and 120 K, $\chi''_E(Q)$ loses intensity in the whole observed Q range, which could either be due to an issue with the Bose factor correction or a very weak and broad additional magnetic contribution.

The diffuse magnetic scattering can also be characterised by its energy de-

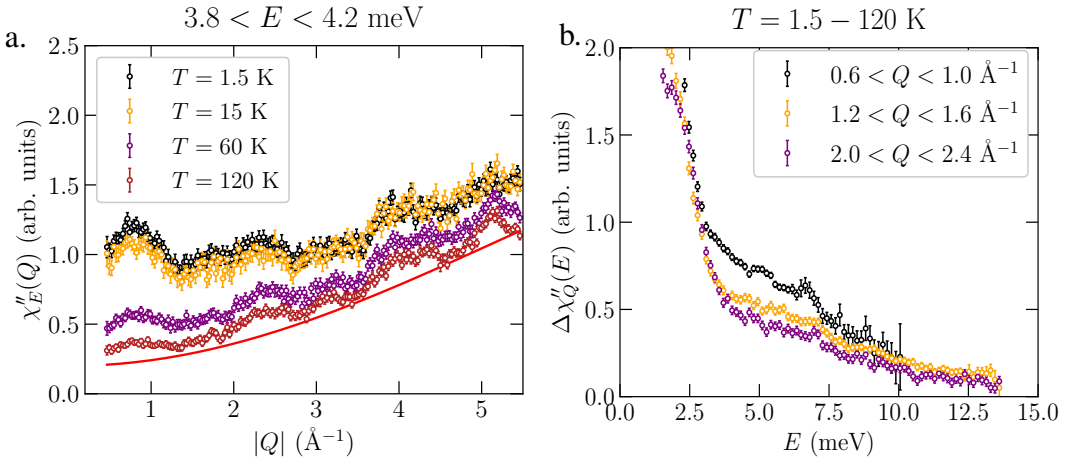

Figure 8.20: Zn_2-averievite measured on IN5 with $E_i = 20.45$ meV. **a.** $\chi''(Q,E)$ integrated over $3.8 < E < 4.2$ meV at $T = 1.5$, 15, 60 and 120 K. The red line is the Q-dependence of incoherent phonons (equation 8.11). **b.** $\Delta\chi''(Q,E)$ integrated over various Q ranges for the temperature difference $T = 1.5 - 120$ K.

pendence. To this end, $\Delta\chi''(Q,E)$ was integrated over various Q ranges (Figure 8.20b): over the magnetic scattering centred at 0.76 Å^{-1} at $0.6 < Q < 1.0$ Å^{-1}; at $1.2 < Q < 1.6$ Å^{-1}, between the scattering near 0.76 Å^{-1} and the possible peak at 2.2 Å^{-1}; and at $2.0 < Q < 2.4$ Å^{-1}. The intensity is highest at low Q, clearly signifying the magnetic scattering near $Q = 0.76$ Å^{-1}, and decreases as Q increases. $\Delta\chi''_Q(E)$ loses most intensity up to $E \approx 10$ meV and at higher E values remains more similar, leading to the conclusion that there is no clear magnetic contribution above ~ 10 meV.

Interestingly, $S(Q,E)$ collected with $E_i = 3.55$ meV (Figure 8.17) indicates intense magnetic scattering near $Q = 0.2$ Å^{-1}, seen at negative energy transfers for temperatures of $T \geq 15$ K. This can be seen in the energy dependence of $S(Q,E)$ in Figure 8.22a. The Q dependence of the magnetic scattering is shown in Figure 8.21, by integrating $\chi''(Q,E)$ over $-0.5 < E < -0.2$ meV. The magnetic scattering decays faster in Q than the Cu^{2+} magnetic form factor, indicating it arises from correlated spins. With increasing temperature, this scattering becomes more intense as the excited magnetic states become more populated. It seems to decrease from $Q = 0$, which agrees with a $\mathbf{k} = \mathbf{0}$ propagation vector. However, strong scattering at $Q = 0$ would suggest a ferromagnetic dynamic component. This could be intrinsic to the

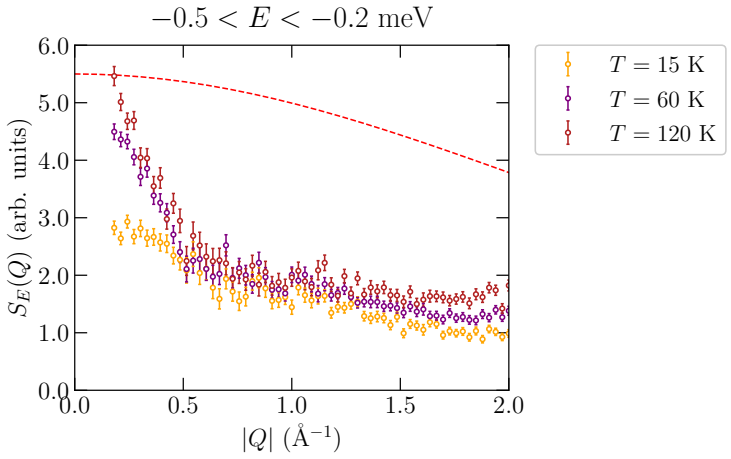

Figure 8.21: Zn_2-averievite measured on IN5 with $E_i = 3.55$ meV. $S(Q,E)$ integrated over $-0.5 < E < -0.2$ meV at $T = 15$, 60 and 120 K. The red line is the Cu^{2+} magnetic form factor squared.

kagome layers or may originate from correlated impurity spins. In comparison, the $x = 1$ Zn-doped sample has a nominal 50% of honeycomb sites occupied by Cu and strong correlations between the honeycomb and kagome sites. Its magnetic scattering differs from that of the $x = 2$ doped sample, with peaks near $Q = 0.39$ and 1.05 Å^{-1}. Since their magnetic excitations differ, an accurate determination of the magnetic impurity fraction is needed in Zn_2-averievite to determine the origin of the low-energy magnetic response. Anomalous x-ray scattering, which is site and element specific, would be useful for this.

8.4.4 Quantum criticality

It is now interesting to analyse the temperature dependence of the magnetic scattering. $S(Q,E)$ was integrated over the centre of the diffuse scattering in the range $0.6 < Q < 0.8$ Å^{-1} (Figure 8.22a). For positive energy transfers, $S_Q(E)$ shows no obvious gap and varies weakly with temperature. For the same Q integration range, $\chi''_Q(E)$ is plotted in Figure 8.22b with quasi-elastic Lorentzian (QEL) fits. At $T = 1.5$ K, there is no peak in $\chi''_Q(E)$ implying that the characteristic energy scale of the magnetic scattering is smaller than the lowest resolved energy $E = 0.3$ meV, or non-existent. A QEL describes purely relaxational excitations such as those expected in systems with uncorrelated magnetic moments. Therefore, at low temper-

ature the absence of a characteristic energy scale suggests the presence of quantum fluctuations. As temperature increases, the spin-spin correlations become weaker (also seen in the magnetic susceptibility, Chapter 7) and the QEL provides a better description of the data.

Near a quantum critical point (QCP), $\chi''_Q(E)$ is expected to show scaling behaviour of type $\chi''_Q(E)k_BT^\alpha = \mathcal{F}(\omega/T)$, where $\mathcal{F}$ is a universal scaling function and the exponent α depends on the universality class of the system [9]. Indeed Zn_2-

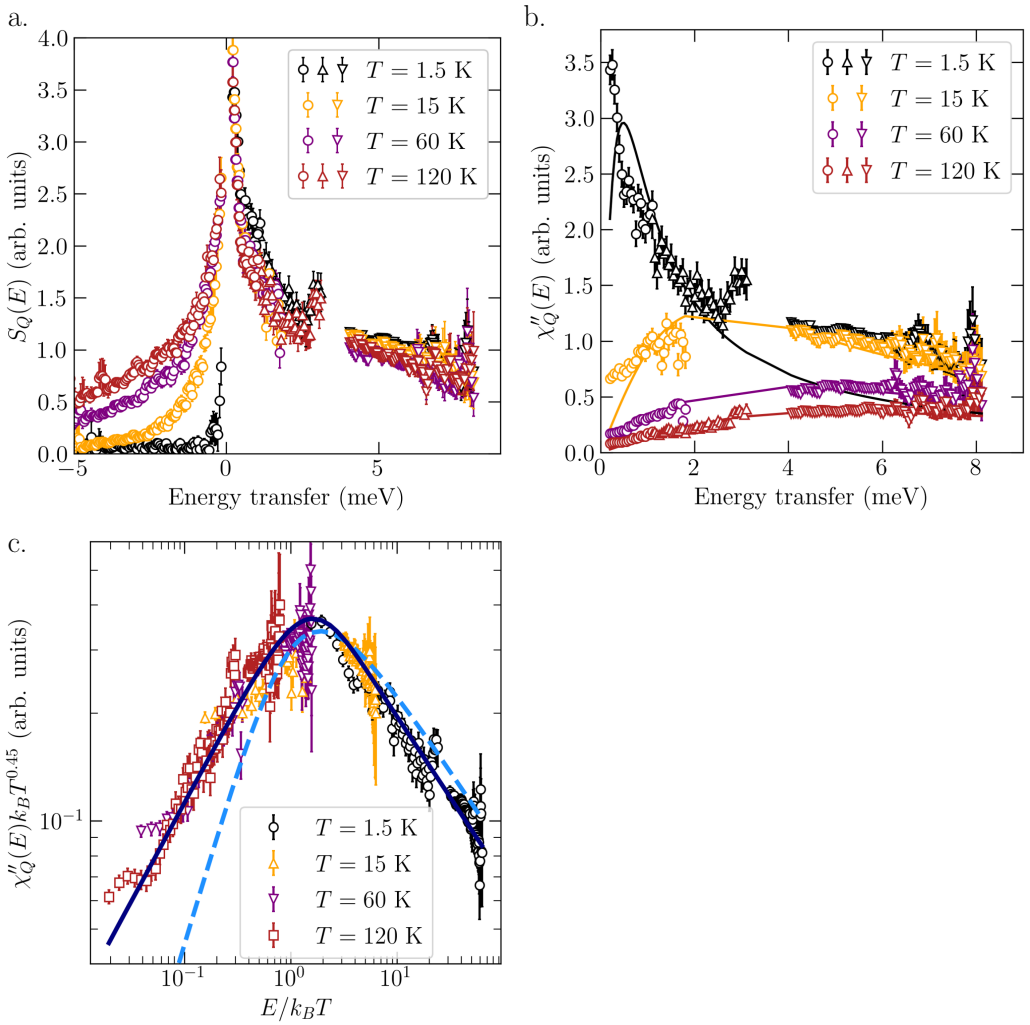

Figure 8.22: Zn_2-averievite, IN5 joint data with $E_i = 3.55, 5.11$ and 20.45 meV integrated over $0.6 < Q < 0.8$ Å^{-1} at $T = 1.5$, 15, 60 and 100 K. **a.** $S_Q(E)$ does not vary much with temperature for positive energy transfers. **b.** $\chi''_Q(E)$ with quasi-elastic Lorentzian fits. **c.** $\chi''_Q(E)k_BT^\alpha$ with $\alpha = 0.45$ plotted against E/k_BT on a log-log scale. The dashed line corresponds to equation 8.12 and the solid line to equation 8.13 ($b = 0.727(7)$). The missing data in the range $2 < E < 4$ meV is due to the kinematic window limits.

averievite shows such scaling behaviour and is plotted as $\chi''_Q(E)k_BT^\alpha$ with $\alpha = 0.45$ against E/k_BT in Figure 8.22c. Such scaling behaviour has previously been seen in herbertsmithite [10] and when measured in quantum antiferromagnets [9] and heavy-fermion systems has been associated with the proximity to a QCP [11]. With reference to the phase diagram shown in Figure 2.8 (Section 2.4.4), these materials lie in the hatched region at a finite temperature and when cooled to $T = 0$ would lie at or very close to g_C. In the case of the averievite series, $Zn_xCu_{5-x}(VO_4)_2O_2CsCl$, the parameter g may correspond to the level of Zn-doping, x, and an increase from $x = 0$ to $x = 2$ increases the proximity of the material to g_C at $T = 0$. The data is reasonably plotted on a single curve and this collapse is acceptable down to exponent values of $\alpha = 0.4$, comparable to the 0.4 value found for SCGO [12] but not the 0.66 value found for herbertsmithite [10]. Similar to the analysis done for herbertsmithite [10], two functional forms are attempted to describe this data. The first was used to describe the heavy-fermion metal $CeCu_{5.9}Au_{0.1}$ [13] and is given as

$$\mathcal{F}(\omega/T) = c\,\sin[\alpha\tan^{-1}(\omega/T)]/[(\omega/T)^2+1]^{\alpha/2}, \tag{8.12}$$

where c is a scale factor. The fit using equation 8.12 is shown as the dashed line in Figure 8.22c. As for herbertsmithite [10], this does not describe the low E/k_BT data well. The second functional form used is

$$\mathcal{F}(\omega/T) = c(T/\omega)^\alpha\tanh(\omega/bT), \tag{8.13}$$

where b is a factor arising from experimental findings in $La_{1.96}Sr_{0.04}CuO_4$ [14] and c is a scale factor. With $b = 0.727(7)$, a good fit to the data is achieved (solid line in Figure 8.22c) and it is noted that this value is different to the 1.66 found for herbertsmithite [10].

8.4.5 Determining the signs of the exchange interactions

A combined zeroth- and first-moment analysis was used to determine the signs of the exchange interactions in Zn_2-averievite. The relevant ones are shown in Figure

8.23 up to the interlayer distance of ~ 8.49 Å and listed with the corresponding Cu-Cu distances in Table 8.6. They correspond to those commonly considered in a regular kagome, apart from the second n.n. bond that is split into two contributions due to the distorted kagome hexagons.

The zeroth moment, equation 8.2, was obtained by integrating the incoherent phonon-subtracted $S_{\mathrm{mag}}(Q,E)$ spectra between 0.5 and 10.0 meV. Reverse Monte Carlo (RMC) modelling in SPINVERT [4] was used to fit $S_{\mathrm{mag}}(Q)$. The large anisotropic displacement parameter determined in Chapter 7 for the Cu site was considered as an isotropic displacement of $U_{\mathrm{iso}} = 0.0853$ Å^2. SPINVERT requires the input unit cell to have orthogonal axes, so the $P3$ structure was converted to an orthogonal basis with $a = 6.24871$ Å, $b = 10.82308$ Å, $c = 8.48727$ Å and 6 Cu^{2+} atoms. The RMC fit was run with 1000 moves per spin for 10 independent cy-

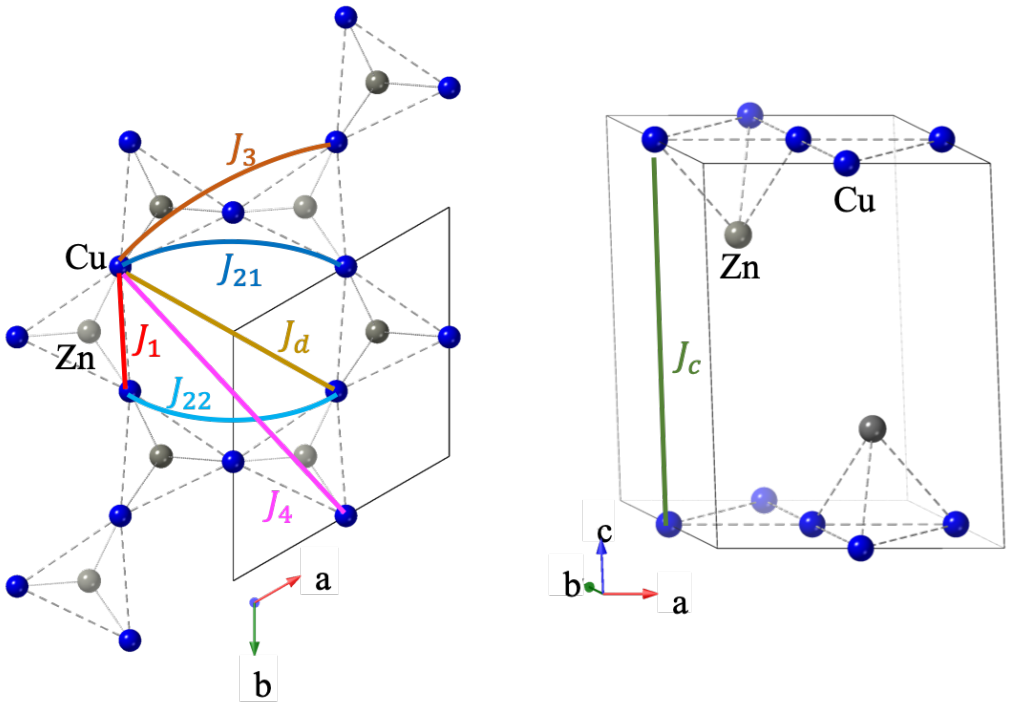

Figure 8.23: Zn_2-averievite. Cu (blue) and Zn (grey) atoms from the HRPD refinements in space group $P3$ at $T = 1.5$ K (Chapter 7). The exchange interactions labelled are those considered for the zeroth- and first-moment analyses. The second n.n. interaction is split into J_{21} and J_{22} due to the distortion in the kagome hexagons.

cles to assess the consistency of the results. Box sizes of $6 \times 6 \times 6$, $8 \times 8 \times 8$ and $10 \times 10 \times 10$ unit cells were trialled and it was found that for box sizes larger than the $8 \times 8 \times 8$ supercell (containing 3072 spins) the refinement began to over-fit the data at low Q. Figure 8.24a shows three of the ten independent fits for the $8 \times 8 \times 8$ supercell, indicating consistent results for each independent run. SPINCORREL was used to calculate the spin correlations, $\langle \mathbf{S}_0 \cdot \mathbf{S}_{d_i} \rangle$, which are shown in Figure 8.24b up to $d_c \approx 8.49$ Å and converge for a supercell larger than $8 \times 8 \times 8$. The spin correlations for the $8 \times 8 \times 8$ supercell, averaged over ten RMC cycles, are shown in Figure 8.24c. For distances larger than the interplanar one, $d_c \approx 8.49$ Å, the correlations become increasingly weaker and average to around zero. The most significant spin correlations are for the second n.n. bonds, $i = 21$ and $i = 22$, and are negative suggesting predominantly antiparallel spin alignment. For the first n.n. distance the spin correlations are positive and given the superexchange angles are 116.8° indicative of antiferromagnetic exchange, this suggests frustrated spins. For $i = c$ the spin correlations are extremely weak, in support of a two-dimensional system in Zn_2-averievite.

The first moment, $\langle E \rangle$, was obtained by multiplying the incoherent phonon-subtracted $S_{\mathrm{mag}}(Q,E)$ by E and integrating between 0.5 and 10.0 meV. $\langle E \rangle$ was fitted using least squares minimisation with equation 8.5, as for Zn_1-averievite, where

i	d_i (Å)	J_i
1	3.15	J_1
21	5.03	J_{21}
22	5.79	J_{22}
3	6.25	J_3
d	6.25	J_d
4	8.02	J_4
c	8.49	J_c

Table 8.6: Zn_2-averievite Cu-Cu bond distances, d_i, for bond i are given with the associated exchange interaction label, J_i, and correspond to Figure 8.23. These were determined from the crystal structure refinements using HRPD data at $T = 1.5$ K.

$N = 3$ and the bond energies, A_i, are given as:

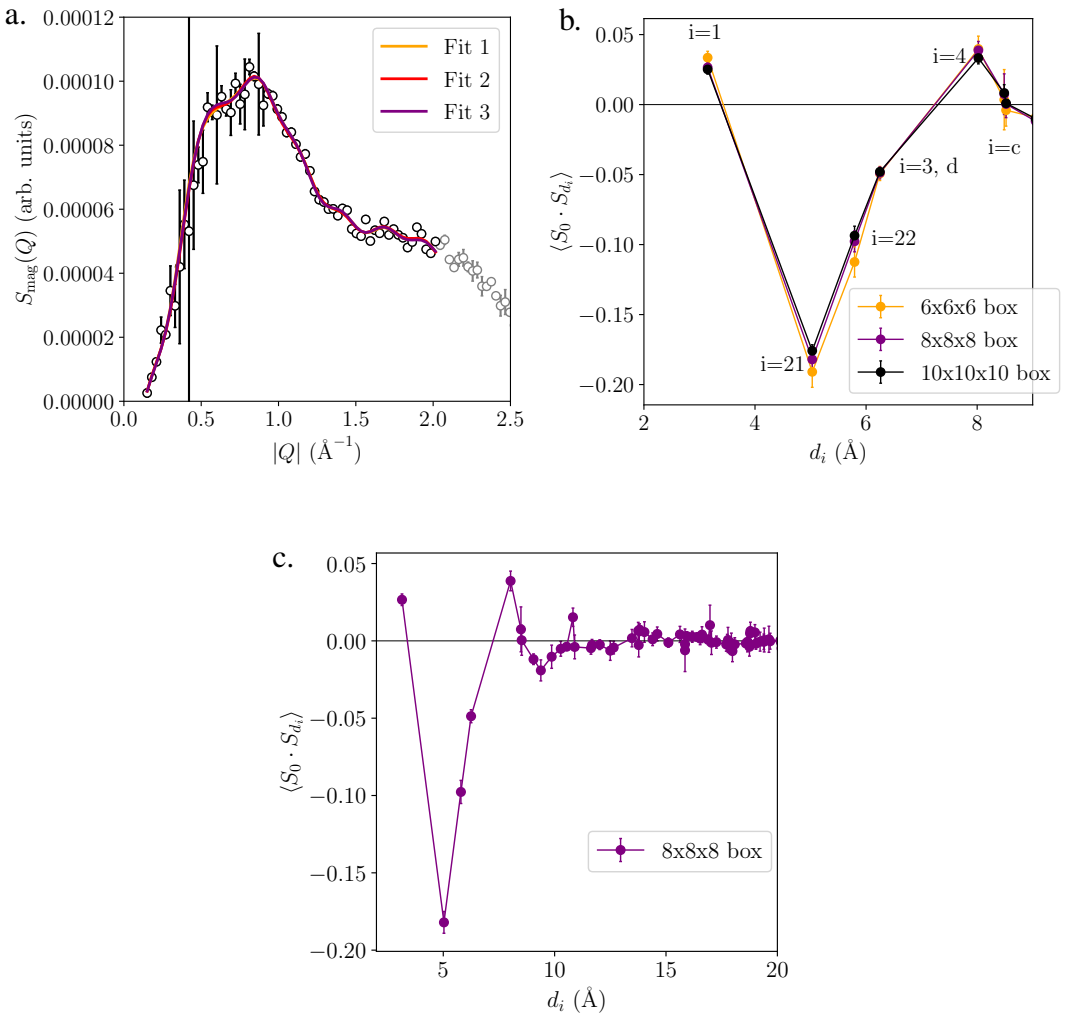

Figure 8.24: Zn_2-averievite, IN5 data. **a.** Zeroth moment calculated by integrating $S(Q,E)$ over $0.5 < E < 10$ meV and normalised as described in the text (grey). The range fitted in SPINVERT is shown in black ($Q < 2$ Å^{-1}), with three independent fits. **b.** Radial spin correlation function up to $d_i = 8.48727$ Å for different box sizes. **c.** Radial spin correlation function for the $8 \times 8 \times 8$ box size.

$$A_1 = 12J_1\langle \mathbf{S}_0 \cdot \mathbf{S}_{d_1} \rangle, \tag{8.14}$$

$$A_{21} = 6J_{21}\langle \mathbf{S}_0 \cdot \mathbf{S}_{d_{21}} \rangle, \tag{8.15}$$

$$A_{22} = 6J_{22}\langle \mathbf{S}_0 \cdot \mathbf{S}_{d_{22}} \rangle, \tag{8.16}$$

$$A_{3,d} = 12J_3\langle \mathbf{S}_0 \cdot \mathbf{S}_{d_3} \rangle + 6J_d\langle \mathbf{S}_0 \cdot \mathbf{S}_{d_3} \rangle, \tag{8.17}$$

$$A_4 = 12J_4\langle \mathbf{S}_0 \cdot \mathbf{S}_{d_4} \rangle, \tag{8.18}$$

$$A_c = 6J_c\langle \mathbf{S}_0 \cdot \mathbf{S}_{d_c} \rangle. \tag{8.19}$$

Figure 8.25a shows the individual bond contributions, i, to the first moment. The first peak at 0.8 Å^{-1} is near the peak maximum of the curve yielded by $i = 21$, rather than $i = 1$ which corresponds to the n.n. distance. However, the amplitude of the $Q = 0.8$ Å^{-1} peak is not well described by the $i = 21$ curve, indicating the importance of other bond energies at low Q. Despite the $i = 22$ curve being slightly shifted to lower-Q compared to $i = 21$, attempts to refine them separately resulted in them being highly correlated and the competition between the two terms led to bond energies of opposite sign. To assess this outcome we consider the crystal structure. In $P3$, Zn_2-averievite has two distinct second n.n. pathways with distances of 5.17 Å and 5.65 Å and equal superexchange angles, suggesting that their superexchange pathways and exchange energies should be similar. Therefore, two second n.n. bond energies with opposite sign are not in agreement with the crystal structure and they were set to be equal for this analysis with the notation $i = 2$.

Weighted least squares minimization was used to fit $\langle E \rangle$ by combining bond energy terms as shown in Figure 8.25b. Figure 8.25b shows that at least five terms were required to describe the observed peak amplitude. However, the resulting parameters were highly correlated and the limited Q range restricts the fit reliability. The results of the best fit are shown by the orange line in Figure 8.25c and indicate that the bond energy for $i = 1$ is negligible. Nevertheless, the signs of the bond energies can be compared to those of the spin correlations to determine the signs of the exchange interactions, which are given in Table 8.7. The first and second n.n.

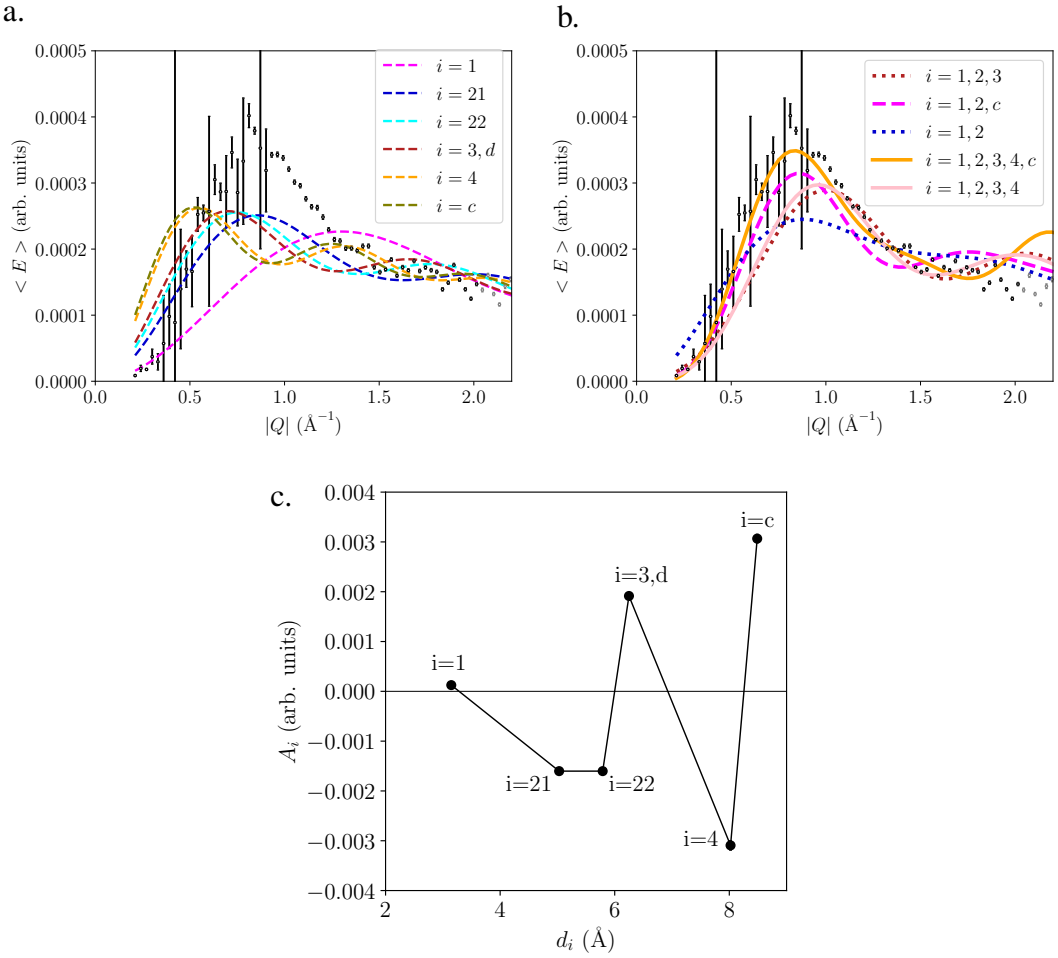

Figure 8.25: Zn_2-averievite, IN5 data. First moment calculated by integrating $ES(Q,E)$ over $0.5 < E < 10$ meV (grey) and the range used for fitting is shown in black. **a.** Each bond energy, A_i, contribution plotted separately (equations 8.14-8.19). **b.** Various combinations of A_i variables, discussed in the text. **c.** Bond energies for the best fit in (**b.**) shown by the orange line.

exchanges, as well as between kagome planes, are antiferromagnetic. Although the bond energy for $i = 1$ was very small and positive, the $\angle$Cu$_k$-O-Cu$_k$ superexchange angles of 116.8° are indicative of antiferromagnetic nearest-neighbour exchange interactions.

The magnetic diffuse scattering was found to be centred at 0.76 Å^{-1}, suggesting short-range correlations of $\mathbf{k} = \mathbf{0}$ type (see Section 8.4.3). Therefore, if this system ordered it is likely that the structure would resemble a type of $\mathbf{k} = \mathbf{0}$ antiferromagnetic order, such as the 120° structure. It is interesting to assess whether the exchange interactions arising from the model-free moment analyses, lead to the same conclusion. As mentioned in Chapter 6, the classical phase diagram for the

i	d_i (Å)	J_i	Sign of J_i
1	3.15	J_1	+
21	5.03	J_{21}	+
22	5.79	J_{22}	+
3, d	6.25	$2J_3$+J_d	−
4	8.02	J_4	−
c	8.49	J_c	+

Table 8.7: Zn_2-averievite Cu-Cu bond distances, d_i, for bond i are given with the associated exchange interaction label, J_i and its sign calculated from the zeroth and first moment analyses. $J_i > 0$ indicates an antiferromagnetic exchange interaction.

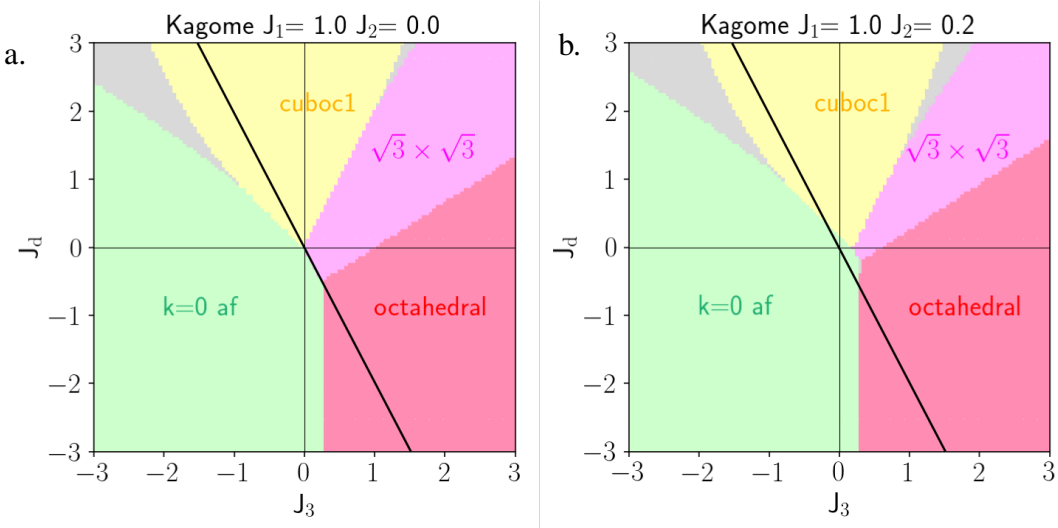

Figure 8.26: Classical phase diagrams for $J_3 - J_d$ on a regular kagome lattice with $J_1 = 1$ and **a.** $J_2 = 0$ or **b.** $J_2 = 0.2$. The grey regions are spiral states. The black lines show the relation $2J_3 + J_d = 0$.

kagome lattice has been previously calculated and indicates most of phase space to be occupied by the regular magnetic orders [7]. Based on the signs of the exchange interactions determined in Table 8.7, the $J_3 - J_d$ phase diagrams for $J_1 > 0$ and $J_2 \geq 0$ are shown in Figures 8.26a and b. Assuming weak coupling between kagome planes and a weak J_4 interaction, a $\mathbf{k} = \mathbf{0}$ type order would be realised for a ferromagnetic J_3 and/or J_d that can satisfy the relation $2J_3 + J_d < 0$.

8.5 Discussion

This chapter has presented inelastic neutron scattering results and analyses for three members of the averievite series separately. Each material has been shown to have a different ground state and although they are interesting in their own regard, it is useful to compare the samples to each other. Furthermore, as quantum spin liquids remain elusive ground states in experimental materials, Section 8.5.2 will summarise the aspects of the data analysis that make Zn_2-averievite a good candidate quantum spin liquid.

8.5.1 Evolution of magnetic behaviour with Zn doping

The spin waves observed for undoped averievite have branches at $Q = 0.37$, 1.16 and 1.97 Å^{-1}, with an $\sim$11 meV bandwidth. The spin wave spectra for averievite are quite different from those observed for claringbullite, which had two magnetic responses separated by a finite energy gap (Chapter 6). For averievite, the spin waves arising from both the kagome and honeycomb Cu_h spins seem to be comprised of many modes close in energy, particularly in the band ranging from ~ 7 meV to ~ 11 meV. The possibility that there are two subsystems where only one orders was considered, but the magnetic structure refinements in Chapter 7 indicated that all moments are ordered. Accordingly, $S(Q,E)$ shows no evidence of diffuse scattering arising from disordered moments. Modelling the spin waves from powder data is quite a complicated task due to the powder averaging, the uncertainty in the magnetic structure and the likelihood of many competing exchange interactions. Nevertheless, it was possible to adequately describe the main features of the spectra by considering only two isotropic exchange interactions between collinear Cu_h spins. The calculations captured the spin wave branches at $Q = 0.37,\ 1.16$ and 1.97 Å^{-1} and the ~ 11 meV bandwidth. The small distortion in the kagome lattice triangles of $\sim 2\%$ and the $\angle$Cu$_k$-O$_k$-Cu$_k$ superexchange angles of 115°–119°, make it structurally similar to Zn_2-averievite that has undistorted kagome triangles and $\angle \mathrm{Cu}_k\mathrm{-O}_k\mathrm{-Cu}_k$ angles of 117°. This suggests that the exchange interactions between kagome spins are similar in averievite and its Zn-doped variants. Therefore, determining the exchanges in the kagome lattice of averievite, using single crystal

inelastic measurements for example, may enable Zn_2-averievite to be placed in a quantum spin liquid phase diagram.

On doping with Zn to the $x = 1$ level, the magnetic excitations become more diffuse and are centred at Q =0.39 and 1.04 Å^{-1}, which could not be indexed by the propagation vectors of the regular magnetic orders on the kagome lattice. Despite the magnetic susceptibility indicating a phase transition at $T = 3.5$ K (Chapter 7), magnetic Bragg peaks were not observed in the elastic scattering of the IN5 data. However, it is possible that the ordered moments are too small to be differentiated from the background of the data and a higher flux would be required to observe them. Alternatively, the phase transition and absence of magnetic Bragg peaks could indicate a spin glass-like system. The magnetic excitations of Zn_1-averievite are reminiscent of dispersive spin waves and notably differ from those of the Zn_2-averievite quantum spin liquid, suggesting a different ground state to Zn_2-averievite. Furthermore, the FWHM for both magnetic excitation columns observed for Zn_1-averievite were approximately 0.5 Å^{-1} indicating correlation lengths of $\sim$ 13 Å, which are longer than those found in Zn_2-averievite of $\sim$ 9 Å but not "long-ranged" as in averievite.

The zeroth moment analyses for the $x = 1$ and $x = 2$ Zn-doped samples are consistent, as they reveal that the average spin correlations between neighbouring kagome spins are positive implying a predominantly parallel spin alignment. The radial spin correlation function is proportional to cosγ, where γ is the angle between the spins, so averaging over a range of cosγ values could result in a positive spin correlation without necessarily implying ferromagnetic exchange couplings. The spin correlation function of Zn_2-averievite cannot be matched to any of those corresponding to the regular magnetic orders (RMOs) on the kagome lattice [7], but this may be due to the distortion in the kagome hexagons leading to different spin correlations. Although it was not possible to determine the magnitude of the nearest-neighbour exchange energy in the kagome planes J_1, the first moment analysis of Zn_2-averievite indicated it to be antiferromagnetic in agreement with the $\angle$Cu$_k$-O$_k$-Cu$_k$ angle. The Q position of the magnetic scattering corresponds to $\mathbf{k} = \mathbf{0}$ type

short-range correlations. This was also supported by the model-free moment analyses, which showed that if Zn_2-averievite ordered the signs of the exchange interactions would lead to $\mathbf{k} = \mathbf{0}$ type order. The determination of the exchange coupling magnitudes, was hindered by the limitation in Q range of the magnetic scattering due to coherent phonon scattering. To circumvent this issue, polarised neutrons can be used to isolate the magnetic scattering from the phonons. Additionally, single crystal experiments, with or without polarised neutrons, would provide the spatial component of the excitations to determine the important Cu-Cu bond distances in different crystallographic directions.

It is interesting to note that in the kagome planes of undoped averievite and Zn_2-averievite, the spin correlations are described by the characteristic wave vector $\mathbf{k}_{\text{kagome}} = (0,\ 0)$. Due to their similar kagome layer geometries, this may suggest similar spin correlations in the two materials where the additional Cu atoms in averievite cause a rotation of the spins in the kagome plane. However, it should be noted that the diffuse excitation near $Q = 0.76$ Å^{-1} in Zn_2-averievite is indexed by the (0, 0, 1) peak, indicating correlations between kagome planes that is not consistent with a 2-D system. A 2-D system was expected from the large inter-kagome distance of ~ 8.49 Å and supported by the zeroth-moment analysis indicating negligible spin correlations for this distance. Interestingly, the magnetic excitations observed for the $x = 1$ sample could be indexed by $\mathbf{k}_x = 1/3$, indicating a different spin configuration than in the $x = 0$ and $x = 2$ systems.

8.5.2 Zn_2-averievite as a candidate quantum spin liquid

The analysis of the magnetic excitations of Zn_2-averievite indicated gapless diffuse magnetic scattering down to at least $E = 0.3$ meV. Its magnetic susceptibility combined with the absence of magnetic Bragg peaks in the elastic line of the INS data, provide strong evidence that this material does not order magnetically down to $T = 1.5$ K. A power law was used to fit the energy dependence of the magnetic scattering and gave a good description over a large energy and temperature range. This scaling relation is similar to previous observations in herbertsmithite and was attributed to the system being near a quantum critical point or being a crit-

ical quantum spin liquid [10]. For herbertsmithite, it was suggested that the scaling behaviour may originate from impurity spins with a wide range of couplings [10]. For Zn_2-averievite, this scenario must also be considered though it is noted that the DC susceptibility indicated only $\sim 6.5\%$ of the Cu spins are impurities. On the other hand, the low-energy magnetic scattering, best observed at negative energy transfers, might also be attributed to impurity spins on the honeycomb sites. Although the SEM-EDX measurements in Chapter 7 indicated the Zn_2-averievite sample to have an almost nominal stoichiometry, the percentage of impurity spins will have to be refined using site-specific measurements such as anomalous x-ray scattering that is site and element specific. This will allow a better understanding of the observed magnetic behaviour.

8.6 Future work

Accurate determination of the exchange interactions in undoped averievite will require a better characterisation of the magnetic structure. Single crystal measurements may help with this and could allow the exchange interactions to be determined using the already available powder INS data. However, inelastic neutron scattering measurements on future single crystals will give direct access to the dispersion of the magnetic excitations rather than just the density of states, and thereby allow a more accurate determination of the exchanges.

The nature of the ground state of Zn_1-averievite is not clear from our measurements. To further investigate its ground state, muon spin relaxation (μSR) spectroscopy measurements have been planned in collaboration with Dr. G. Simutis, Prof. F. Bert and Prof. P. Mendels. The experiments will use pressure to alter the crystal structure of Zn_1-averievite, thereby tuning the exchange interactions and driving it into either a long-range ordered state or a spin liquid state. For Zn_2-averievite, μSR measurements have been done at temperatures below $T = 1.5$ K and the data are being analysed by Dr. G. Simutis, Prof. F. Bert and Prof. P. Mendels. As this is a local probe measurement, where the muon interacts with local magnetic fields in the sample, the results can distinguish between static and dynamic fields

from fluctuating magnetic moments.

8.7 Conclusions

This chapter presented inelastic neutron scattering measurements for averievite and its Zn-doped variants, $Zn_xCu_{5-x}(VO_4)_2O_2CsCl$ for $x = 0$, 1 and 2. The spin waves measured for undoped averievite had several branches with an excitation bandwidth of 11 meV. For the branch near $Q = 1.16$ Å^{-1} a zero-energy gap of 0.4(2) meV was determined, although from this data we cannot exclude the possibility that the spin waves are gapless. An energy gap is indicative of anisotropy in the system, most likely arising from Dzyaloshinskii-Moriya interactions (DMIs). The Q positions of the spin wave branches and the $\sim$ 11 meV bandwidth were adequately described by a two-parameter exchange model based on collinear Cu_h spins that occupy the interlayer honeycomb sites. As the magnetic structure was simplified to not include any spin canting, the DM interaction was not taken into account. Its value may be determined from future non-collinear spin models based on a more well-defined magnetic structure, which will likely also help to refine the exchange energy values.

Doping averievite with Zn to the $x = 1$ and $x = 2$ levels resulted in diffuse magnetic excitations and an absence of magnetic Bragg peaks down to $T = 1.5$ K. For Zn_1-averievite, the magnetic susceptibility indicated a transition at $T = 3.5$ K, but the INS measurements did not evidence a long-range ordered state. Although its ground state must be more accurately characterised using local probe experiments, the INS results combined with the magnetic susceptibility suggest it is spin glass-like. For the $S = 1/2$ kagome antiferromagnet Zn_2-averievite, synthesised and characterised here for the first time, a magnetic transition is not observed in its magnetic susceptibility and the absence of hysteresis in the magnetisation measurements as a function of external field, indicate that the glassiness of Zn_1-averievite has been suppressed (see Chapter 7). The inelastic neutron scattering data further support an absence of long-range magnetic order as no magnetic Bragg peaks are observed. Analysis of the inelastic magnetic excitations of Zn_2-averievite shows that its ground state is proximal to a quantum critical point, strongly suggesting that

it is a candidate quantum spin liquid.

Bibliography

[1] A. S. Botana, H. Zheng, S. H. Lapidus, J. F. Mitchell, and M. R. Norman, Phys. Rev. B **98**, 054421 (2018).

[2] S. Toth and B. Lake, J. Phys. Condens. Matter **27**, 166002 (2015).

[3] J. B. Goodenough, Scholarpedia **3**, 7382 (2008).

[4] J. A. M. Paddison, J. Ross Stewart, and A. L. Goodwin, J. Phys. Condens. Matter **25**, 454220 (2013).

[5] A.-J. Dianoux and G. Lander, *Neutron Data Booklet*, 2nd (2003), pp. 5–1.

[6] M. B. Stone, Y. Chen, J. Rittner, H. Yardimci, D. H. Reich, C. Broholm, D. V. Ferraris, and T. Lectka, Phys. Rev. B **65**, 064423 (2002).

[7] L. Messio, C. Lhuillier, and G. Misguich, Phys. Rev. B **83**, 184401 (2011).

[8] G. L. Squires, *Introduction to the Theory of Thermal Neutron Scattering*, 3rd ed. (Cambridge University Press, Cambridge, 2012).

[9] S. Sachdev and J. Ye, Phys. Rev. Lett. **69**, 2411 (1992).

[10] J. S. Helton, K. Matan, M. P. Shores, E. A. Nytko, B. M. Bartlett, Y. Qiu, D. G. Nocera, and Y. S. Lee, Phys. Rev. Lett. **104**, 147201 (2010).

[11] P. Coleman and C. Pépin, Phys. B: Condens. Matter **312-313**, 383 (2002).

[12] C. Mondelli, H. Mutka, C. Payen, B. Frick, and K. Andersen, Phys. B: Condens. Matter **284-288**, 1371 (2000).

[13] A. Schröder, G. Aeppli, E. Bucher, R. Ramazashvili, and P. Coleman, Phys. Rev. Lett. **80**, 5623 (1998).

[14] B. Keimer, R. J. Birgeneau, A. Cassanho, Y. Endoh, R. W. Erwin, M. A. Kastner, and G. Shirane, Phys. Rev. Lett. **67**, 1930 (1991).

Chapter 9

Conclusions

The search for $S = 1/2$ kagome Heisenberg antiferromagnets that host a quantum spin liquid ground state remains at the forefront of experimental condensed matter physics. These highly entangled states of matter provide grounds for robust quantum computation, so a better understanding of quantum entanglement and how to manipulate it is required. However, there are few good experimental examples, the most widely studied being the hydroxide material herbertsmithite. Although it shows a continuum of magnetic excitations in inelastic neutron scattering and an absence of spin freezing using μSR and NMR, there is ongoing debate about whether its excitations are gapped. Its polymorph kapellasite and the closely related hydroxide material barlowite have also gained attention in the literature, demonstrating the different flavours of QSLs that can be realised as a result of different competing exchange interactions. Beyond the proposal that QSLs underpin the transition to high-T_C superconductivity, they represent a new branch of topological physics. As they lack spontaneous symmetry breaking and Landau-type order parameters, they are classified into universality classes and the presence of a gap in their magnetic excitations together with the length scales of the spin interactions, can help to categorise them. This thesis expands the library of materials that host a quantum spin liquid ground state and furthers our understanding of the interplay of quantum fluctuations and short-range spin correlations.

Crystallographic and magnetic studies of high-quality samples in the claringbullite series, $Zn_xCu_{4-x}(OD)_6FCl$ for $x = 0$ and 1, are detailed in Chapter 5. Clar-

ingbullite is formed of a Cu^{2+} distorted pyrochlore lattice with *AA* stacking of the kagome layers and Zn-claringbullite represents the 'ideal' $S = 1/2$ kagome antiferromagnet. The DC magnetometry measurements on Zn-claringbullite show a suppression of the magnetic phase transition down to at least $T = 2$ K and the inelastic neutron scattering measurements presented in Chapter 6 evidence gapless, diffuse excitations. Linear spin wave theory (LSWT) was used to calculate the spin wave spectra of claringbullite and despite the complexity of the magnetic structure and the spectra themselves, solutions were found that closely match the experimental data. The exchange model proposed in this thesis includes four nearest-neighbour and two further-neighbour exchanges, as well as anisotropic Dzyaloshinskii-Moriya interactions. It was shown that this many exchange parameters were required by the complexity of the magnetic excitations, as well as the difficulty to stabilise the observed magnetic structure. In order to probe the sizeable phase space of possible exchange models which also stabilise the experimentally determined magnetic structure, a new protocol was developed in the new program Serendipity. In conjunction with LSWT, this allowed us to push the limits of inelastic powder data analysis and demonstrated the possibilities of using it to study complicated spin wave spectra of other complex magnets.

A comparison of the Q-dependence of the spin correlations between undoped claringbullite and $x = 1$ Zn-claringbullite, together with a zeroth- and first-moment analysis of the Zn-claringbullite magnetic scattering, indicates that the correlations between the kagome layers must be taken into account for an understanding of their magnetic behaviours. Zn-claringbullite is suggested to host a quantum spin liquid ground state, due to the absence of a magnetic phase transition in the DC susceptibility measurements down to $T = 2$ K and the absence of magnetic Bragg peaks together with a diffuse continuum of excitations in the INS data at $T = 1.5$ K. However, the interlayer correlations imply that the system deviates from the two-dimensional kagome limit and this aspect remains to be further investigated through single crystal studies.

The other series of materials studied in this thesis was the averievite series,

$Zn_xCu_{5-x}(VO_4)_2O_2CsCl$ for $x = 0$, 1 and 2, where Zn_2-averievite, to the best of our knowledge, is synthesised and studied here for the first time. The undoped averievite was previously reported to have two crystallographic phase transitions at $T = 310$ K and $T = 127$ K, where the crystal structure was not determined below the second one. Chapter 7 presents room temperature neutron and x-ray diffraction studies that are in agreement with previous reports and the synchrotron data at $T = 100$ K indicates a commensurately modulated crystal structure with propagation vector $\mathbf{k} = (0, \frac{1}{3}, 0)$. The diffraction studies on the $x = 1$ and $x = 2$ Zn-doped samples showed them to have similar kagome layer geometries, formed of equilateral triangles rotated in the plane thereby distorting the kagome hexagons. In both materials the Cu^{2+} atoms forming the kagome layers have large anisotropic displacement parameters suggesting a dynamic in-plane displacement. The magnetic excitations investigated using inelastic neutron scattering in Chapter 8, suggest three different ground states for the three samples. A preliminary exchange model for the spin wave excitations observed for undoped averievite, was devised solely based on the capping Cu_h sites and 3-dimensional spin correlations are supported by the study of the order parameter in Chapter 7. For Zn_1-averievite, the magnetic susceptibility data evidences a transition at $T = 3.5$ K, but no magnetic Bragg peaks are observed using neutron scattering suggesting a spin glass-like ground state. Doping to the $x = 2$ level shows a suppression of magnetic order and glassiness down to $T = 1.5$ K. The magnetic excitations are diffuse and their Q dependence indicates short-range correlations. Furthermore, they are gapless with no characteristic energy scale and the energy dependence could be well-fitted with a power law, evidencing proximity to a quantum critical point.

These five materials, of which two are good quantum spin liquid candidates, demonstrate the variety of electronic ground states that can be realised in highly frustrated antiferromagnets and how they can be tuned by chemical doping. The two series of materials are found to be dominated by a different set of exchange interactions, primarily due to their structural differences. Although both QSLs exhibit gapless ($E \gtrsim 0.3$ meV) diffuse magnetic excitations, which could be indexed

by the $\mathbf{k} = \mathbf{0}$ characteristic wave vector, the differences in their exchange models result in different magnetic excitations. These results encourage further experimental investigation into the exchange interactions of these materials, as well as theoretical calculations of their exchange models to place the $S = 1/2$ kagome antiferromagnets in a quantum spin liquid phase diagram.

Appendix A

Appendix for Chapter 4

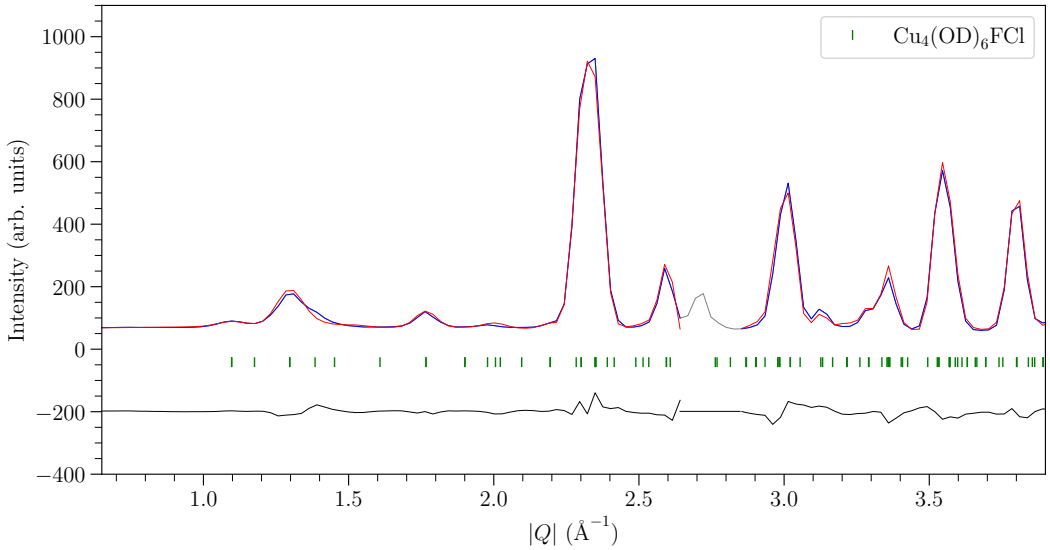

Figure A.1: Claringbullite PANTHER data with $E_i = 19.2$ meV at $T = 25$ K. $S(Q,E)$integrated over $-0.2 < E < 0.2$ meV (blue). A Rietveld refinement in space group *Pnma* was done with the structure obtained at $T = 1.5$ K on D2B (red, $\lambda = 1.595226$ Å), with the difference plot in black. The green tick marks correspond to the main phase. The excluded regions are Bragg peaks from the aluminium sample can.

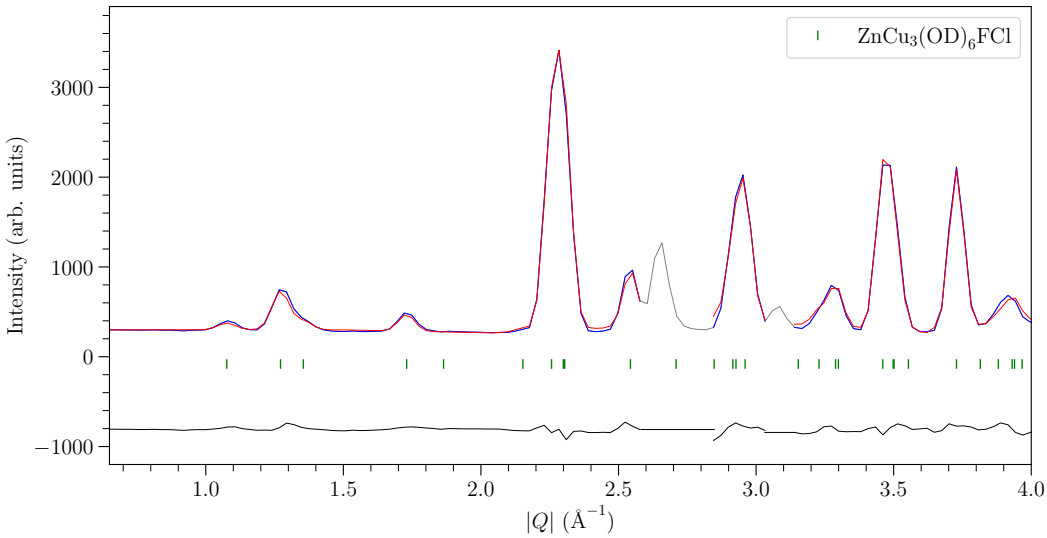

Figure A.2: Zn-claringbullite LET data with $E_i = 20.03$ meV at $T = 1.7$ K. $S(Q,E)$integrated over $-0.2 < E < 0.2$ meV (blue). A Rietveld refinement in space group $P6_3/mmc$ was done with the structure obtained at $T = 1.5$ K on D2B (red, $\lambda = 1.595226$ Å), with the difference plot in black. The green tick marks correspond to the main phase. The excluded regions are Bragg peaks from the aluminium sample can.

Appendix B

Appendix for Chapter 5

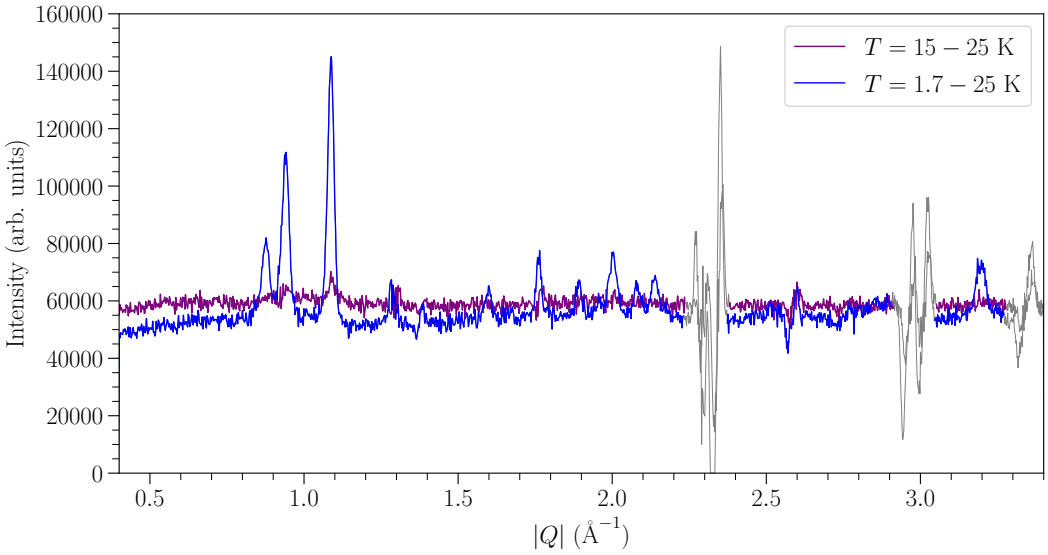

Figure B.1: Claringbullite D20 data ($\lambda = 2.41$ Å). Temperature subtractions $T = 15$–25 K (purple) and $T = 1.7$–25 K (blue), showing no new magnetic peaks appear below $T = 15$ K.

Atom number	Coordinates	Basis vector	m_a	m_b	m_c
Atom 1	(0.5, 0, 0.5)	ψ_1	1	0	0
		ψ_2	0	1	0
		ψ_3	0	0	1
Atom 2	(0, 0.5, 0)	ψ_1	–1	0	0
		ψ_2	0	1	0
		ψ_3	0	0	1
Atom 3	(0.5, 0.5, 0.5)	ψ_1	1	0	0
		ψ_2	0	–1	0
		ψ_3	0	0	1
Atom 4	(0, 0, 0)	ψ_1	–1	0	0
		ψ_2	0	–1	0
		ψ_3	0	0	1

Table B.1: The basis vectors of the Γ_7 irreducible representation of the space group *Pnma* with $\mathbf{k} = (0,\ 0,\ 0)$ for the Cu1 4*a* site, where m_a, m_b and m_c are the moment components along the crystallographic unit cell directions *a*, *b* and *c*.

Atom number	Coordinates	Basis vector	m_a	m_b	m_c
Atom 1	(0.74838, 0.51002, 0.74705)	ψ_1	1	0	0
		ψ_2	0	1	0
		ψ_3	0	0	1
Atom 2	(0.24838, 0.98998, 0.75295)	ψ_1	–1	0	0
		ψ_2	0	1	0
		ψ_3	0	0	1
Atom 3	(0.25162, 0.01002, 0.25295)	ψ_1	1	0	0
		ψ_2	0	–1	0
		ψ_3	0	0	1
Atom 4	(0.75162, 0.48998, 0.24705)	ψ_1	–1	0	0
		ψ_2	0	–1	0
		ψ_3	0	0	1
Atom 5	(0.25162, 0.48998, 0.25295)	ψ_1	1	0	0
		ψ_2	0	1	0
		ψ_3	0	0	1
Atom 6	(0.75162, 0.01002, 0.24705)	ψ_1	–1	0	0
		ψ_2	0	1	0
		ψ_3	0	0	1
Atom 7	(0.74838, 0.98998, 0.74705)	ψ_1	1	0	0
		ψ_2	0	–1	0
		ψ_3	0	0	1
Atom 8	(0.24838, 0.51002, 0.75295)	ψ_1	–1	0	0
		ψ_2	0	–1	0
		ψ_3	0	0	1

Table B.2: The basis vectors of the Γ_7 irreducible representation of the space group *Pnma* with $\mathbf{k} = (0,\ 0,\ 0)$ for the Cu2 8*d* site, where m_a, m_b and m_c are the moment components along the crystallographic unit cell directions *a*, *b* and *c*.

Atom number	Coordinates	Basis vector	m_a	m_b	m_c
Atom 1	(0.31643, 0.75, 0.43983)	ψ_1	1	0	0
		ψ_2	0	0	1
Atom 2	(0.81643, 0.75, 0.06017)	ψ_1	–1	0	0
		ψ_2	0	0	1
Atom 3	(0.68357, 0.25, 0.56017)	ψ_1	1	0	0
		ψ_2	0	0	1
Atom 4	(0.18357, 0.25, 0.93983)	ψ_1	–1	0	0
		ψ_2	0	0	1

Table B.3: The basis vectors of the Γ_7 irreducible representation of the space group *Pnma* with $\mathbf{k} = (0,\ 0,\ 0)$ for the Cu3 4*c* site, where m_a, m_b and m_c are the moment components along the crystallographic unit cell directions *a*, *b* and *c*.

Appendix C

Appendix for Chapter 6

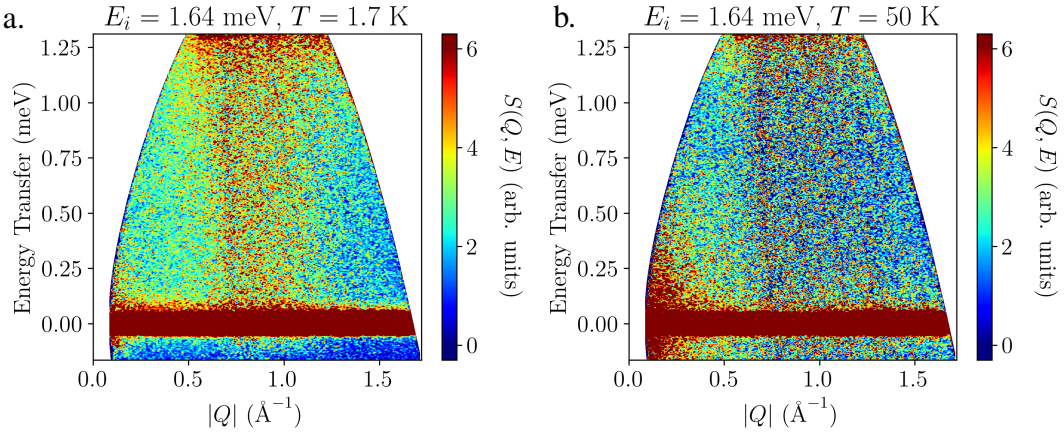

Figure C.1: Zn-claringbullite, $S(Q,E)$ from LET with an incident neutron energy of $E_i = 1.64$ meV at temperatures of **a.** $T = 1.7$ K and **b.** $T = 50$ K.

Appendix D

Appendix for Chapter 7

D.1 Diffraction studies on averievite

Refinements for undoped averievite using data collected on HRPD, D2B and 11-BM.

Instrument	Temperature (K)	No. of refined variables	R_{wp}	χ^2
D2B	300	107	4.51	2.33
11-BM	300	102	5.37	1.45
HRPD	100	77	3.49	4.11
HRPD	75	76	3.92	2.28
HRPD	50	76	4.12	2.40
HRPD	25	76	4.32	2.51
HRPD	1.5	76	4.21	4.52

Table D.1: Averievite. Details on the refinements for data collected on D2B ($\lambda =$ 1.595226 Å), the backscattering bank of HRPD and 11-BM ($\lambda = 0.457794$ Å). All refinements were done in space group $P12_1/c1$ (no. 14) and included a CuO impurity phase.

T (K)	a (Å)	b (Å)	c (Å)	β (°)	Cell volume (Å^3)
1.5	8.37297(5)	6.38330(10)	10.92444(18)	90.1882(12)	583.878(13)
25	8.37296(5)	6.38231(10)	10.92551(18)	90.1828(12)	583.843(14)
50	8.37211(5)	6.38010(9)	10.92671(16)	90.1751(11)	583.647(12)
75	8.37070(4)	6.37654(8)	10.92816(14)	90.1658(10)	583.300(11)
100	8.36936(4)	6.37369(7)	10.93099(12)	90.1557(9)	583.097(9)
300	8.37483(2)	6.36088(3)	11.02000(6)	90.0216(6)	587.049(5)

Table D.2: Averievite. Lattice parameters and cell volume from Rietveld refinements in the $P12_1/c1$ space group (no. 14) using data collected on HRPD (backscattering bank) between $1.5 \leq T \leq 100$ K and on 11-BM ($\lambda = 0.457841$ Å) at $T = 300$ K.

Atom	Wyckoff site	x	y	z	Occupation	U_{iso} (Å^2)
Cu_{k1}	2*c*	0	0	0.5	1	0.00115(43)
Cu_{k2}	4*e*	0	0.8005(4)	0.2288(3)	1	0.00115(43)
Cu_h	4*e*	0.7296(4)	0.5334(5)	0.1668(3)	1	0.00415(55)
Cl	2*a*	0	0	0	1	0.0177(8)
Cs	4*e*	0.4242(7)	0	0	0.5	0.0120(16)
O_1	4*e*	0.7610(4)	0.6732(5)	0.7418(3)	1	0.00174(31)
O_2	4*e*	0.7640(4)	0.2663(5)	0.2700(4)	1	0.00174(31)
O_3	4*e*	0.7626(4)	0.4958(5)	–0.02130(31)	1	0.00174(31)
O_{Cs}	4*e*	0.4950(4)	0.03215(66)	0.3309(4)	1	0.00174(31)
O_k	4*e*	0.9597(4)	0.5339(7)	0.1689(4)	1	0.00174(31)
V	4*e*	0.2997(49)	0.5326(85)	0.1867(47)	1	0.00127

Table D.3: Averievite. Atomic positions and displacement parameters from a Rietveld refinement in the $P12_1/c1$ (no. 14) space group using data collected on HRPD (backscattering bank) at $T = 1.5$ K. The isotropic displacement parameters were refined for all atoms except for vanadium.

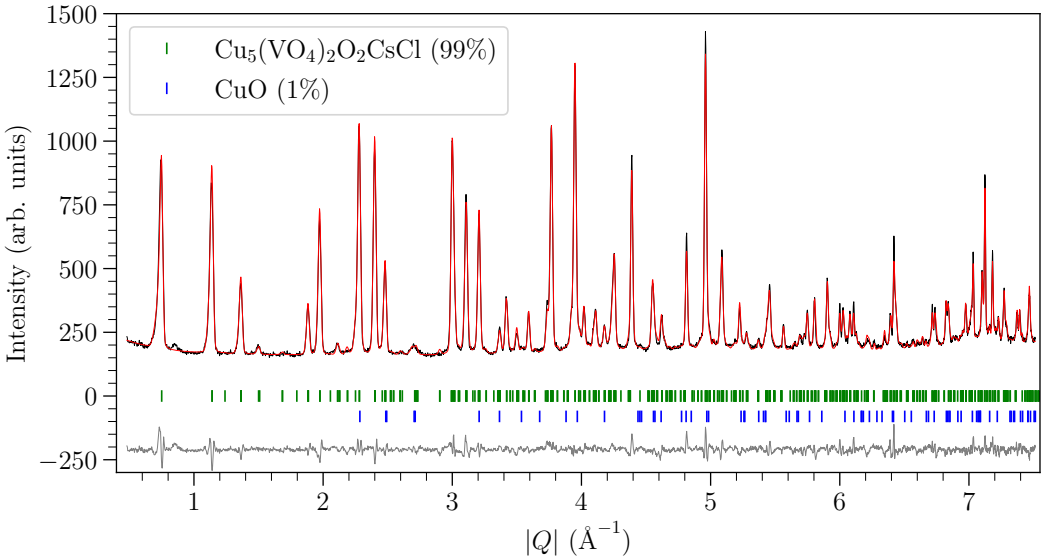

Figure D.1: Averievite, $T = 300$ K. Rietveld refinement (red) in space group $P12_1/c1$ (green ticks) using data collected on the D2B neutron diffractometer (black, $\lambda = 1.595226$ Å) with the difference plot (grey). The refinement showed a $\sim 1\%$ CuO impurity in the sample (blue ticks).

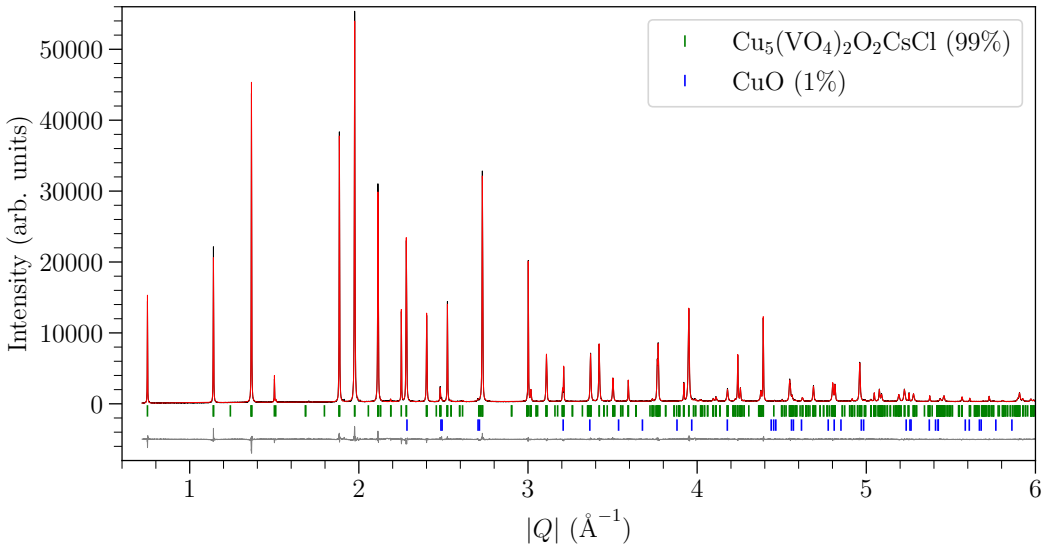

Figure D.2: Averievite, $T = 300$ K. Rietveld refinement (red) in space group $P12_1/c1$ (green ticks) using data collected on the 11-BM synchrotron diffractometer (black, $\lambda = 0.457794$ Å) with the difference plot (grey). The refinement showed a $\sim 1\%$ CuO impurity in the sample (blue ticks).

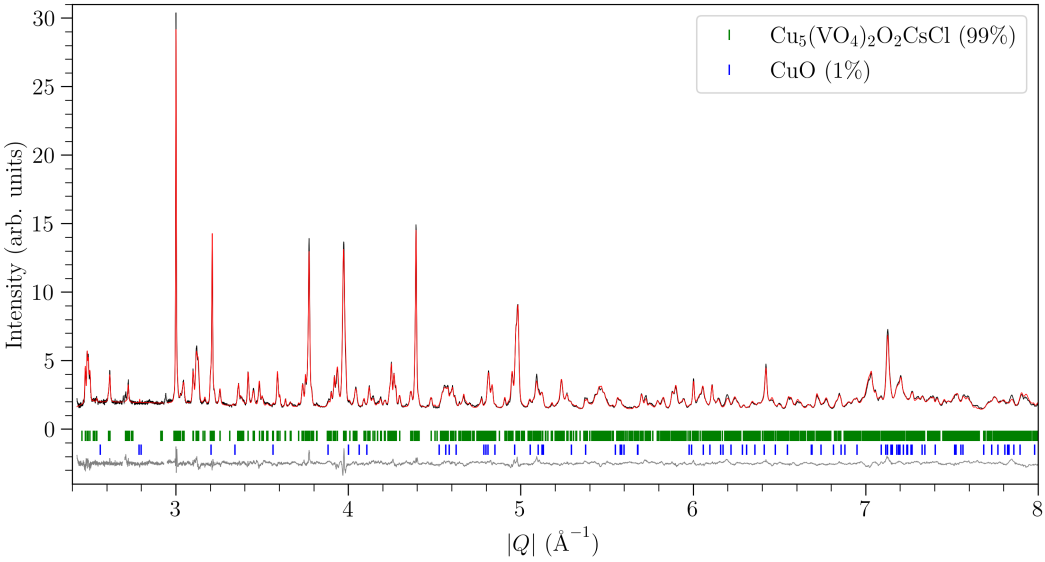

Figure D.3: Averievite, $T = 25$ K. Rietveld refinement in the $P12_1/c1$ space group using data collected on the HRPD backscattering bank (black). There is a $\sim 1\%$ CuO impurity shown by the blue ticks.

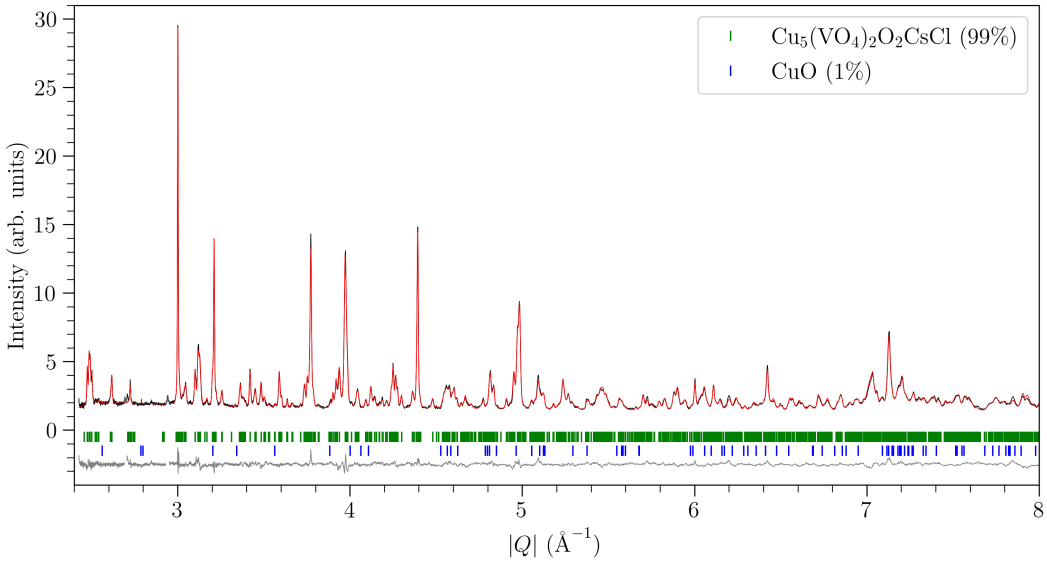

Figure D.4: Averievite, $T = 50\,\mathrm{K}$. Rietveld refinement (red) in the $P12_1/c1$ space group at using data collected on the HRPD backscattering bank (black). There is a $\sim 1\%$ CuO impurity shown by the blue ticks.

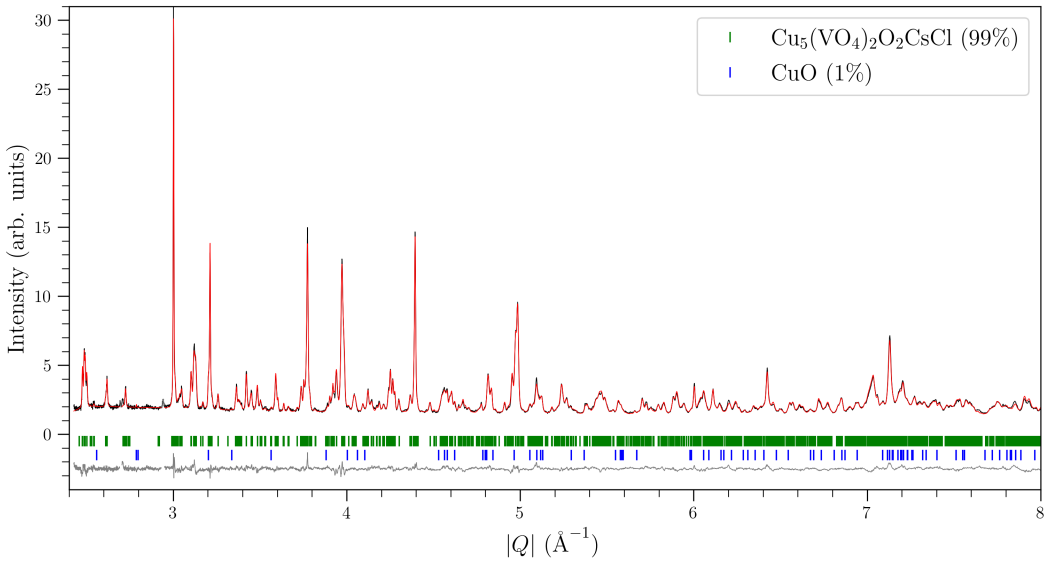

Figure D.5: Averievite, $T = 75\,\mathrm{K}$. Rietveld refinement (red) in the $P12_1/c1$ space group using data collected on the HRPD backscattering bank (black). There is a $\sim 1\%$ CuO impurity shown by the blue ticks.

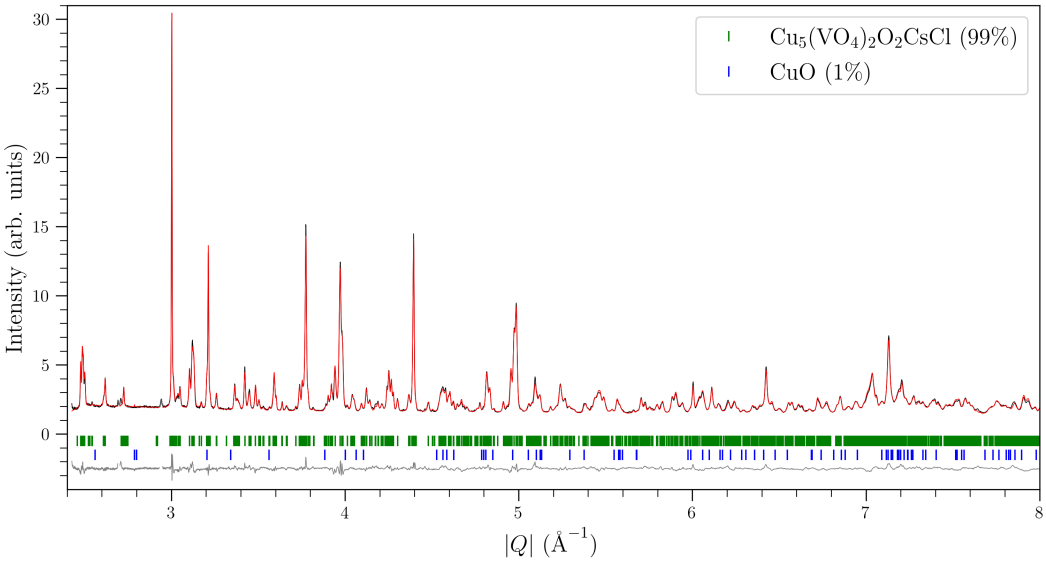

Figure D.6: Averievite, $T = 100$ K. Rietveld refinement (red) in the $P12_1/c1$ space group using data collected on the HRPD backscattering bank (black). There is a $\sim 1\%$ CuO impurity shown by the blue ticks.

D.2 Diffraction studies on Zn_2-averievite

Lattice parameters						
a (Å)		b (Å)	c (Å)	α (°)	β (°)	γ (°)
6.25384(2)		6.25384(2)	8.49215(3)	90	90	120
Atomic parameters						
Atom	Wyckoff site	x	y	z	Occupation	U_{iso} (Å^2)
Cu_k	6g	0.4681(95)	0	0	0.5	0.0989
Zn_h	2d	1/3	2/3	0.7270(1)	1	0.0180
Cl	1a	0	0	0	1	0.0182
Cs	1b	0	0	0.4911(409)	0.5	0.0481
O_{Cs}	2d	1/3	2/3	0.5017(9)	1	0.0118(10)
O_h	12j	0.4343(8)	0.4664(7)	0.2424(3)	0.5	0.0331(12)
O_k	2d	1/3	2/3	0.9605(6)	1	0.0201(18)
V	2d	1/3	2/3	0.3068(1)	1	0.0152
Anisotropic displacement parameters (Å^2)						
Atom	U_{11}	U_{22}	U_{33}	U_{12}	U_{13}	U_{23}
Cu_k	0.2111(193)	0.0152(5)	0.0051(5)	0.0076(3)	0.0003(3)	0.0007(6)
Zn_h	0.0015(12)	0.0015(12)	0.0007(6)	0.0132(3)	0	0
Cl	-	-	-	-	-	-
Cs	0.0221(4)	0.0221(4)	0.1044(539)	0.0110(2)	0	0
O_{Cs}	-	-	-	-	-	-
O_h	-	-	-	-	-	-
O_k	-	-	-	-	-	-
V	0.0198(8)	0.0198(8)	0.0061(11)	0.0099(4)	0	0

Table D.4: Zn_2-averievite. Lattice parameters, atomic positions and displacement parameters from a Rietveld refinement in the $P\bar{3}m1$ (no. 164) space group using synchrotron data collected on 11-BM ($\lambda = 0.457794$ Å) at $T = 100$ K. Anisotropic displacement parameters were refined for the heaviest atoms: Cu, Zn, Cs and V.

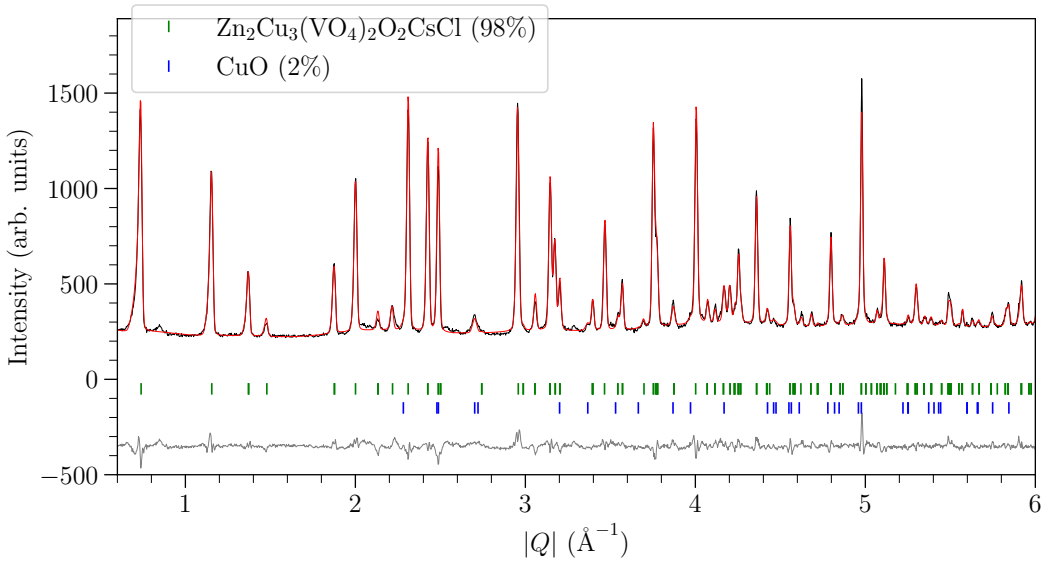

Figure D.7: Zn_2-averievite. Rietveld refinement with 100 parameters in the $P3$ space group at $T = 300$ K using neutron data collected on D2B ($\lambda = 1.595226$ Å, $r_{wp} = 3.82$ and $\chi^2 = 2.30$). There is a $\sim 2\%$ CuO impurity shown by the blue ticks.

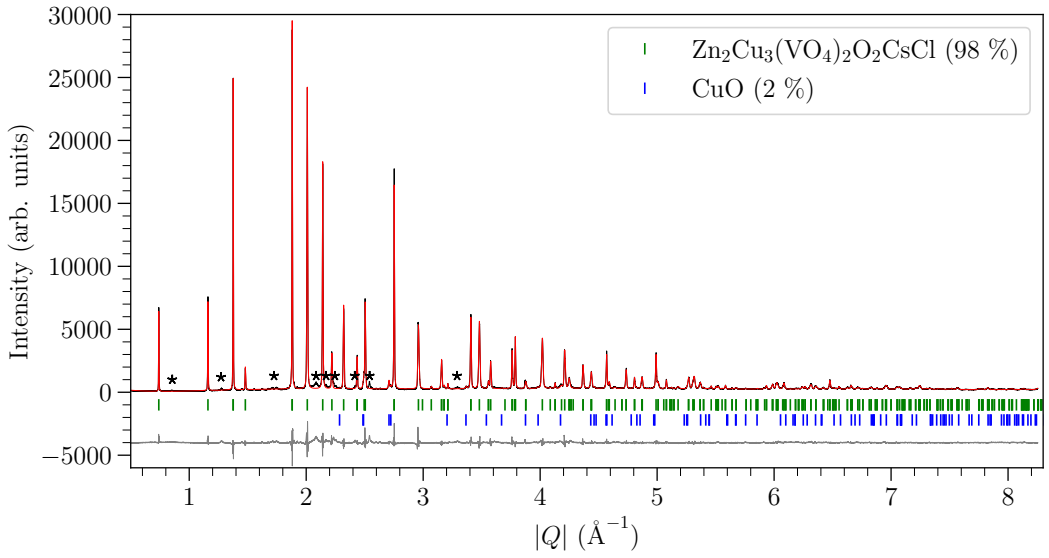

Figure D.8: Zn_2-averievite Rietveld refinement with 56 parameters in the $P\bar{3}m1$ space group using synchrotron data collected on 11-BM ($\lambda = 0.457794$ Å) at $T = 100$ K ($r_{wp} = 10.52$ and $\chi^2 = 2.62$). There is a $\sim 2\%$ CuO impurity shown by the blue ticks and an unidentifiable impurity marked by asterisks.

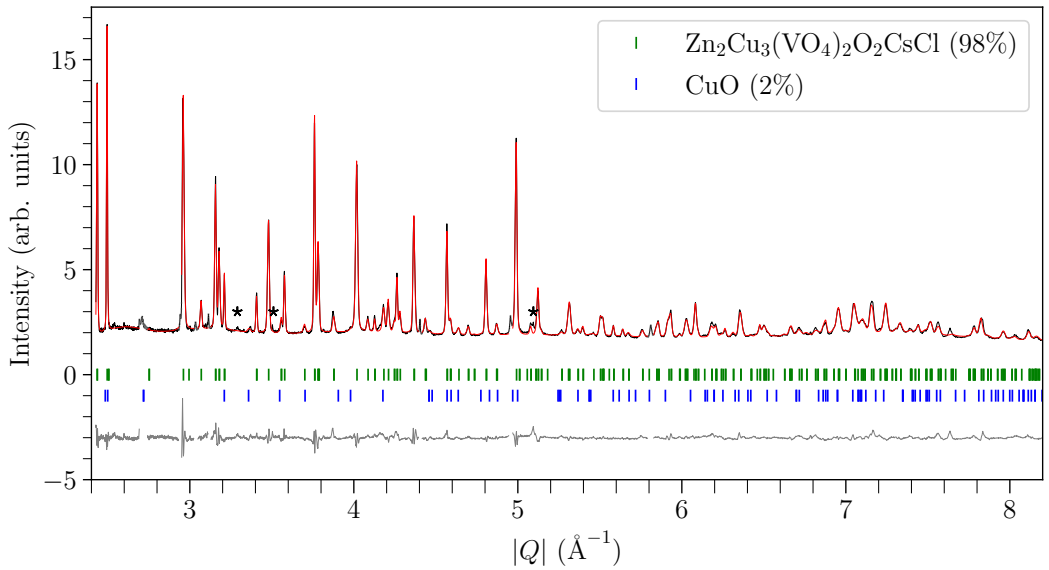

Figure D.9: Zn_2-averievite Rietveld refinement with 66 parameters in the $P\bar{3}m1$ space group using data collected on the HRPD backscattering bank at $T = 100$ K ($r_{wp} = 3.59$ and $\chi^2 = 3.64$). There is a $\sim 2\%$ CuO impurity shown by the blue ticks and an unidentifiable impurity marked by asterisks.

Lattice parameters						
a (Å)		b (Å)	c (Å)	α (°)	β (°)	γ (°)
6.24865(4)		6.24865(4)	8.48753(8)	90	90	120
Atomic parameters						
Atom	Wyckoff site	x	y	z	Occupation	U_{iso} (Å^2)
Cu_k	3d	0.5200(44)	0	0	1	0.0934
Zn_{h1}	1b	1/3	2/3	0.7314(5)	1	0.0114
Zn_{h2}	1c	2/3	1/3	0.2686(2)	1	0.0114
Cl	1a	0	0	0	1	0.0253
Cs_1	1a	0	0	0.5	0.5	0.0550
Cs_2	1a	0	0	0.5	0.5	0.0550
O_{Cs1}	1b	1/3	2/3	0.5025(28)	1	0.0311
O_{Cs2}	1c	2/3	1/3	0.4975(28)	1	0.0311
O_{h1}	3d	0.4859(33)	0.5140(35)	0.23974(21)	1	0.0689
O_{h2}	3d	0.4859(33)	0.4399(35)	0.76026(67)	1	0.0689
O_{k1}	1b	1/3	2/3	0.9612(3)	1	0.0311
O_{k2}	1c	2/3	1/3	0.0388(1)	1	0.0311
V_1	1b	1/3	2/3	0.30743	1	0.0451
V_2	1c	2/3	1/3	0.69257	1	0.0451
Anisotropic displacement parameters (Å^2)						
Atom	U_{11}	U_{22}	U_{33}	U_{12}	U_{13}	U_{23}
Cu_k	0.1969(99)	0.0314(18)	0.0116(14)	0.0271(59)	–0.0371(42)	–0.0031(14)
Zn_{h1}	0.0169(19)	0.0172(117)	0.0079(19)	0.0142(45)	0	0
Zn_{h2}	0.0169(19)	0.0172(117)	0.0079(19)	0.0142(45)	0	0
Cl	0.0369(30)	0.0366(30)	0.0234(19)	0.0270(39)	0	0
Cs_1	0.0202(43)	0.0461(512)	0.0892(44)	0.0128(157)	0	0
Cs_2	0.0202(43)	0.0461(512)	0.0892(44)	0.0128(157)	0	0
O_{Cs1}	0.0191(14)	0.0607(134)	0.0065(13)	0.0154(43)	0	0
O_{Cs2}	0.0191(14)	0.0607(134)	0.0065(13)	0.0154(43)	0	0
O_{h1}	0.1166(38)	0.1587(70)	0.0106(11)	0.1288(48)	0.0210(36)	0.0253(38)
O_{h2}	0.1166(38)	0.1587(70)	0.0106(11)	0.1288(48)	0.0210(36)	0.0253(38)
O_{k1}	0.0191(14)	0.0607(134)	0.0065(13)	0.0154(43)	0	0
O_{k2}	0.0191(14)	0.0607(134)	0.0065(13)	0.0154(43)	0	0
V_1	0.0065	0.0987	0.0085	0.0102	0	0
V_2	0.0065	0.0987	0.0085	0.0102	0	0

Table D.5: Zn_2-averievite. Atomic positions and displacement parameters from the Rietveld refinement in the $P3$ space group (no. 143) using neutron data collected on HRPD (backscattering bank) at $T = 1.5$ K. Anisotropic displacement parameters (ADPs) were stably refined for all atoms apart from vanadium. The position and ADPs of vanadium were fixed at the values refined from the synchrotron data at $T = 100$ K.

D.3 Diffraction studies on Zn_1-averievite

Lattice parameters						
a (Å)		b (Å)	c (Å)	α (°)	β (°)	γ (°)
6.27980(5)		6.27980(5)	8.41823(6)	90	90	120
Atomic parameters						
Atom	Wyckoff site	x	y	z	Occupation	U_{iso} (Å^2)
Cu_k	6g	0.5473(8)	0	0	0.5	0.1012
Zn_{h1}/Cu_{h1}	2d	1/3	2/3	0.7339(4)	1	0.0108
Cl	1a	0	0	0	1	0.03075
Cs	2c	0	0	0.5373(7)	0.5	0.0463
O_{Cs}	2d	1/3	2/3	0.5052(4)	1	0.0229
O_h	12j	0.4489(19)	0.486(2)	0.2407(2)	0.5	0.0257
O_k	2d	1/3	2/3	0.9587(3)	1	0.0251
V	2d	1/3	2/3	0.3111	1	0.0153
Anisotropic displacement parameters (Å^2)						
Atom	U_{11}	U_{22}	U_{33}	U_{12}	U_{13}	U_{23}
Cu_k	0.067(4)	0.0376(15)	0.0101(9)	0.0188(8)	0.0009(5)	0.0018(9)
Zn_{h1}/Cu_{h1}	0.0164(8)	0.0164(8)	0.0035(12)	0.0082(4)	0	0
Cl	0.0276(11)	0.0276(11)	0.052(2)	0.0138(6)	0	0
Cs	0.044(3)	0.044(3)	0.033(5)	0.0219(15)	0	0
O_{Cs}	0.0324(1)	0.0324(1)	0.0141(1)	0.0162(2)	0	0
O_h	0.094(5)	0.094(5)	0.0203(11)	0.082(5)	–0.034(3)	–0.034(3)
O_k	0.0293(11)	0.0293(11)	0.0118(14)	0.0146(6)	0	0

Table D.6: Zn_1-averievite. Lattice parameters, atomic positions and displacement parameters from the Rietveld refinement in the $P\bar{3}m1$ (no. 164) space group using neutron data collected on HRPD (backscattering bank) at $T = 1.5$ K. Anisotropic displacement parameters were refined for all atoms except vanadium.

Lattice parameters						
a (Å)		b (Å)	c (Å)	α (°)	β (°)	γ (°)
6.27989(4)		6.27989(4)	8.41826(4)	90	90	120
Atomic parameters						
Atom	Wyckoff site	x	y	z	Occupation	U_{iso} (Å^2)
Cu_k	3d	0.5053(55)	0	0	1	0.06967
Zn_{h1}/Cu_{h1}	1b	1/3	2/3	0.7321(3)	1	0.0125
Zn_{h2}/Cu_{h2}	1c	2/3	1/3	0.2678(1)	1	0.0125
Cl	1a	0	0	0	1	0.0195
Cs_1	1a	0	0	0.4586(5)	0.5	0.0354
Cs_2	1a	0	0	0.5414(6)	0.5	0.0354
O_{Cs1}	1b	1/3	2/3	0.500(37)	1	0.0279
O_{Cs2}	1c	2/3	1/3	0.500(37)	1	0.0279
O_1	3d	0.4880(29)	0.5255(44)	0.2386(1)	1	0.0501
O_2	3d	0.4880(29)	0.4493(43)	0.7613(4)	1	0.0501
O_{k1}	1b	1/3	2/3	0.9586(2)	1	0.0279
O_{k2}	1c	2/3	1/3	0.04141(1)	1	0.0279
V_1	1b	1/3	2/3	0.3061	1	0.0465
V_2	1c	2/3	1/3	0.6939	1	0.0465
Anisotropic displacement parameters (Å^2)						
Atom	U_{11}	U_{22}	U_{33}	U_{12}	U_{13}	U_{23}
Cu_k	0.1664(51)	0.0182(12)	0.0088(8)	0.0268(36)	–0.0332(28)	–0.0055(10)
Zn_{h1}/Cu_{h1}	0.1844(60)	0.1844(60)	0.0009(9)	0.0092(3)	0	0
Zn_{h2}/Cu_{h2}	0.1844(60)	0.1844(60)	0.0009(9)	0.0092(3)	0	0
Cl	0.0431(24)	0.0431(24)	0.0203(11)	0.0414(28)	0	0
Cs_1	0.0570(30)	0.0570(30)	0.0286(32)	0.0285(15)	0	0
Cs_2	0.0570(30)	0.0570(30)	0.0286(32)	0.0285(15)	0	0
O_{Cs1}	0.0254(12)	0.0537(91)	0.0059(9)	0.0215(28)	0	0
O_{Cs2}	0.0254(12)	0.0537(91)	0.0059(9)	0.0215(28)	0	0
O_1	0.0798(24)	0.1153(49)	0.0090(7)	0.0892(25)	0.0086(2)	0.0110(22)
O_2	0.0798(24)	0.1153(49)	0.0090(7)	0.0892(25)	0.0086(2)	0.0110(22)
O_{k1}	0.0254(12)	0.0537(91)	0.0059(9)	0.0215(28)	0	0
O_{k1}	0.0254(12)	0.0537(91)	0.0059(9)	0.0215(28)	0	0
V_1	0.0223	0.1079	0.0061	0.0302	0	0
V_2	0.0223	0.1079	0.0061	0.0302	0	0

Table D.7: Zn_1-averievite. Atomic positions and displacement parameters from the Rietveld refinement in the space group $P3$ (no. 143) using neutron data collected on HRPD (backscattering bank) at $T = 1.5$ K. Anisotropic displacement parameters were stably refined for all atoms apart from vanadium. The positions and ADPs of the vanadium atoms were fixed to the values from the synchrotron data at $T = 100$ K .

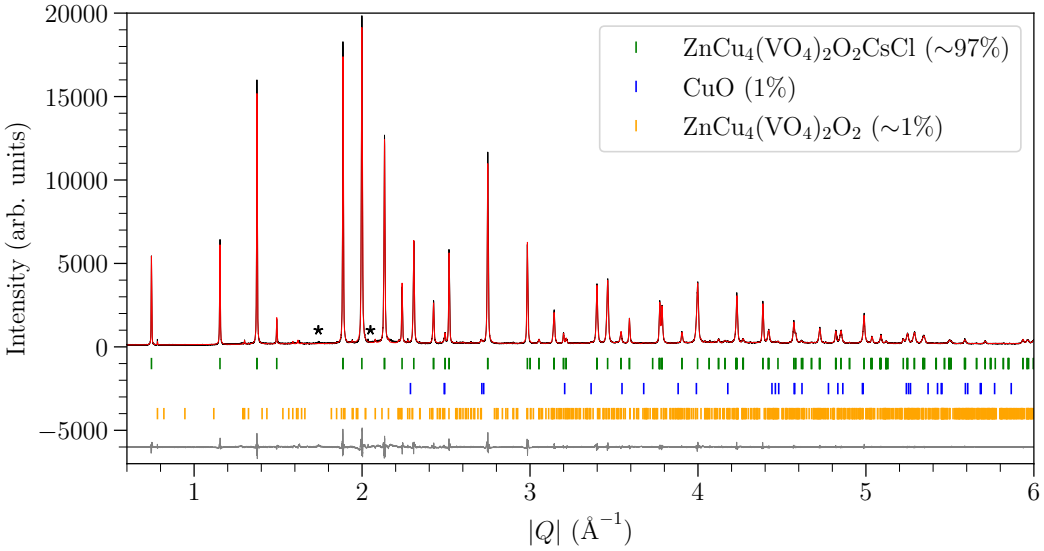

Figure D.10: Zn_1-averievite, $T = 100$ K. Rietveld refinement (red) in the space group $P3$ (green ticks) using 11-BM ($\lambda = 0.457794$ Å) synchrotron diffraction data (black) with the difference plot (grey). The refinement showed impurities of the order of a few % identified as CuO (blue ticks, Rietveld refined), $ZnCu_4(VO_4)_2O_2$ (orange ticks, Pawley refinement) and an unidentified impurity marked by asterisks. $R_{wp} = 6.70$, $\chi^2 = 1.48$ for 69 parameters.

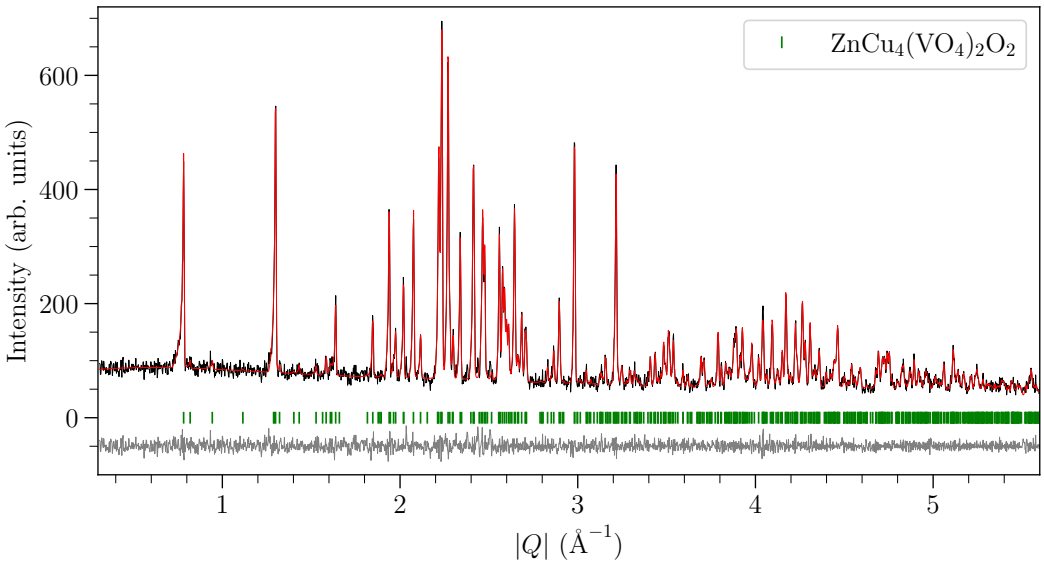

Figure D.11: Zn-doped stoiberite, $ZnCu_4(VO_4)_2O_2$. Lab powder x-ray diffraction collected on a STOE Stadi-P ($\lambda = 0.7093$ Å) at room temperature (black). Pawley fit (red) with the difference plot (grey) in space group $P12_1/c1$. The lattice parameters are $a = 8.439282(683)$ Å, $b = 6.054994(434)$ Å, $c = 16.121176(1033)$ Å and $\beta = 107.82738(447)°$.

D.4 Magnetic structure refinement of averievite

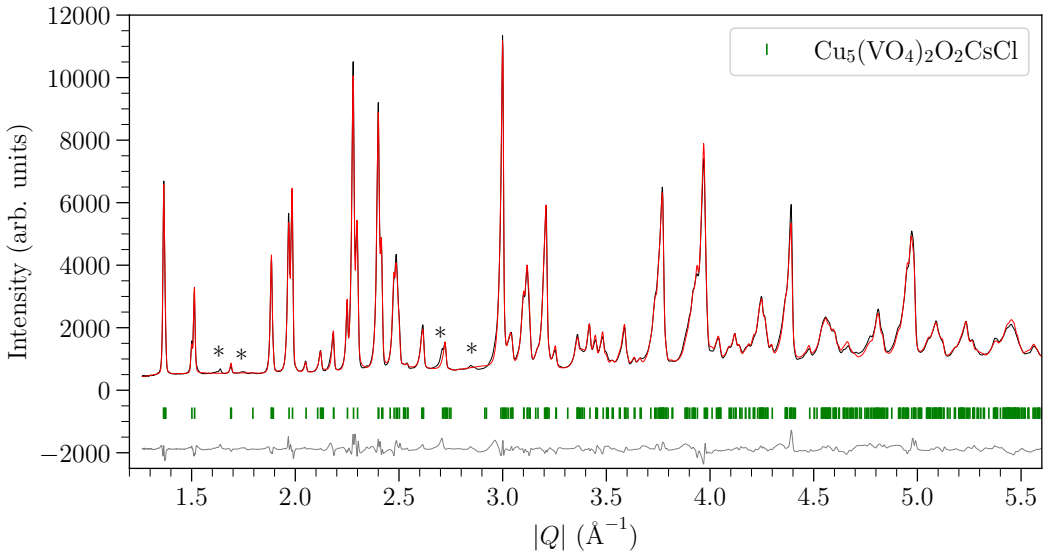

Figure D.12: Averievite $T = 1.5$ K data collected on WISH in the highest resolution bank, bank 5 (black). The Rietveld refinement (red) was done in the $P12_1/c1$ space group, excluding the peaks corresponding to the modulated crystal structure at $Q = 1.64$, 1.71 and 2.85 Å^{-1} (marked by asterisks). The peak marked by the asterisk at 2.7 Å^{-1} is from the aluminium sample can.

Tables of basis vectors for the irreducible representations Γ_1 and Γ_3 in space group $P12_1/c1$ with k=(0.5, 0, 0).

Atom number	Coordinates	Basis vector	m_a	m_b	m_c
Atom 1	(0, 0, 0.5)	ψ_1	1	0	0
		ψ_2	0	1	0
		ψ_3	0	0	1
Atom 2	(0, 0.5, 0)	ψ_1	−1	0	0
		ψ_2	0	1	0
		ψ_3	0	0	−1

Table D.8: The basis vectors of the Γ_1 irreducible representation of the space group $P12_1/c1$ with $k = (0.5,\ 0,\ 0)$ for the Cu_{k1} $2c$ site, where m_a, m_b and m_c are the moment components along the crystallographic unit cell directions a, b and c.

Atom number	Coordinates	Basis vector	m_a	m_b	m_c
Atom 1	(0, 0.80048, 0.23059)	ψ_1	1	0	0
		ψ_2	0	1	0
		ψ_3	0	0	1
Atom 2	(0, 0.30048, 0.26941)	ψ_1	−1	0	0
		ψ_2	0	1	0
		ψ_3	0	0	−1
Atom 3	(0, 0.19952, 0.76941)	ψ_1	1	0	0
		ψ_2	0	1	0
		ψ_3	0	0	1
Atom 4	(0, 0.69952, 0.73059)	ψ_1	−1	0	0
		ψ_2	0	1	0
		ψ_3	0	0	−1

Table D.9: The basis vectors of the Γ_1 irreducible representation of the space group $P12_1/c1$ with $k = (0.5,\ 0,\ 0)$ for the Cu_{k2} $4e$ site, where m_a, m_b and m_c are the moment components along the crystallographic unit cell directions a, b and c.

Atom number	Coordinates	Basis vector	m_a	m_b	m_c
Atom 1	(0.72862, 0.53568, 0.16828)	ψ_1	1	0	0
		ψ_2	0	1	0
		ψ_3	0	0	1
Atom 2	(0.27138, 0.03568, 0.33172)	ψ_1	1	0	0
		ψ_2	0	–1	0
		ψ_3	0	0	1
Atom 3	(0.27138, 0.46432, 0.83172)	ψ_1	–1	0	0
		ψ_2	0	–1	0
		ψ_3	0	0	–1
Atom 4	(0.72862, 0.96432, 0.66828)	ψ_1	–1	0	0
		ψ_2	0	1	0
		ψ_3	0	0	–1

Table D.10: The basis vectors of the Γ_1 irreducible representation of the space group $P12_1/c1$ with $k = (0.5,\ 0,\ 0)$ for the Cu_h $4e$ site, where m_a, m_b and m_c are the moment components along the crystallographic unit cell directions a, b and c.

Atom number	Coordinates	Basis vector	m_a	m_b	m_c
Atom 1	(0, 0, 0.5)	ψ_1	1	0	0
		ψ_2	0	1	0
		ψ_3	0	0	1
Atom 2	(0, 0.5, 0)	ψ_1	1	0	0
		ψ_2	0	–1	0
		ψ_3	0	0	1

Table D.11: The basis vectors of the Γ_3 irreducible representation of the space group $P12_1/c1$ with $k = (0.5,\ 0,\ 0)$ for the Cu_{k1} $2c$ site, where m_a, m_b and m_c are the moment components along the crystallographic unit cell directions a, b and c.

Atom number	Coordinates	Basis vector	m_a	m_b	m_c
Atom 1	(0, 0.80048, 0.23059)	ψ_1	1	0	0
		ψ_2	0	1	0
		ψ_3	0	0	1
Atom 2	(0, 0.30048, 0.26941)	ψ_1	1	0	0
		ψ_2	0	−1	0
		ψ_3	0	0	1
Atom 3	(0, 0.19952, 0.76941)	ψ_1	1	0	0
		ψ_2	0	1	0
		ψ_3	0	0	1
Atom 4	(0, 0.69952, 0.73059)	ψ_1	1	0	0
		ψ_2	0	−1	0
		ψ_3	0	0	1

Table D.12: The basis vectors of the Γ_3 irreducible representation of the space group $P12_1/c1$ with $k = (0.5,\ 0,\ 0)$ for the Cu_{k2} $4e$ site, where m_a, m_b and m_c are the moment components along the crystallographic unit cell directions a, b and c.

Atom number	Coordinates	Basis vector	m_a	m_b	m_c
Atom 1	(0.72862, 0.53568, 0.16828)	ψ_1	1	0	0
		ψ_2	0	1	0
		ψ_3	0	0	1
Atom 2	(0.27138, 0.03568, 0.33172)	ψ_1	−1	0	0
		ψ_2	0	1	0
		ψ_3	0	0	−1
Atom 3	(0.27138, 0.46432, 0.83172)	ψ_1	−1	0	0
		ψ_2	0	−1	0
		ψ_3	0	0	−1
Atom 4	(0.72862, 0.96432, 0.66828)	ψ_1	1	0	0
		ψ_2	0	−1	0
		ψ_3	0	0	1

Table D.13: The basis vectors of the Γ_3 irreducible representation of the space group $P12_1/c1$ with $k = (0.5,\ 0,\ 0)$ for the Cu_h $4e$ site, where m_a, m_b and m_c are the moment components along the crystallographic unit cell directions a, b and c.

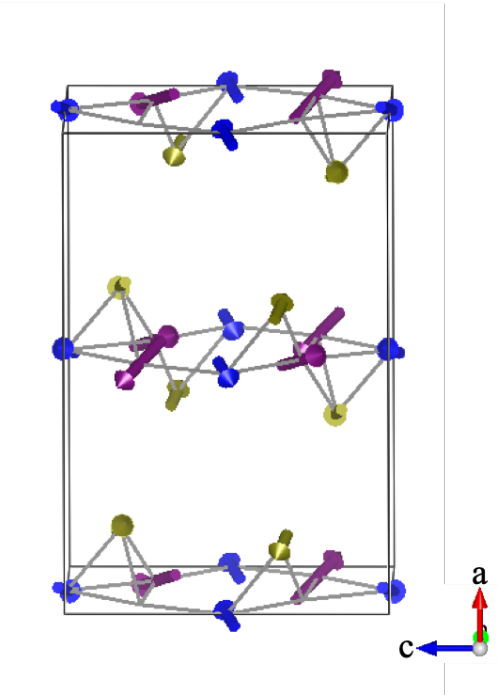

Figure D.13: Averievite magnetic structure viewed from the side, refined from WISH data (banks 1 and 2) in Γ_1 of space group $P12_1/c1$ for the three Cu sites Cu_{k1} (blue), Cu_{k2} (purple) and Cu_h (yellow). There is a net directional component in the kagome layer along the b direction.

Appendix E

Appendix for Chapter 8

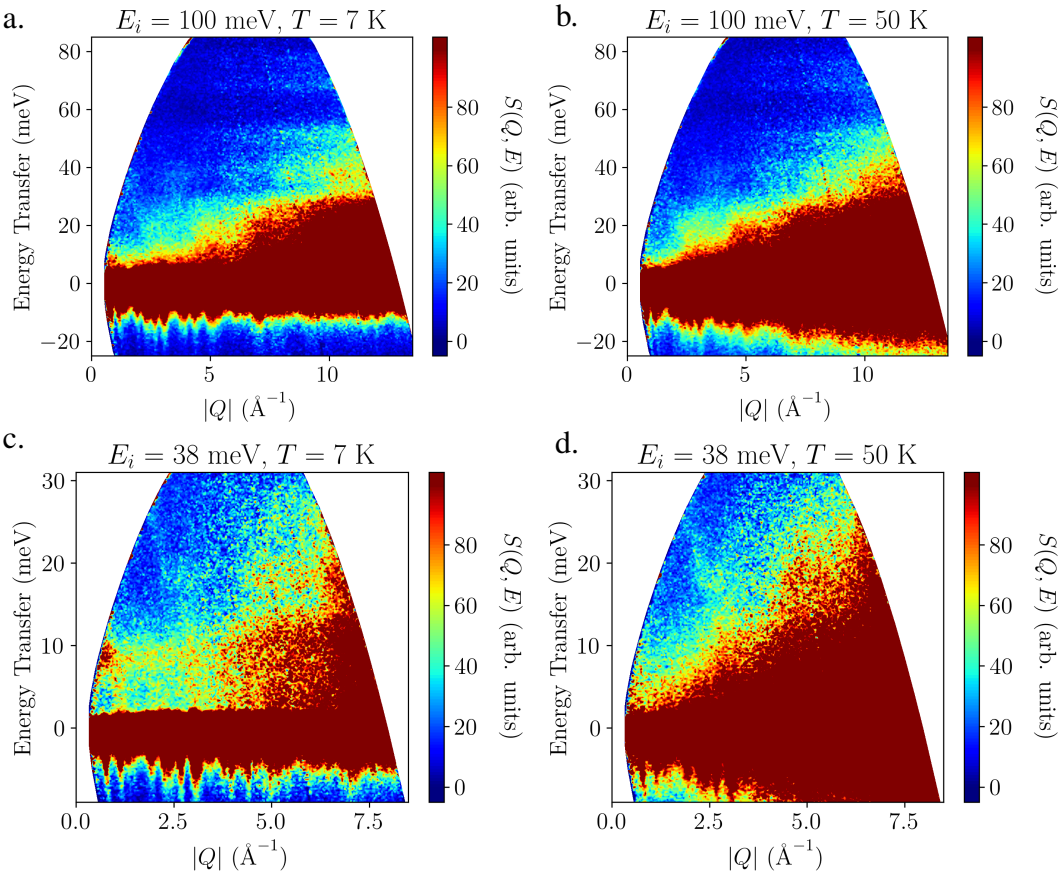

Figure E.1: Averievite, $S(Q,E)$ measured on MERLIN with E_i =100 meV (**top.**) and $E_i = 38$ meV (**bottom.**) at $T = 7$ K (**left.**) and $T = 50$ K (**right.**).

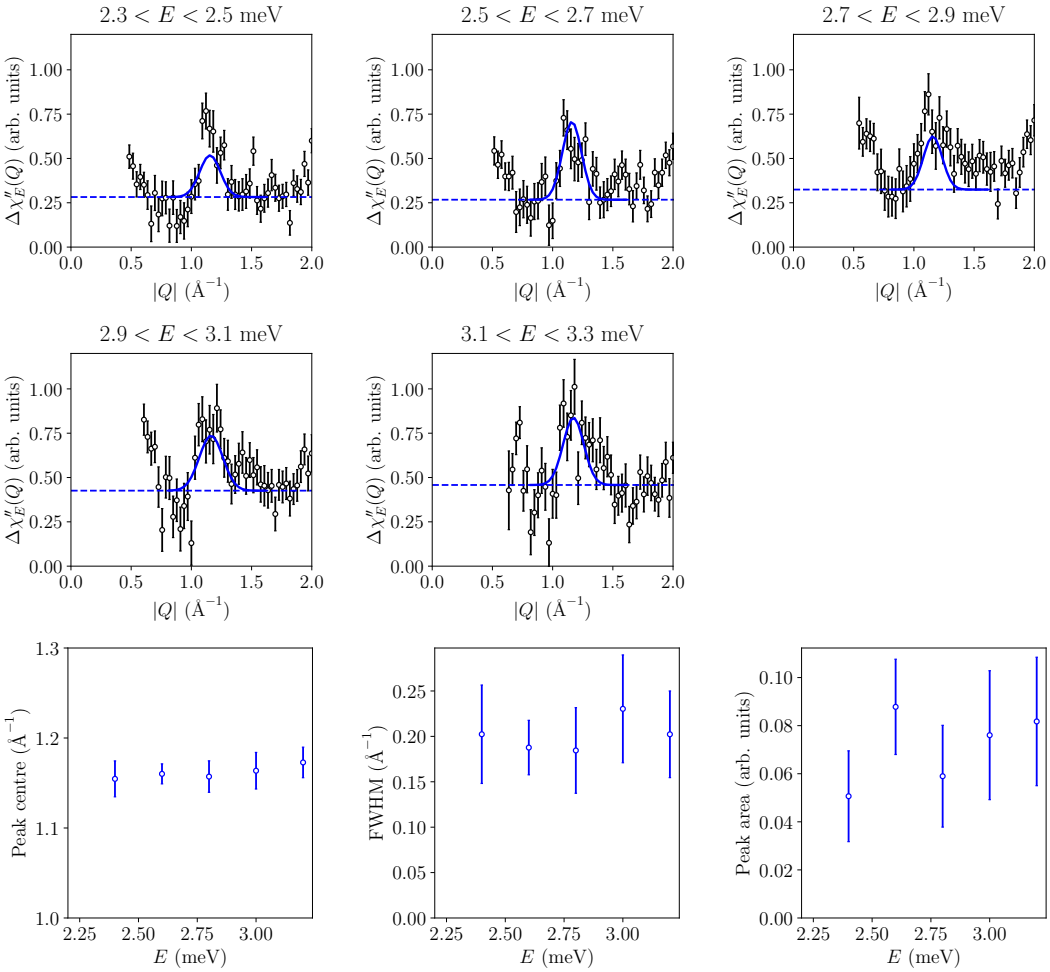

Figure E.2: Averievite IN5 data obtained with $E_i = 5.11$ meV at $T = 1.5$ K. (**Top.**) $\Delta\chi''_E(Q)$ obtained by integrating $\Delta\chi''(Q,E)$ over various energy ranges (black) fitted with two Gaussians and a flat background (red lines). (**Bottom.**) Parameters obtained from the Gaussian fits.

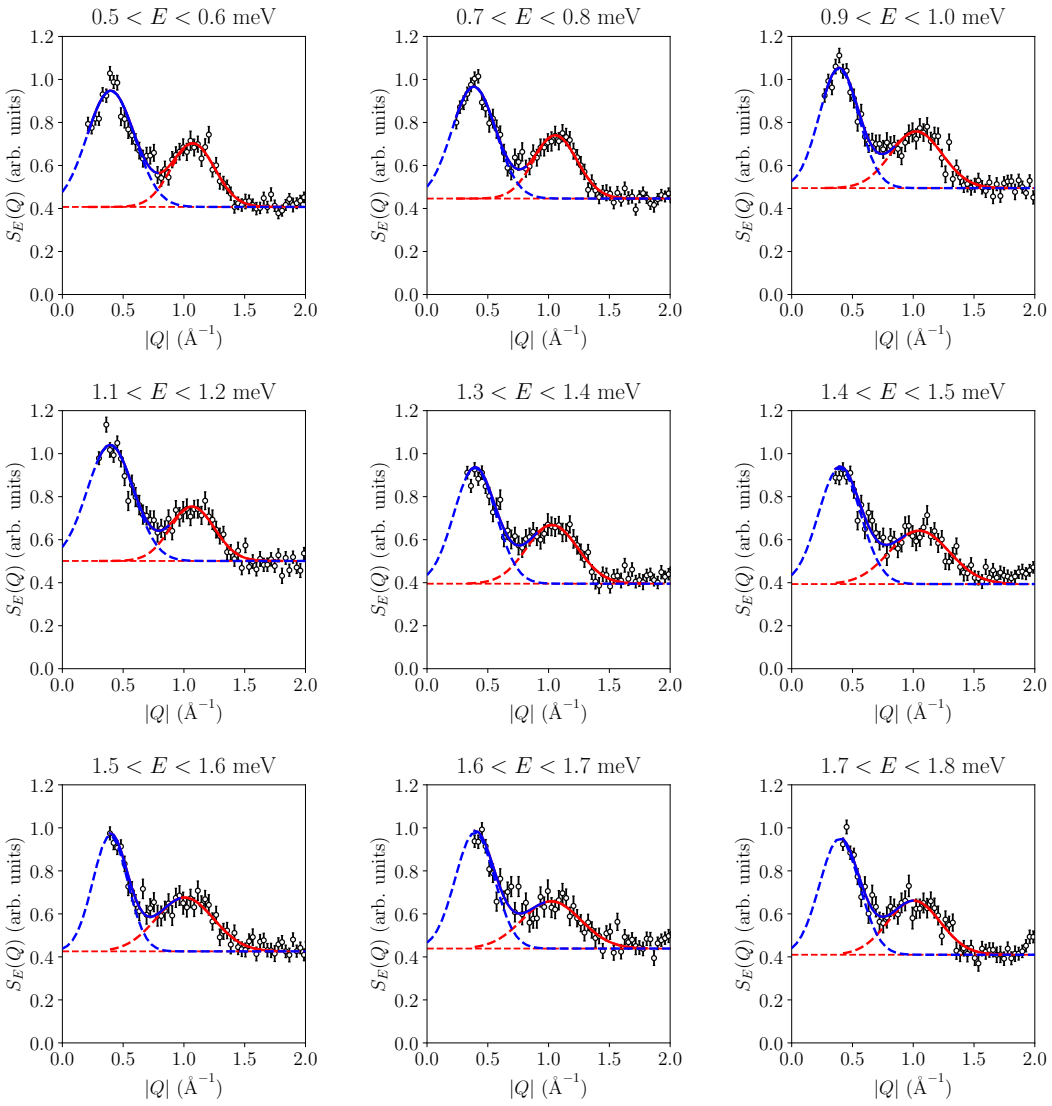

Figure E.3: Zn_1-averievite IN5 data obtained with $E_i = 3.55$ meV at $T = 1.5$ K. $S_E(Q)$ obtained by integrating $S(Q,E)$ over various energy ranges (black) fitted with two Gaussians and a flat background.

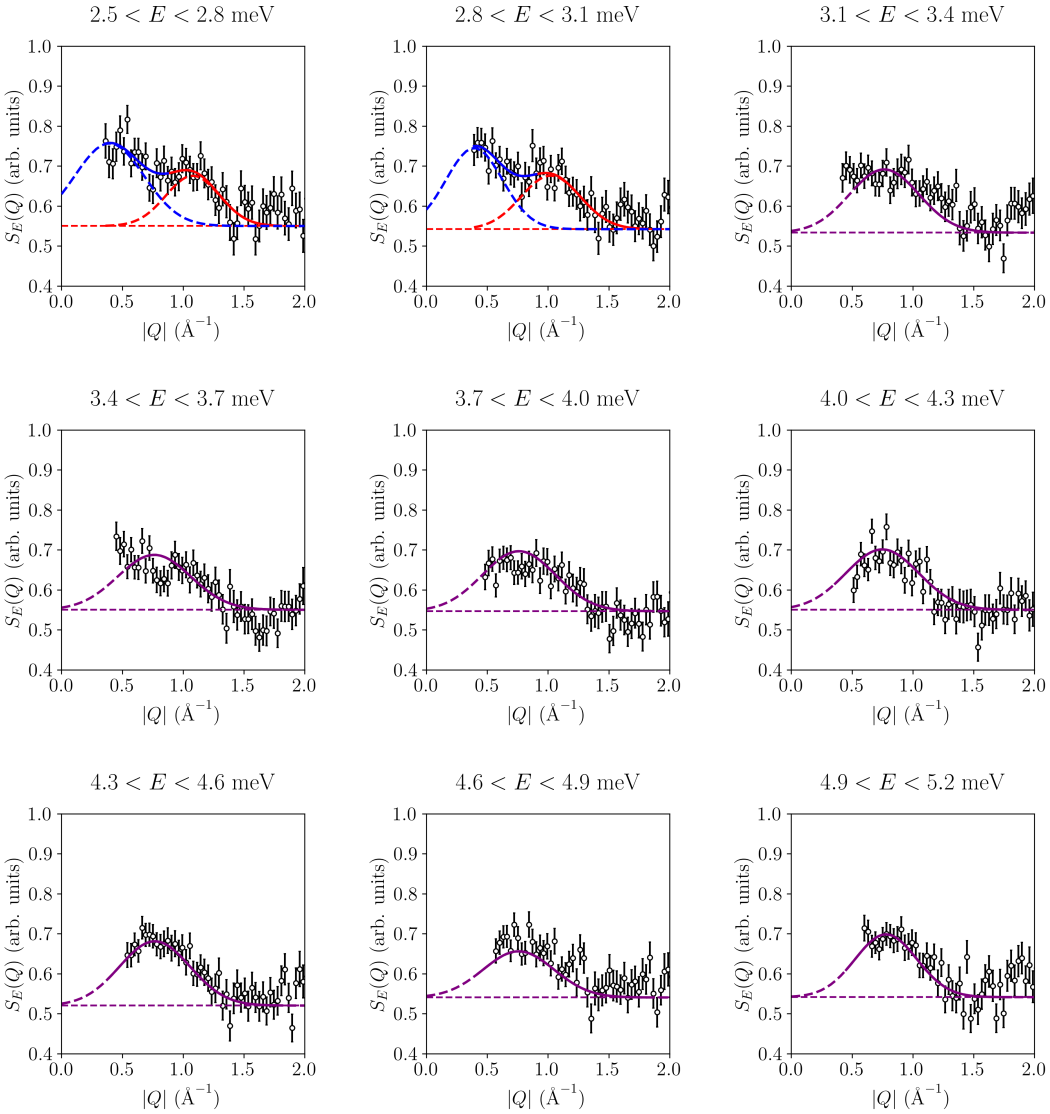

Figure E.4: Zn_1-averievite PANTHER data obtained with $E_i = 12.5$ meV at $T = 1.5$ K. $S_E(Q)$ obtained by integrating $S(Q,E)$ over various energy ranges (black) fitted with Gaussians and a flat background.

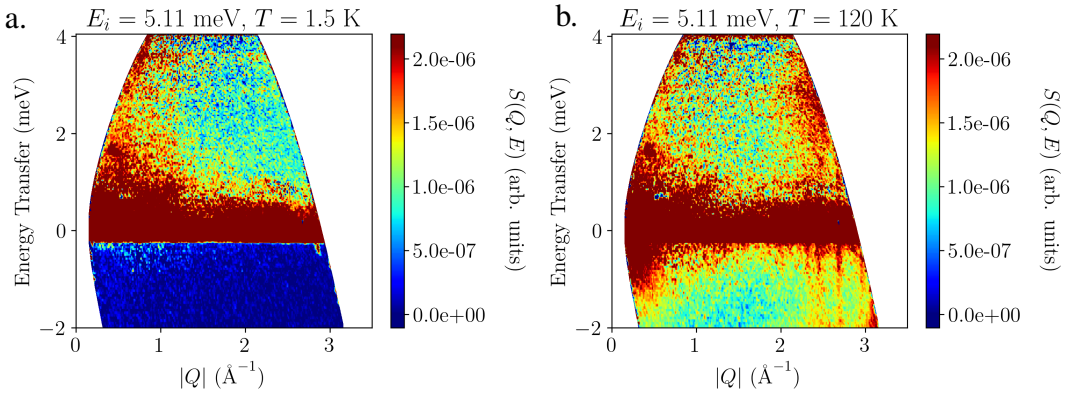

Figure E.5: Zn_2-averievite, $S(Q,E)$ measured on IN5 with $E_i = 5.11$ meV. **a.** $T = 1.5$ K. **b.** $T = 120$ K.